



รายงานวิจัยฉบับสมบูรณ์

โครงการ "การดูดซับคาร์บอนไดออกไซด์ในช่วงการไหลใหม่
ของเครื่องปฏิกรณ์ฟลูอิไดซ์เบดแบบหมุนเวียน
ที่มีอัตราการไหลอนุภาคของแข็งสูงด้วยการทดลอง
และการจำลองพลศาสตร์ของไหลเชิงคำนวณ"

โดย รองศาสตราจารย์ ดร.เบญจพล เฉลิมสินสุวรรณ และคณะ

มิถุนายน 2559

สัญญาเลขที่ TRG5780205

รายงานวิจัยฉบับสมบูรณ์

โครงการ "การดูดซับคาร์บอนไดออกไซด์ในช่วงการไหลใหม่
ของเครื่องปฏิกรณ์ฟลูอิไดซ์เบดแบบหมุนเวียน
ที่มีอัตราการไหลอนุภาคของแข็งสูงด้วยการทดลอง
และการจำลองพลศาสตร์ของไหลเชิงคำนวณ"

ผู้วิจัย

รองศาสตราจารย์ ดร.เบญจพล เฉลิมสินสุวรรณ ศาสตราจารย์ ดร.พรพจน์ เปี่ยมสมบูรณ์ ภาควิชาเคมีเทคนิค คณะวิทยาศาสตร์ จุฬาลงกรณ์มหาวิทยาลัย

สนับสนุนโดยสำนักงานคณะกรรมการการอุดมศึกษา และ จุฬาลงกรณ์มหาวิทยาลัย

(ความเห็นในรายงานนี้เป็นของผู้วิจัย สกว. ไม่จำเป็นต้องเห็นด้วยเสมอไป)

บทคัดย่อ

รหัสโครงการ: TRG5780205

ชื่อโครงการ: การดูดซับคาร์บอนไดออกไซด์ในช่วงการไหลใหม่ของเครื่องปฏิกรณ์

ฟลูอิไดซ์เบดแบบหมุนเวียนที่มีอัตราการไหลอนุภาคของแข็งสูงด้วย

การทดลองและการจำลองพลศาสตร์ของไหลเชิงคำนวณ

ชื่อนักวิจัย: รองศาสตราจารย์ ดร.เบญจพล เฉลิมสินสุวรรณ

ภาควิชาเคมีเทคนิค คณะวิทยาศาสตร์

จุฬาลงกรณ์มหาวิทยาลัย

ทื่อยู่อีเมล : benjapon.c@chula.ac.th

ระยะเวลาโครงการ: 2 ปี

โครงการนี้มีวัตถุประสงค์เพื่อทำการทดลองและการจำลองพลศาสตร์ของใหลเชิง คำนวณสำหรับวิเคราะห์การดักจับคาร์บอนไดออกไซด์ในช่วงการไหลใหม่ของเครื่องปฏิกรณ์ ฟลูอิไดซ์เบดแบบหมุนเวียนที่มีอัตราการใหลอนุภาคของแข็งสูง นอกจากนี้ ผลของตัวแปร กระบวนการต่างๆ ที่มีต่อการดักจับคาร์บอนไดออกไซด์และรูปแบบวิธีการดำเนินการช่วงการ ไหลใหม่ของเครื่องปฏิกรณ์ฟลูอิไดซ์เบดแบบหมุนเวียนที่มีอัตราการไหลอนุภาคของแข็งสูง สำหรับการประยุกต์ใช้ในอุตสาหกรรมต่างๆ ได้ถูกเสนอ การดำเนินการวิจัยจะประกอบด้วยการ ทบทวนวรรณกรรมที่เกี่ยวข้อง การออกแบบและสร้างเครื่องปฏิกรณ์ฟลูอิไดซ์เบดแบบ หมุนเวียนที่มีอัตราการใหลอนุภาคของแข็งสูง การทำการทดลองและวิเคราะห์การดักจับ คาร์บอนไดออกไซด์ การพัฒนาแบบจำลองพลศาสตร์ของไหลเชิงคำนวณของเครื่องปฏิกรณ์ ต้นแบบฟลูอิไดซ์เบดแบบหมุนเวียนที่มีอัตราการใหลอนุภาคของแข็งสูง การจำลองพลศาสตร์ ของใหลเชิงคำนวณและวิเคราะห์การดักจับคาร์บอนไดออกไซด์ การสรุปผลของตัวแปร กระบวนการต่างๆ และ การเสนอวิธีการดำเนินการเครื่องปฏิกรณ์กับการประยุกต์ใช้งานต่างๆ สำหรับผลที่ได้รับ ผลการทดลองและผลการจำลองพลศาสตร์ของไหลเชิงคำนวณที่ได้จากเครื่อง ปฏิกรณ์ฟลูอิไดซ์เบดแบบหมุนเวียนที่มีอัตราการไหลอนุภาคของแข็งสูงให้ผลสอดคล้องกัน รูปแบบการใหลที่ค้นพบใหม่ หรือ รูปแบบการใหลแบบปั่นป่วนหมุนเวียน จะส่งผลให้มีการ กระจายตัวของอนุภาคของแข็งเกิดได้ดี และ มีความเหมาะสมกับกระบวนการที่มีปฏิกิริยาเคมีที่ มีอัตราการเกิดปฏิกิริยาสูง โดยรูปแบบการใหลแบบปั่นป่วนหมุนเวียนจะมีการดักจับแก๊ส คาร์บอนไดออกไซด์สูงที่สุดเมื่อเปรียบเทียบกับรูปแบบการไหลข้างเคียงอื่นๆ และ ตัวแปรความ เข้มข้นของไอน้ำจะส่งผลต่อประสิทธิภาพในการดักจับแก๊สคาร์บอนไดออกไซด์สูงที่สุด

คำหลัก: เครื่องปฏิกรณ์ฟลูอิไดซ์เบดแบบหมุนเวียน, การจำลองพลศาสตร์ของไหลเชิง คำนวณ, การทดลอง, ช่วงการไหล, การดักจับแก๊สคาร์บอนไดออกไซด์

Abstract

Project Code: TRG5780205

Project Title: Carbon Dioxide Sorption in Novel Flow Regime of Circulating Fluidized

Bed Reactor with High Solid Particle Flux using Experiment and

Computational Fluid Dynamics Simulation

Investigator: Associate Professor Dr.Benjapon Chalermsinsuwan

Department of Chemical Technology, Faculty of Science,

Chulalongkorn University

E-mail Address: benjapon.c@chula.ac.th

Project Period: 2 years

In this study, the objective is to conduct the experiment and computational fluid dynamics simulation for analyzing the carbon dioxide sorption in novel flow regime of circulating fluidized bed reactor with high solid particle flux. In addition, the summary of the effect of system parameters on carbon dioxide sorption and the operating methodology for other applications in novel flow regime of circulating fluidized bed reactor with high solid particle flux are proposed. The research methodologies are consisting of surveying the literatures, designing and constructing the circulating fluidized bed reactor unit system with high solid particle flux, conducting the experiment and analyzing the carbon dioxide sorption, developing the computational fluid dynamics model of circulating fluidized bed reactor with high solid particle flux, performing the simulation and analyzing the carbon dioxide sorption, summarizing the effect of various parameters and proposing the operating methodology of the reactor with various applications. About the obtained results, the experiment and computational fluid dynamics simulation results in circulating fluidized bed reactor with high solid particle flux are consistent with each other. The novel flow regime or the circulating-turbulent flow regime gives high efficiency of solid particles dispersing and is suitable for occurring the chemical reaction with high rate of reaction. In addition, the circulating-turbulent flow regime captures the carbon dioxide higher than the conventional neighbor flow regimes. The results from the design of experiment show that water concentration provides the highest effect to the carbon dioxide capture efficiency.

Keywords: Circulating Fluidized Bed Reactor, Computational Fluid Dynamics
Simulation, Experiment, Flow Regime, Carbon Dioxide Sorption

Executive Summary

รหัสโครงการ: TRG5780205

ชื่อโครงการ (ภาษาไทย): การดูดซับคาร์บอนไดออกไซด์ในช่วงการไหลใหม่ของเครื่อง

ปฏิกรณ์ฟลูอิไดซ์เบดแบบหมุนเวียนที่มีอัตราการไหลอนุภาค ของแข็งสูงด้วยการทดลองและการจำลองพลศาสตร์ของไหลเชิง

คำนวณ

(ภาษาอังกฤษ): Carbon Dioxide Sorption in Novel Flow Regime of

Circulating Fluidized Bed Reactor with High Solid Particle Flux using Experiment and Computational Fluid Dynamics

Simulation

ชื่อหัวหน้าโครงการ หน่วยงานสังกัด และที่อยู่

ชื่อ-สกุล: รองศาสตราจารย์ ดร.เบญจพล เฉลิมสินสุวรรณ

หน่วยงาน: ภาควิชาเคมีเทคนิค คณะวิทยาศาสตร์

จุฬาลงกรณ์มหาวิทยาลัย

ที่อยู่ : 254 ถนนพญาไท แขวงวังใหม่ เขตปทุมวัน กรุงเทพฯ 10330

โทรศัพท์: 02-218-7682, 087-547-1155 โทรสาร : 02-255-5831

Email address: benjapon.c@chula.ac.th

งบประมาณทั้งโครงการ: 480,000 บาท

ระยะเวลาดำเหินงาน: 2 ปี (ตั้งแต่วันที่ 2 มิถุนายน 2557 ถึงวันที่ 1 มิถุนายน 2559)

ปัญหาที่ทำวิจัยและความสำคัญ

ปัจจุบัน ภาวะโลกร้อนเป็นปัญหาสำคัญที่ประชากรโลกกำลังเผชิญกันอยู่ ในช่วงยี่สิบปีที่ ผ่านมา อุณหภูมิเฉลี่ยของชั้นบรรยากาศโลกมีค่าสูงที่สุดเป็นประวัติการณ์ และ ยังมีแนวโน้ม เพิ่มขึ้นอีกอย่างต่อเนื่อง เป็นที่ทราบกันดีว่าภาวะโลกร้อนได้ส่งผลกระทบต่อความหลากหลาย ทางชีวภาพของโลกและก่อให้เกิดภัยพิบัติทางธรรมชาติต่าง ๆ หนึ่งในสาเหตุหลักที่ก่อให้เกิด ปัญหานี้ขึ้น คือ กิจกรรมในการดำรงชีวิตของมนุษย์ที่ปลดปล่อยแก๊สเรือนกระจก อันได้แก่ แก๊ส คาร์บอนไดออกไซด์ แก๊สในตรัสออกไซด์ และ แก๊สมีเทน ออกสู่ชั้นบรรยากาศ ซึ่งเมื่อทำการ พิจารณาในแง่ของปริมาณแก๊สเรือนกระจกที่ถูกปล่อยและเวลาชั่วชีวิตที่คงอยู่ในชั้นบรรยากาศ พบว่า แก๊สคาร์บอนไดออกไซด์เป็นแก๊สเรือนกระจกที่ก่อให้เกิดปัญหานี้มากที่สุด และกิจกรรม หลักที่ปลดปล่อยแก๊สคาร์บอนไดออกไซด์ออกสู่บรรยากาศปริมาณมากที่สุด คือ การผลิตพลังงาน

จากเชื้อเพลิงถ่านหิน ดังนั้น จึงมีความจำเป็นที่จะพิจารณาทางเลือกใหม่ในการลดปริมาณการ ปลดปล่อยแก๊สคาร์บอนไดออกไซด์ ทางเลือกในการกำจัดหรือแยกแก๊สคาร์บอนไดออกไซด์ที่ เกิดขึ้นจากการผลิตพลังงานดังกล่าวจึงเป็นทางออกหนึ่งที่ได้รับความสนใจ โดยมีแนวคิดเป็นสาม กระบวนการหลัก คือ กระบวนการก่อนการเผาไหม้ กระบวนการหลังการเผาไหม้ และ กระบวนการเผาไหม้ด้วยเชื้อเพลิงที่มีความเข้มข้นออกซิเจนสูง เพื่อที่จะดักจับ คาร์บอนไดออกไซด์จากกระบวนการดั้งเดิม กระบวนการหลังการเผาไหม้ได้ถูกใช้ ทั้งนี้ การดัก จับด้วยตัวดูดซับของแข็งถือเป็นเทคโนโลยีที่กำลังได้รับความสนใจเนื่องจากข้อดีหลายประการ

การดักจับด้วยตัวดูดซับของแข็งประกอบด้วยสองขั้นตอน คือ การดูดซับและการคายซับ ในขั้นแรก แก๊สเผาไหม้จะถูกส่งเข้าไปในเครื่องปฏิกรณ์ตัวที่หนึ่งเพื่อสัมผัสกับตัวดูดซับของแข็ง และ เกิดการดูดซับคาร์บอนไดออกไซด์ ในขั้นต่อมา ตัวดูดซับของแข็งจะถูกส่งไปยังเครื่อง ปฏิกรณ์ตัวที่สองเพื่อเกิดปฏิกิริยาคายซับคาร์บอนไดออกไซด์ด้วยความร้อน จากนั้น ตัวดูดซับ ของแข็งที่ผ่านการคายซับจะถูกส่งกลับไปยังเครื่องปฏิกรณ์ตัวที่หนึ่ง และ ดำเนินการซ้ำเป็น วงรอบต่อไป ตัวดูดซับของแข็งโพแทสเซียมคาร์บอเนตมีความน่าสนใจในการนำมาใช้งาน โดย จากงานวิจัยที่ผ่านมา พบว่า มีผู้วิจัยจำนวนมากสนใจการปรับปรุงประสิทธิภาพการดูดซับ คาร์บอนไดออกไซด์ของตัวดูดซับของแข็ง อย่างไรก็ตาม ยังพบปัญหาเรื่องการเกิดปฏิกิริยาเคมีที่ ช้า และ การมีความจุของการดูดซับคาร์บอนไดออกไซด์เพียงแค่ร้อยละ 80 ของค่าทางทฤษฎี ทั้งนี้เป็นผลมาจากการสัมผัสกันที่ไม่เหมาะสมภายในเครื่องปฏิกรณ์ และ ภาวะการดำเนินการ เครื่องปฏิกรณ์ที่ไม่เหมาะสม ดังนั้น พฤติกรรมการไหลของเครื่องปฏิกรณ์ฟลูอิไดซ์เบด/เครื่อง ปฏิกรณ์ฟลูอิไดซ์เบดแบบหมุนเวียนที่เหมาะสมจึงถูกเสนอเป็นคำตอบของปัญหานี้ โดยเครื่อง ปฏิกรณ์ฟลูอิไดซ์เบด/เครื่องปฏิกรณ์ฟลูอิไดซ์เบดแบบหมุนเวียนถูกใช้งานอย่างแพร่หลายใน กระบวนการที่มีการใหลหลายสถานะ พฤติกรรมการใหลต่างๆ จะเปลี่ยนไปเมื่อทำการเพิ่ม ความเร็วแก๊สป้อนเข้า ได้แก่ เบดแบบฟองแก๊ส เบดแบบปั่นป่วน เบดแบบฟลูอิไดเซชันความเร็ว ัสูง และ เบดแบบเบาบาง อย่างไรก็ตาม การใช้งานเครื่องปฏิกรณ์ฟลูอิไดซ์เบด/เครื่องปฏิกรณ์ ฟลูอิไดซ์เบดแบบหมุนเวียนยังถูกใช้สำหรับกระบวนการที่มีอัตราการไหลของแข็งต่ำ เมื่อเร็ว ๆ นี้ ช่วงการไหลใหม่ภายในเครื่องปฏิกรณ์ฟลูอิไดซ์เบดแบบหมุนเวียนที่มีอัตราการไหลของแข็งสูงได้ ถูกคันพบ เครื่องปฏิกรณ์นี้มีข้อดี คือ มีความเข้มขันของแข็งสูงและมีการกระจายตัวสม่ำเสมอ การดำเนินการด้วยกระบวนการที่มีอัตราการไหลของแข็งสูงน่าจะช่วยให้มีการดักจับ คาร์บอนไดออกไซด์ที่สูงขึ้น โดยงานวิจัยที่ผ่านมาส่วนใหญ่จะใช้วิธีการทดลองจริง อย่างไรก็ตาม ยังมีอีกวิธีการหนึ่งที่ใช้ศึกษาได้ คือ วิธีการพลศาสตร์ของไหลเชิงคำนวณ ที่เป็นวิธีการสำคัญที่ใช้ ออกแบบกระบวนการทางวิศวกรรม วิธีการนี้เป็นสาขาหนึ่งของกลศาสตร์ของไหลที่ใช้ระเบียบวิธี ทางคณิตศาสตร์ในการวิเคราะห์ปัญหาที่สนใจ สำหรับเครื่องปฏิกรณ์ฟลูอิไดซ์เบด/เครื่องปฏิกรณ์ ฟลูอิไดซ์เบดแบบหมุนเวียน วิธีออยเลอเลียนร่วมกับทฤษฎีจลน์การไหลของของแข็งจะเหมาะสม ในการแก้ปัญหาซึ่งจะแก้สมการอนุรักษ์ของแต่ละวัฏภาคแยกกัน นอกจากนี้ สำหรับกระบวนการ ที่มีปฏิกิริยาเคมีเกิดขึ้น จะต้องมีการป้อนสมการจลนศาสตร์เข้าไปร่วมในการคำนวณด้วย

ผลการดำเนินงาน

ในการวิจัยนี้เป็นการศึกษาเพื่อหาอุทกพลศาสตร์และปฏิกิริยาเคมีที่เกิดขึ้นในเครื่อง ปฏิกรณ์ฟลูอิไดซ์เบด/เครื่องปฏิกรณ์ฟลูอิไดซ์เบดแบบหมุนเวียนเพื่อนำไปใช้ในกระบวนการที่มี การดูดซับแก๊สคาร์บอนไดออกไซด์เกิดขึ้น ทำการศึกษาเพื่อหาสมการอัตราการเกิดปฏิกิริยาการ ดูดซับแก๊สคาร์บอนไดออกไซด์ที่สอดคล้องกับผลการทดลองจริง หาภาวะในการดำเนินการที่ เหมาะสมต่อกระบวนการการดูดซับแก๊สคาร์บอนไดออกไซด์และมีประสิทธิภาพในการดูดซับที่สูง ที่สุดเพื่อให้ได้แนวทางนำไปใช้ในการออกแบบเครื่องปฏิกรณ์จริงได้ รวมทั้ง เสนอรูปแบบวิธีการ ดำเนินการช่วงการไหลใหม่ของเครื่องปฏิกรณ์ฟลูอิไดซ์เบดแบบหมุนเวียนสำหรับการประยุกต์ใช้ ในอุตสาหกรรมต่าง ๆ

ผลของรูปแบบการใหลในเครื่องปฏิกรณ์ฟลูอิไดซ์เบด/เครื่องปฏิกรณ์ฟลูอิไดซ์เบดแบบ หมุนเวียนที่มีอัตราการใหลอนุภาคของแข็งสูงด้วยตัวดูดซับของแข็งสามารถคำนวณปริมาณการ ดักจับคาร์บอนไดออกไซด์ที่ขึ้นอยู่กับรูปแบบการใหลภายในเครื่องปฏิกรณ์ รูปแบบการใหลแบบ เบดนิ่งและรูปแบบการใหลฟลูอิไดเซชันแบบสลักกิ้งมีค่าปริมาณการดักจับต่ำ รูปแบบการใหล ฟลูอิไดเซชันแบบปั่นป่วน (แบบปั่นป่วนหมุนเวียน) มีค่าสูงสุด อย่างไรก็ตาม ปริมาณความ เข้มขันที่ทางออกของรูปแบบการใหลเบดนิ่งให้ปริมาณแก๊สคาร์บอนไดออกไซด์สูงเนื่องจาก ระยะเวลาในการทำปฏิกิริยานานแต่ปริมาณการดักจับแก๊สคาร์บอนไดออกไซด์มีค่าต่ำสุด และจาก พฤติกรรมของการจัดเรียงตัวตัวดูดซับของแข็งในเบดนิ่งทำให้สูญเสียพื้นที่ในการทำปฏิกิริยาของ แก๊สคาร์บอนไดออกไซด์ที่เข้ามา ในงานวิจัยนี้รูปแบบการไหลแบบปั่นป่วน (แบบปั่นป่วน หมุนเวียน) มีปริมาณการดักจับแก๊สคาร์บอนไดออกไซด์สูงสุดเนื่องจากระบบการผสมย้อนกลับสูง

ในการศึกษาถึงรูปแบบการไหลที่เกิดขึ้น พบว่า ช่วงความเร็วที่ทำให้รูปแบบการไหลมี ความเหมาะสมมากที่สุด คือ รูปแบบการไหลแบบปั่นป่วนหมุนเวียน ที่จะมีการกระจายตัวของ อนุภาคของแข็งในท่อไรเซอร์ได้ดี มีสัดส่วนของอนุภาคของแข็งที่มากและใกล้เคียงกันตลอด ช่วงความสูงของท่อไรเซอร์ ทำให้การใช้รูปแบบการไหลดังกล่าวมีความเหมาะสมที่จะนำไปใช้ใน กระบวนการที่มีปฏิกิริยาเคมี ในการหาภาวะในการดำเนินการที่เหมาะสมที่สุดนั้น ตัวแปรอิสระที่ นำมาศึกษาจะประกอบไปด้วย อุณหภูมิ ความเข้มขันของแก๊สคาร์บอนไดออกไซด์ ความเข้มขันของไอน้ำและความเร็วของแก๊สขาเข้า พบว่า ปริมาณของแก๊สคาร์บอนไดออกไซด์ที่สามารถดูด ซับได้มากที่สุด คือ ร้อยละ 93.36 โดยมวล โดยมีภาวะในการดำเนินการของอุณหภูมิเท่ากับ 60 องศาเซลเซียส ความเข้มขันของแก๊สคาร์บอนไดออกไซด์ที่กูกดูดซับน้อยที่สุดเท่ากับร้อยละ 20 โดยมวล ความเข้มขันของได้สามารถดำเนินการดำเนินการของอุณหภูมิเท่ากับ 80 องศาเซลเซียส ความเข้มขันของแก๊สคาร์บอนไดออกไซด์ที่กูกดูดซับน้อยที่สุดเท่ากับร้อยละ 77.38 โดยมวลที่ ภาวะในการดำเนินการของอุณหภูมิเท่ากับ 80 องศาเซลเซียส ความเข้มขันของแก๊สคาร์บอนไดออกไซด์ที่กูกดูดซับน้อยที่สุดเท่ากับร้อยละ 77.38 โดยมวลที่ กาวะในการดำเนินการของอุณหภูมิเท่ากับ 80 องศาเซลเซียส ความเข้มขันของแก๊สคาร์บอนไดออกไซด์ที่กาวบร้อยละ 20 โดยมวล ความเข้มขันของน้ำเท่ากับร้อยละ 10 โดยมวล และ ความเร็วของแก๊สคาร์บอนไดออกไซด์

ที่ดูดซับได้นั้นมีปริมาณมากกว่าการใช้เครื่องปฏิกรณ์ชนิดอื่น ตัวแปรอิสระที่ส่งผลต่อ ประสิทธิภาพในการดูดซับแก๊สคาร์บอนไดออกไซด์สูงที่สุดนั้น คือ ความเข้มข้นของไอน้ำ เมื่อ เปรียบเทียบผลเชิงอุทกพลศาสตร์ พบว่า สัดส่วนของอนุภาคของแข็งที่อยู่ภายในท่อไรเซอร์ที่ ภาวะในการดำเนินการของอุณหภูมิเท่ากับ 60 องศาเซลเซียส ความเข้มขันของแก๊ส คาร์บอนไดออกไซด์เท่ากับร้อยละ 20 โดยมวล ความเข้มขันของไอน้ำเท่ากับร้อยละ 15 โดยมวล และความเร็วของแก๊สขาเข้าเท่ากับ 1.75 เมตรต่อวินาที มีค่าในช่วง 0.38 ถึง 0.40 ตลอด ช่วงความสูงของท่อไรเซอร์ ในขณะที่ ที่ภาวะในการดำเนินการของอุณหภูมิเท่ากับ 80 องศา เซลเซียส ความเข้มข้นของแก๊สคาร์บอนไดออกไซด์เท่ากับร้อยละ 20 โดยมวล ความเข้มข้นของ ไอน้ำเท่ากับร้อยละ 10 โดยมวลและความเร็วของแก๊สขาเข้าเท่ากับ 1.25 เมตรต่อวินาที มีสัดส่วน ของอนุภาคของแข็งเท่ากับ 0.40 ถึง 0.41 แต่มีการกระจายตัวที่น้อยกว่า ประสิทธิภาพในการดูด ซับจึงน้อยกว่า นอกจากนี้ ผลของความเร็วในแนวแกนของของแข็งแล็ดงให้เห็นถึงการลดลงของ รูปแบบการไหลแบบแกนใน-วงนอก ทำมีประสิทธิภาพการดูดซับแก๊สคาร์บอนไดออกไซด์ดีขึ้น

สรุปผลการวิจัย

โครงการนี้มีวัตถุประสงค์เพื่อทำการทดลองและการจำลองพลศาสตร์ของใหลเชิงคำนวณ สำหรับวิเคราะห์การดักจับคาร์บอนไดออกไซด์ในช่วงการไหลใหม่ของเครื่องปฏิกรณ์ฟลูอิไดซ์เบด แบบหมุนเวียนที่มีอัตราการใหลอนุภาคของแข็งสูง นอกจากนี้ ผลของตัวแปรกระบวนการต่างๆ ที่มีต่อการดักจับคาร์บอนไดออกไซด์และรูปแบบวิธีการดำเนินการช่วงการไหลใหม่ของเครื่อง ปฏิกรณ์ฟลูอิไดซ์เบดแบบหมุนเวียนที่มีอัตราการไหลอนุภาคของแข็งสูงสำหรับการประยุกต์ใช้ใน อุตสาหกรรมต่างๆ ได้ถูกเสนอ การดำเนินการวิจัยจะประกอบด้วยการทบทวนวรรณกรรมที่ เกี่ยวข้อง การออกแบบและสร้างเครื่องปฏิกรณ์ฟลูอิไดซ์เบดแบบหมุนเวียนที่มีอัตราการไหล อนุภาคของแข็งสูง การทำการทดลองและวิเคราะห์การดักจับคาร์บอนไดออกไซด์ การพัฒนา แบบจำลองพลศาสตร์ของใหลเชิงคำนวณของเครื่องปฏิกรณ์ต้นแบบฟลูอิไดซ์เบดแบบหมุนเวียน ที่มีอัตราการไหลอนุภาคของแข็งสูง การจำลองพลศาสตร์ของไหลเชิงคำนวณและวิเคราะห์การดัก จับคาร์บอนใดออกไซด์ การสรุปผลของตัวแปรกระบวนการต่างๆ และ การเสนอวิธีการ ดำเนินการเครื่องปฏิกรณ์กับการประยุกต์ใช้งานต่างๆ สำหรับผลที่ได้รับ ผลการทดลองและผล การจำลองพลศาสตร์ของใหลเชิงคำนวณที่ได้จากเครื่องปฏิกรณ์ฟลูอิไดซ์เบดแบบหมุนเวียนที่มี อัตราการใหลอนุภาคของแข็งสูงให้ผลสอดคล้องกัน รูปแบบการใหลที่ค้นพบใหม่ หรือ รูปแบบ การใหลแบบปั่นป่วนหมุนเวียน จะส่งผลให้มีการกระจายตัวของอนุภาคของแข็งเกิดได้ดี และ มี ความเหมาะสมกับกระบวนการที่มีปฏิกิริยาเคมีที่มีอัตราการเกิดปฏิกิริยาสูง โดยรูปแบบการใหล แบบปั่นป่วนหมุนเวียนจะมีการดักจับแก๊สคาร์บอนไดออกไซด์สูงที่สุดเมื่อเปรียบเทียบกับรูปแบบ การใหลข้างเคียงอื่นๆ และ ตัวแปรความเข้มข้นของไอน้ำจะส่งผลต่อประสิทธิภาพในการดักจับ แก๊สคาร์บอนไดออกไซด์สูงที่สุด

ข้อเสนอแนะ

กระบวนการการดูดซับแก๊สคาร์บอนไดออกไซด์โดยใช้ตัวดูดซับของแข็งในเครื่องปฏิกรณ์ ฟลูอิไดซ์เบดแบบหมุนเวียนในงานวิจัยนี้ เป็นการศึกษาถึงกระบวนการการดูดซับเพียงอย่างเดียว เท่านั้น ยังต้องมีการศึกษาในส่วนของการคายซับของตัวดูดซับของแข็ง เพื่อให้ผลที่ได้เป็นผลที่ สามารถนำไปใช้ในกระบวนการการดูดซับได้จริงต่อไป

ผลงานทางวิชาการ

ผู้วิจัยมีงานวิจัยตีพิมพ์หัวข้อเรื่องที่เกี่ยวข้องกับการปฏิกิริยาต่างๆ ในช่วงการไหลต่างๆ (รวมทั้งช่วงการไหลใหม่) ของเครื่องปฏิกรณ์ฟลูอิไดซ์เบด/เครื่องปฏิกรณ์ฟลูอิไดซ์เบดแบบ หมุนเวียนที่มีอัตราการไหลอนุภาคของแข็งสูงด้วยการทดลองและการจำลองพลศาสตร์ของไหลเชิง คำนวณที่ได้รับการยอมรับ (Accepted Manuscript) ให้ตีพิมพ์ในวารวารวิชาการระดับนานาชาติ ใน รอบ 2 ปีที่ผ่านมา จำนวน 9 หัวข้อเรื่อง ได้แก่

- Chalermsinsuwan, B., Boonprasop, T., Nimmanterdwong, P., Piumsomboon, P. Revised fluidization regime characterization in high solid particle concentration circulating fluidized bed reactor. International Journal of Multiphase flow 66 (2014) 26-37.
- Jaiboon, O., Chalermsinsuwan, B., Mekasut, L., Piumsomboon, P. Effect of regeneration temperature on the composition and carbon dioxide sorption ability of a K_2CO_3/Al_2O_3 solid sorbent in a bubbling fluidized bed reactor. Chemical Engineering Communications 202 (3) (2015) 361-365.
- Chaiwang, P., Chalermsinsuwan, B., Piumsomboon, P. Thermogravimetric analysis and chemical kinetic for regeneration of sodium carbonate solid sorbent. Advanced Materials Research 1101 (2015) 40-45.
- Jongartklang, N., Piemjaiswang, R., Piumsomboon, P., Chalermsinsuwan, B. CO₂ sorption using Na₂CO₃/Al₂O₃ sorbent with various flow patterns of fixed/fluidized bed reactors. Jurnal Teknologi (2015) Accepted manuscript.
- Rukthong, W., Weerapakkaroon, W., Wongsiriwan, U., Piumsomboon, P., Chalermsinsuwan, B. Integration of computational fluid dynamics simulation and statistical factorial experimental design of thick-wall crude oil pipeline with heat loss. Advances in Engineering Software 86 (2015) 49-54.
- Rukthong, W., Thanatawee, P., Sunphorka, S., Piumsomboon, P., Chalermsinsuwan, B. Computation of biomass combustion characteristics and kinetic parameters by using thermogravimetric analysis. Engineering Journal 19(2) (2015) 41-57.
- Chayaporn, S., Sungsuk, P., Sunphorka, S., Kuchonthara, P., Piumsomboon, P., Chalermsinsuwan, B. Evaluation of biomass components effect on kinetic values for biomass pyrolysis using simplex-lattice design. Korean Journal of Chemical Engineering 32 (2015) 1081-1093.
- Chaiwang, P., Chalermsinsuwan, B., Piumsomboon, P. Thermogravimetric analysis and chemical kinetic for regeneration of sodium and potassium carbonate solid sorbents. Chemical Engineering Communications 203 (2016) 581-588.
- Jongartklang, N., Chanchairoek, S., Piumsomboon, P., Chalermsinsuwan, B. Correlations of kinetic parameters with various system operating conditions for CO_2 sorption using K_2CO_3/Al_2O_3 solid sorbent in a fixed/fluidized bed reactor. Journal of Environmental Chemical Engineering 4 (2016) 1938-1047.

เนื้อหางานวิจัย

วัตถุประสงค์

วัตถุประสงค์ของโครงการศึกษาวิจัย มีดังต่อไปนี้

- เพื่อทำการทดลองและวิเคราะห์การดักจับคาร์บอนไดออกไซด์ในช่วงการไหลใหม่ ของเครื่องปฏิกรณ์ฟลูอิไดซ์เบดแบบหมุนเวียนที่มีอัตราการไหลอนุภาคของแข็งสูง
- เพื่อทำการจำลองพลศาสตร์ของใหลเชิงคำนวณและวิเคราะห์การดักจับ คาร์บอนใดออกใชด์ในช่วงการใหลใหม่ของเครื่องปฏิกรณ์ฟลูอิไดซ์เบดแบบ หมุนเวียนที่มีอัตราการใหลอนุภาคของแข็งสูง
- เพื่อทำการสรุปผลของตัวแปรกระบวนการต่างๆ ที่มีต่อการดักจับ คาร์บอนไดออกไซด์และเสนอรูปแบบวิธีการดำเนินการช่วงการไหลใหม่ของเครื่อง ปฏิกรณ์ฟลูอิไดซ์เบดแบบหมุนเวียนที่มีอัตราการไหลอนุภาคของแข็งสูงสำหรับการ ประยุกต์ใช้ในอุตสาหกรรมต่างๆ

วิธีทดลอง

การดำเนินงานวิจัยของโครงการศึกษาวิจัยตามวัตถุประสงค์ มีดังต่อไปนี้

- การทบทวนวรรณกรรมที่เกี่ยวข้องเกี่ยวกับการดักจับคาร์บอนไดออกไซด์ในเครื่อง ปฏิกรณ์ฟลูอิไดซ์เบดแบบหมุนเวียนที่มีอัตราการไหลอนุภาคของแข็งสูง
- การออกแบบและสร้างเครื่องปฏิกรณ์ฟลูอิไดซ์เบดแบบหมุนเวียนที่มีอัตราการไหล อนุภาคของแข็งสูง
- การทำการทดลองและวิเคราะห์การดักจับคาร์บอนไดออกไซด์ในช่วงการไหลใหม่ ภายในเครื่องปฏิกรณ์ฟลูอิไดซ์เบดแบบหมุนเวียนที่มีอัตราการไหลอนุภาคของแข็ง สูง
- การพัฒนาแบบจำลองพลศาสตร์ของไหลเชิงคำนวณของเครื่องปฏิกรณ์ฟลูอิไดซ์เบด แบบหมุนเวียนที่มีอัตราการไหลอนุภาคของแข็งสูงสำหรับการดักจับ คาร์บอนไดออกไซด์
- การทำการจำลองพลศาสตร์ของไหลเชิงคำนวณและวิเคราะห์การดักจับ คาร์บอนไดออกไซด์ในช่วงการไหลใหม่ภายในเครื่องปฏิกรณ์ฟลูอิไดซ์เบดแบบ หมุนเวียนที่มีอัตราการไหลอนุภาคของแข็งสูง

- การสรุปผลของตัวแปรกระบวนการต่าง ๆ ที่มีต่อการดักจับคาร์บอนไดออกไซด์และ เสนอรูปแบบวิธีการดำเนินการช่วงการไหลใหม่ของเครื่องปฏิกรณ์ฟลูอิไดซ์เบดแบบ หมุนเวียนที่มีอัตราการไหลอนุภาคของแข็งสูงสำหรับการประยุกต์ใช้ในอุตสาหกรรม ต่าง ๆ
- การเขียนบทความวิชาการและการนำเสนอผลงานวิชาการ

ผลงานวิจัยที่ได้รับ (ผลการทดลอง)

ผลงานวิจัยที่ได้รับสามารถอธิบายเป็นข้อๆ ตามขั้นตอนการดำเนินงานวิจัย ดังต่อไปนี้

- การทบทวนวรรณกรรมที่เกี่ยวข้องเกี่ยวกับการดักจับคาร์บอนไดออกไซด์ในเครื่อง ปฏิกรณ์ฟลูอิไดซ์เบดแบบหมุนเวียนที่มีอัตราการไหลอนุภาคของแข็งสูง

ผู้วิจัยทบทวนวรรณกรรมที่เกี่ยวข้องเกี่ยวกับการดักจับคาร์บอนไดออกไซด์ในเครื่อง ปฏิกรณ์ฟลูอิไดซ์เบดแบบหมุนเวียนที่มีอัตราการไหลอนุภาคของแข็งสูง ดังนี้

Carbon dioxide is a greenhouse gas which is mainly released into the atmosphere from the electricity generation or combustion of fossil fuel (Chen-Chia and Shu-Chun, 2013). This carbon dioxide emission plays a vital role in the global warming problem. Therefore, the carbon dioxide mitigation or sequestration is the major concerns to prevent the world climate changes. Various methods for carbon dioxide capturing have been investigated in the literature. These methods can be divided into three basic systems including post-combustion, oxy-fuel combustion and pre-combustion capturing systems (Wang et al., 2011). In order to connect the carbon dioxide capturing system to the regular combustion system without requiring extensive change, the post-combustion capturing system is recommended which captures the carbon dioxide from flue gases in the downstream of fossil fuel combustion unit. The sorption-regeneration using dry solid sorbents is the promising technologies because of many advantages such as highly cost-effective process and ease of material handling.

The carbon dioxide capture process with a dry solid sorbent generally consists of two steps which are sorption and regeneration. The combustion flue gas is passed through the suitable reactor where the flue gas contacts with the solid sorbent. During this step, the carbon dioxide is chemically adsorbed on solid sorbent. Then, a carbon dioxide-rich solid sorbent is transported to the sorbent regeneration step. The carbon dioxide-rich solid

sorbent can be desorbed the carbon dioxide by heat. Finally, the regenerated solid sorbent is sent back to start the capturing cycle again. Data from several literatures confirm that carbon dioxide is effectively adsorbed on the alkaline metal carbonate solid sorbent (Wu et al., 2013). Among various alkaline metal carbonate, potassium carbonate has been found to provide the best results for carbon dioxide sorption (Xiao et al., 2011). Currently, most literature research studies have been focused their works on the improvement of the sorption performance. However, all researchers faced the same problem and concluded on the same issue that the reaction rate was rather slow and the capture capacity reached only 80% of theoretical values (Jaiboon et al., 2013) as a result of the improper gas-solid sorbent mixing in the fixed bed reactor and the improper used operating parameter (such as gas inlet velocity and solid particle type). Thus, the flow behavior of fluidized bed / circulating fluidized bed is proposed to be an answer for this problem and the capture capacity in this study is expected to be higher than 90% of theoretical values.

The fluidized bed / circulating fluidized bed are a type of reactors that can be commonly used for carrying a variety of multiphase flow processes. Different general gassolid sorbent particles phenomena or flow regimes can occur when the gas velocity passing through the solid sorbent particles changes including bubbling, turbulent, fast fluidization and pneumatic transport flow regimes (Figure 1). However, the flow regimes in the literature is major concerned with the low solid particle flux. Recently, the novel flow regime inside circulating fluidized bed reactor with high solid particle flux is found (solid particle flux > 200 kg/m2 s and solid concentration > 0.10) (Chalermsinsuwan et al., 2013). Both the high solid sorbent concentration and uniformity of gas-solid sorbent mixing were observed. The high solid particle flux operation is proposed to be one of the alternatives over the commonly used low solid particle flux operation for the carbon dioxide sorption reaction. In low solid particle flux, the turbulent flow regime provided the best carbon dioxide capture capacity at

90% of theoretical values (Chalermsinsuwan et al., 2010; Jaiboon et al., 2013). Most of the literature research studies are conducted using experimental method. Still, there is another method called computational fluid dynamics simulation which is an important design tool for chemical processes. It is one of the branches of fluid mechanics that uses numerical methods to analyze phenomena

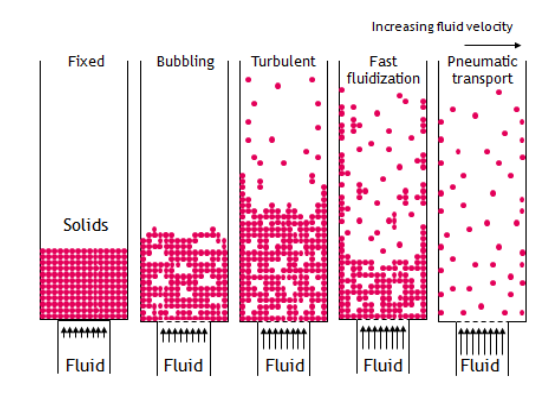


Figure 1 General fluidization regimes

that involve fluid and chemically reacting flows. The principle of the computational fluid dynamics is the calculation of mass, momentum, energy and species conservation equations, simultaneously. For the fluidized bed / circulating fluidized bed, the Eulerian approach is suitable for the calculation which separately solves the conservation equations for each phase. The momentum, heat and mass interphase exchanged coefficient models are used for coupling between phases. Among the various attempts to close the gas-solid flow, the kinetic theory of granular flow has found the widest use as a constitutive equation. This theory is an extension of the classical kinetic theory of gases to dense gas-solid flows with a description of the solid particle collisions. For the chemically reacting flows, the chemical kinetics is also required as an input for explaining the reaction.

References:

Chalermsinsuwan, B., Piumsomboon, P., Gidspow, D. A computational fluid dynamics design of a carbon dioxide sorption circulating fluidized bed. AIChE Journal 56(11) (2010) 2805-2824.

Chalermsinsuwan, B., Prajongkan, Y., Piumsomboon, P. Three-dimensional CFD simulation of the system inlet and outlet boundary condition effects inside a high solid particle flux circulating fluidized bed riser. Powder Technology 245 (2013) 80-93.

Chen-Chia, H., Shu-Chun, S. Adsorption of CO₂ on chitosan modified CMK-3 at ambient temperature. Journal of the Taiwan Institute of Chemical Engineers 44 (2013) 89-94.

Jaiboon, O.A., Chalermsinsuwan, B., Mekasut, L., Piumsomboon, P. Effect of flow patterns/regimes on CO_2 capture using K_2CO_3 solid sorbent in fluidized bed/circulating fluidized bed. Chemical Engineering Journal 219 (2013) 262-272.

Wang, M., Lawal, A., Stephenson, P., Sidders, J., Ramshaw, C. Post-combustion CO₂ capture with chemical absorption: A state-of-the-art review. Chemical Engineering Research and Design 89 (2011) 1609-1624.

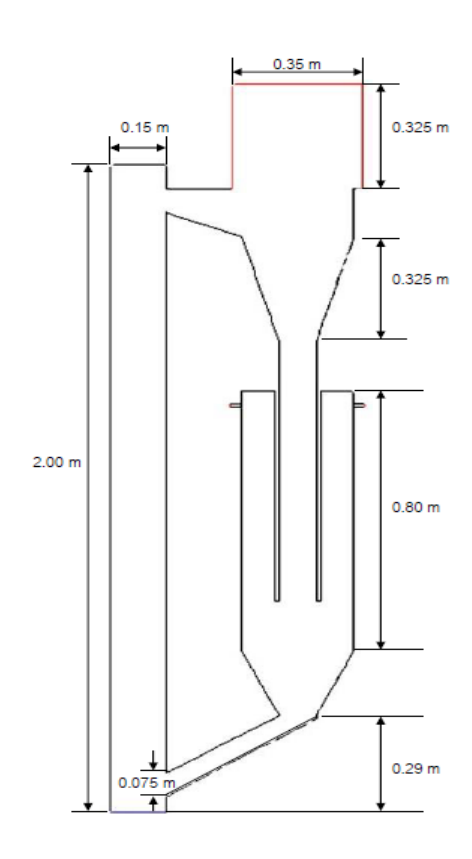
Wu, Y., Xiaoping, C., Wei, D., Chuanwen, Z., Zhonglin, Z., Daoyin, L., Cai, L. K_2CO_3/AI_2O_3 for capturing CO_2 in flue gas from power plants. Part 5: Carbonation and failure behavior of K_2CO_3/AI_2O_3 in the continuous CO_2 sorption-desorption system. Energy & Fuels 27 (2013) 4804-4809.

Xiao, G., Singh, R., Chaffee, A., Webley, P. Advanced adsorbents based on MgO and K_2CO_3 for capture of CO_2 at elevated temperatures. International Journal of Greenhouse Gas Control 5 (2011) 634-639.

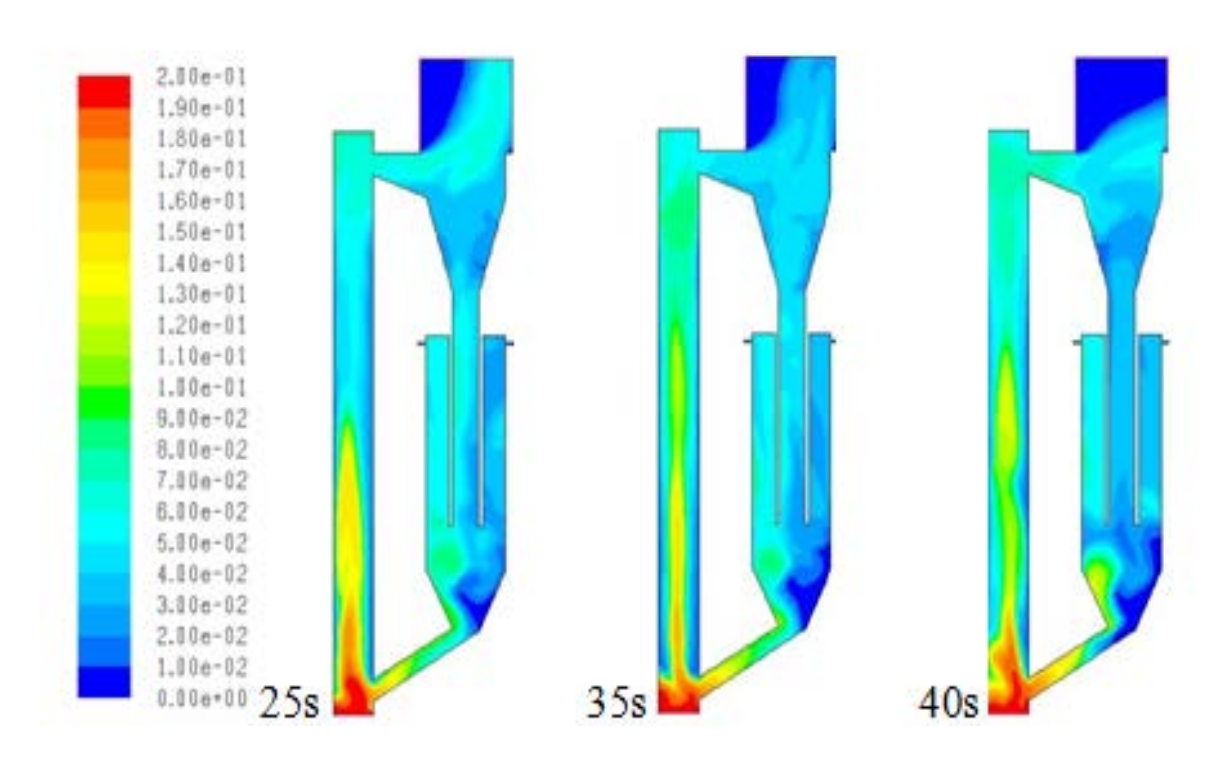
- การออกแบบและสร้างเครื่องปฏิกรณ์ฟลูอิไดซ์เบดแบบหมุนเวียนที่มีอัตราการไหล อนุภาคของแข็งสูง

ผู้วิจัยออกแบบและสร้างเครื่องปฏิกรณ์ฟลูอิไดซ์เบดแบบหมุนเวียนที่มีอัตราการใหลอนุภาค ของแข็งสูง มีขั้นตอนการออกแบบ คือ

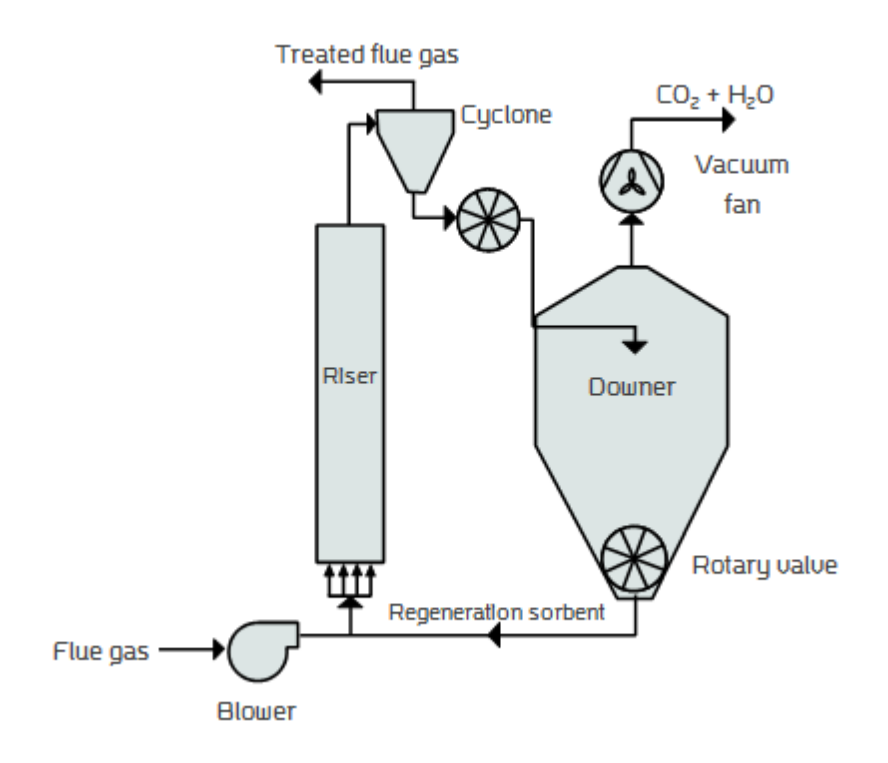
- 1) จากการทบทวนวรรณกรรมที่เกี่ยวข้องเกี่ยวกับการดักจับคาร์บอนไดออกไซด์ในเครื่อง ปฏิกรณ์ฟลูอิไดซ์เบดแบบหมุนเวียนที่มีอัตราการไหลอนุภาคของแข็งสูง ทำการออกแบบเครื่อง ปฏิกรณ์โดยใช้แนวคิดที่ได้จากการทบทวนวรรณกรรม (ดังรูปที่ 2)
- 2) ทำการจำลองกระบวนการพลศาสตร์ของไหลเชิงคำนวณเบื้องตันเพื่อพิจารณาความ เป็นไปได้ในการเกิดช่วงการไหลใหม่และการดักจับคาร์บอนไดออกไซด์ภายในเครื่องปฏิกรณ์ที่ได้ ออกแบบไว้ (ดังรูปที่ 3)
- 3) หากมีอุทกพลศาสตร์ที่ไม่เหมาะสมภายในเครื่องปฏิกรณ์ที่ได้ออกแบบไว้ ทำการปรับปรุง การออกแบบเครื่องปฏิกรณ์ หากไม่มีอุทกพลศาสตร์ไม่เหมาะสมภายในเครื่องปฏิกรณ์ที่ได้ ออกแบบไว้ ทำการสร้างเครื่องปฏิกรณ์ที่ได้ออกแบบไว้ (แบบลดส่วนด้วยตัวเลขไร้หน่วย) (ดังรูปที่ 4)



รูปที่ 2 ระบบการดักจับคาร์บอนไดออกไซด์ในเครื่องปฏิกรณ์ฟลูอิไดซ์เบดแบบหมุนเวียน ที่มีอัตราการไหลอนุภาคของแข็งสูง



รูปที่ 3 การดักจับคาร์บอนไดออกไซด์ภายในช่วงการไหลใหม่ของเครื่องปฏิกรณ์ฟลูอิไดซ์เบด แบบหมุนเวียนที่มีอัตราการไหลอนุภาคของแข็งสูง



รูปที่ 4 ระบบการดักจับคาร์บอนไดออกไซด์ในเครื่องปฏิกรณ์ฟลูอิไดซ์เบดแบบหมุนเวียนที่มีอัตรา การไหลอนุภาคของแข็งสูงจากการทดลองจริง

สำหรับเครื่องปฏิกรณ์ที่ออกแบบไว้สร้างขึ้นจากแก้วควอทซ์ เหล็กกล้าไร้สนิม และ พลาสติก อะคริลิค ประกอบด้วย 3 ส่วนหลัก ได้แก่

- 1) ท่อไรเซอร์ สร้างขึ้นจากแก้วควอทซ์
- 2) ท่อดาวเนอร์ สร้างขึ้นจากเหล็กกล้าไร้สนิม
- 3) ส่วนแยกและป้อนกลับ สร้างขึ้นจากพลาสติกอะคริลิค
- การทำการทดลองและวิเคราะห์การดักจับคาร์บอนไดออกไซด์ในช่วงการไหลใหม่ ภายในเครื่องปฏิกรณ์ฟลูอิไดซ์เบดแบบหมุนเวียนที่มีอัตราการไหลอนุภาคของแข็งสูง

ผู้วิจัยทำการทดลองและวิเคราะห์การดักจับคาร์บอนไดออกไซด์ในช่วงการไหลใหม่ภายใน เครื่องปฏิกรณ์ฟลูอิไดซ์เบดแบบหมุนเวียนที่มีอัตราการไหลอนุภาคของแข็งสูง สรุปผลการทดลองที่ ได้ ดังต่อไปนี้

การเตรียมโลหะแอลคาไลบนตัวบนตัวรองรับอะลูมินา (AI₂O₃) คือ โพแทสเซียมคาร์บอเนต โซเดียมคาร์บอเนต ลิเทียมคาร์บอเนต และ รูบิเดียมคาร์บอเนต ทำด้วยวิธีอิมเพรกเนชัน (Impregnation) โดยเติมอะลูมินา 5 กรัม ลงในสารละลายโลหะคาร์บอเนตที่ประกอบด้วยโลหะ คาร์บอเนต 5 กรัมในน้ำที่ปราศจากไอออน ปริมาตร 25 มิลลิลิตร หลังจากนั้น ผสมสารละลายด้วย การเขย่าสารละลายเป็นเวลา 24 ชั่วโมง ที่อุณหภูมิห้อง ทำให้แห้งในเครื่องอบระบบสุญญากาศที่ อุณหภูมิ 105 องศาเซลเซียส สุดท้าย นำตัวอย่างไปเผาภายใต้อัตราการไหลของในโตรเจนที่ 100 มิลลิลิตรต่อนาทีเป็นเวลา 4 ชั่วโมง ที่อุณหภูมิ 300 องศาเซลเซียส ผังงานสำหรับการเตรียมตัวดูด ซับด้วยวิธีอิมเพรกเนชัน แสดงดังในรูปที่ 5



รูปที่ 5 ผังงานสำหรับการเตรียมตัวดูดซับด้วยวิธีอิมเพรกเนชัน

ลักษณะของตัวดูดซับของแข็ง

- เครื่องวิเคราะห์พื้นผิวและรูพรุน (BET) หาพื้นที่ผิวและขนาดอนุภาครูพรุนด้วยการใช้การดูด
 ซับและคายซับในโตรเจนที่ -196 องศาเซลเซียส (Micromeritics 2020)
- เครื่องวิเคราะห์หาธาตุด้าน X Ray (Energy Dispersive X-Ray Fluorescence Spectrometer, EDX) ตรวจปริมาณที่แท้จริงของโลหะบนตัวรองรับ
- กล้องจุลทรรศน์อิเล็กตรอนแบบส่องกราด (SEM) หาสัณฐานวิทยาของตัวดูดซับที่แตกต่าง กัน ที่กำลังขยาย 10000 เท่า
- เทคนิคเอกซ์เรย์ดิฟแฟรกชัน (X-ray diffractmeter, XRD) ตรวจวิเคราะห์ชนิดของเฟสที่ ปรากฏในตัวดูดซับเบื้องต้น

โครงสร้างระดับโมเลกุลของโลหะแอลคาไลต่างชนิด

พื้นที่ผิวทั้งหมดและปริมาณโลหะแอลคาไลคาร์บอเนตบนตัวรองรับอะลูมินาออกไซด์ของตัว ดูดซับโลหะแอลคาไลคาร์บอเนตต่างชนิด แสดงในตารางที่ 1 จากตารางค่าปริมาณร้อยละโลหะ แอลคาไลคาร์บอเนตบนตัวรองรับอะลูมินามีค่าใกล้เคียงกันอยู่ในช่วงร้อยละ 10-13 ยกเว้น ลิเทียม คาร์บอเนตซึ่งเครื่องวิเคราะห์ไม่สามารถอธิบายได้ (เครื่องวิเคราะห์หาธาตุ EDX ไม่สามารถวิเคราะห์ธาตุที่มีเลขอะตอมน้อยกว่า 5 คือ H He Li และ Be)

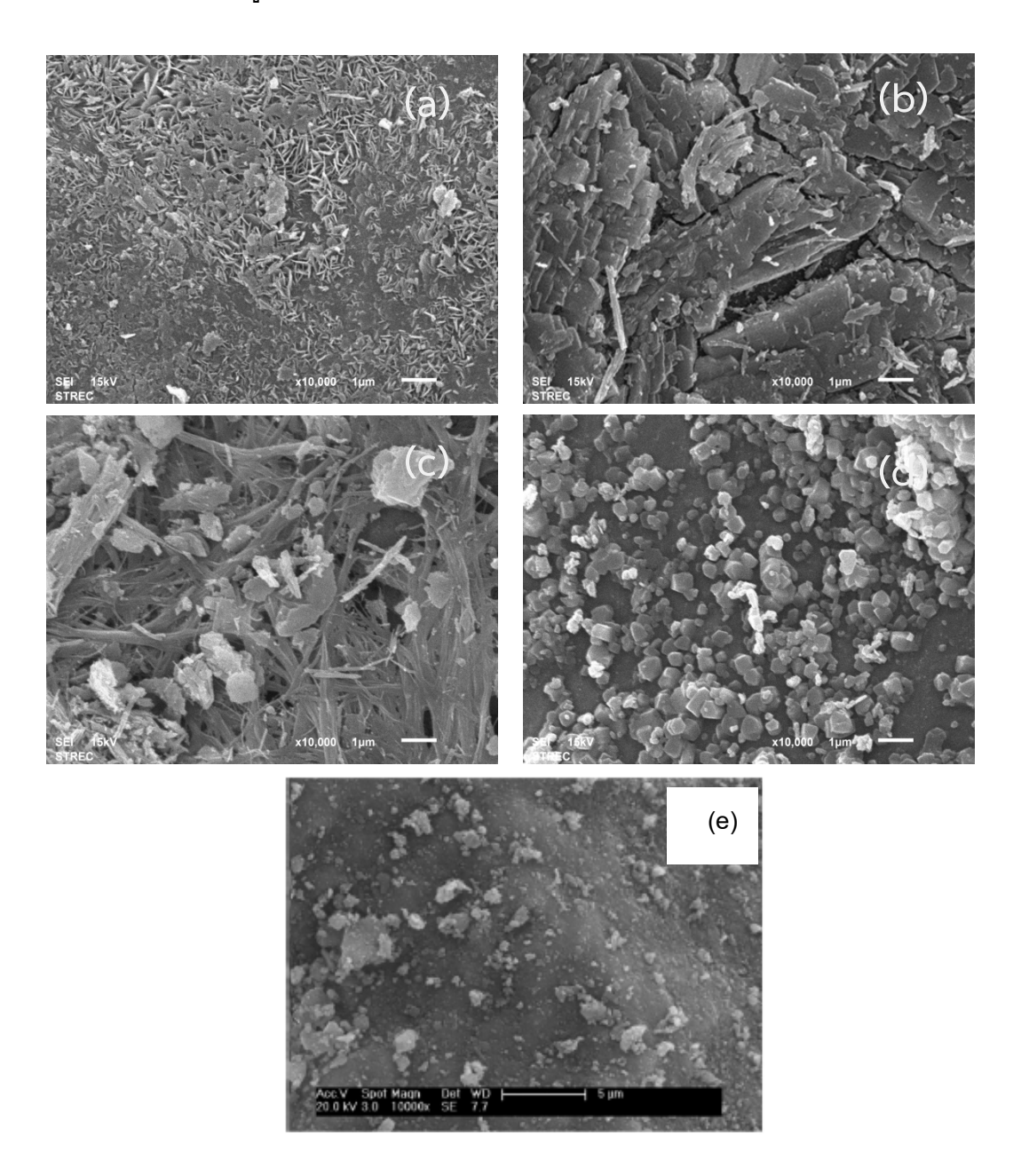
ตารางที่ 1 โครงสร้างระดับโมเลกุลของตัวดูดซับโลหะแอลคาไล

 ตัวดูดซับ	ร้อยละปริมาณโลหะ	พื้นที่ผิวรวม
	แอลคาไลบนตัวรองรับ	(ตารางเมตรต่อกรัม)
Li ₂ CO ₃ /Al ₂ O ₃	N/A	127.27
Na ₂ CO ₃ /Al ₂ O ₃	10±3.344	105.4
K_2CO_3/AI_2O_3	13±3.173	99.4
Rb ₂ CO ₃ /Al ₂ O ₃	12±1.512	129.1

ค่าพื้นที่ผิวของตัวดูดซับโลหะแอลคาไลคาร์บอเนตบนตัวรองรับอะลูมินามีค่าสูงอยู่ในช่วง 99.4-127.1 ตารางเมตรต่อกรัม เนื่องจากตัวรองรับอะลูมินาที่ทำหน้าที่เป็นเมทริกซ์ที่มีรูพรุน/พื้นที่ ผิวสูง ความแตกต่างของค่าพื้นที่ผิวสามารถอธิบายจากลักษณะพื้นที่ผิวของภาพถ่าย SEM โดยทั่วไป โลหะแอลคาไลจะมีสัณฐานแบบผลึกและเส้นใย ในการศึกษานี้ รูบิเดียมคาร์บอเนตและ โพแทสเซียมคาร์บอเนตที่มีสัณฐานส่วนใหญ่เป็นแบบผลึกกลมและเส้นใยจึงเป็นเหตุผลให้ตัวดูดซับ ทั้งสองมีค่าพื้นที่ผิวสูงและต่ำที่สุด ตามลำดับ

สัณฐานวิทยาของโลหะแอลคาไล

สัณฐานวิทยาของอนุภาคตัวดูดซับของแข็งก่อนการดูดซับถูกทดสอบด้วยกล้องจุลทรรศน์ อิเล็กตรอนแบบส่องกราด (SEM) ที่กำลังขยาย 10000 เท่า แสดงในรูปที่ 6 ส่วนประกอบว่องไวที่ กระจายบนพื้นที่ผิวอะลูมินาออกไซด์ของโลหะแอลคาไลทั้ง 4 ชนิดมีความแตกต่างกัน



รูปที่ 6 ภาพถ่าย SEM ที่กำลังขยาย 10000 เท่าของพื้นผิวของ (a) $\rm Li_2CO_3/Al_2O_3$ (b) $\rm Na_2CO_3/Al_2O_3$ (c) $\rm K_2CO_3/Al_2O_3$ (d) $\rm Rb_2CO_3/Al_2O_3$ และ (e) $\rm Al_2O_3$

รูปที่ 6 (a) แสดงรูปบนพื้นที่ผิวของตัวดูดซับลิเทียมคาร์บอเนตบนตัวรองรับอะลูมินา จาก งานวิจัยที่ผ่านมาพื้นผิวของลิเทียมคาร์บอเนตจะมีลักษณะเป็นกลุ่มก้อนผลึกทรงเรียวยาว เมื่อผสม อนุภาคอะลูมินาออกไซด์ จากรูปพบว่า กลุ่มก้อนผลึกทรงเรียวยาวของลิเทียมคาร์บอเนตจะปกคลุม พื้นผิวอะลูมินา รูปที่ 6 (b) แสดงรูปบนพื้นผิวของตัวดูดซับโซเดียมคาร์บอเนตที่มีโครงสร้างพื้นผิว เชื่อมต่อกันเป็นผลึกเหมือนกับงานวิจัยของ Dong และคณะ (2012) รูปที่ 6 (c) แสดงรูปบนพื้นที่ผิว บนของตัวดูดซับโพแทสเซียมคาร์บอเนต พบว่า พื้นผิวมีการกระจายตัวของเส้นใยกับผลึกกลม เช่นเดียวกันกับ Zhao และคณะ (2012) ที่อธิบายโครงสร้างของโพแทสเซียมคาร์บอเนตที่มีเส้นใย กับผลึกกลมเป็นส่วนประกอบที่ว่องไวกระจายบนพื้นผิวอะลูมินาออกไซด์ทั้งนี้ปริมาณของส่วนที่ ว่องไวขึ้นอยู่กับปริมาณของโลหะแอลคาไล รูปที่ 6 (d) แสดงรูปบนพื้นผิวของตัวดูดซับรูบิเดียม คาร์บอเนตที่มีโครงสร้างเป็นผลึกขนาดเล็กจำนวนมากสะสมอยู่บนพื้นผิว ซึ่งเป็นลักษณะโครงสร้าง ของรูบิเดียมคาร์บอเนตที่อธิบายจากงานวิจัยของ Hwang และคณะ (2009) และรูป 6 (e) แสดง พื้นที่ผิวอะลูมินาออกไซด์จากงานวิจัยของ Zhao และคณะ (2012)

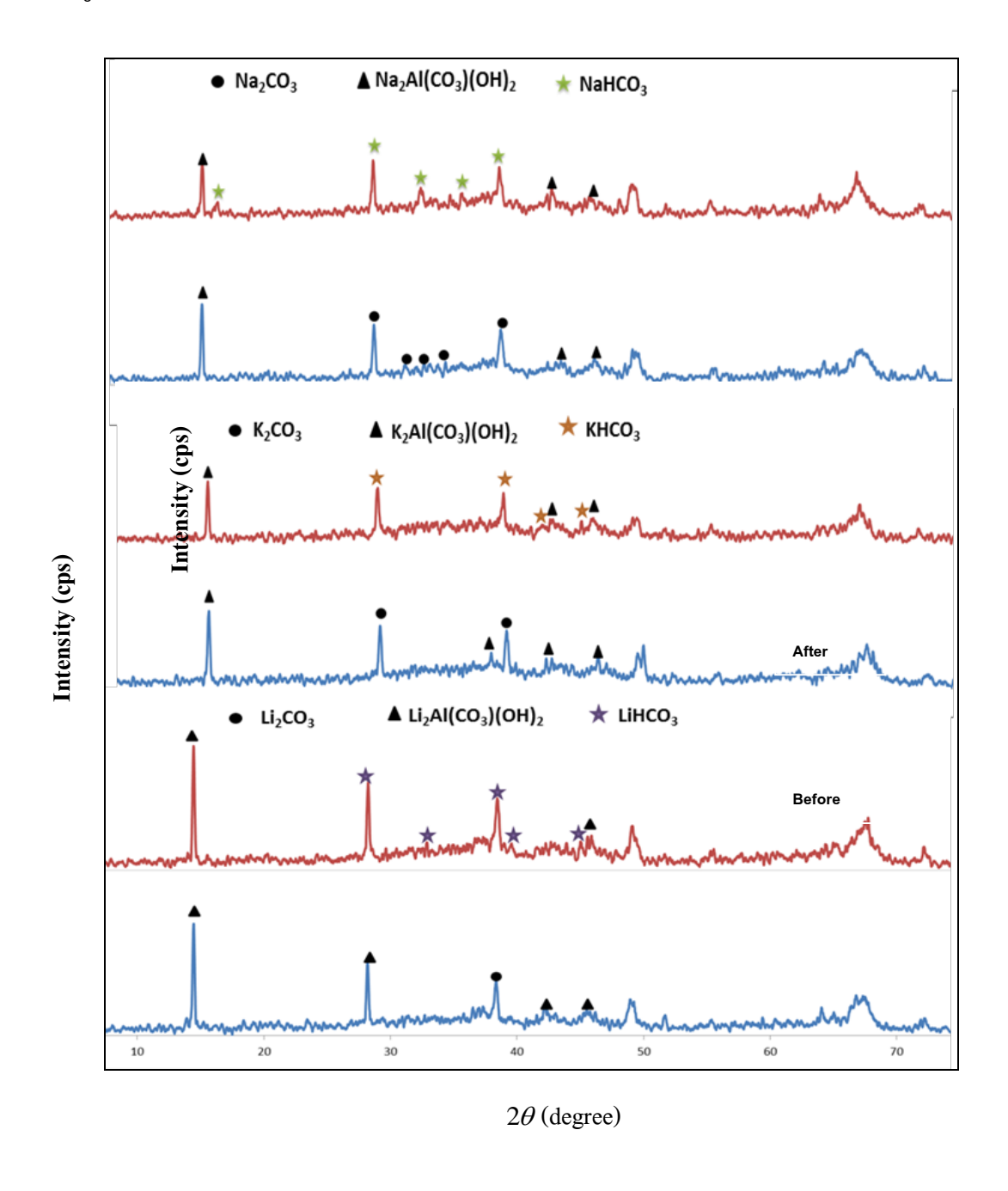
โครงสร้างของตัวดูดซับโลหะแอลคาใลคาร์บอเนตซับก่อนและหลังการดักจับแก๊ส คาร์บอนใดออกใชด์

ในการสำรวจสมบัติของการดูดซับของตัวดูดซับโลหะแอลคาไลตัวอย่าง ได้แก่ ลิเทียม คาร์บอเนต โซเดียมคาร์บอเนต และโพแทสเซียมคาร์บอเนต การเปลี่ยนแปลงโครงสร้างก่อนและ หลังการดูดซับด้วยเทคนิคเอกซ์เรย์ดิฟแฟรกชัน (X-ray diffractmeter, XRD) จากรูปที่ 7 แสดง รูปแบบ XRD ของตัวดูดซับโลหะแอลคาไล พบว่า

ผลของ XRD ของตัวดูดซับลิเทียมคาร์บอเนตที่เผาที่อุณหภูมิ 573 เคลวิน ภายใต้แก๊ส ในโตรเจนก่อนการเกิดปฏิกิริยาคาร์บอเนซันมี 2 วัฏภาค คือ ${\rm Li_2CO_3}$ และ ${\rm Li_2Al(CO_3)(OH)_2}$ วัฏภาค ${\rm Li_2Al(CO_3)(OH)_2}$ เกิดจากการทำปฏิกิริยาของตัวรองรับอะลูมินากับลิเทียมคาร์บอเนต ระหว่างการเผาที่อุณหภูมิ 573 เคลวิน หลังจากดูดซับแก๊สคาร์บอนไดออกไซด์จากแก๊สผสม คาร์บอนไดออกไซด์ ร้อยละ 12 โดยปริมาตรและปริมาณไอน้ำขาเข้าร้อยละ 18.4 โดยปริมาตร ผล ของ XRD แสดง 2 วัฏภาคคือ ${\rm Li_2Al(CO_3)(OH)_2}$ และ ${\rm LiHCO_3}$

ผลของ XRD ของตัวดูดซับโซเดียมคาร์บอเนตที่เผาที่อุณหภูมิ 573 เคลวิน ภายใต้แก๊ส ในโตรเจนก่อนการเกิดปฏิกิริยาคาร์บอเนชันมี 2 วัฏภาค คือ Na₂CO₃ และ Na₂Al(CO₃)(OH)₂ วัฏภาค Na₂Al(CO₃)(OH)₂ เกิดจากการทำปฏิกิริยาของตัวรองรับอะลูมินากับโซเดียมคาร์บอเนต ระหว่างการเผาที่อุณหภูมิ 573 เคลวิน หลังจากดูดซับแก๊สคาร์บอนไดออกไซด์จากแก๊สผสม คาร์บอนไดออกไซด์ร้อยละ 12 โดยปริมาตรและปริมาณไอน้ำขาเข้าร้อยละ 18.4 โดยปริมาตร ผลของ XRD แสดง 2 วัฏภาค คือ Na₂Al(CO₃)(OH)₂ และ NaHCO₃

ผลของ XRD ของตัวดูดโพแทสเซียมคาร์บอเนตที่เผาที่อุณหภูมิ 573 เคลวิน ภายใต้แก๊ส ในโตรเจนก่อนการเกิดปฏิกิริยาคาร์บอเนชันมี 2 วัฏภาค คือ K_2CO_3 และ $K_2AI(CO_3)(OH)_2$ วัฏ ภาค $K_2AI(CO_3)(OH)_2$ เกิดจากการทำปฏิกิริยาของตัวรองรับอะลูมินากับโพแทสเซียมคาร์บอเนต ระหว่างการเผาที่อุณหภูมิ 573 เคลวิน หลังจากดูดซับแก๊สคาร์บอนไดออกไซด์จากแก๊สผสม คาร์บอนไดออกไซด์ร้อยละ 12 โดยปริมาตรและปริมาณไอน้ำขาเข้าร้อยละ 18.4 โดยปริมาตร หลังจากดูดซับแก๊สคาร์บอนไดออกไซด์ ผลของ XRD แสดง 2 วัฏภาคคือ $K_2AI(CO_3)(OH)_2$ และ KHCO $_3$



รูปที่ 7 XRD ของโลหะแอลคาไลคาร์บอเนตก่อนและหลังปฏิกิริยาคาร์บอเนชัน

การศึกษาการดักจับแก๊สคาร์บอนไดออกไซด์ด้วยระบบฟลูอิไดเซชันของแก๊ส-ของแข็ง ระบบ ฟลูอิไดเซชันเป็นระบบที่มีการสัมผัสกันที่สูงระหว่างแก๊สและตัวดูดซับของแข็งส่งผลให้มีอัตราการ ถ่ายโอนมวลและความร้อนที่สูง ประสิทธิภาพของการสัมผัสกันของแก๊ส-ของแข็งภายในระบบ ฟลูอิไดเซชัน ขึ้นอยู่กับรูปแบบการไหลภายในเครื่องปฏิกรณ์ที่มีพฤติกรรมการสัมผัสกันระหว่าง แก๊ส-ของแข็งที่แตกต่างกัน ความเร็วของการเปลี่ยนแปลงรูปแบบการไหลแสดงในตารางที่ 2 โดย แบ่งเป็น 4 ช่วงความแตกต่างของความเร็วแก๊สกับชนิดรูปแบบการไหล ที่ความเร็วต่ำกว่าความเร็ว ต่ำสุดในการเกิดฟลูอิไดเซชัน (U_{mf}) จะเป็นรูปแบบการไหลแบบเบดนิ่ง สำหรับความเร็วระหว่าง ความเร็วต่ำสุดในการเกิดฟลูอิไดเซชัน (U_{mf}) กับความเร็วทรานซิชัน (U_{c}) คือ ความเร็วของ รูปแบบการไหลฟลูอิไดเซชันแบบฟองแก๊สและฟลูอิไดเซชันแบบสลักกิ้ง หรือค่า 0.06-0.84 เมตร ต่อวินาที (แบ่งจากการสังเกตรูปแบบการไหลของของแข็ง) เมื่อความเร็วของแก๊สอยู่ระหว่าง ความเร็วทรานซิชันและความเร็วในการส่งผ่าน (U_{r}) หรือช่วง 0.84-2.30 เมตรต่อวินาที เป็นช่วง การไหลที่เปลี่ยนรูปแบบการไหลฟลูอิไดเซชันแบบ ปั่นป่วนหมุนเวียน) (แบ่งจากการสังเกตรูปแบบการไหลฟลูอิไดเซชันแบบ ปั่นป่วน (ฟลูอิไดเซชันแบบปั่นป่วนหมุนเวียน) (แบ่งจากการสังเกตรูปแบบการไหลของของแข็ง) และที่ความเร็วมากกว่า 2.30 เมตรต่อนาที เป็นรูปแบบการไหลฟลูอิไดเซชันแบบความเร็วสูง

ตารางที่ 2 รูปแบบการใหลของโลหะคาร์บอเนตบนตัวรองรับอะลูมินา

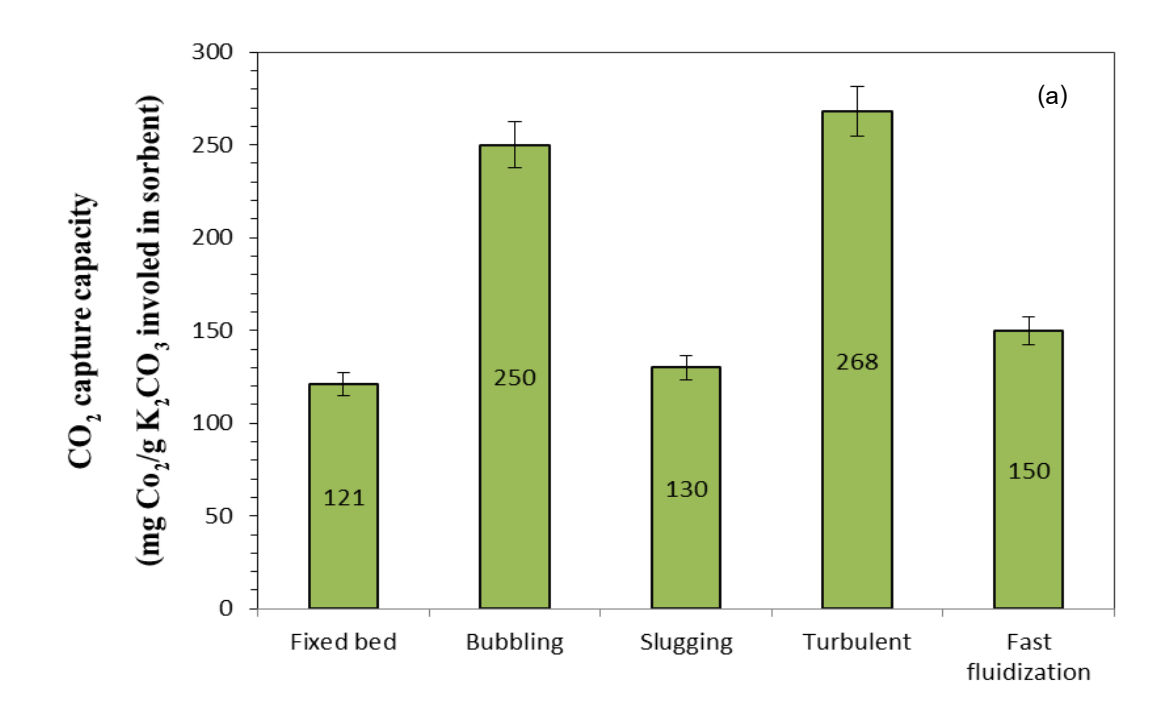
ช่วงความเร็ว	ช่วงของ $U_{\scriptscriptstyle g}$ (m/s)	รูปแบบการไหล
$U_g < U_{mf}$	<0.06	แบบเบดนิ่ง
U_{mf} $<$ U_{g} $<$ U_{c}	0.06-0.84	ฟลูอิไดเซชันแบบฟองแก๊สและ
		ฟลูอิไดเซชันแบบสลักกิ้ง
$U_c < U_g < U_{tr}$	0.84-2.30	ฟลูอิไดเซชันแบบปั่นป่วน
		(ฟลูอิไดเซชันแบบปั่นป่วนหมุนเวียน)
$U_{\it tr}$	>2.30	ฟลูอิไดเซชันแบบการไหลความเร็วสูง

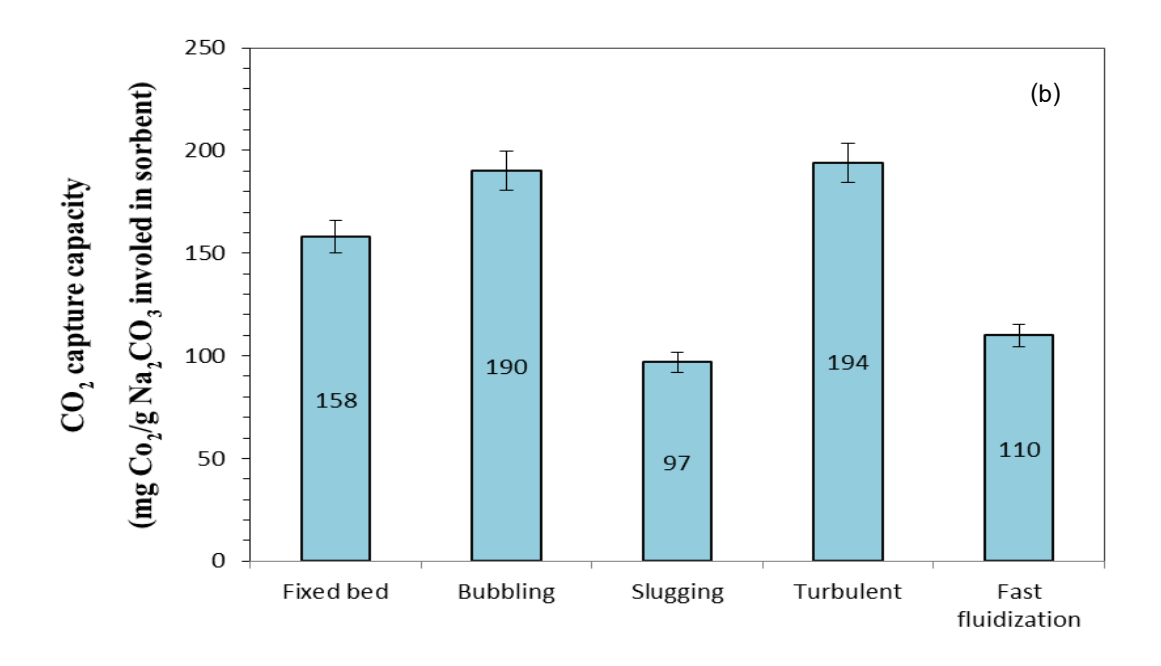
เมื่อพิจารณาการดูดซับแก็สคาร์บอนไดออกไซด์ มี 2 ตัวแปรหลักที่มีผลต่อการดูดซับ คาร์บอนไดออกไซด์ คือ รูปแบบการไหล และ อุณหภูมิในการดูดซับ ในการศึกษาขั้นแรก แก๊ส คาร์บอนไดออกไซด์ความเข้มขันร้อยละ 12 โดยปริมาตร จะถูกศึกษาผลของรูปแบบการไหล 5 รูปแบบการไหลที่แตกต่าง คือ แบบเบดนิ่ง ฟลูอิไดเซชันแบบฟองแก๊ส ฟลูอิไดเซชันแบบสลักกิ้ง ฟลูอิไดเซชันแบบปั่นป่วน (หรือ ฟลูอิไดเซชันแบบปั่นป่วนหมุนเวียน ซึ่งเป็นช่วงการไหลใหม่) และฟลูอิไดเซชันแบบความเร็วสูง ของแข็งที่ใช้งานจะมีปริมาณ 40 กรัม สำหรับแบบเบดนิ่ง ฟลูอิไดเซชันแบบฟองแก๊ส ฟลูอิไดเซชันแบบสลักกิ้ง และ ฟลูอิไดเซชันแบบปั่นป่วน ของแข็งที่ใช้ งานจะมีปริมาณ 200 กรัม สำหรับฟลูอิไดเซชันแบบความเร็วสูง สำหรับผลของอุณหภูมิ ตัวดูดซับ ของแข็งปริมาณ 40 กรัมของตัวดูดซับตัวอย่างสองชนิด คือ K₂CO₃/Al₂O₃ และ Na₂CO₃/Al₂O₃

จะถูกศึกษาด้วยรูปแบบการใหลที่มีการดูดซับแก๊สคาร์บอนไดออกไซด์มากสุดที่อุณหภูมิการดูดซับ 4 อุณหภูมิ คือ 323 333 343 และ 353 เคลวิน สุดท้าย ผลของประเภทตัวดูดซับชนิดต่างๆ คือ ${\rm Li_2CO_3/AI_2O_3}$ ${\rm K_2CO_3/AI_2O_3}$ ${\rm Na_2CO_3/AI_2O_3}$ และ ${\rm Rb_2CO_3/AI_2O_3}$ ได้ถูกพิจารณาผลต่อ ความสามารถในการดูดซับแก๊สคาร์บอนไดออกไซด์ ภายใต้รูปแบบการใหลที่ดูดซับแก๊ส คาร์บอนไดออกไซด์มากสุด และ อุณหภูมิการดูดซับเหมาะสม

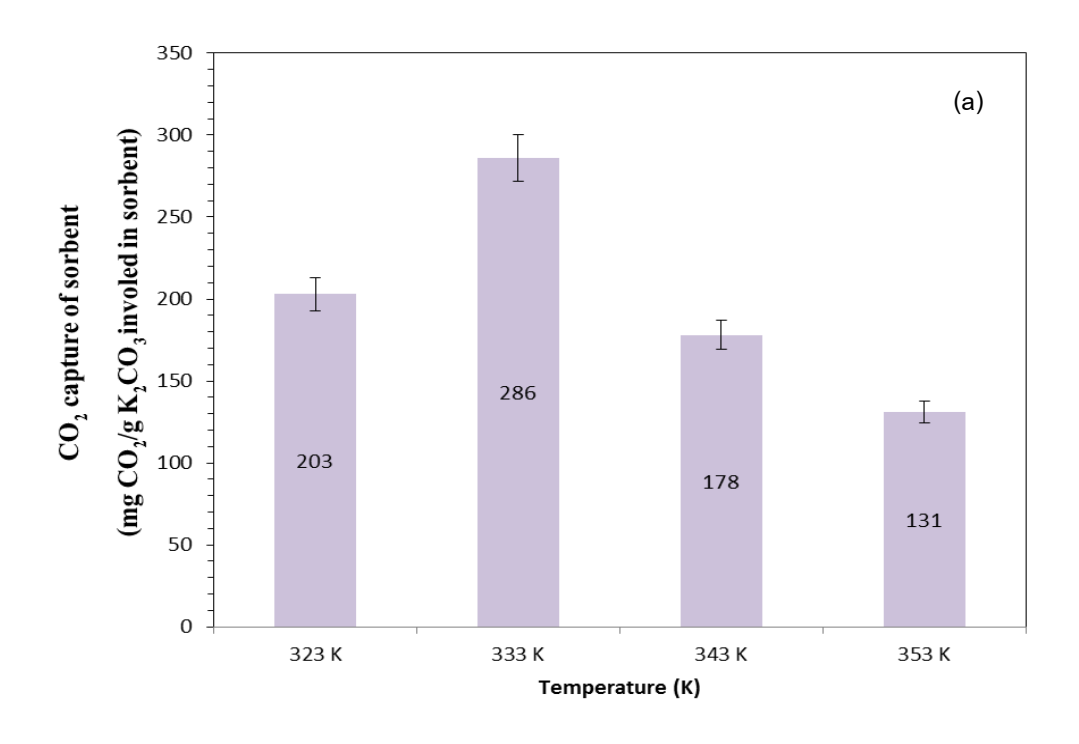
รูปที่ 8 แสดงผลของรูปแบบการใหลในเครื่องปฏิกรณ์ฟลูอิไดเซชันที่มีอัตราการใหลอนุภาค ของแข็งสูงต่อการดูดซับด้วยตัวดูดซับโพแทสเซียมคาร์บอเนตและโซเดียมคาร์บอเนตสามารถ คำนวณปริมาณการดักจับที่มีค่าสูงสุดขึ้นอยู่กับรูปแบบการไหลภายในเครื่องปฏิกรณ์ รูปแบบการ ใหลแบบเบดนิ่งและรูปแบบการใหลฟลูอิไดเซชันแบบสลักกิ้งมีค่าปริมาณการดักจับต่ำ รูปแบบการ ใหลฟลูอิไดเซชันแบบปั่นปวน (แบบปั่นป่วนหมุนเวียน) มีค่าสูงสุด รูปแบบการใหลแบบ ฟลูอิไดเซชันแบบปั่นป่วน (แบบปั่นป่วนหมุนเวียน) และรูปแบบการไหลฟลูอิไดเซชันแบบฟองแก๊ส มีปริมาณการดูดซับใกล้เคียงกันที่ 268 และ 250 มิลลิกรัมคาร์บอนไดออกไซด์ต่อกรัมโพแทสเซียม คาร์บอเนตและมีปริมาณการดักจับ 194 และ 190 มิลลิกรัมคาร์บอนไดออกไซด์ต่อกรัมโซเดียม คาร์บอเนต ตามลำดับ อย่างไรก็ตาม ปริมาณความเข้มข้นที่ทางออกของรูปแบบการไหลเบดนิ่งให้ ปริมาณแก๊สคาร์บอนไดออกไซด์สูงเนื่องจากระยะเวลาในการทำปฏิกิริยานานแต่ปริมาณการดักจับ แก๊สคาร์บอนไดออกไซด์มีค่าต่ำสุด และจากพฤติกรรมของการจัดเรียงตัวตัวดูดซับของแข็งใน เบดนิ่งทำให้สูญเสียพื้นที่ในการทำปฏิกิริยาของแก๊สคาร์บอนไดออกไซด์ที่เข้ามา ในรูปแบบการไหล แบบฟองแก๊ส สัดส่วนความเข้มข้นของแก๊สที่ทางออกมีค่าสูงแต่น้อยกว่ารูปแบบเบดนิ่ง แต่ปริมาณ การดูดซับมีค่ามากกว่าเบดนิ่ง แสดงว่ามีการสัมผัสของแก๊ส-ของแข็งที่สูงกว่ารูปแบบเบดนิ่ง สำหรับรูปแบบการใหลแบบฟลูอิไดเซชันสลักกิ้งและรูปแบบการใหลแบบฟลูอิไดเซชันความเร็วสูง ตัวดูดซับของแข็งโพแทสเซียมคาร์บอเนตและโซเดียมคาร์บอเนตสามารถกำจัดแก๊ส คาร์บอนไดออกได้ทั้งหมดในเวลาไม่ถึง 1 นาที หมายความว่า เวลาในการทำปฏิกิริยาไม่ได้ส่งผล ต่อปริมาณการดักจับแก๊สคาร์บอนไดออกไซด์ จะเห็นว่าปริมาณการดักจับแก๊สคาร์บอนไดออกไซด์ ในรูปแบบการใหลฟลูอิไดเซชันแบบสลักกิ้งและฟลูอิไดเซชันแบบความเร็วสูงมีค่าต่ำใกล้เคียงกับ แบบเบดนิ่ง เนื่องจากการเกิดฟองแก๊สขนาดใหญ่ในรูปแบบการไหลฟลูอิไดเซชันแบบสลักกิ้งทำให้ พื้นที่การสัมผัสกันของแก๊สและของแข็งน้อยลงและสำหรับรูปแบบความเร็วสูงที่มีปริมาณพื้นที่ใน การสัมผัสกันของแก๊สและของแข็งสูงแต่เนื่องจากมีการกระจายตัวของเบดของแข็งทำให้ปริมาณ การดักจับแก๊สคาร์บอนไดออกไซด์มีค่าต่ำ ในงานวิจัยนี้รูปแบบการไหลแบบปั่นป่วน (แบบปั่นป่วน หมุนเวียน) มีปริมาณการดักจับแก๊สคาร์บอนไดออกไซด์สูงสุดเนื่องจากระบบการผสมย้อนกลับสูง

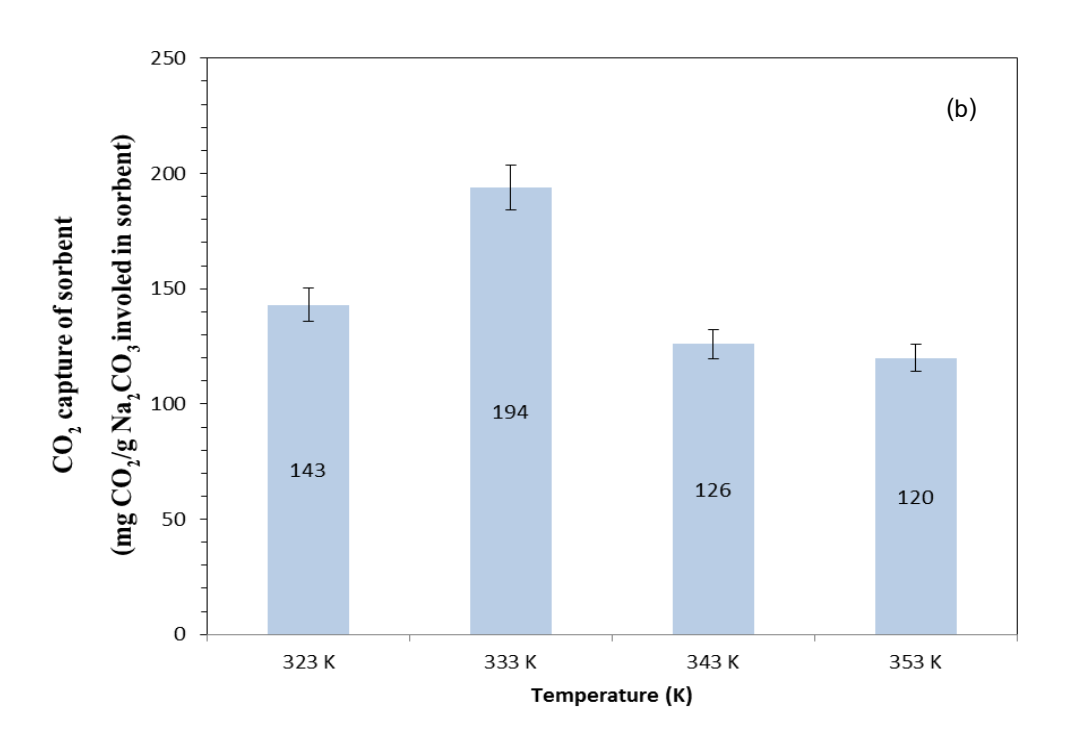
ผลของอุณหภูมิในท่อไรเซอร์ต่อความเข้มข้นของแก๊สที่ทางออกของตัวดูดซับโพแทสเซียม คาร์บอเนตและโซเดียมคาร์บอเนตแสดงดังรูปที่ 9 ผลที่ได้จะพบแนวโน้มของความเข้มข้นแก๊สที่ขา ออก 2 แบบที่ช่วงอุณหภูมิ 323-333 เคลวิน ปริมาณการดูดซับเพิ่มขึ้นตามการเพิ่มอุณหภูมิ ขณะที่ ช่วงอุณหภูมิ 333-353 เคลวิน ปริมาณการดูดซับลดลงเมื่อเพิ่มอุณหภูมิ จากทฤษฎีทาง เทอร์โมไดนามิกส์ปฏิกิริยาในกระบวนการจะมีร้อยละการเปลี่ยนแปลงสูงเมื่ออุณหภูมิต่ำเพราะเป็น ปฏิกิริยาคายความร้อน แต่ที่อุณหภูมิ 323 เคลวิน มีปริมาณการดูดซับต่ำ อธิบายจากการควบแน่น ของไอน้ำที่อุณหภูมินี้ โดยมีปริมาณการดูดซับสูงที่สุดที่อุณหภูมิประมาณ 333 เคลวิน





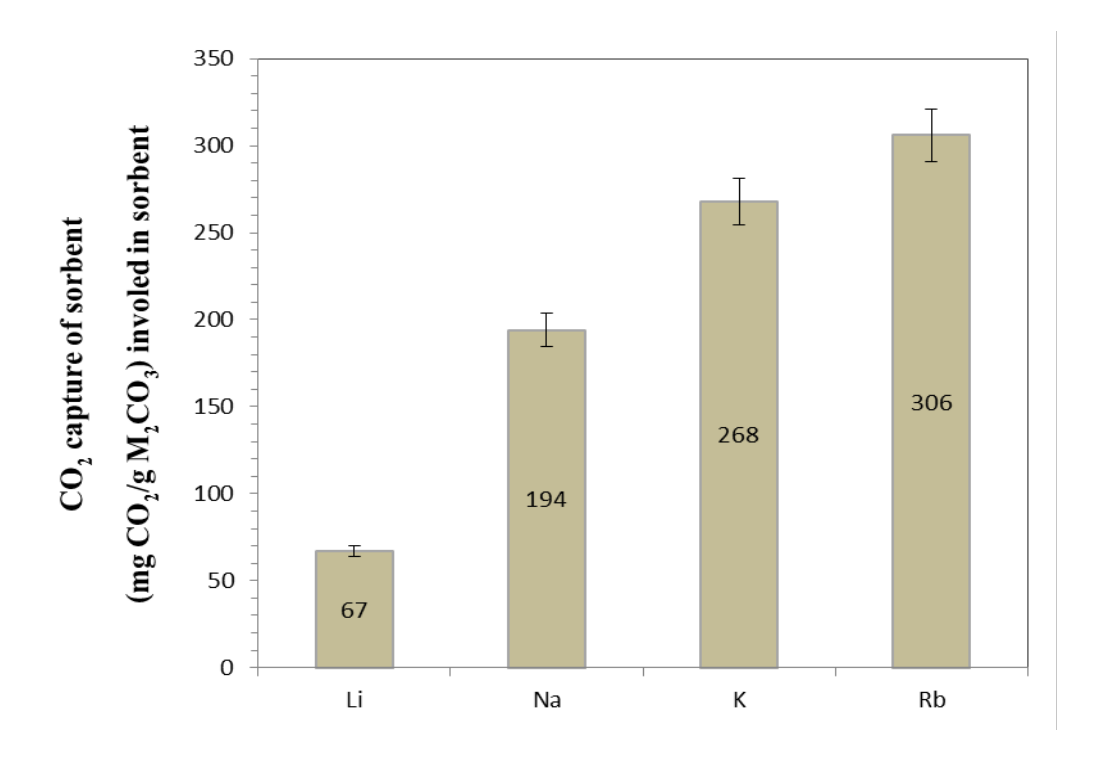
รูปที่ 8 ปริมาณการดักจับทั้งหมดของตัวดูดซับ (a) K₂CO₃/Al₂O₃ และ (b) Na₂CO₃/Al₂O₃ ที่ความ เข้มข้นคาร์บอนไดออกไซด์ร้อยละ 12 โดยปริมาตร ปริมาณไอน้ำร้อยละ 19.5 โดยปริมาตร และ อุณหภูมิในการดูดซับ 333 เคลวิน





รูปที่ 9 ผลของอุณหภูมิต่อปริมาณการดักจับทั้งหมดของตัวดูดซับ (a) K₂CO₃/Al₂O₃ และ (b) Na₂CO₃/Al₂O₃ ที่ความเข้มข้นคาร์บอนไดออกไซด์ร้อยละ 12 โดยปริมาตรและ ปริมาณไอน้ำร้อยละ 19.5 โดยปริมาตร

รูปที่ 10 แสดงปริมาณการดักจับแก๊สคาร์บอนไดออกไซด์ของโลหะแอลคาไลต่างชนิด ผลที่ ได้ให้ค่าการดักจับแก๊สคาร์บอนไดออกไซด์สูงสุดที่ 306 มิลลิกรัมคาร์บอนไดออกไซด์ต่อกรัม รูบิเดียมคาร์บอเนต เนื่องจากลักษณะพื้นผิวที่มีส่วนประกอบที่ว่องไวเป็นผลึกก้อนกลมสม่ำเสมอ จำนวนมากที่มีค่าสูงกว่าพื้นผิวที่ไม่มีความสม่ำเสมอของลิเทียมคาร์บอเนต โพแทสเซียมคาร์บอเนต และโซเดียมคาร์บอเนต



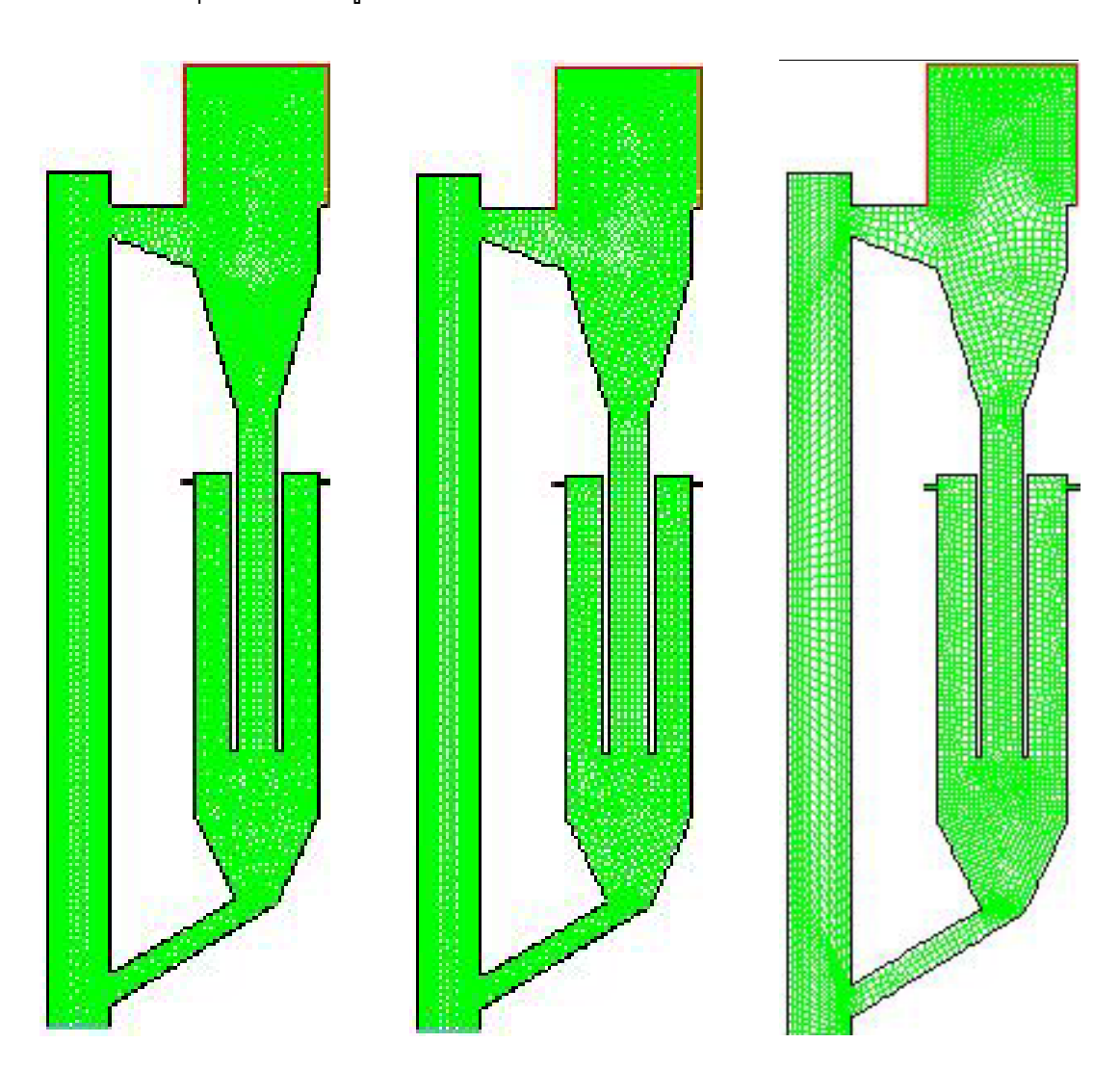
รูปที่ 10 ผลของชนิดโลหะแอลคาไลคาร์บอเนตต่อปริมาณการดักจับแก๊สคาร์บอนไดออกไซด์ ที่ความเข้มข้นคาร์บอนไดออกไซด์ร้อยละ 12 โดยปริมาตร ปริมาณน้ำร้อยละ 19.5 โดยปริมาตร และอุณหภูมิในการดูดซับ 333 เคลวิน

- การพัฒนาแบบจำลองพลศาสตร์ของไหลเชิงคำนวณของเครื่องปฏิกรณ์ฟลูอิไดซ์เบด แบบหมุนเวียนที่มีอัตราการไหลอนุภาคของแข็งสูงสำหรับการดักจับ คาร์บอนไดออกไซด์

ผู้วิจัยทำการพัฒนาแบบจำลองพลศาสตร์ของไหลเชิงคำนวณของเครื่องปฏิกรณ์ฟลูอิไดซ์เบด แบบหมุนเวียนที่มีอัตราการไหลอนุภาคของแข็งสูงสำหรับการดักจับคาร์บอนไดออกไซด์ ดังนี้

1) จากการทบทวนวรรณกรรมที่เกี่ยวข้องเกี่ยวกับการดักจับคาร์บอนไดออกไซด์ในเครื่อง ปฏิกรณ์ฟลูอิไดซ์เบดแบบหมุนเวียนที่มีอัตราการไหลอนุภาคของแข็งสูง ทำการสรุปแบบจำลอง พลศาสตร์ของไหลเชิงคำนวณที่ใช้งานกันอย่างแพร่หลาย

- 2) ทำการเขียนแบบเครื่องปฏิกรณ์ต้นแบบฟลูอิไดซ์เบดแบบหมุนเวียนสำหรับการดักจับ คาร์บอนไดออกไซด์ในเครื่องปฏิกรณ์ฟลูอิไดซ์เบดแบบหมุนเวียนที่มีอัตราการไหลอนุภาคของแข็ง สูง (ดังรูปที่ 11)
- 3) ทำการศึกษาผลของขนาดพื้นที่ช่องการคำนวณ แบบจำลอง (แบบจำลองแรงต้านทานการ เคลื่อนที่ของวัตถุ และ แบบจำลองความดันของแข็ง เป็นต้น) ตัวแปรการจำลอง (สัมประสิทธิ์ restitution และ สัมประสิทธิ์ specularity เป็นตัน) และ ตัวแปรดำเนินการ (ความเร็วแก๊สป้อนเข้า กระบวนการ และ อุณหภูมิกระบวนการ เป็นต้น) ที่มีต่อผลการจำลองพลศาสตร์ของไหลเชิงคำนวณ เพื่อหาขนาดพื้นที่ช่องการคำนวณ แบบจำลอง ตัวแปรการจำลอง และตัวแปรดำเนินการที่เหมาะสม สำหรับการจำลองการดักจับคาร์บอนไดออกไซด์ในเครื่องปฏิกรณ์ฟลูอิไดซ์เบดแบบหมุนเวียนที่มี อัตราการไหลอนุภาคของแข็งสูง



รูปที่ 11 เครื่องปฏิกรณ์ต้นแบบฟลูอิไดซ์เบดแบบหมุนเวียนสำหรับการดักจับคาร์บอนไดออกไซด์ ในเครื่องปฏิกรณ์ฟลูอิไดซ์เบดแบบหมุนเวียนที่มีอัตราการไหลอนุภาคของแข็งสูง (ที่ขนาดพื้นที่ช่องการคำนวณต่าง ๆ)

สำหรับขนาดพื้นที่ช่องการคำนวณ แบบจำลอง ตัวแปรการจำลอง และตัวแปรดำเนินการที่ เหมาะสมสำหรับการจำลองการดักจับคาร์บอนไดออกไซด์ในเครื่องปฏิกรณ์ฟลูอิไดซ์เบดแบบ หมุนเวียนที่มีอัตราการไหลอนุภาคของแข็งสูงสามารถสรุปได้ดังตารางที่ 3 และ 4

ตารางที่ 3 แบบจำลองพลศาสตร์ของไหลเชิงคำนวณที่ใช้ในโครงการศึกษาวิจัยนี้

- A. Governing equations;
- (a) Conservation of mass;
 - Gas phase;

$$\frac{\partial}{\partial t} \left(\varepsilon_{g} \rho_{g} \right) + \nabla \cdot \left(\varepsilon_{g} \rho_{g} v_{g} \right) = 0$$

- Solid particle phase;

$$\frac{\partial}{\partial t} (\varepsilon_s \rho_s) + \nabla \cdot (\varepsilon_s \rho_s v_s) = 0$$

- (b) Conservation of momentum;
 - Gas phase;

$$\frac{\partial}{\partial t} \left(\varepsilon_{g} \rho_{g} v_{g} \right) + \nabla \cdot \left(\varepsilon_{g} \rho_{g} v_{g} v_{g} \right) = -\varepsilon_{g} \nabla P + \nabla \cdot \tau_{g} + \varepsilon_{g} \rho_{g} g - \beta_{gs} \left(v_{g} - v_{s} \right)$$

- Solid particle phase;

$$\frac{\partial}{\partial t} (\varepsilon_s \rho_s v_s) + \nabla \cdot (\varepsilon_s \rho_s v_s v_s) = -\varepsilon_s \nabla P + \nabla \cdot \tau_s - \nabla P_s + \varepsilon_s \rho_s g + \beta_{gs} (v_g - v_s)$$

(c) Conservation of solid particle fluctuating energy;

$$\frac{3}{2} \left[\frac{\partial}{\partial t} (\varepsilon_{s} \rho_{s} \theta) + \nabla \cdot (\varepsilon_{s} \rho_{s} \theta v_{s}) \right] = (-\nabla P_{s} \bar{I} + \tau_{s}) : \nabla v_{s} + \nabla \cdot (\kappa_{s} \nabla \theta) - \gamma_{s} + \varphi_{gs}$$

- B. Constitutive equations;
- (a) Gas phase stress;

$$\tau_{g} = \varepsilon_{g} \mu_{g} \left[\nabla v_{g} + (\nabla v_{g})^{T} \right] - \frac{2}{3} \varepsilon_{g} \mu_{g} (\nabla \cdot v_{g}) I$$

(b) Solid particle phase stress;

$$\tau_s = \varepsilon_s \mu_s \left[\nabla v_s + (\nabla v_s)^T \right] - \varepsilon_s \left(\xi_s - \frac{2}{3} \mu_g \right) \nabla \cdot v_g I$$

(c) Collisional dissipation of solid particle fluctuating energy;

$$\gamma_s = 3(1 - e^2)\varepsilon_s^2 \rho_s g_0 \theta \left(\frac{4}{d_p} \sqrt{\frac{\theta}{\pi}}\right)$$

(d) Radial distribution function;

$$g_0 = \left[1 - \left(\frac{\varepsilon_s}{\varepsilon_{s,\text{max}}}\right)^{1/3}\right]^{-1}$$

(e) Solid particle phase pressure;

$$P_{s} = \varepsilon_{s} \rho_{s} \theta [1 + 2g_{0} \varepsilon_{s} (1 + e)]$$

(f) Solid particle phase shear viscosity;

$$\mu_s = \frac{4}{5} \varepsilon_s \rho_s d_p g_0 (1+e) \sqrt{\frac{\theta}{\pi}} + \frac{10 \rho_s d_p \sqrt{\pi \theta}}{96(1+e) g_0 \varepsilon_s} \left[1 + \frac{4}{5} g_0 \varepsilon_s (1+e) \right]^2$$

(g) Solid particle phase bulk viscosity;

$$\xi_s = \frac{4}{3} \varepsilon_s \rho_s d_p g_0 (1 + e) \sqrt{\frac{\theta}{\pi}}$$

(h) Conductivity of the solid particle fluctuating energy;

$$\kappa_{s} = \frac{150\rho_{s}d_{p}\sqrt{\theta\pi}}{384(1+e)g_{0}} \left[1 + \frac{6}{5}\varepsilon_{s}g_{0}(1+e)\right]^{2} + 2\rho_{s}\varepsilon_{s}^{2}d_{p}(1+e)g_{0}\sqrt{\frac{\theta}{\pi}}$$

(i) Exchange of the solid particle fluctuating energy between phases;

$$\varphi_{gs} = -3\beta_{gs}\theta$$

- (j) Gas-solid particle phase interphase exchange coefficient;
 - Gidaspow model;

$$\begin{aligned} &\text{when } \varepsilon_{g} > 0.80 \,; \; \beta_{gs} = 150 \frac{\left(1 - \varepsilon_{g}\right)^{2} \mu_{g}}{\varepsilon_{g} d_{p}^{2}} + 1.75 \frac{\left(1 - \varepsilon_{g}\right) \rho_{g} \left| v_{g} - v_{s} \right|}{d_{p}} \\ &\text{when } \varepsilon_{g} \leq 0.80 \,; \; \beta_{gs} = \frac{3}{4} \frac{\left(1 - \varepsilon_{g}\right) \varepsilon_{g}}{d_{p}} \; \rho_{g} \left| v_{g} - v_{s} \right| C_{D0} \varepsilon_{g}^{-2.65} \\ &\text{with } Re_{k} < 1000 \,; \qquad C_{D0} = \frac{24}{Re_{k}} \left(1 + 0.15 \, Re_{k}^{0.687}\right) \,; Re_{k} = \frac{\rho_{g} \varepsilon_{g} \left| v_{g} - v_{s} \right| d_{p}}{\mu_{g}} \\ ℜ_{k} \geq 1000 \,; \qquad C_{D0} = 0.44 \end{aligned}$$

C. Chemical reaction equations;

$$K_2CO_3 + CO_2 + H_2O \rightarrow 2KHCO_3$$

$$R = kC_{CO2}C_{H2O}\mathcal{E}$$

$$k = 600 exp(3609/RT)$$

ตารางที่ 4 ขนาดพื้นที่ช่องการคำนวณ ตัวแปรการจำลอง และ ตัวแปรดำเนินการที่ใช้ในโครงการศึกษาวิจัยนี้

Description	Value
Width of circulating fluidized bed riser (m)	0.15
Height of circulating fluidized bed riser (m)	2.00
Depth of circulating fluidized bed riser (m)	0.05
Width of circulating fluidized bed downer (m)	0.30
Height of circulating fluidized bed downer (m)	1.00
Depth of circulating fluidized bed downer (m)	0.05
N ₂ density (kg/m ³)	1.138
N ₂ viscosity (kg/m·s)	1.66E-05
N ₂ heat capacity (J/kg K)	1.14
N ₂ molecular weight (kg/kgmol)	28.01
CO ₂ density (kg/m ³)	1.788
CO ₂ viscosity (kg/m·s)	1.37E-05
CO ₂ heat capacity (J/kg K)	840.37
CO ₂ molecular weight (kg/kgmol)	44.00
H ₂ O density (kg/m ³)	0.554
H ₂ O viscosity (kg/m·s)	1.34E-05
H ₂ O heat capacity (J/kg K)	2,014.00
H ₂ O molecular weight (kg/kgmol)	18.01
K ₂ CO ₃ density (kg/m ³)	2,394
K ₂ CO ₃ heat capacity (J/kg K)	868.28
K ₂ CO ₃ molecular weight (kg/kgmol)	138.21
KHCO ₃ density (kg/m ³)	2,394
KHCO ₃ heat capacity (J/kg K)	1,196.62
KHCO ₃ molecular weight (kg/kgmol)	100.12
Al ₂ O ₃ density (kg/m ³)	2,719
Al ₂ O ₃ heat capacity (J/kg K)	775.00
Al ₂ O ₃ molecular weight (kg/kgmol)	101.96
Solid particle diameter (µm)	385

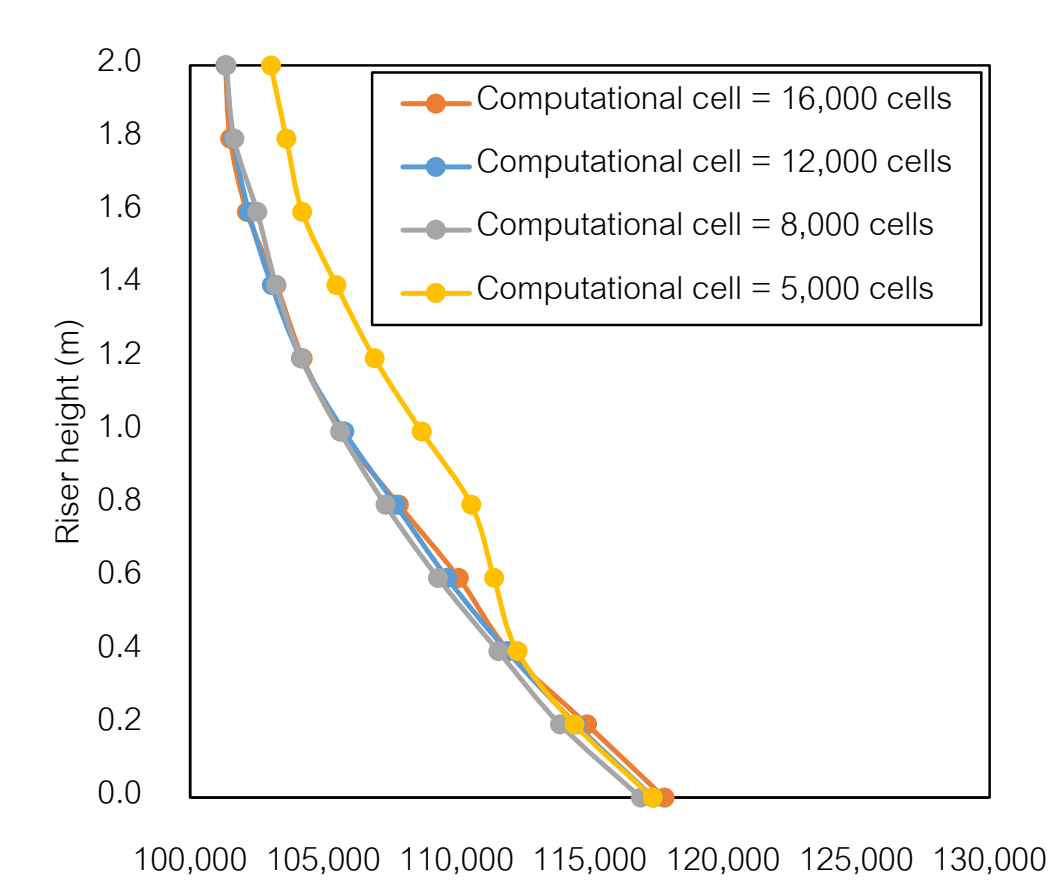
Description	Value
	0.25, 1,00,
Gas inlet velocity (m/s)	1.25, 1.75, 2,00,
	2.50, 5.00, 10.00
N ₂ inlet mass fraction (-)	0.75
CO ₂ inlet mass fraction (-)	0.10
H ₂ O inlet mass fraction (-)	0.15
Initial solid particle inside the circulating fluidized bed reacto (kg)	21.00
K ₂ CO ₃ inlet mass fraction (-)	0.35
KHCO ₃ inlet mass fraction (-)	0.00
Al ₂ O ₃ inlet mass fraction (-)	0.65
Outlet system pressure (Pa)	101,325
Specularity coefficient (-)	0.01
Restitution coefficient between solid particle and wall (-)	0.90
Restitution coefficient between solid particles (-)	0.90
Computational call (Calla)	5,000, 8,000, 12,000,
Computational cell (Cells)	16,000

- การทำการจำลองพลศาสตร์ของไหลเชิงคำนวณและวิเคราะห์การดักจับ คาร์บอนไดออกไซด์ในช่วงการไหลใหม่ภายในเครื่องปฏิกรณ์ฟลูอิไดซ์เบดแบบ หมุนเวียนที่มีอัตราการไหลอนุภาคของแข็งสูง

ผู้วิจัยทำการจำลองพลศาสตร์ของไหลเชิงคำนวณและวิเคราะห์การดักจับคาร์บอนไดออกไซด์ ในช่วงการไหลใหม่ภายในเครื่องปฏิกรณ์ฟลูอิไดซ์เบดแบบหมุนเวียนที่มีอัตราการไหลอนุภาค ของแข็งสูง สามารถสรุปผลการทดลองที่ได้ ดังต่อไปนี้

ผลการทดลองสำหรับแบบจำลองที่มีปริมาณของพื้นที่การคำนวณที่ไม่เท่ากันนั้น ย่อมส่งผล ต่อผลที่ได้จากการทดลอง การคำนวณโดยใช้ขนาดของพื้นที่ที่มากกว่า ย่อมให้ผลที่มีความละเอียด และแม่นยำมากกว่า เนื่องจากพื้นที่ได้ถูกแบ่งขนาดให้มีขนาดที่เล็กและมีปริมาณที่มากกว่า อย่างไร ก็ตาม ในการศึกษาพื้นที่ที่มีจำนวนมากจะส่งผลต่อเวลาที่ใช้ในการคำนวณ การทราบปริมาณพื้นที่ การคำนวณที่มีความละเอียดกับเวลาการคำนวณที่เหมาะสมนั้นจึงเป็นเรื่องที่สำคัญ ในงานวิจัยนี้จะ ใช้ขนาดของพื้นที่การคำนวณที่มีขนาดแตกต่างกันดังนี้ 5,000 8,000 12,000 และ 16,000 เซลล์

ในการศึกษาถึงพื้นที่ที่ใช้ในการคำนวณนั้น ภาวะในการดำเนินการที่ใช้จะมีค่าของความเร็ว ของแก๊สเท่ากับ 1.25 เมตรต่อวินาที ผลที่ได้จากการศึกษาเมื่อใช้ขนาดของพื้นที่การคำนวณที่ แตกต่างกันจะแสดงดังรูปที่ 12 ซึ่งแสดงผลของความดันที่ตำแหน่งต่าง ๆ ตลอดช่วงความสูงตลอด ทั้งท่อไรเซอร์ พบว่า การใช้ปริมาณพื้นที่การคำนวณที่แตกต่างกันจะส่งผลให้ผลที่เกิดขึ้นแตกต่าง กันตามไปด้วย จากกราฟจะสังเกตได้ว่ากราฟที่มีขนาดของพื้นที่ที่ใช้ในการคำนวณเท่ากับ 5,000 เซลล์ มีการเบี่ยงเบนออกไปอย่างเห็นได้ชัดที่ช่วงความสูงตั้งแต่ 0.40 เมตรขึ้นไป ในขณะที่ ช่วงความสูงด้านล่างนั้นจะมีค่าความดันที่ได้ที่ใกล้เคียงกัน เนื่องจากในบริเวณด้านล่างของท่อ ไรเซอร์นั้นมีปริมาณของแข็งอยู่เป็นจำนวนมาก ในขณะที่บริเวณตรงกลางของท่อไรเซอร์จะมีความ ปั่นป่วนที่มากกว่า ส่งผลให้การเคลื่อนที่ที่เกิดขึ้นในบริเวณนี้มีลักษณะเป็นแบบสุ่ม การใช้พื้นที่ที่มี ขนาดที่มีความละเอียดไม่เพียงพอ จะส่งผลให้การคำนวณที่ได้มีความคลาดเคลื่อนเกิดขึ้น

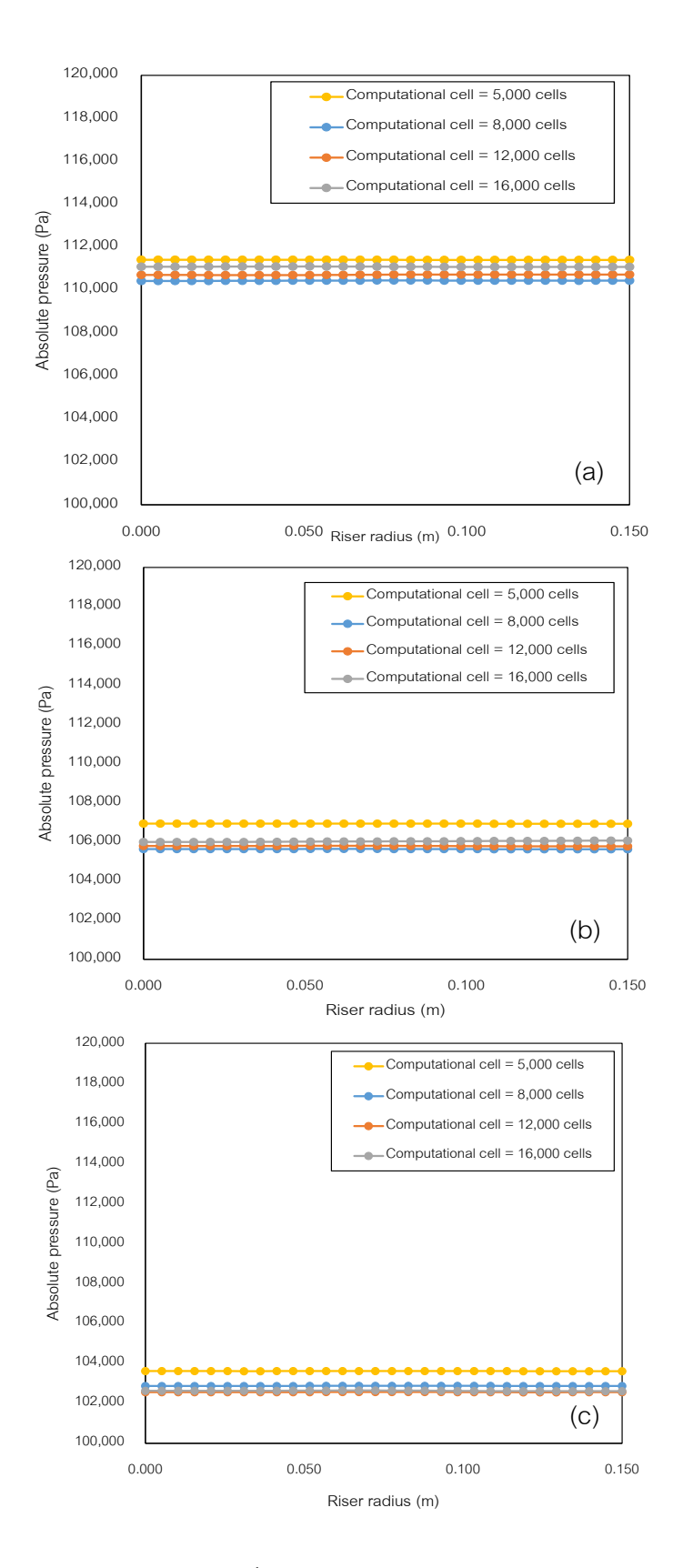


รูปที่ 12 ผลของความดันที่ตำแหน่งความสูงต่างๆ ของท่อไรเซอร์ที่มีพื้นที่ในการคำนวณเท่ากับ 5,000 8,000 12,000 และ 16,000 เซลล์

Absolute pressure (Pa)

เมื่อพิจารณาถึงผลที่เกิดขึ้นในช่วงของความสูงของไรเซอร์ที่ตำแหน่งต่าง ๆ ในแนวรัศมี จะ พบว่า ค่าที่ได้ในแต่ละขนาดของพื้นที่นั้นมีค่าไม่เท่ากันอย่างเห็นได้ชัด อย่างไรก็ตาม ค่าที่ได้ส่วน ใหญ่จะคลาดเคลื่อนไปจากกันเพียงเล็กน้อยเท่านั้น ยกเว้นเมื่อมีการใช้พื้นที่การคำนวณที่มีขนาด เท่ากับ 5,000 เซลล์ จะพบว่าค่าที่ได้เบี่ยงเบนออกมาอย่างเห็นได้ชัด ดังรูปที่ 13 (a) ถึง 13 (b) โดยเฉพาะที่บริเวณตรงกลางและบริเวณด้านบนของท่อไรเซอร์ เนื่องจากเป็นส่วนที่มีความปั้นป่วน เกิดขึ้นเป็นอย่างมาก ค่าที่ได้นั้นจะสูงกว่าการใช้พื้นที่ในการคำนวณที่สูงกว่า เนื่องจากความ ละเอียดที่น้อยกว่า ส่งผลให้ปริมาตรควบคุมที่ใช้ในการคำนวณนั้นมีขนาดใหญ่การคำนวณที่ได้จึง หยาบกว่า ในขณะที่การใช้พื้นที่การคำนวณที่เล็กและละเอียดกว่านั้น จะทำให้การคำนวณสมการใน ปริมาตรควบคุม สามารถคำนวณในตำแหน่งที่เหมาะสม ผลที่ได้จึงมีความแม่นยำและน่าเชื่อถือได้ มากกว่า ดังที่ได้กล่าวไปแล้วข้างต้น การแบ่งพื้นที่การคำนวณที่มีความละเอียดที่สูง ถึงแม้จะมีข้อดี อยู่ แต่ข้อเสียที่ตามมาคือ เวลาที่ใช้ในการคำนวณ ซึ่งพบว่าการใช้พื้นที่ในการคำนวณเท่ากับ 16,000 เซลล์ จะใช้เวลาในการคำนวณถึง 3 สัปดาห์ ที่พื้นที่ในการคำนวณเท่ากับ 12,000 เซลล์ จะ ใช้เวลาในการคำนวณเท่ากับ 1 สัปดาห์ ที่พื้นที่ในการคำนวณเท่ากับ 8,000 เซลล์ จะใช้เวลาในการ คำนวณเท่ากับ 3 วัน และเมื่อใช้พื้นที่ในการคำนวณเท่ากับ 5,000 เซลล์ จะใช้เวลาในการคำนวณ เพียงประมาณ 1 วัน ดังนั้น ในการเลือกพื้นที่ที่ใช้ในการคำนวณ เวลาก็เป็นสิ่งที่สำคัญเช่นเดียวกัน ซึ่งเมื่อดูจากข้อมูลความแม่นยำถูกต้องและระยะเวลาที่ใช้ พบว่า การใช้พื้นที่ในการคำนวณเท่ากับ 8,000 เซลล์ จะให้ผลที่ใกล้เคียงกับผลที่ได้จากการคำนวณโดยใช้พื้นที่เท่ากับ 12,000 และ 16,000 เซลล์ โดยจะมีระยะเวลาที่ใช้ในคำนวณที่เหมาะสมที่สุด

ในการศึกษาเพื่อหาสมการอัตราการเกิดปฏิกิริยาการดูดซับแก๊สคาร์บอนไดออกไซด์โดยใช้ โพแทสเซียมคาร์บอเนตเป็นตัวดูดซับของแข็ง จะอ้างอิงผลการจำลองกับผลการทดลองของงานวิจัย ของ Abbasi และ Arastoopour (2011) ซึ่งทำการจำลองการดูดซับแก๊สคาร์บอนไดออกไซด์ในท่อ ไรเซอร์ที่มีขนาดของความสูงเท่ากับ 6.00 เมตร ความกว้างเท่ากับ 35 มิลลิเมตร ฟลักซ์การไหล โดยมวลของของแข็งมีค่าเท่ากับ 21 กิโลกรัมต่อเมตรยกกำลังสองวินาที สัดส่วนของของแข็งเท่ากับ 0.60 สัดส่วนโดยมวลของโพแทสเซียมคาร์บอเนตเท่ากับ 0.35 ความเร็วของแก๊สขาเข้าเท่ากับ 2.00 เมตรต่อวินาที สัดส่วนโดยมวลของแก๊สคาร์บอนไดออกไซด์เท่ากับ 0.10 สัดส่วนโดยมวลของน้ำ เท่ากับ 0.15 และสัดส่วนโดยมวลของในโตรเจนเท่ากับ 0.75 แบบจำลองจากงานวิจัยนี้จะใช้ แบบจำลองสัมประสิทธิ์ของแรงต้านการเคลื่อนที่ระหว่างวัฏภาคแบบ EMMS ขนาดของพื้นที่ที่ใช้ใน การคำนวณเท่ากับ 10,000 เซลล์ ในงานวิจัยนี้ระบบจะเริ่มเข้าสู่ภาวะเสมือนคงตัวตั้งแต่เวลา 90 วินาทีขึ้นไป ดังนั้นในการวิเคราะห์ผลที่ได้จากการทดลองจะเริ่มนำค่าตั้งแต่เวลาที่ 100 วินาทีขึ้นไป มาทำการศึกษา แบบจำลองที่ใช้ในการศึกษานี้จะใช้ภาวะในการดำเนินการที่เหมือนกัน แต่สมการ อัตราการเกิดปฏิกิริยาการดูดซับแก๊สคาร์บอนไดออกไซด์ด้วยโพแทสเซียมคาร์บอเนตจะใช้สมการ จากงานวิจัยของ Khongprom และ Gidaspow (2010) โดยจะทำการเปลี่ยนแปลงปัจจัยความถี่ที่อยู่ ด้านหน้าของค่าเอกโพเนนเชียลเพื่อให้ผลการทดลองที่ได้มีความใกล้เคียงกับงานวิจัยของ Abbasi และ Arastoopour (2011) ทั้งปริมาณของแก๊สคาร์บอนไดออกไซด์และความดันลดภายในระบบ

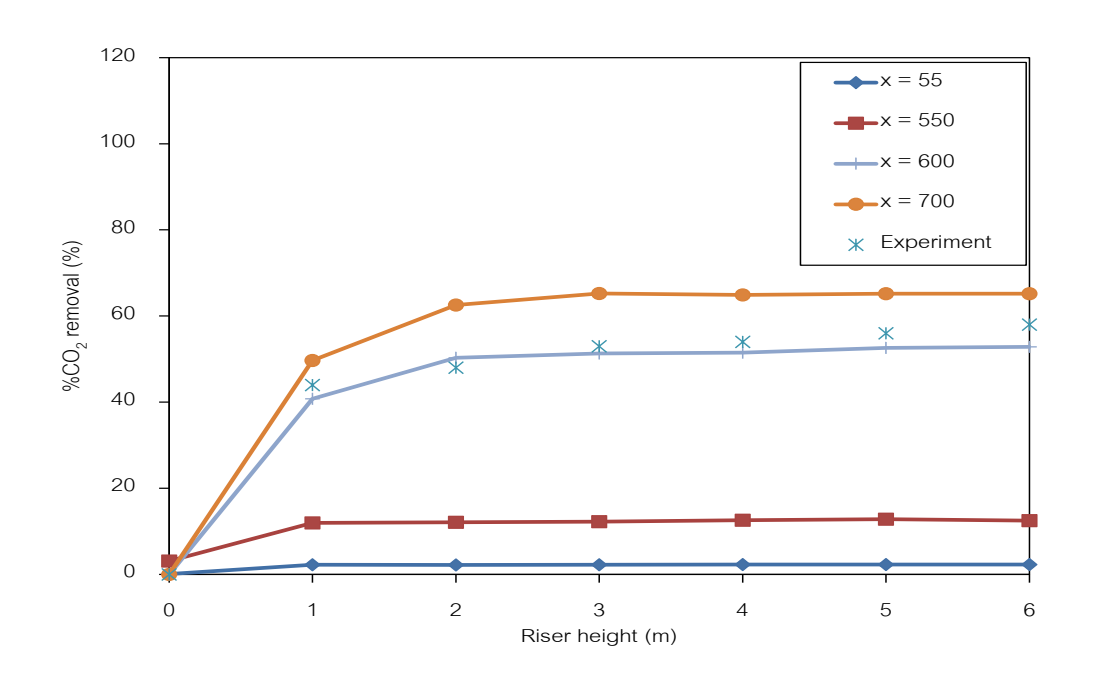


รูปที่ 13 ผลของความดันภายในระบบที่ตำแหน่งความสูงเท่ากับ (a) 0.50 เมตร (b) 1.00 เมตร และ (c) 1.50 เมตร ของท่อไรเซอร์ที่มีพื้นที่ในการคำนวณเท่ากับ 5,000 8,000 12,000 และ 16,000 เซลล์

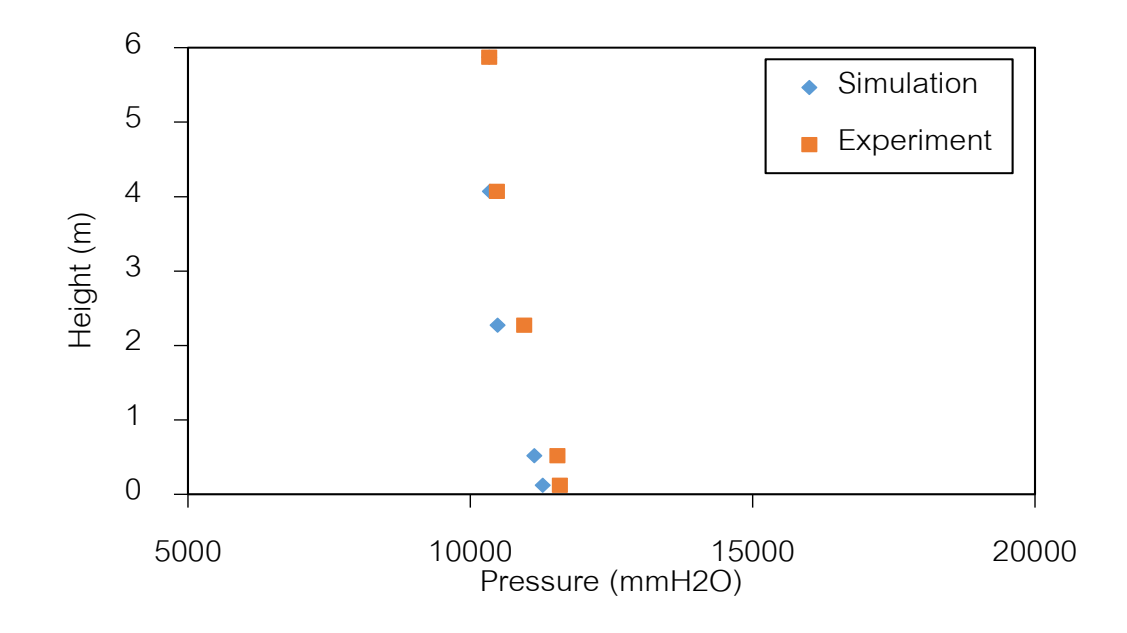
ในส่วนนี้จะเป็นการอภิปรายผลการทดลองที่เกิดขึ้นในแง่ของประสิทธิภาพในการดูดซับแก๊ส คาร์บอนไดออกไซด์ การเปรียบเทียบผลการทดลองที่ได้ในเชิงปริมาณของแก๊สคาร์บอนไดออกไซด์ ที่ถูกดูดซับนั้น จะถูกนำมาวิเคราะห์ตลอดช่วงความสูงของท่อไรเซอร์ โดยจะคำนวณจากผลต่าง ระหว่างสัดส่วนโดยมวลของแก๊สคาร์บอนไดออกไซด์ขาเข้ากับสัดส่วนโดยมวลของแก๊ส คาร์บอนไดออกไซด์ขาออกดังรูปที่ 14 พบว่า ปริมาณของแก๊สคาร์บอนไดออกไซด์ส่วนใหญ่จะมี ปริมาณที่ลดลงมากในบริเวณช่วงด้านล่างของท่อไรเซอร์ เนื่องจากเป็นบริเวณที่มีความแตกต่าง ของความเข้มข้นของแก๊สคาร์บอนไดออกไซด์ที่สูง ความเข้มข้นของแก๊สคาร์บอนไดออกไซด์จะ ลดลงเมื่อความสูงของท่อไรเซอร์เพิ่มขึ้นและจะคงที่อยู่ที่ค่า ๆ หนึ่งซึ่งเท่ากับร้อยละ 58 ของสัดส่วน โดยมวล ค่านี้จะเป็นปริมาณของแก๊สคาร์บอนไดออกไซด์ที่ถูกดูดซับได้ ประสิทธิภาพในการดูดซับ แก๊สคาร์บอนไดออกไซด์ของเครื่องปฏิกรณ์นี้จึงอยู่ที่ร้อยละ 58 จากผลในส่วนนี้แสดงให้เห็นว่า กระบวนการการดูดซับแก๊สคาร์บอนไดออกไซด์ส่วนใหญ่จะเกิดขึ้นบริเวณด้านล่างของท่อไรเซอร์ เนื่องจากมีความเข้มข้นที่สูง ในขณะที่บริเวณด้านบนการเกิดปฏิกิริยาจะลดลง ดังนั้น การออกแบบ ้ เครื่องปฏิกรณ์ฟลูอิไดซ์เบดที่สูงเกินไปไม่สามารถส่งผลให้ประสิทธิภาพในการดูดซับนั้นดีขึ้น การ จะเพิ่มประสิทธิภาพนั้นควรพิจารณาถึงขนาดของเครื่องปฏิกรณ์ รูปแบบการไหล ความเร็วของแก๊ส ขาเข้า ฟลักซ์การไหลของของแข็งร่วมด้วย เมื่อวิเคราะห์ผลจากการใช้สมการอัตราการเกิดปฏิกิริยา ที่มีค่าปัจจัยความถี่หน้าเอกโพเนนเซียลค่าต่างๆ พบว่าเมื่อใช้ค่าที่น้อยเกินไปจะส่งผลให้ ประสิทธิภาพที่ได้มีค่าที่น้อยกว่าค่าที่ได้จากงานวิจัย Abbasi และ Arastoopour (2011) ซึ่งมี ประสิทธิภาพการดูดซับเท่ากับร้อยละ 58 ในขณะที่การใช้ค่าที่สูงมากจะส่งผลให้ปฏิกิริยาการดูดซับ เกิดขึ้นเร็ว ประสิทธิภาพที่ได้จะมีค่าสูงถึงร้อยละ 100 ซึ่งเป็นไปไม่ได้ในระบบจริงเนื่องจากแก๊ส คาร์บอนไดออกไซด์ไม่ได้ถูกดูดซับทั้งหมดในระบบได้ เมื่อทำการวิเคราะห์ค่าปัจจัยความถี่หน้า เอกโพเนนเชียลเท่ากับ 600 พบว่าประสิทธิภาพในการดูดซับแก๊สคาร์บอนไดออกไซด์ที่เกิดขึ้นมีค่า เท่ากับร้อยละ 56 ซึ่งใกล้เคียงกับงานวิจัยของ Abbasi และ Arastoopour (2011) สมการอัตราการ เกิดปฏิกิริยาที่มีค่าปัจจัยความถี่หน้าเอกโพเนนเชียลเท่ากับ 600 จึงเหมาะสมที่จะนำไปใช้ใน แบบจำลองการดูดซับแก๊สคาร์บอนไดออกไซด์ในเครื่องปฏิกรณ์ฟลูอิไดซ์เบดแบบหมุนเวียน

ผลของค่าความดันลดภายในระบบที่ตำแหน่งต่าง ๆ ตลอดช่วงความสูงของท่อไรเซอร์ สามารถนำมาใช้เปรียบเทียบผลการทดลองที่เกิดขึ้นในเครื่องปฏิกรณ์ได้ ค่าของความดันลดภายใน ระบบที่ได้นำมาใช้ในการวิเคราะห์เป็นค่าความดันลดที่จากการวิจัยของ Yi และคณะ (2007) ซึ่งทำ การทดลองโดยใช้เครื่องปฏิกรณ์จริง ค่าความดันที่ได้นั้นจะแสดงได้ดังรูปที่ 15 ซึ่งแสดงถึงความดัน ลดที่เกิดขึ้นที่ความสูงของท่อไรเซอร์เท่ากับ 120 มิลลิเมตรถึง 520 มิลลิเมตร (DP1) 520 มิลลิเมตร ถึง 2270 มิลลิเมตร (DP2) 2270 มิลลิเมตรถึง 4070 มิลลิเมตร (DP3) และ 4070 มิลลิเมตรถึง 5870 มิลลิเมตร (DP4) พบว่า ค่าของความดันลดที่เกิดขึ้นนั้นมีค่าที่ใกล้เคียงกับงานวิจัยที่ได้นำมา เปรียบเทียบ หรือแบบจำลองที่สร้างขึ้นมีค่าของความดันลดที่ใกล้เคียงกับงานวิจัยที่ใช้เครื่อง ปฏิกรณ์จริง เนื่องจากค่าความดันลดเป็นค่าที่บ่งบอกถึงปริมาณของอนุภาคของแข็งได้ตัวหนึ่ง อัน เป็นค่าที่เกิดขึ้นเนื่องจากแรงเสียดทานของอนุภาคของแข็ง ตำแหน่งที่มีค่าความดันลดที่มากจะ

แสดงถึงปริมาณของแข็งที่มาก การใช้ค่าความดันลดในการเปรียบเทียบปริมาณของอนุภาค ของแข็งที่มีความเหมาะสมกับการใช้ในกระบวนการฟลูอิไดซ์เบด เพราะระบบไม่สามารถวัดปริมาณ ของอนุภาคของแข็งได้โดยตรง



รูปที่ 14 การดูดซับแก๊สคาร์บอนไดออกไซด์ที่เกิดขึ้นเมื่อแทนค่าปัจจัยความถี่ของสมการการ เกิดปฏิกิริยาต่างๆ หน้าพจน์เอกโพเนนเชียล



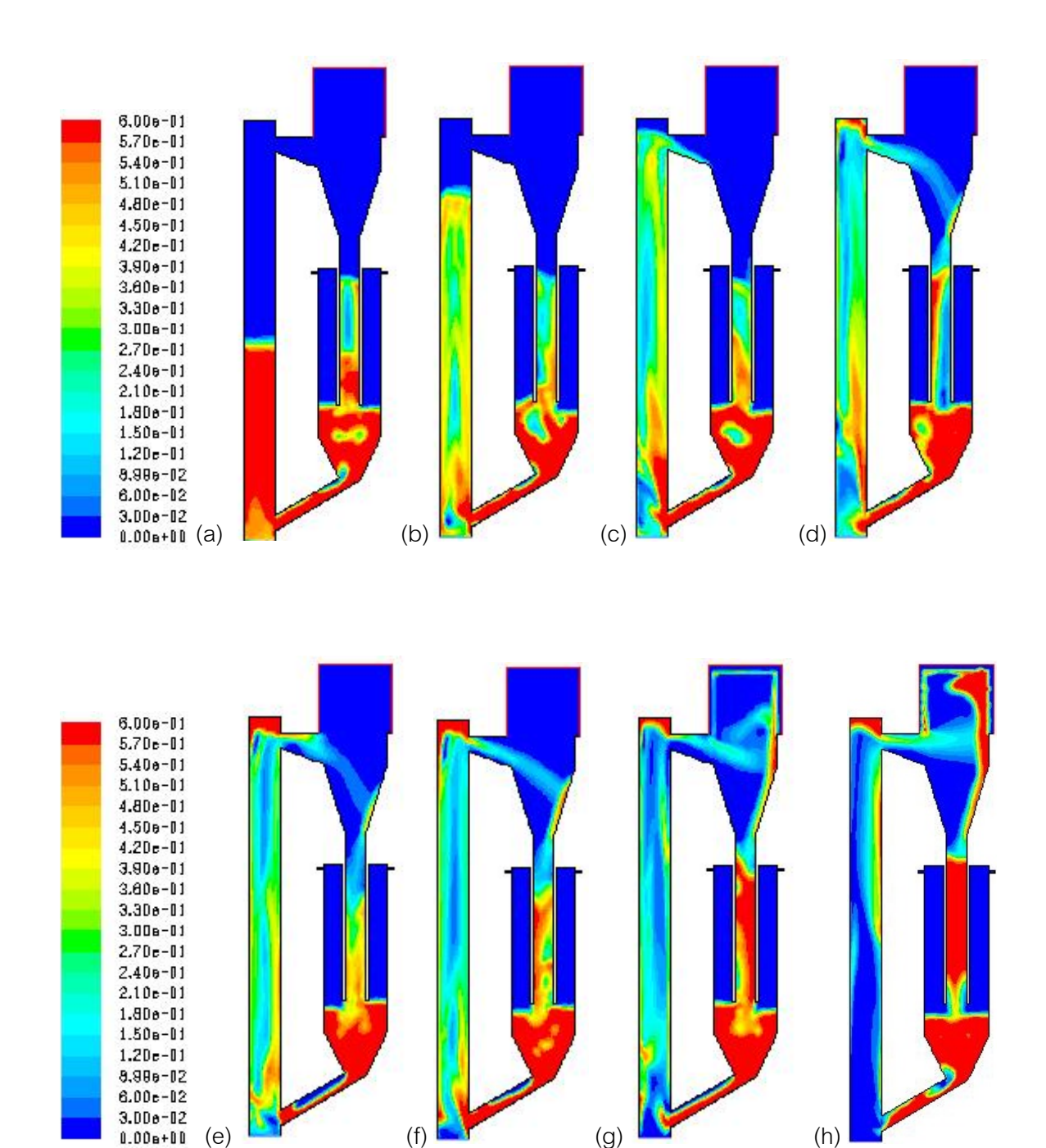
รูปที่ 15 ผลของความดันลดที่ตำแหน่งความสูงต่าง ๆ ของท่อไรเซอร์เทียบกับงานวิจัยของ Abbasi และ Arastoopour (2011)

กระบวนการฟลูอิไดเซชันนั้นเป็นกระบวนการที่ทำการเปลี่ยนการประพฤติตัวของแข็งให้มี ลักษณะที่ใกล้เคียงกับของไหล โดยการป้อนแก๊สหรือของเหลวเข้าทางด้านล่างของท่อไรเซอร์ เพื่อให้ของแข็งลอยขึ้นในลักษณะของของไหล การเคลื่อนที่ของอนุภาคของแข็งนั้นจะขึ้นอยู่กับตัว แปรหลายตัว เช่น ความเป็นทรงกลม ความหนาแน่น ขนาดของอนุภาค ความเร็วของของใหล เป็น ต้น ซึ่งตัวแปรเหล่านี้จะส่งผลให้ลักษณะการเคลื่อนที่เปลี่ยนแปลงไป รูปแบบการไหลที่ได้มี การศึกษาและค้นพบโดยทั่วไปนั้นจะประกอบไปด้วย รูปแบบการไหลแบบฟองแก๊ส รูปแบบการ ไหลแบบปั่นป่วน รูปแบบการไหลแบบความเร็วสูงและรูปแบบการไหลแบบเบาบาง แต่ละรูปแบบ การใหลนั้นก็จะมีข้อดีและข้อเสียที่แตกต่างกันออกไป ในงานวิจัยนี้ต้องการรูปแบบการใหลที่จะช่วย ส่งผลให้พื้นที่ผิวสัมผัสกันของอนุภาคของแข็งและแก๊สเพิ่มขึ้นและมีการถ่ายโอนอนุภาคของแข็งไป ยังฝั่งดาวเนอร์ได้ ซึ่งพบว่ารูปแบบการไหลแบบปั่นป่วนและรูปแบบการไหลแบบความเร็วสูงจะ สามารถตอบสนองความต้องการดังกล่าวได้ ดังนั้น ในงานวิจัยนี้จึงทำการศึกษารูปแบบการไหลที่ เกิดขึ้นให้อยู่ในช่วงความเร็วของแก๊สตั้งแต่ความเร็วเท่ากับ 0.25 เมตรต่อวินาที่จนถึงความเร็วของ ้แก๊สเท่ากับ 10.00 เมตรต่อวินาที เพื่อครอบคลุมรูปแบบการใหลที่สามารถเกิดขึ้นได้ทั้งหมด และ ทำการเลือกช่วงความเร็วที่เหมาะสม ซึ่งจะอยู่ระหว่างช่วงรูปแบบการไหลแบบปั่นป่วนและรูปแบบ การใหลแบบความเร็วสูง โดยจะทำการศึกษาถึงผลที่เกิดขึ้นในรูปของการกระจายตัวของอนุภาค ของแข็ง เพื่อทำการอธิบายอุทกพลศาสตร์ที่เกิดขึ้น

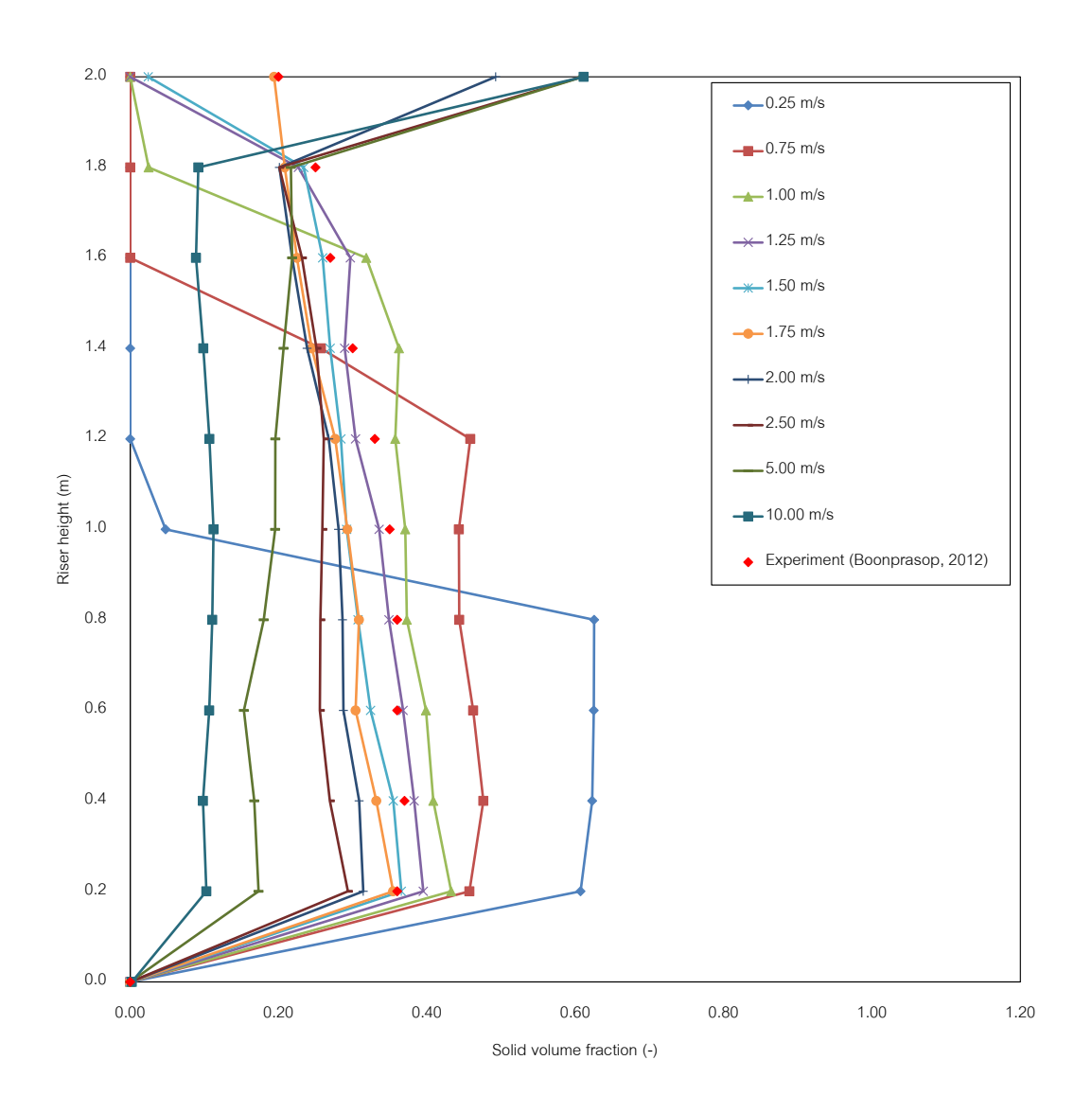
ผลที่ได้จากการศึกษาที่ความเร็วต่างๆ นั้นพบว่าลักษณะการกระจายตัวของอนุภาคจะมี ความแตกต่างกันเมื่อมีการป้อนแก๊สที่ความเร็วแตกต่างกัน ดังรูปที่ 16 โดยพบว่าในช่วงความเร็ว ของแก๊สเท่ากับ 0.25 เมตรต่อวินาทีถึง 1.00 เมตรต่อวินาที อนุภาคของแข็งที่อยู่ภายในท่อไรเซอร์ จะมีการขยายตัวเพิ่มมากขึ้นเมื่อมีการใช้ความเร็วของแก๊สที่มากขึ้น อย่างไรก็ตาม ที่ความเร็วของ แก๊สเท่ากับ 1.00 เมตรต่อวินาที เบดของอนุภาคของแข็งสามารถขยายตัวไปได้ใกล้กับบริเวณปาก ทางออกบริเวณด้านบนของท่อไรเซอร์ที่เชื่อมกับไซโคลน ลักษณะรูปแบบการไหลนี้จะอยู่ในช่วง ของรูปแบบการใหลแบบฟองแก๊สและรูปแบบการใหลแบบปั่นป่วน เมื่อทำการป้อนแก๊สที่มี ความเร็วเท่ากับ 1.25 เมตรต่อวินาที่จนถึง 1.75 เมตรต่อวินาที่ ลักษณะการประพฤติตัวของอนุภาค ของแข็งนั้นมีการขยายตัวจนถึงบริเวณทางออกด้านบนของท่อไรเซอร์ นอกจากนี้ อนุภาคของแข็ง ยังสามารถกระจายตัวได้ดีทั่วทั้งท่อไรเซอร์ ซึ่งแสดงให้เห็นดังรูปที่ 16 จากการศึกษาผลการทดลอง ด้วยรูปคอนทัวร์นี้ จึงได้มีการตั้งสมมติฐานขึ้นว่า ลักษณะรูปแบบการไหลนี้สามารถส่งผลให้ ประสิทธิภาพในการเกิดปฏิกิริยากันของอนุภาคของแข็งและแก๊สเพิ่มสูงขึ้น เนื่องจากอนุภาค ของแข็งมีการกระจายตัวที่ดีตลอดทั้งความสูงของท่อไรเซอร์และมีการถ่ายโอนมวลสารของอนุภาค ของแข็งไปยังฝั่งดาวเนอร์อย่างต่อเนื่อง เมื่อทำการป้อนความเร็วของแก๊สเพิ่มขึ้นจาก 1.75 เมตรต่อ วินาที เป็น 2.00 เมตรต่อวินาที พบว่าลักษณะการประพฤติตัวของอนุภาคของแข็งจะคล้ายกันกับที่ ความเร็วของแก๊สเท่ากับ 1.75 เมตรต่อวินาที แต่จะพบช่องว่างที่เกิดขึ้นในท่อไรเซอร์เพิ่มขึ้น ซึ่งใน รูปที่ 16 จะแสดงถึงสีที่แตกต่างกันที่เกิดขึ้นในคอลัมน์ของท่อไรเซอร์ให้เห็นอย่างชัดเจน การแบ่งสี ของอนุภาคของแข็งในท่อไรเซอร์จะสามารถอธิบายถึงการเกิดปรากฏการณ์การไหลแบบแกนใน-วง

นอก รูปแบบการไหลแบบแกนในวงนอกนี้เป็นรูปแบบการไหลที่ส่งผลให้พื้นที่สัมผัสของอนุภาค ของแข็งและแก๊สลดลงเนื่องจากบริเวณที่อนุภาคของแข็งมีปริมาณน้อย จะทำหน้าที่เป็นช่องทางให้ แก๊สไหลผ่าน อนุภาคของแข็งส่วนใหญ่จะถูกดันออกจากช่องว่างนี้ไปรวมตัวกันบริเวณผนังด้านใด ด้านหนึ่งหรือทั้งสองด้าน เมื่ออนุภาคของแข็งจับตัวกันมากก็จะมีน้ำหนักที่มากขึ้นและเคลื่อนที่ใน ทิศทางสวนทางกับการเคลื่อนที่ ก้อนของอนุภาคของแข็งนี้จะมีพื้นที่ผิวที่น้อย ทำให้บริเวณตรง กลางของก้อนอนุภาคนี้ไม่สามารถเกิดปฏิกิริยาเคมีได้ ส่งผลให้ประสิทธิภาพในการเกิดปฏิกิริยา เคมีลดลง ลักษณะการไหลนี้จะเริ่มเห็นได้เมื่อมีการป้อนความเร็วของแก๊สตั้งแต่ 2.00 เมตรต่อวินาที และจะแสดงความชัดเจนขึ้นเมื่อความเร็วของแก๊สเพิ่มมากขึ้น รูปแบบการไหลที่เกิดขึ้นนี้เป็น ลักษณะที่สำคัญของรูปแบบการไหลความเร็วสูง เมื่อป้อนความเร็วของแก๊สตั้งแต่ 5.00 เมตรต่อ วินาทีขึ้นไป พบว่าปริมาณของอนุภาคของแข็งที่อยู่ในท่อไรเซอร์นั้นจะลดลงอย่างมาก จนกระทั่ง เหลือน้อยมากจนเกือบจะไม่พบอนุภาคของแข็งเมื่อเพิ่มความเร็วของแก๊สถึง 10.00 เมตรต่อวินาที ลักษณะของรูปแบบการไหลนี้เป็นลักษณะของรูปแบบการไหลแบบเบาบาง เนื่องจากในท่อไรเซอร์ นั้นปริมาณของแข็งนั้นจะเบามาก ในขณะที่ฝั่งดาวเนอร์จะพบการกองของอนุภาคของแข็งแทน

เมื่อทำการศึกษาในเชิงของปริมาณ ปริมาณของอนุภาคของแข็งนั้นจะถูกทำการเก็บค่าและ นำมาแสดงได้ดังรูปที่ 17 ซึ่งแสดงถึงปริมาณของอนุภาคของแข็งที่ตำแหน่งความสูงต่างๆ ของท่อ ไรเซอร์ ที่ความเร็วของแก๊สเท่ากับ 0.25 เมตรต่อวินาทีถึง 1.00 เมตรต่อวินาที ปริมาณของอนุภาค ของแข็งบริเวณด้านล่างของท่อไรเซอร์นั้นมีปริมาณที่มากที่สุด ในขณะที่บริเวณด้านบนไม่มีปริมาณ ของอนุภาคของแข็ง เนื่องจากการกระจายตัวของเบดของแข็งในท่อไรเซอร์นั้นยังมีการกระจายตัวที่ ไม่ทั่วถึง เมื่อทำการศึกษาในช่วงความเร็วของแก๊สเท่ากับ 1.25 เมตรต่อวินาทีถึง 2.00 เมตรต่อ วินาที พบว่า ปริมาณของอนุภาคของแข็งที่พบจะมีปริมาณอยู่ในช่วง 0.30 ถึง 0.50 อย่างไรก็ตาม ์ ตั้งแต่ช่วงความสูงเท่ากับ 0.20 เมตร ถึง 1.80 เมตร ของท่อไรเซอร์ ปริมาณของอนุภาคของแข็งนี้ จะไม่สามารถขยายตัวไปจนสัมผัสกับด้านบนสุดของท่อไรเซอร์ได้แต่อนุภาคเหล่านี้ก็สามารถ เคลื่อนที่ไปยังฝั่งดาวเนอร์ได้ ช่วงความเร็วของแก๊สในช่วงนี้จึงเป็นช่วงความเร็วที่เหมาะแก่การ นำไปใช้ในระบบที่เกิดปฏิกิริยาเคมี หลังจากช่วงความเร็วของแก๊สเท่ากับ 1.25 เมตรต่อวินาทีถึง 2.00 เมตรต่อวินาที ก็ไม่พบว่าปริมาณของอนุภาคของแข็งที่ตำแหน่งต่างๆของท่อไรเซอร์มีค่า มากกว่าค่าที่ได้ในช่วงความเร็วดังกล่าว แสดงให้เห็นได้อย่างชัดเจนว่าช่วงความเร็วของแก๊สที่มี ความเหมาะสมนั้นอยู่ในช่วงตั้งแต่ 1.25 เมตรต่อวินาทีถึง 1.75 เมตรต่อวินาที สำหรับที่ความเร็ว ของแก๊สเท่ากับ 2.00 เมตรต่อวินาทีนั้น ถึงแม้ว่าจะมีปริมาณของอนุภาคของแข็งที่ใกล้เคียงกับที่ 1.75 เมตรต่อวินาที แต่ผลในส่วนของรูปคอนทัวร์ที่แสดงถึงการประพฤติตัวของอนุภาคของแข็ง แสดงให้เห็นถึงรูปแบบการไหลแบบแกนใน-วงนอก ซึ่งเป็นรูปแบบที่ส่งผลเสียต่อกระบวนการที่มี การเกิดปฏิกิริยาเคมี ดังนั้น ที่ความเร็วเท่ากับ 2.00 เมตรต่อวินาทีจึงไม่เหมาะที่จะนำไปใช้ใน กระบวนการที่จำเป็นต้องอาศัยการสัมผัสกันของอนุภาคของแข็งและแก๊สคาร์บอนไดออกไซด์ที่สูง เช่น การดูดซับแก๊สคาร์บอนไดออกไซด์ เมื่อนำผลของการกระจายตัวของอนุภาคของแข็งมา เปรียบเทียบกับงานวิจัยจริง (Boonprasop, 2012) พบว่าผลที่ได้มีค่าใกล้เคียงกัน ดังรูปที่ 17



รูปที่ 16 แสดงลักษณะการประพฤติตัวของอนุภาคของแข็งที่ความเร็วของแก๊สขาเข้าเท่ากับ (a) 0.25 (b) 1.00 (c) 1.25 (d) 1.75 (e) 2.00 (f) 2.50 (g) 5.00 และ (h) 10.00 เมตรต่อวินาที



รูปที่ 17 สัดส่วนของแข็งที่อยู่ในท่อไรเซอร์ที่ตำแหน่งความสูงต่างๆ และมีความเร็วของแก๊สขาเข้าที่แตกต่างกัน

การศึกษาส่วนที่ผ่านมาเป็นการศึกษาถึงอุทกพลศาสตร์ที่เกิดขึ้น พบว่า ช่วงความเร็วของ แก๊สเท่ากับ 1.25 เมตรต่อวินาทีถึง 1.75 เมตรต่อวินาที เป็นช่วงที่ทำให้การผสมกันของอนุภาค ของแข็งและเกิดขึ้นได้ดีที่สุด ลักษณะการไหลที่เกิดขึ้นจะอยู่ระหว่างรูปแบบการไหลแบบปั่นป่วน และรูปแบบการไหลแบบความเร็วสูง มีการนิยามชื่อเรียกว่า รูปแบบการไหลแบบปั่นป่วนหมุนเวียน นอกจากนี้ การศึกษาเพื่อหาสมการอัตราการเกิดปฏิกิริยาการดูดซับแก๊สคาร์บอนไดออกไซด์ซึ่ง สามารถให้ผลการทดลองที่ใกล้เคียงกับผลการทดลองจริง เมื่อเทียบกับงานวิจัยที่เกี่ยวข้อง ค่า ปัจจัยความถี่ที่อยู่หน้าเอกโพเนนเซียลที่ทำให้ผลที่ได้มีความใกล้เคียงกับงานวิจัยที่นำมา เปรียบเทียบ มีค่าเท่ากับ 600 การศึกษาในส่วนนี้จะเป็นการนำผลจากหัวข้อที่ผ่านมามาใช้งาน โดย จะนำภาวะในการดำเนินการต่างๆ ได้แก่ พื้นที่ที่ใช้ในการคำนวณ ช่วงเวลาที่เข้าสู่ภาวะเสมือนคง ตัว และความเร็วที่ใช้ในการคำนวณที่เหมาะสม มาใช้ในเครื่องปฏิกรณ์ที่มีการเกิดปฏิกิริยาการดูด

ซับแก๊สคาร์บอนไดออกไซด์ มีเป้าหมายหลัก คือ เพื่อหาภาวะในการดำเนินการที่จะส่งผลให้มี ประสิทธิภาพในการดูดซับแก๊สคาร์บอนไดออกไซด์สูงที่สุด ซึ่งตั้งเป้าหมายให้มีค่าสูงกว่างานวิจัย จากการทดลองที่ผ่านมา ซึ่งมีประสิทธิภาพในการดูดซับอยู่ที่ร้อยละ 58 โดยตัวแปรดำเนินการใน การทดสอบ ได้แก่ อุณหภูมิของกระบวนการ ความเข้มข้นของแก๊สคาร์บอนไดออกไซด์ ความ เข้มขันของไอน้ำ และ ช่วงความเร็วของแก๊สบริเวณทางเข้า ผลการทดลองที่ได้จะอภิปรายโดย แบ่งเป็น 2 หัวข้อคือ ผลที่ได้จากการออกแบบการทดลอง และอุทกพลศาสตร์ที่เกิดขึ้น

ผลที่ได้จากการออกแบบการทดลอง

จากการศึกษาตัวแปรดำเนินการศึกษาดังแสดงในตารางที่ 5 โดยมีตัวแปรตอบสนองคือ ปริมาณแก๊สคาร์บอนไดออกไซด์ที่ลดลง

ตารางที่ 5 ผลของตัวแปรอิสระต่อประสิทธิภาพในการดูดซับแก๊สคาร์บอนไดออกไซด์

กรณีศึกษา	ความเร็ว แก๊สขาเข้า (เมตรต่อ วินาที)	อุณหภูมิ (องศา เซลเซียส)	ความเข้มข้นของ แก๊ส คาร์บอนไดออกไซด์ (ร้อยละโดยมวล)	ความ เข้มข้นของ ไอน้ำ (ร้อย ละโดยมวล)	ร้อยละโดยมวลของแก๊ส คาร์บอนไดออกไซด์ ที่ลดลง (ร้อยละโดยมวล)
1	1.25	60	10	10	86.15%
2	1.25	60	10	15	92.69%
3	1.25	60	20	10	78.65%
4	1.25	60	20	15	91.12%
5	1.25	80	10	10	86.39%
6	1.25	80	10	15	91.39%
7	1.25	80	20	10	77.38%
8	1.25	80	20	15	91.05%
9	1.75	60	10	10	87.57%
10	1.75	60	10	15	85.39%
11	1.75	60	20	10	85.08%
12	1.75	60	20	15	93.36%
13	1.75	80	10	10	80.63%
14	1.75	80	10	15	86.89%
15	1.75	80	20	10	82.19%
16	1.75	80	20	15	91.73%

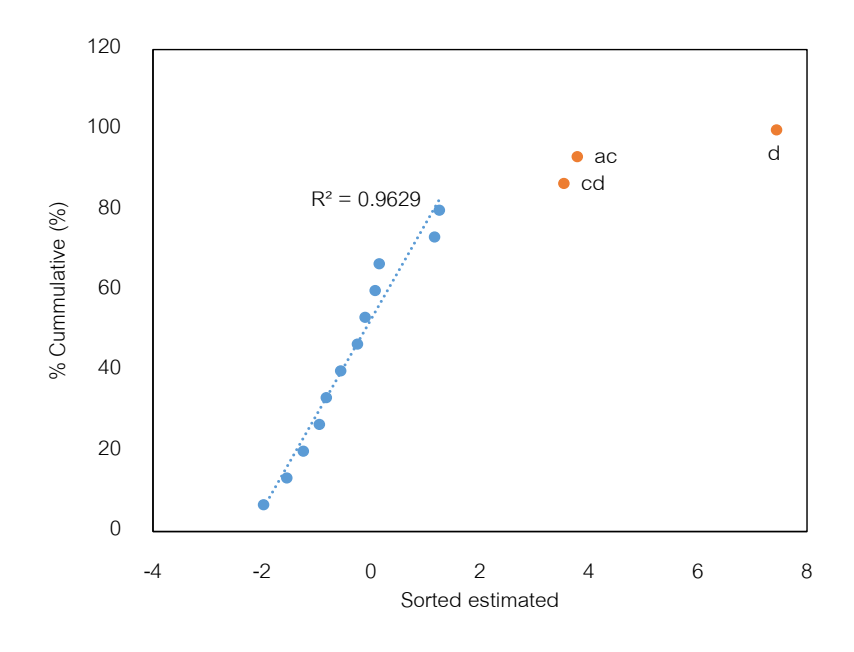
ผลที่ได้พบว่าตัวแปรตอบสนองมีค่าที่มากที่สุดในกรณีศึกษาที่ 12 ซึ่งปริมาณของแก๊ส คาร์บอนไดออกไซด์ที่สามารถดูดซับได้เท่ากับร้อยละ 93.36 มีภาวะในการดำเนินการคือ มีอุณหภูมิ ที่ใช้ในการดำเนินการเท่ากับ 60 องศาเซลเซียส มีค่าความเร็วของแก๊สขาเข้าเท่ากับ 1.75 เมตรต่อ วินาที ความเข้มขันของแก๊สคาร์บอนไดออกไซด์ เท่ากับร้อยละ 20 โดยมวล และมีความเข้มขันของ น้ำเท่ากับร้อยละ 15 โดยมวล ในกรณีศึกษาที่ 7 จะมีตัวแปรตอบสนองที่มีค่าต่ำที่สุดเท่ากับร้อยละ 77.38 และมีภาวะในการดำเนินการคือ มีอุณหภูมิที่ใช้ในการดำเนินการเท่ากับ 80 องศาเซลเซียส มีค่าความเร็วของแก๊สขาเข้าเท่ากับ 1.25 เมตรต่อวินาที ความเข้มขันของแก๊สคาร์บอนไดออกไซด์ เท่ากับร้อยละ 20 โดยมวล และมีความเข้มขันของไอน้ำเท่ากับร้อยละ 10 โดยมวล

เมื่อนำประสิทธิภาพในการดูดซับแก๊สคาร์บอนไดออกไซด์มาทำการวิเคราะห์ความแปรปรวน ดังตารางที่ 6 และรูปที่ 18 จะพบว่า ตัวแปรที่ส่งผลต่อประสิทธิภาพในการดูดซับแก๊ส คาร์บอนไดออกไซด์นั้นจะมีค่าของ p-value ที่น้อยกว่า 0.05 (ความเชื่อมั่นร้อยละ 95) ซึ่งตัวแปร ้ดังกล่าวได้แก่ ความเข้มข้นของไอน้ำ อันตรกิริยาระหว่างความเร็วของแก๊สขาเข้าและความเข้มข้น ของแก๊สคาร์บอนไดออกไซด์ อันตรกิริยาระหว่างความเข้มข้นของแก๊สคาร์บอนไดออกไซด์และ ความเข้มข้นของไอน้ำ เนื่องจากน้ำเป็นสารตั้งต้นในปฏิกิริยาการดูดซับแก๊สคาร์บอนไดออกไซด์ และขั้นตอนการดูดซับแก๊สคาร์บอนไดออกไซด์โดยใช้โพแทสเซียมคาร์บอนเนตนั้นจะเริ่มต้นจาก กระบวนการการดูดซับไอน้ำลงบนผิวของตัวดูดซับของแข็งเป็นขั้นตอนแรก (Zhao และคณะ, 2012) จากนั้น แก๊สคาร์บอนไดออกไซด์จะเข้ามาทำปฏิกิริยาต่อเกิดเป็นโพแทสเซียมไบคาร์บอเนต ในขั้นตอนต่อมา ดังนั้น ความเข้มข้นของไอน้ำจึงส่งผลโดยตรงต่อประสิทธิภาพในการดูดซับแก๊ส คาร์บอนไดออกไซด์ โดยปริมาณไอน้ำที่สูงขึ้นจะส่งผลให้ปริมาณของแก๊สคาร์บอนไดออกไซด์ เพิ่มขึ้นเช่นเดียวกัน เมื่อพิจารณาตัวแปรอิสระดังรูปที่ 19 พบว่า ตัวแปรของความเข้มข้นของไอน้ำ จะส่งผลในทางบวกต่อประสิทธิภาพในการดูดซับ ในขณะที่ตัวแปรของอุณหภูมิจะส่งผลทางลบมาก ที่สุด รองลงมาคือ ความเข้มข้นของแก๊สคาร์บอนไดออกไซด์ และสุดท้ายคือ ความเร็วของแก๊สขา เข้า อย่างไรก็ตาม ตัวแปรอิสระทั้ง 3 ตัวดังกล่าว จะส่งผลต่อประสิทธิภาพในการดูดซับเพียง ้ เล็กน้อยเท่ากันเมื่อเทียบกับความเข้มข้นของไอน้ำ เมื่อพิจารณาถึงอันตรกิริยาระหว่างความเร็วของ แก๊สขาเข้าและความเข้มข้นของแก๊สคาร์บอนไดออกไซด์ พบว่าผลที่ได้นั้นจะตรงกันข้ามกัน เมื่อ พิจารณาที่ความเข้มข้นของแก๊สคาร์บอนไดออกไซด์ที่สูงจะพบว่า การเพิ่มขึ้นของความเร็วแก๊สขา เข้าจะส่งผลให้ประสิทธิภาพของการดูดซับเพิ่มมากขึ้น เนื่องจากการเพิ่มความเร็วของแก๊สขาเข้า จะเจือจางความเข้มข้นของแก๊สคาร์บอนไดออกไซด์ที่อยู่ภายในท่อไรเซอร์ส่งผลให้เหมาะสมต่อการ เกิดปฏิกิริยาเคมีตามปริมาณสารสัมพันธ์ ประสิทธิภาพในการดูดซับจึงสูงขึ้น ในขณะที่เมื่อพิจารณา ้ที่ความเข้มข้นของแก๊สคาร์บอนไดออกไซด์ที่ต่ำ พบว่า การเพิ่มความเร็วขาเข้าของแก๊สจะส่งผลให้ ประสิทธิภาพในการดูดซับลดลงดังรูปที่ 20 (a) เนื่องจากการเพิ่มความเร็วของแก๊สขาเข้าที่มีความ เข้มข้นของสารตั้งต้นน้อย จะส่งผลให้เวลาที่ใช้ในการสัมผัสกันของอนุภาคของแข็งและแก๊สลดลง ประสิทธิภาพที่ได้จากกระบวนการดูดซับนี้จึงลดลง ผลของอันตรกิริยาระหว่างอันตรกิริยาระหว่าง ความเข้มข้นของแก๊สคาร์บอนไดออกไซด์และความเข้มข้นของไอน้ำ จะแสดงได้ดังรูปที่ 20 (b) ผล

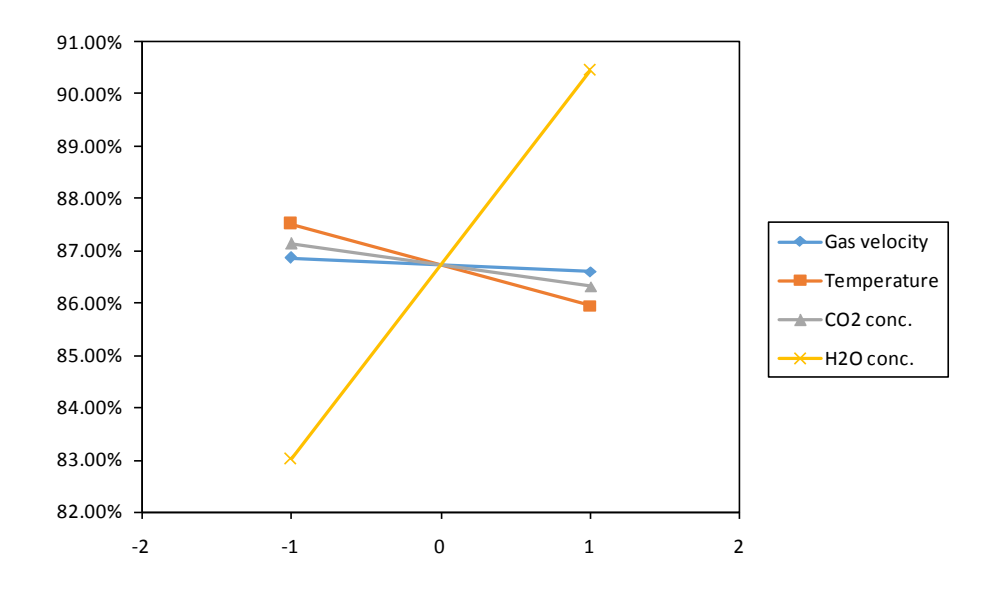
ของอันตรกิริยาระหว่างความเข้มข้นของแก๊สคาร์บอนไดออกไซด์และความเข้มข้นของน้ำจะเป็นไป ในแนวทางที่แตกต่างกันคือ เมื่อพิจารณาที่ความเข้มข้นของไอน้ำสูง พบว่าเมื่อเพิ่มความเข้มข้น ของแก๊สคาร์บอนไดออกไซด์ ประสิทธิภาพในการดูดซับก็จะเพิ่มสูงขึ้นตามไปด้วย เนื่องจากทั้งแก๊ส คาร์บอนไดออกไซด์และไอน้ำต่างก็เป็นสารตั้งต้นในกระบวนการการเกิดปฏิกิริยา ในขณะที่เมื่อ พิจารณาที่ความเข้มข้นของไอน้ำที่ต่ำ จะพบว่า ยิ่งเพิ่มความเข้มข้นของแก๊สคาร์บอนไดออกไซด์ ประสิทธิภาพที่ได้จะลดลง โดยถึงแม้ว่าจะมีสารตั้งต้นเพิ่มแต่ก็เพิ่มขึ้นเพียงแค่แก๊ส คาร์บอนไดออกไซด์ เท่านั้น เมื่อไอน้ำเกิดปฏิกิริยาดูดซับจนหมด แก๊สคาร์บอนไดออกไซด์ที่เหลือ ไม่สามารถทำปฏิกิริยาต่อได้ ทำให้ประสิทธิภาพการดูดซับโดยรวมที่ได้ลดลง

ตารางที่ 6 ผลการวิเคราะห์ ANOVA ของตัวแปรอิสระกับตัวแปรตอบสนอง

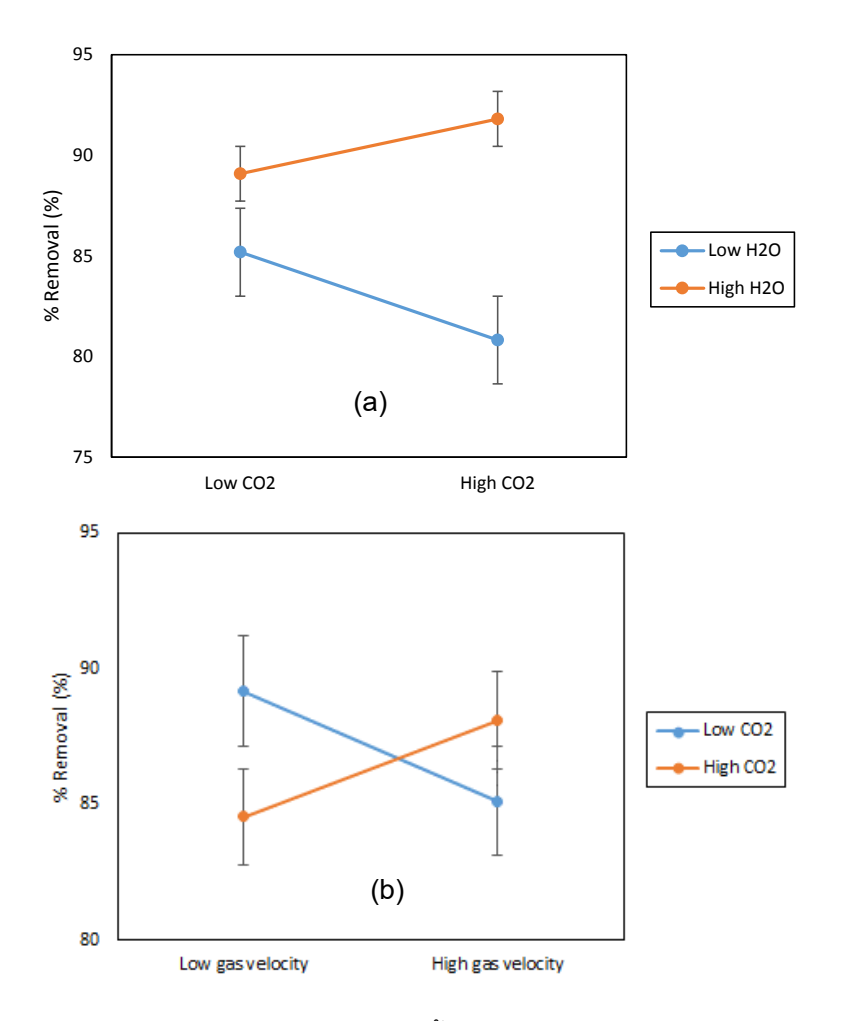
Source of variance	SS	df	MS	F_0	p-value
Α	0.24691	1	0.24691	0.05145	0.82513
С	2.69411	1	2.69411	0.5614	0.47095
D	221.722	1	221.722	46.2024	0.00005
AC	57.3803	1	57.3803	11.9569	0.00614
CD	50.188	1	50.188	10.4582	0.00896
Error	47.9891	10	4.79891		
Total	380.22	15			



รูปที่ 18 ตัวแปรอิสระที่ส่งผลต่อตัวแปรตอบสนอง



รูปที่ 19 ผลของตัวแปรอิสระเดียวต่อตัวแปรตอบสนอง



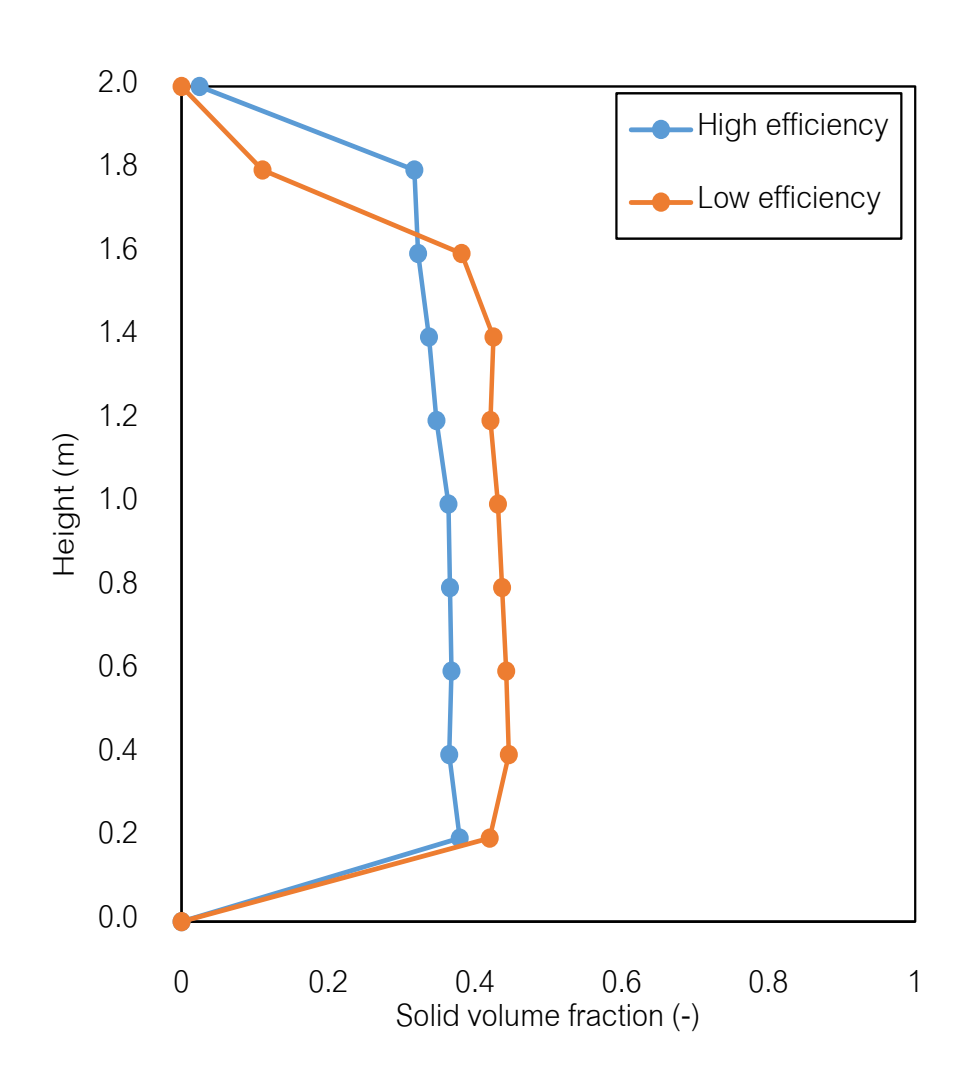
รูปที่ 20 อันตรกิริยาระหว่าง (a) ความเข้มข้นของไอน้ำและความเข้มข้นของแก๊สคาร์บอนไดออกไซด์ และ (b) ความเร็วแก๊สและความเข้มข้นของแก๊สคาร์บอนไดออกไซด์

การอภิปรายผลที่เกิดขึ้นในส่วนของอุทกพลศาสตร์ที่เกิดขึ้นภายในเครื่องปฏิกรณ์ฟลูอิไดซ์ เบดที่มีปฏิกิริยาการดูดซับแก๊สคาร์บอนไดออกไซด์เกิดขึ้น จะเลือกเฉพาะกรณีศึกษาที่ 12 และ กรณีศึกษาที่ 7 ซึ่งเป็นกรณีศึกษาที่มีประสิทธิภาพในการดูดซับที่สูงที่สุดและต่ำที่สุดเท่านั้น ภาวะ ในการดำเนินการในกรณีศึกษาที่ 12 คือ มีอุณหภูมิที่ใช้ในการดำเนินการเท่ากับ 60 องศาเซลเซียส มีค่าความเร็วของแก๊สขาเข้าเท่ากับ 1.75 เมตรต่อวินาที ความเข้มขันของแก๊สคาร์บอนไดออกไซด์ เท่ากับร้อยละ 20 โดยมวล และมีความเข้มขันของไอน้ำเท่ากับร้อยละ 15 โดยมวล และ ภาวะใน การดำเนินการในกรณีศึกษาที่ 7 คือ มีอุณหภูมิที่ใช้ในการดำเนินการเท่ากับ 80 องศาเซลเซียส มีค่าความเร็วของแก๊สขาเข้าเท่ากับ 1.25 เมตรต่อวินาที ความเข้มขันของแก๊สคาร์บอนไดออกไซด์ เท่ากับร้อยละ 20 โดยมวล และมีความเข้มขันของไอน้ำเท่ากับร้อยละ 10 โดยมวลผลที่ได้จะ แสดงผลที่เกิดขึ้นของปริมาณของอนุภาคของแข็งที่อยู่ภายในท่อไรเซอร์ ความเร็วอนุภาคของแข็ง ในแนวแกนและในแนวรัศมี

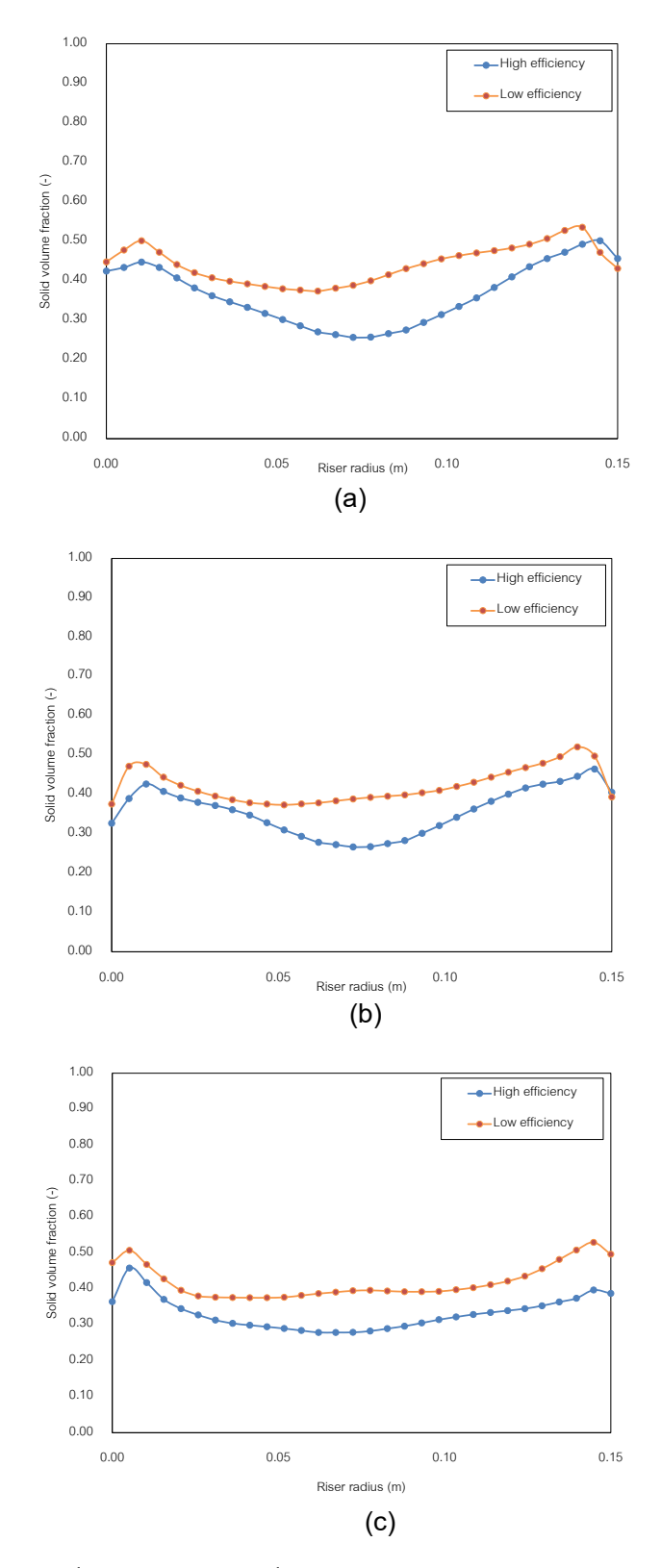
รูปที่ 21 แสดงผลของปริมาณของอนุภาคของแข็งตลอดแนวความสูงของท่อไรเซอร์ ซึ่งพบว่า สัดส่วนของอนุภาคของแข็งในกรณีศึกษาที่ 12 จะอยู่ในช่วง 0.38 ถึง 0.40 ในขณะที่ที่กรณีศึกษาที่ 7 จะมีสัดส่วนของอนุภาคของแข็ง 0.40 ถึง 0.41 แต่ไม่ทั่วทั้งท่อไรเซอร์ ทำให้ประสิทธิภาพในการ ดูดซับที่น้อยกว่ากรณีศึกษาที่ 12 นอกจากนี้ อุทกพลศาสตร์ที่เกิดขึ้นในท่อไรเซอร์นี้มีลักษณะต่าง จากรูปแบบการไหลแบบความเร็วสูง เนื่องจากในรูปแบบการไหลแบบความเร็วสูง กราฟจะมี ลักษณะเป็นรูปตัว S มากกว่า แต่รูปแบบการไหลแบบปั่นป่วนหมุนเวียนที่ได้จะมีลักษณะที่เป็น เส้นตรงคล้ายกับรูปแบบการไหลแบบปั่นป่วน แต่ก็จะแตกต่างจากรูปแบบการไหลแบบปั่นป่วน คือ มีการถ่ายโอนอนุภาคของแข็งไปยังฝั่งดาวเนอร์ได้ ผลของสัดส่วนอนุภาคของแข็งแสดงดังรูปที่ 22 (a) ถึง 22 (c) เมื่อพิจารณาที่ช่วงความสูงตำแหน่งต่างๆ ของท่อไรเซอร์ พบว่า สัดส่วนของ อนุภาคของแข็งในกรณีศึกษาที่ 12 พบว่า มีสัดส่วนที่น้อยกว่าในกรณีศึกษาที่ 7 เช่นเดียวกับรูปที่ 21 โดยในกรณีศึกษาที่ 7 จะมีสัดส่วนของของแข็งในช่วง 0.50 ถึง 0.40 และในกรณีศึกษาที่ 12 มีสัดส่วนของของแข็งในกรณีศึกษาที่ 7 จะมีสัดส่วนของของแข็งในช่วง 0.50 ถึง 0.40 และในกรณีศึกษาที่ 1 สอดคล้องกับรูปแบบการไหลแบบปั่นป่วน ในขณะที่กรณีศึกษาที่ 12 มีลักษณะสอดคล้องกับรูปแบบการไหลแบบความเร็วสูง สัดส่วนของอนุภาคของแข็งในกรณีศึกษาที่ 7 จึงมีมากกว่า

เมื่อพิจารณาที่ความเร็วในแนวแกนซึ่งบอกถึงลักษณะการเคลื่อนที่ของอนุภาคของแข็งใน แนวแกนดังรูปที่ 23 (a) และ 23 (b) พบว่า มีลักษณะที่คล้ายรูปแบบการไหลแบบแกนใน-วงนอก เกิดขึ้นทั้งสองกรณีศึกษา เนื่องจากมีความเร็วที่มีค่าน้อยกว่า 0.00 เมตรต่อวินาที เกิดขึ้นที่บริเวณ ผนัง รูปแบบการไหลแบบปั่นป่วนหมุนเวียนนี้เป็นรูปแบบการไหลที่มีช่วงสั้น และอยู่ระหว่างรูปแบบการไหลแบบปั่นป่วนและรูปแบบการไหลแบบความเร็วสูง จึงทำให้มีลักษณะของรูปแบบการไหล แบบความเร็วสูงเกิดขึ้นได้ การจะแยกความแตกต่างกันของรูปแบบการไหลแบบความเร็วสูงกับ รูปแบบการไหลแบบปั่นป่วนหมุนเวียนจำเป็นต้องพิจารณาถึงตัวแปรอื่น โดยเมื่อพิจารณาจากค่า

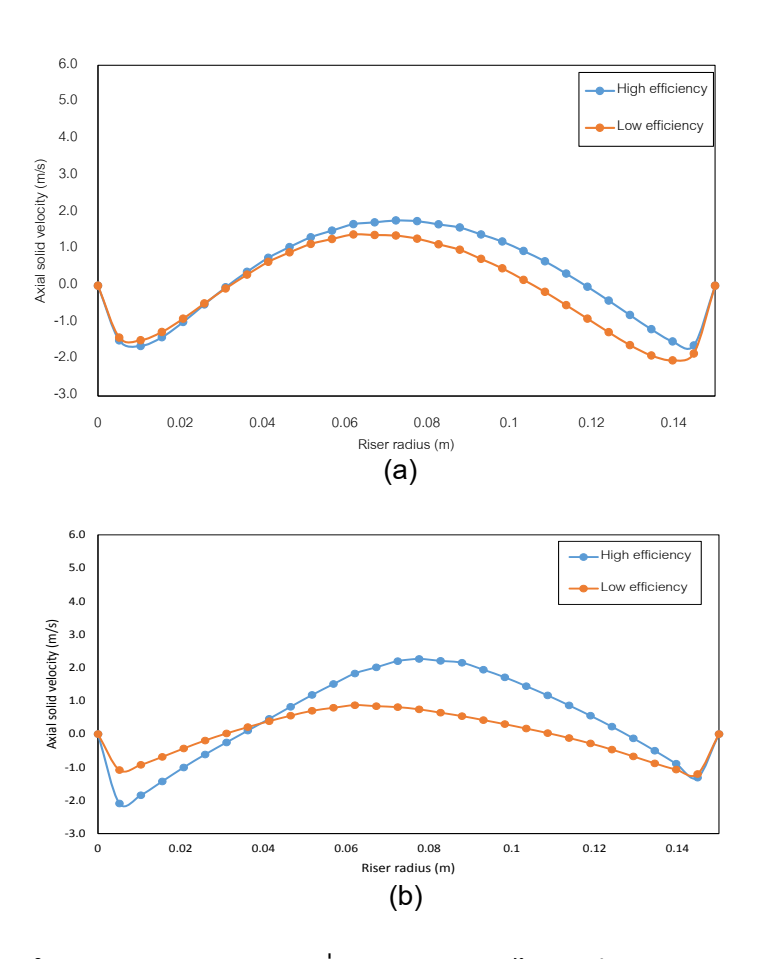
ความเร็วในแนวแกนตลอดความสูงของท่อไรเซอร์จะพบว่า ผลที่ได้จะมีลักษณะดังรูปที่ 24 ลักษณะ ของกราฟจะเป็นเส้นตรงเมื่อเปรียบเทียบกับรูปแบบการไหลแบบความเร็วสูง เนื่องจากในรูปแบบ การไหลแบบความเร็วสูงอนุภาคของแข็งจะไม่คงที่ตลอดทั้งท่อไรเซอร์ ทำให้ความเร็วของอนุภาค ของแข็งไม่คงที่เหมือนรูปแบบการไหลแบบปั่นป่วนหมุนเวียน สำหรับในกรณีศึกษาที่ 7 พบว่า ค่า ความเร็วในแนวแกนที่ได้นั้นมีค่าที่ต่ำกว่ากรณีศึกษาที่ 12 แสดงให้เห็นว่าอนุภาคของแข็งในระบบ นั้นมีการเคลื่อนที่ไปยังด้านบนน้อยกว่า อนุภาคของแข็งจึงเกิดการหมุนเวียนไปยังฝั่งดาวเนอร์ที่ น้อยเช่นเดียวกับรูปแบบการไหลแบบปั่นป่วน เมื่ออนุภาคของแข็งเคลื่อนที่ไปได้ต่ำกว่า อนุภาคของแข็งที่ไม่ใช่สารตั้งตันในการดูดซับแก๊สคาร์บอนไดออกไซด์จึงลดลง ส่งผลให้ประสิทธิภาพการ ดูดซับแก๊สคาร์บอนไดออกไซด์ลดลง



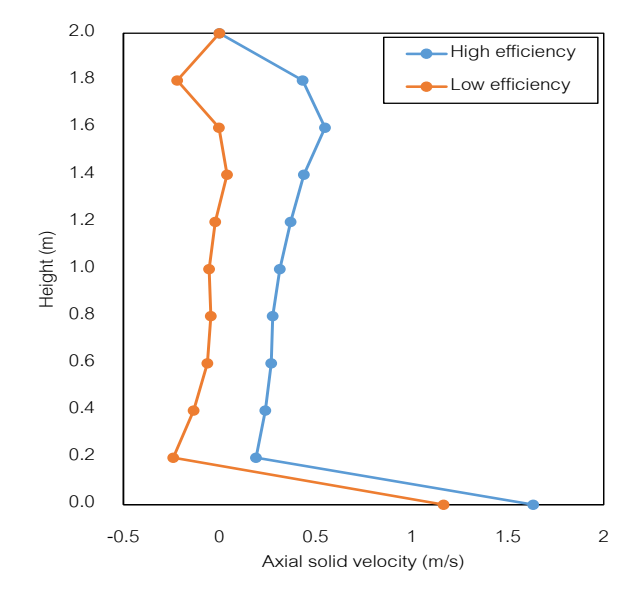
รูปที่ 21 สัดส่วนของของแข็งในท่อไรเซอร์ที่มีปฏิกิริยาการดูดซับแก๊สคาร์บอนไดออกไซด์ ใน ภาวะการดำเนินการที่ให้ประสิทธิภาพการดูดซับสูงที่สุดและต่ำที่สุด



รูปที่ 22 สัดส่วนของแข็งที่อยู่ในท่อไรเซอร์ที่ตำแหน่งความสูงเท่ากับ (a) 0.50 เมตร (b) 1.00 เมตร และ (c) 1.50 เมตร



รูปที่ 23 ความเร็วในแนวแกนของของแข็งที่ความสูงของท่อไรเซอร์เท่ากับ (a) 0.50 เมตร และ (b) 1.50 เมตร ที่มีปฏิกิริยาการดูดซับแก๊สคาร์บอนไดออกไซด์ในภาวะการดำเนินการที่ให้ประสิทธิภาพ การดูดซับสูงที่สุดและต่ำที่สุด



รูปที่ 24 ความเร็วในแนวแกนของของแข็งตลอดช่วงความสูงของท่อไรเซอร์ที่มีปฏิกิริยาการดูดซับ แก๊สคาร์บอนไดออกไซด์ ในภาวะการดำเนินการที่ให้ประสิทธิภาพสูงที่สุดและต่ำที่สุด

เอกสารอ้างอิง

Abbasi, E., Arastoopour, H. CFD simulation of CO₂ sorption in a circulating fluidized bed using the deactivation model. Engineering Conference International, New York (2011) 736-743.

Boonprasob S., Hydrodynamics of flow regimes in two dimensional circulating fluidized bed reactor. Master of Science Thesis, Chulalongkorn University (2012).

Dong, W., Wu, Y., Zhao, C., Liu, C.L. Carbonation characteristics of dry sodium-based sorbents for CO₂ capture. Energy & Fuels 26 (2012) 6040-6046.

Hwang, K.S., Park, S.W., Park, D.W., Oh, K.J., Kim, S.S. Sorption kinetics of carbon dioxide onto rubidium carbonate. Korean Journal of Chemical Engineering 26(5) (2009) 1383-1388.

Khongprom, P., Gidaspow, D., Compact fluidized bed sorber for CO_2 capture. Particuology 8 (2010) 531-535.

Yi, C.K., Jo, S.J., Seo, Y., Lee, J.B., Ryu, C.K. Continuous operation of the potassium-based dry sorbent CO_2 capture process with two fluidized-bed reactors. International journal of greenhouse gas control 1 (2007) 31-36.

Zhao, C., Chen, X., Wu, Y., Dong, W. K₂CO₃/Al₂O₃ for capturing CO₂ in flue gas from power plants. Part 3: CO₂ capture behaviors of K₂CO₃/Al₂O₃ in a bubbling fluidized-bed reactor. Energy & Fuels 26 (2012) 3062-3068.

- การสรุปผลของตัวแปรกระบวนการต่างๆ ที่มีต่อการดักจับคาร์บอนไดออกไซด์และ เสนอรูปแบบวิธีการดำเนินการช่วงการไหลใหม่ของเครื่องปฏิกรณ์ฟลูอิไดซ์เบดแบบ หมุนเวียนที่มีอัตราการไหลอนุภาคของแข็งสูงสำหรับการประยุกต์ใช้ในอุตสาหกรรม ต่างๆ
- การเขียนบทความวิชาการและการนำเสนอผลงานวิชาการ

ในการวิจัยนี้เป็นการศึกษาเพื่อหาอุทกพลศาสตร์และปฏิกิริยาเคมีที่เกิดขึ้นในเครื่อง ปฏิกรณ์ฟลูอิไดซ์เบดแบบหมุนเวียนเพื่อนำไปใช้ในกระบวนการที่มีการดูดซับแก๊ส คาร์บอนไดออกไซด์เกิดขึ้น ทำการศึกษาเพื่อหาสมการอัตราการเกิดปฏิกิริยาการดูดซับแก๊ส คาร์บอนไดออกไซด์ที่สอดคล้องกับผลการทดลองจริง หาภาวะในการดำเนินการที่เหมาะสมต่อ กระบวนการการดูดซับแก๊สคาร์บอนไดออกไซด์และมีประสิทธิภาพในการดูดซับที่สูงที่สุด เพื่อให้ ได้แนวทางนำไปใช้ในการออกแบบเครื่องปฏิกรณ์จริงได้ รวมทั้ง เสนอรูปแบบวิธีการดำเนินการ ช่วงการใหลใหม่ของเครื่องปฏิกรณ์ฟลูอิไดซ์เบดแบบหมุนเวียนสำหรับการประยุกต์ใช้ใน อุตสาหกรรมต่างๆ

ผลของรูปแบบการใหลในเครื่องปฏิกรณ์ฟลูอิไดเซชันที่มีอัตราการใหลอนุภาคของแข็งสูง ต่อการดูดซับด้วยตัวดูดซับสามารถคำนวณปริมาณการดักจับที่มีค่าสูงสุดขึ้นอยู่กับรูปแบบการ ใหลภายในเครื่องปฏิกรณ์ รูปแบบการใหลแบบเบดนิ่งและรูปแบบการใหลฟลูอิไดเซชันแบบ สลักกิ้งมีค่าปริมาณการดักจับต่ำ รูปแบบการใหลฟลูอิไดเซชันแบบปั่นปวน (แบบปั่นป่วน หมุนเวียน) มีค่าสูงสุด รูปแบบการใหลแบบฟลูอิไดเซชันแบบปั่นป่วน (แบบปั่นป่วนหมุนเวียน) และรูปแบบการใหลฟลูอิไดเซชันแบบฟองแก๊สมีปริมาณการดูดซับใกล้เคียงกัน อย่างไรก็ตาม ปริมาณความเข้มข้นที่ทางออกของรูปแบบการไหลเบดนิ่งให้ปริมาณแก๊สคาร์บอนไดออกไซด์สูง มีระยะเวลาในการทำปฏิกิริยานานแต่ปริมาณการดักจับแก๊สคาร์บอนไดออกไซด์มีค่าต่ำสุด เนื่องจากพฤติกรรมของการจัดเรียงตัวตัวดูดซับของแข็งในเบดนิ่งทำให้สูญเสียพื้นที่ในการทำ ปฏิกิริยาของแก๊สคาร์บอนไดออกไซด์ที่เข้ามา ในรูปแบบการไหลแบบฟองแก๊ส สัดส่วนความ เข้มข้นของแก๊สที่ทางออกมีค่าสูงแต่น้อยกว่ารูปแบบเบดนิ่ง แต่ปริมาณการดูดซับมีค่ามากกว่า เบดนิ่ง แสดงว่ามีการสัมผัสของแก๊ส-ของแข็งที่สูงกว่ารูปแบบเบดนิ่ง สำหรับรูปแบบการใหลแบบ ฟลูอิไดเซชันสลักกิ้งและรูปแบบการใหลแบบฟลูอิไดเซชันความเร็วสูง ตัวดูดซับของแข็ง โพแทสเซียมคาร์บอเนตและโซเดียมคาร์บอเนตสามารถกำจัดแก๊สคาร์บอนไดออกได้ทั้งหมดใน เวลาไม่ถึง 1 นาที หมายความว่า เวลาในการทำปฏิกิริยาไม่ได้ส่งผลต่อปริมาณการดักจับแก๊ส คาร์บอนไดออกไซด์ จะเห็นว่าปริมาณการดักจับแก๊สคาร์บอนไดออกไซด์ในรูปแบบการไหล ฟลูอิไดเซชันแบบสลักกิ้งและฟลูอิไดเซชันแบบความเร็วสูงมีค่าต่ำใกล้เคียงกับแบบเบดนิ่ง เนื่องจากการเกิดฟองแก๊สขนาดใหญ่ในรูปแบบการไหลฟลูอิไดเซชันแบบสลักกิ้งทำให้พื้นที่การ สัมผัสกันของแก๊สและของแข็งน้อยลงและสำหรับรูปแบบความเร็วสูงที่มีปริมาณพื้นที่ในการสัมผัส กันของแก๊สและของแข็งสูงแต่เนื่องจากมีการกระจายตัวของเบดของแข็งทำให้ปริมาณการดักจับ แก๊สคาร์บอนไดออกไซด์มีค่าต่ำ ในงานวิจัยนี้รูปแบบการไหลแบบปั่นป่วน (แบบปั่นป่วน หมุนเวียน) มีปริมาณการดักจับแก๊สคาร์บอนไดออกไซด์สูงสุดเนื่องจากระบบการผสมย้อนกลับสูง

จากการจำลองกระบวนการ ช่วงความเร็วที่ทำให้รูปแบบการไหลมีความเหมาะสมมากที่สุด คือ ช่วงความเร็วของแก๊สขาเข้าเท่ากับ 1.25 เมตรต่อวินาที ถึง 1.75 เมตรต่อวินาที ช่วงความเร็ว ดังกล่าวจะอยู่ระหว่างช่วงรูปแบบการไหลแบบปั่นป่วนและรูปแบบการไหลแบบความเร็วสูง ซึ่งมี ชื่อเรียกว่า รูปแบบการไหลแบบปั่นป่วนหมุนเวียน ที่จะมีการกระจายตัวของอนุภาคในท่อไรเซอร์ ได้ดี มีสัดส่วนของอนุภาคของแข็งที่มากและใกล้เคียงกันตลอดช่วงความสูงของท่อไรเซอร์ ทำให้ การใช้รูปแบบการไหลแบบปั่นป่วนหมุนเวียนมีความเหมาะสมที่จะนำไปใช้ในกระบวนการที่มี ปฏิกิริยาเคมี ในการหาภาวะในการดำเนินการที่เหมาะสมที่สุดนั้น ตัวแปรอิสระต่างๆ ได้ถูกนำมาศึกษา พบว่าปริมาณของแก๊สคาร์บอนไดออกไซด์ที่สามารถดูดซับได้สูงที่สุดคือร้อยละ 93.36 โดย มวล โดยมีภาวะในการดำเนินการของอุณหภูมิเท่ากับ 60 องศาเซลเซียส ความเข้มขันของแก๊ส คาร์บอนไดออกไซด์ที่กากับร้อยละ 20 โดยมวล ความเข้มขันของไอน้ำเท่ากับร้อยละ 15 โดยมวล และความเร็วของแก๊สขาเข้าเท่ากับ 1.75 เมตรต่อวินาที และปริมาณของแก๊สคาร์บอนไดออกไซด์ ที่ถูกดูดซับต่ำที่สุดเท่ากับร้อยละ 77.38 โดยมวล ที่ภาวะในการดำเนินการของอุณหภูมิเท่ากับ 80

องศาเซลเซียส ความเข้มข้นของแก๊สคาร์บอนไดออกไซด์เท่ากับร้อยละ 20 โดยมวล ความเข้มข้น ของน้ำเท่ากับร้อยละ 10 โดยมวลและความเร็วของแก๊สขาเข้าเท่ากับ 1.25 เมตรต่อวินาที ซึ่ง ปริมาณของแก๊สคาร์บอนไดออกไซด์ที่ดูดซับได้นั้นมีปริมาณมากกว่าการใช้เบดนิ่ง เครื่องปฏิกรณ์ แบบฟองแก๊สและเครื่องปฏิกรณ์แบบความเร็วสูง (ผลจากงานวิจัยที่ผ่านมา) ตัวแปรอิสระที่ส่งผล ต่อประสิทธิภาพในการดูดซับแก๊สคาร์บอนไดออกไซด์สูงที่สุดนั้น คือ ความเข้มข้นของไอน้ำ

เมื่อเปรียบเทียบผลเชิงอุทกพลศาสตร์ พบว่า สัดส่วนของอนุภาคของแข็งที่อยู่ภายในท่อ ไรเซอร์ที่ภาวะในการดำเนินการของอุณหภูมิเท่ากับ 60 องศาเซลเซียส ความเข้มขันของแก๊ส คาร์บอนไดออกไซด์เท่ากับร้อยละ 20 โดยมวล ความเข้มขันของไอน้ำเท่ากับร้อยละ 15 โดยมวล และความเร็วของแก๊สขาเข้าเท่ากับ 1.75 เมตรต่อวินาที มีค่าในช่วง 0.38 ถึง 0.40 ตลอด ช่วงความสูงของท่อไรเซอร์ ในขณะที่ ที่ภาวะในการดำเนินการของอุณหภูมิเท่ากับ 80 องศา เซลเซียส ความเข้มขันของแก๊สคาร์บอนไดออกไซด์เท่ากับร้อยละ 20 โดยมวล ความเข้มขันของ ไอน้ำเท่ากับร้อยละ 10 โดยมวลและความเร็วของแก๊สขาเข้าเท่ากับ 1.25 เมตรต่อวินาที มีสัดส่วน ของอนุภาคของแข็งเท่ากับ 0.40 ถึง 0.41 แต่มีการกระจายตัวที่น้อยกว่า ประสิทธิภาพในการดูด ซับจึงน้อยกว่า ผลของความเร็วในแนวแกนของของแข็งแสดงให้เห็นถึงการลดลงของรูปแบบการ ไหลแบบแกนใน-วงนอก ทำให้ประสิทธิภาพการดูดซับแก๊สคาร์บอนไดออกไซด์ดีขึ้น

ข้อเสนอแนะสำหรับงานวิจัยในอนาคต

ในงานวิจัยนี้ เป็นการศึกษาถึงกระบวนการการดูดซับเพียงอย่างเดียวเท่านั้น ยังต้องมี การศึกษาในส่วนของการฟื้นฟูสภาพให้กับตัวดูดซับของแข็ง เพื่อให้ผลที่ได้เป็นผลที่สามารถ นำไปใช้ในกระบวนการการดูดซับได้จริง

Output จากโครงการวิจัยที่ได้รับทุนจาก สกว.

1. ผลงานตีพิมพ์ในวารสารวิชาการนานาชาติหรือผลงานที่คาดไว้ในสัญญาโครงการ

ผู้วิจัยมีงานวิจัยตีพิมพ์หัวข้อเรื่องที่เกี่ยวข้องกับการปฏิกิริยาต่างๆ ในช่วงการไหลต่างๆ ของ เครื่องปฏิกรณ์ฟลูอิไดซ์เบดแบบหมุนเวียนที่มีอัตราการไหลอนุภาคของแข็งสูงด้วยการทดลองและ การจำลองพลศาสตร์ของไหลเชิงคำนวณที่ได้รับการยอมรับ (Accepted Manuscript) ให้ตีพิมพ์ใน วารวารวิชาการระดับนานาชาติ ในรอบ 2 ปีที่ผ่านมา จำนวน 9 หัวข้อเรื่อง ได้แก่

Chalermsinsuwan, B., Boonprasop, T., Nimmanterdwong, P., Piumsomboon, P. Revised fluidization regime characterization in high solid particle concentration circulating fluidized bed reactor. International Journal of Multiphase flow 66 (2014) 26-37. (ภาคมนวก 1)

Jaiboon, O., Chalermsinsuwan, B., Mekasut, L., Piumsomboon, P. Effect of regeneration temperature on the composition and carbon dioxide sorption ability of a K₂CO₃/Al₂O₃ solid sorbent in a bubbling fluidized bed reactor. Chemical Engineering Communications 202 (3) (2015) 361-365. (ภาคผนวก 2)

Chaiwang, P., Chalermsinsuwan, B., Piumsomboon, P. Thermogravimetric analysis and chemical kinetic for regeneration of sodium carbonate solid sorbent. Advanced Materials Research 1101 (2015) 40-45. (ภาคผนาก 3)

Jongartklang, N., Piemjaiswang, R., Piumsomboon, P., Chalermsinsuwan, B. CO₂ sorption using Na₂CO₃/Al₂O₃ sorbent with various flow patterns of fixed/fluidized bed reactors. Jurnal Teknologi (2015) Accepted manuscript. (ภาคผนวก 4)

Rukthong, W., Weerapakkaroon, W., Wongsiriwan, U., Piumsomboon, P., Chalermsinsuwan, B. Integration of computational fluid dynamics simulation and statistical factorial experimental design of thick-wall crude oil pipeline with heat loss. Advances in Engineering Software 86 (2015) 49-54. (ภาคผนวก 5)

Rukthong, W., Thanatawee, P., Sunphorka, S., Piumsomboon, P., Chalermsinsuwan, B. Computation of biomass combustion characteristics and kinetic parameters by using thermogravimetric analysis. Engineering Journal 19(2) (2015) 41-57. (ภาคผนาก 6)

Chayaporn, S., Sungsuk, P., Sunphorka, S., Kuchonthara, P., Piumsomboon, P., Chalermsinsuwan, B. Evaluation of biomass components effect on kinetic values for biomass pyrolysis using simplex-lattice design. Korean Journal of Chemical Engineering 32 (2015) 1081-1093. (ภาคผนวก 7)

Chaiwang, P., Chalermsinsuwan, B., Piumsomboon, P. Thermogravimetric analysis and chemical kinetic for regeneration of sodium and potassium carbonate solid sorbents. Chemical Engineering Communications 203 (2015) 581-588. (ภาคผนวก 8)

Jongartklang, N., Chanchairoek, S., Piumsomboon, P., Chalermsinsuwan, B. Correlations of kinetic parameters with various system operating conditions for CO₂ sorption using K₂CO₃/Al₂O₃ solid sorbent in a fixed/fluidized bed reactor. Journal of Environmental Chemical Engineering 4 (2016) 1938-1947. (ภาคมนาก 9)

หมายเหตุ: ทุกงานวิจัยที่ได้รับการยอมรับให้ตีพิมพ์ในวารสารวิชาการระดับนานาชาติมีการ ระบุกิตติกรรมประกาศ (Acknowledgement) ทุนส่งเสริมนักวิจัยรุ่นใหม่ ประจำปังบประมาณ 2557 รหัส TRG5780205

2. การนำผลงานวิจัยไปใช้ประโยชน์

- เชิงสาธารณะ (มีเครือข่ายความร่วมมือ/สร้างกระแสความสนใจในวงกว้าง)
การเชื่อมโยงทางวิชาการกับนักวิชาการในประเทศ — ผู้วิจัยได้เป็นหนึ่งในนักวิจัยของ
ศูนย์วิจัยเชื้อเพลิง (ภาควิชาเคมีเทคนิค คณะวิทยาศาสตร์) ศูนย์ความเป็นเลิศด้าน
เทคโนโลยีปิโตรเคมีและวัสดุขั้นสูง (สำนักพัฒนาบัณฑิตศึกษาและวิจัยด้านวิทยาศาสตร์
และเทคโนโลยี) และได้รับเชิญจากนักวิชาการท่านอื่นที่ทำงานเกี่ยวกับการจำลอง
พลศาสตร์ของไหลเชิงคำนวณในการเป็นอาจารย์ที่ปรึกษาวิทยานิพนธ์ร่วมหรือกรรมการ
สอบวิทยานิพนธ์ของนิสิต จึงทำให้มีโอกาสในการแลกเปลี่ยนความคิดเห็นทางด้านวิชาการ
ให้ทันสมัยอยู่เป็นประจำ

การเชื่อมโยงทางวิชาการกับนักวิชาการต่างประเทศ – ผู้วิจัยมีความร่วมมือกับ Prof. Dimitri Gidaspow ซึ่งเป็นผู้เชี่ยวชาญเกี่ยวกับเครื่องปฏิกรณ์ฟลูอิไดซ์เบดแบบหมุนเวียนและการ จำลองพลศาสตร์ของไหลเชิงคำนวณ ทั้งในส่วนของการทำงานวิจัยหรือปรึกษาปัญหา เกี่ยวกับการทำงานในภาพรวม ดังจะเห็นได้จากการมีบทความวิชาการระดับนานาชาติ ตีพิมพ์ร่วมกันอย่างสม่ำเสมอ

เชิงวิชาการ (มีการพัฒนาการเรียนการสอน/สร้างนักวิจัยใหม่)
 ได้ใช้ความรู้ที่มีในการเรียนการสอนรายวิชาบรรยาย 2306514 Fluidization และ 2306605
 Fluid and Particle Mechanics และได้มีส่วนร่วมในการสร้างนักวิจัยใหม่ 10 คน ซึ่งเป็น นิสิตระดับปริญญาโทและเอกในสาขาวิชาเคมีเทคนิคและสาขาเทคโนโลยีเชื้อเพลิง

3. อื่น ๆ เช่น การเสนอผลงานในที่ประชุมวิชาการ และ การได้รับเชิญไปเป็นวิทยากร

ผู้วิจัยมีการไปเสนอผลงานหัวข้อเรื่องที่เกี่ยวข้องกับการปฏิกิริยาต่างๆ ในช่วงการไหลต่างๆ ของเครื่องปฏิกรณ์ฟลูอิไดซ์เบดแบบหมุนเวียนที่มีอัตราการไหลอนุภาคของแข็งสูงด้วยการทดลอง และการจำลองพลศาสตร์ของไหลเชิงคำนวณ ในรอบ 2 ปีที่ผ่านมา จำนวน 5 หัวข้อเรื่อง ได้แก่

Jongartklang, N., Piemjaiswang, R., Piumsomboon, P., Chalermsinsuwan, B. CO₂ sorption using Na₂CO₃/Al₂O₃ sorbent with various flow patterns of fixed/fluidized bed reactors. Advancement in Petroleum and Chemical Engineering Technology and Applications International Conference 2015 (APCETA 2015), Krabi, Thailand (2015). (ภาคผนวก 10)

Tritippayanon, R., Jiradilok, V., Piumsomboon, P., Chalermsinsuwan, B. CFD modeling of SO₂ capture using limestone in industrial scale circulating fluidized bed boiler. Advancement in Petroleum and Chemical Engineering Technology and Applications International Conference 2015 (APCETA 2015), Krabi, Thailand (2015). (ภาคผนวก 11)

Chaiwang, P., Chalermsinsuwan, B., Piumsomboon, P. Thermogravimetric analysis and chemical kinetic for regeneration of sodium carbonate solid sorbent. 2014 International Conference on Chemical and Material Engineering, Xiamen, China (2014). (ภาคผนวก 12)

Laiarpatorn, P., Piumsomboon, P., Chalermsinsuwan, B. Effect of operating parameters on system mixing inside air reactor of chemical looping combustion using CFD simulation. The 4th Asian Conference on Innovative Energy & Environmental Chemical Engineering (ASCON-IEECE), Yeosu, Korea (2014). (ภาคผนวก 13)

Sornumpol, R., Chalermsinsuwan, B., Piumsomboon, P. Effect of operating parameters in fuel reactor of chemical looping combustion using computational fluid dynamics simulation. The 4th TIChE International Conference, Chiang Mai, Thailand (2014). (ภาคผนวก 14)

หมายเหตุ: ทุกงานวิจัยที่ได้รับการยอมรับให้ตีพิมพ์ในวารสารวิชาการระดับนานาชาติมีการ ระบุกิตติกรรมประกาศ (Acknowledgement) ทุนส่งเสริมนักวิจัยรุ่นใหม่ ประจำปังบประมาณ 2557 รหัส TRG5780205

สำหรับผลงานอื่นๆ ที่ผู้วิจัยได้ดำเนินการในรอบปีที่ผ่านมา ยกตัวอย่างเช่น

- เป็นอาจารย์ที่ปรึกษาโครงการและได้เข้ารอบสุดท้ายจากการประกวดความคิดริเริ่มทาง วิทยาศาสตร์และเทคโนโลยีเพื่อการพัฒนาอย่างยั่งยืน ครั้งที่ 7 (มิถุนายน 2014)
- เป็นผู้แต่งหลักและได้รับเกียรติบัตรเสนอผลงานวิจัยดีเยี่ยมแบบโปสเตอร์ ในงานการ ประชุมนักวิจัยรุ่นใหม่พบเมธีวิจัยอาวุโส สำนักงานกองทุนสนับสนุนการวิจัย (ตุลาคม 2014)
- เป็นกรรมการตัดสินผลงานในการประชุมวิชาการระดับนานาชาติ The 6th and 7th Research Symposium on Petrochemical and Materials Technology (เมษายน 2015 และ 2016)

ภาคผนวก

(reprint หรือ manuscript และบทความสำหรับการเผยแพร่ กิจกรรมที่เกี่ยวข้องกับการ นำผลจากโครงการไปใช้ประโยชน์)



Contents lists available at ScienceDirect

International Journal of Multiphase Flow

journal homepage: www.elsevier.com/locate/ijmulflow



Revised fluidization regime characterization in high solid particle concentration circulating fluidized bed reactor



Benjapon Chalermsinsuwan ^{a,b,*}, Sutthichai Boonprasop ^a, Prathana Nimmanterdwong ^a, Pornpote Piumsomboon ^{a,b}

^a Fuels Research Center, Department of Chemical Technology, Faculty of Science, Chulalongkorn University, 254 Phayathai Road, Patumwan, Bangkok 10330, Thailand ^b Center of Excellence on Petrochemical and Materials Technology, Chulalongkorn University, 254 Phayathai Road, Patumwan, Bangkok 10330, Thailand

ARTICLE INFO

Article history: Received 15 January 2014 Received in revised form 25 May 2014 Accepted 28 June 2014 Available online 8 July 2014

Keywords:
Circulating fluidized bed reactor
Experimental measurement
Fluidization
Hydrodynamics
Multiphase flow
Regime

ABSTRACT

The hydrodynamics inside high solid particle concentration circulating fluidized bed reactor (CFBR) was investigated using computational fluid dynamics simulation (CFDS) and experimental measurement. In order to verify the CFDS obtained results they were compared with the experimental ones by qualitative and quantitative assessments. The CFDS model, with the appropriate initial and boundary conditions, for simulating the high solid particle concentration CFBR were successfully developed, and the obtained results matched with the experimentally-derived ones. Further fluidization regime mapping was performed and the results were summarized based on the statistical parameters of the average solid volume fraction (ASVF) and the standard deviation (SD) of the horizontal and vertical SVFs. The ASVF had a maximum value in the circulating-turbulent fluidization regime, while the SD of the horizontal and vertical SVFs had minimum and maximum values in the bubbling fluidization regime, respectively. As the gas inlet velocity increased, the SD of the SVF tended to approach an invariable value. In addition, the relationships between these three statistical parameters and the positions of the unconventional fluidization regimes (using only primary gas injection) on the general simplified fluidization regime mapping were summarized.

© 2014 Elsevier Ltd. All rights reserved.

1. Introduction

Gas and solid particle multiphase flow plays an important role in various chemical and petrochemical industries. The solid particles can be used as a chemical reaction catalyst in a fluid catalytic cracking unit, heating medium in a boiler unit or fuel in combustion and gasification units (Kunii and Levenspiel, 1991; Yang, 2003; Gidaspow and Jiradilok, 2010). The circulating fluidized bed reactor (CFBR) is one of the commonly employed chemical reactors for this multiphase flow system due to its many advantages, such as having a good system mixing (Basu, 2006), easy handling (Kunii and Levenspiel, 1991) and good heat control (Basu and Fraser, 1991), when compared with a fixed bed operation. The riser section is the part of CFBR that the chemical or physical operation normally occurs within. Many studies have been successfully conducted in CFBRs operating with a low solid particle concentration (Salvaterra et al., 2005; Masuda et al., 2006;

Chalermsinsuwan et al., 2010a). Recently, the operation of CFBRs with a high solid particle concentration has gained more attention, because innovative applications of CFBRs need a more uniform gas-solid particle contact area and solid volume fraction (SVF), such as in purification or gas sorption units (Chalermsinsuwan et al., 2010b; Li et al., 2011; Jaiboon et al., 2013a) and agricultural product drying units (Kunii and Levenspiel, 1991; Tatemoto et al., 2007; da Silva et al., 2012).

With respect to the classification of CFBR operation at high and low solid particle concentrations, systems that operate with a solid particle mass flux of more than 200 kg/m² s are defined as a high solid particle concentration CFBR (Bi and Zhu, 1993; Issangya et al., 1999). Compared with low solid particle concentration CFBRs, less knowledge is available for high solid particle concentration CFBRs. Only, a new method to run a CFBR with a high solid particle concentration and their observed hydrodynamics have been reported (Kim et al., 2004; Li et al., 2004; Bastos et al., 2008; Zhu, 2010; Zhu et al., 2013). As the solid particle density increased inside the system, the gas–solid particle and solid particle-solid particle interactions play an important role in the performance of the CFBR (Manyele et al., 2002, 2006). Particle clusters or aggregates are formed and alter the conventional system

^{*} Corresponding author at: Fuels Research Center, Department of Chemical Technology, Faculty of Science, Chulalongkorn University, 254 Phayathai Road, Patumwan, Bangkok 10330, Thailand. Tel.: +66 2218 7682; fax: +66 2255 5831.

E-mail address: benjapon.c@chula.ac.th (B. Chalermsinsuwan).

hydrodynamics (Chalermsinsuwan et al., 2013). Fluctuations in the high solid particle concentration CFBRs are significantly greater than those in low solid particle concentration ones, leading to more vigorous interactions between the gas and solid particle phases (Wang et al., 2014). As a result, the better gas—solid particle contact and mixing obtained under a high solid particle concentration provide a better reactor performance. From the available literature, the fluidization regimes obtained when operating under a high solid particle concentration are then expected to be different from those when operating under a low solid particle concentration, but this assumption remains to be verified.

The fluidization regime diagrams with increasing gas inlet velocities, in terms of the gas-solid particle fluidization and upward transport, have been proposed (Bi and Grace, 1995; Lim et al., 1995; Bai and Kato, 1999). Excluding the fixed bed operation, these fluidization regimes included bubbling, turbulent, fast fluidization and dilute-phase or pneumatic transport. Each reported fluidization regime had its own distinct flow structures or characteristics (Das et al., 2004; Chalermsinsuwan et al., 2009, 2014a; Chalermsinsuwan and Piumsomboon, 2011). Most recent studies have focused on the methodology to identify each fluidization regime, where various different analyses to quantitatively and qualitatively classify the different fluidization regimes have been conducted (Zijerveld et al., 1998; Johnsson et al., 2000; Makkawi and Wright, 2002; Llauró and Llop, 2006; Cody et al., 2008; Tamadondar et al., 2012). Hou et al. (2012) examined the roles of various forces among solid particles, and between the solid particles and gas, on the different fluidization regimes, whilst Jaiboon et al. (2013b) used the power spectral density of pressure fluctuation by Fast Fourier Transform analysis to differentiate various flow patterns. Their sources of observed pressure fluctuation in the gassolid particle fluidization included bubble eruption, oscillation due to bubble/slug passage, and self-excited oscillation of fluidized particles. Under a high solid particle concentration operating condition, two novel flow patterns have recently been reported, which are the circulating-turbulent fluidization flow (CTFB) and the dense suspension upflow regimes. In the CTFB regime, the dense solid particle concentration was uniform in both system directions, horizontal and vertical, (Chalermsinsuwan et al., 2010b). With no downward flux at the reactor wall at high suspension densities, the flow pattern corresponds to a dense suspension upflow (Grace, 2000; Kim et al., 2004). However, as previously mentioned, their positions in the fluidization regime diagram and their indepth characteristics are not well-defined.

For a high solid particle concentration operating condition, Wei et al. (1998) used the Boltzman function correlation to determine the radial solid particle fraction profiles in a high solid particle concentration CFBR, and observed different solid particle profiles between the dilute and dense flow patterns. The definition of the transition points from the dilute to dense CFBRs was proposed by Issangya et al. (1999). The refluxing of solid particles near the reactor wall disappeared in the high solid particle concentration reactor and was replaced by a more homogeneous flow structure (Issangya et al., 2000). Within a high solid particle concentration CFBR, the fast fluidization regime with a core-annulus flow structure was found to co-exist with a dense suspension upflow pattern (Kim et al., 2004). Increasing the solid particles flux at a constant gas inlet velocity led to a dense suspension upflow pattern in the bottom region of the reactor, and a fast fluidization in the upper region (Mei et al., 2007). The feeding and exiting device configuration influenced the flow behaviors (Kim et al., 2008), where a combination of L-valve feeding and C-shape exiting was found to be the optimum configuration for achieving a dense suspension flow pattern. In contrast to using a high gas inlet velocity, some researchers have suggested using a low gas inlet velocity or CTFB pattern (Zhu and Zhu, 2008; Qi et al., 2012a). The hydrodynamics of the gas-solid particle flow in the system were experimentally measured and verified for a CTFB pattern over a wide range of gas inlet velocities and solid circulation rates (Qi et al., 2012a). Homogeneous axial profiles with a cross-sectional average solid particle holdup of higher than 0.25 and parabolic radial profiles of solid particle holdup from 0.15 to 0.50, were obtained throughout the bottom region of the reactor with a decreased solid particle hold up in the upper region of the reactor (Qi et al., 2012b), which was due to the effect of secondary gas injection. Therefore, both the dense suspension upflow and CTFB patterns should be the multiregime flow characteristics of a high solid particle concentration condition.

In this study, the system hydrodynamics inside high solid particle concentration CFBR was explored using computational fluid dynamics simulation (CFDS) and experimental measurement. The experimental results were used to compare against the CFDS results. In addition, the relationship between the statistical parameters of the average solid volume fraction (ASVF) and the standard deviation (SD) of the horizontal and vertical SVFs from the CFDS and experimental results were used to explain the system behavior via fluidization regime mapping.

2. Experimental setup

The experimental cold-flow two-dimensional (2D) CFBR used in this study is shown in Fig. 1. Within this 2D system, the difference between the obtained results could be visually observed. The Plexiglas CFBR consisted of the three major parts of the riser, downer and separating and returning systems. The riser had a 2.00 m



Fig. 1. The configuration of the experimental CFBR used in this study.

height, 0.15 m width and 0.05 m depth, whilst the downer had a 1.00 m height, 0.30 m width and 0.05 m depth. For the separating and returning systems, a 200 US standard size mesh was employed to separate the solid particles and the gas at the top of the reactor and at the inserted small tubes inside the downer. The solid particles then flew back to the system and were sent to the riser at a 0.05 m height from the bottom of the reactor. A ball valve was used to control the solid particle flow from the downer to the riser. At the base of the column, a 200 US standard size mesh was used to support the solid particles. A gas distributor was located directly below the mesh. Compressed gas was conditioned prior to enter the reactor.

Both the quantitative and qualitative experimental results were used to validate the CFDS results. Quantitative results were measured using the system absolute pressure via sixteen pressure probes that were mounted along the height of the CFBR riser at 0.10, 0.15, 0.20, 0.25, 0.30, 0.40, 0.50, 0.60, 0.70, 0.85, 1.00, 1.20, 1.40, 1.60, 1.80 and 1.90 m above the gas distributor. The data were then recorded and stored using a plug-in computer. For the qualitative aspect, the contours of the SVF were compared using instantaneous solid particle snapshots over the height of the CFBR.

In this study, various gas inlet velocities were explored to investigate each fluidization regime. The experimental system used gas inlet velocities that ranged between 0.25 and 10.00 m/s using air with a density (ρ_g) of $1.20\,\mathrm{kg/m^3}$ and viscosity (μ_g) of $2.00\times10^{-5}\,\mathrm{kg/m}$ s. The solid particles used were silica sand (Quality Sand Corporation Ltd.), determined to have an average solid particle diameter (d_p) of 380 μ m using a Malvern particle size analyzer (Malvern Instruments Ltd., 2013). The solid particle density (ρ_s) was measured using a pycnometer as reported (Dubrawski et al., 2013; Jaiboon et al., 2013b) and found to be 2650 kg/m³. The silica sand was, therefore, Geldart group B solid particles (Basu, 2006), and 21 kg of solid particles were packed inside the experimental CFBR. The lowest solid particle mass flux (G_s) inside the system was roughly 300 kg/m² s. The other system operating conditions are listed in Table 1.

3. CFDS setup

The Eulerian approach with a kinetic theory of granular flow (Gidaspow, 1994) was performed using the commercial CFDS program ANSYS FLUENT. The CFDS model, as well as the appropriate initial and boundary conditions, for simulating the high solid particle concentration CFBR were developed and the derived conservation and constitutive equations (Eqs. (1)–(17)) are summarized in Table 2. The equations for the conservation of mass (Eqs. (1) and (2)) and momentum (Eqs. (3) and (4)), as well as for the solid particle fluctuating kinetic energy conservation (Eq. (5)), were used based upon the assumption that the system was isothermal. For the conservation of mass, the accumulation of mass

The CFBR system operating conditions used in this study.

Description	Value
Gas inlet velocity for the experiment (m/s)	0.25, 0.75, 1.25, 5.00 and 10.00
Gas inlet velocity for the CFDS (m/s)	0.25, 0.75, 1.25, 5.00, 10.00 and 25.00
Outlet system pressure (kPa)	101.3
Gravity force (m/s ²)	9.81
SVF at maximum packing (-)	0.60
Specularity coefficient (-)	0.01
Restitution coefficient between solid particles and the wall (–)	0.90
Restitution coefficient between the solid particles (-)	0.90

in each phase was balanced by the convective mass fluxes, while for the conservation of momentum the accumulation of momentum in each phase was balanced by the convective momentum fluxes and the other forces due to the pressure, stress tensor, gravity and momentum interphase exchange coefficient. The accumulation of the solid particle fluctuating kinetic energy conservation was balanced by the convective fluctuating kinetic energy fluxes and the other fluctuating kinetic energy terms from the pressure, stress tensor, conductivity and collision dissipation. The behavior of the solid phase was described by taking into account the energy associated with solid particles that arises out of solid particle fluctuating motions and collisions.

The validity of the constitutive equations (Eqs. (6)–(17)) is crucial for explaining the phenomena inside the high solid particle concentration system. The conventional constitutive equation set (Chalermsinsuwan et al., 2014a,b), including the Gidaspow interphase exchanged coefficient model, was used together with suitable restitution and specularity coefficients. The Gidaspow interphase exchanged coefficient model has been recommended for use in the dense fluidized system (Chalermsinsuwan et al., 2009), while the restitution and speculartity coefficients are the adjusting parameters to account for the force between solid particles and between solid particles and the reactor wall. Those values that were found to be reasonable in the existing literature were selected for use in this study, as shown in Table 1. Compared to the previously reported studies, the restitution between solid particles in this study was lower, which is due to the dense system operating condition employed here. Since in this study the CFBR was three-dimensional (3D) with a thin depth, then a 2D computational domain was used. The 2D computational domain has previously been reported to show the same phenomena as that observed in the 3D computational domain (Chalermsinsuwan and Piumsomboon, 2011). Throughout the simulation, non-uniform grids with Cartesian coordinates were used and the time step was limited by a Courant number in order to ensure the numerical accuracy, convergence and stability. Therefore, a time step of 1.00×10^{-3} s with 100 iterations per time step was used. The time-averaged distributions of flow variables were computed after the system reached the quasi-steady state conditions, which was from 20 s to 40 s.

The definition of the appropriate initial and boundary conditions is important for performing a realistic simulation. The solid silica sand particles (21 kg) were filled inside the CFBR and the gas velocity at the system inlet was set to the specified level, whilst the system pressure was defined as at atmospheric pressure at the system outlet. In addition, the solid particle velocity was set as zero near the outlet region to match with the realistic wire mesh phenomenon. At the system wall, a no-slip condition was applied for all velocities, except for the tangential velocity of the solid particle phase and the granular temperature. At those points, the boundary conditions of Johnson and Jackson (1987) were used, which accounted for the effect of the conduction that was generated by the solid particle slips and dissipation from inelastic collisions of granular energy to the wall. The other system conditions were similar to the above experimental ones (Table 1). With respect to the validation of the 2D CFDS model, the grid and time independent studies have already been verified for this system (Chalermsinsuwan et al., 2014a,b). However, there were two assumptions or limitations for the current experiment and the CFDS, which were:

(i) The solid particles in the CFDS were assumed to be of a uniform single size, while those in the experimental system were unimodal size-distributed solid particles. This is because the CFDS with a solid particle distribution is still under development (Chew et al., 2011; You and Li, 2013). The effect of the particle size distribution can significantly impact upon the fluidization behavior, particularly with a

Table 2

The CFDS model and conditions used in this study.

A. Governing equations
(a) Conservation of mass
-Gas phase (g)

$$\frac{\partial}{\partial t} \left(\varepsilon_g \rho_g \right) + \nabla \cdot \left(\varepsilon_g \rho_g \vec{v}_g \right) = 0 \tag{1}$$

-Solid particle phase (s)

$$\frac{\partial}{\partial t}(\varepsilon_s \rho_s) + \nabla \cdot (\varepsilon_s \rho_s \vec{v}_s) = 0 \tag{2}$$

where ϵ is the volume fraction, \vec{v} is the velocity and t is the time

(b) Conservation of momentum -Gas phase (g)

$$\frac{\partial}{\partial t} \left(\varepsilon_{g} \rho_{g} \vec{v}_{g} \right) + \nabla \cdot \left(\varepsilon_{g} \rho_{g} \vec{v}_{g} \vec{v}_{g} \right) = -\varepsilon_{g} \nabla P + \nabla \cdot \vec{\tau}_{g} + \varepsilon_{g} \rho_{g} \vec{g} - \beta_{gs} (\vec{v}_{g} - \vec{v}_{s})$$

$$(3)$$

-Solid particle phase (s)

$$\frac{\partial}{\partial t}(\varepsilon_s \rho_s \vec{v}_s) + \nabla \cdot (\varepsilon_s \rho_s \vec{v}_s \vec{v}_s) = -\varepsilon_s \nabla P + \nabla \cdot \vec{\tau}_s - \nabla P_s + \varepsilon_s \rho_s \vec{g} + \beta_{gs} (\vec{v}_g - \vec{v}_s)$$

$$\tag{4}$$

where P is the gas pressure, P_s is the solid particle pressure, $\vec{\tau}_g$ is the gas phase stress, $\vec{\tau}_s$ is the solid particle phase stress, β_{gs} is the gas–solid particle phase interphase exchange coefficient and \vec{g} is the gravitational acceleration (c) Conservation of solid particle fluctuating energy (θ)

$$\frac{3}{2} \left[\frac{\partial}{\partial t} (\varepsilon_{s} \rho_{s} \theta) + \nabla \cdot (\varepsilon_{s} \rho_{s} \theta \vec{\nu}_{s}) \right] = \left(-\nabla P_{s} \vec{I} + \vec{\tau}_{s} \right) : \nabla \vec{\nu}_{s} + \nabla \cdot (\kappa_{s} \nabla \theta) - \gamma_{s}$$

$$(5)$$

where \vec{l} is the unit tensor, κ_s is the conductivity of the solid particle fluctuating energy and γ_s is the collisional dissipation of the solid particle fluctuating energy B. Constitutive equations

(a) Gas phase stress $(\vec{\tau}_g)$

$$\vec{\tau}_g = \varepsilon_g \mu_g \left[\nabla \vec{v}_g + \left(\nabla \vec{v}_g \right)^T \right] - \frac{2}{3} \varepsilon_g \mu_g \left(\nabla \cdot \vec{v}_g \right) \vec{I} \tag{6}$$

(b) Solid particle phase stress $(\vec{\tau}_s)$

$$\vec{\tau}_s = \varepsilon_s \mu_s \left[\nabla \vec{v}_s + (\nabla \vec{v}_s)^T \right] - \varepsilon_s \left(\xi_s - \frac{2}{3} \mu_g \right) \nabla \cdot \vec{v}_g \vec{I}$$
(7)

where ξ_s is the bulk viscosity of solid particle phase

(c) Radial distribution function (correction factor that indicates the probability of collisions between solid particles when the solid particles become dense) (g₀)

$$g_0 = \left[1 - \left(\frac{\varepsilon_s}{\varepsilon_{s,\text{max}}}\right)^{1/3}\right]^{-1} \tag{8}$$

where $\varepsilon_{s,max}$ is the SVF at maximum packing

(d) Collisional dissipation of solid particle fluctuating energy (γ_s)

$$\gamma_s = 3(1 - e^2)\varepsilon_s^2 \rho_s g_0 \theta \left(\frac{4}{d_p} \sqrt{\frac{\theta}{\pi}}\right) \tag{9}$$

where e is the restitution coefficient between solid particles

(e) Solid particle pressure (Ps)

$$P_{s} = \varepsilon_{s} \rho_{s} \theta [1 + 2g_{0} \varepsilon_{s} (1 + e)] \tag{10}$$

(continued on next page)

(f) Shear viscosity of solid particle phase (μ_s)

$$\mu_{s} = \frac{4}{5} \varepsilon_{s} \rho_{s} d_{p} g_{0}(1+e) \sqrt{\frac{\theta}{\pi}} + \frac{10 \rho_{s} d_{p} \sqrt{\pi \theta}}{96(1+e) g_{0} \varepsilon_{s}} \left[1 + \frac{4}{5} g_{0} \varepsilon_{s} (1+e) \right]^{2}$$

$$\tag{11}$$

(g) Bulk viscosity of solid particle phase (ξ_s)

$$\xi_{s} = \frac{4}{3} \varepsilon_{s} \rho_{s} d_{p} g_{0}(1+e) \sqrt{\frac{\theta}{\pi}}$$

$$\tag{12}$$

(h) Conductivity of the solid particle fluctuating energy (κ_s)

$$\kappa_{s} = \frac{150\rho_{s}d_{p}\sqrt{\theta\pi}}{384(1+e)g_{0}} \left[1 + \frac{6}{5}\varepsilon_{s}g_{0}(1+e)\right]^{2} + 2\rho_{s}\varepsilon_{s}^{2}d_{p}(1+e)g_{0}\sqrt{\frac{\theta}{\pi}}$$

$$\tag{13}$$

(i) Gas–solid particle phase interphase exchange coefficient ($\beta_{\rm gs})$ –Gidaspow model when $\epsilon_{\rm g}$ > 0.80

$$\beta_{gs} = 150 \frac{\left(1 - \varepsilon_g\right)^2 \mu_g}{\varepsilon_g d_p^2} + 1.75 \frac{\left(1 - \varepsilon_g\right) \rho_g \left|\vec{v}_g - \vec{v}_s\right|}{d_p} \tag{14}$$

when $\varepsilon_g \leqslant 0.80$

$$\beta_{gs} = \frac{3}{4} \frac{(1 - \varepsilon_g) \varepsilon_g}{d_n} \rho_g |\vec{v}_g - \vec{v}_s| C_{D0} \varepsilon_g^{-2.65}$$
(15)

with

Re < 1000;
$$C_{D0} = \frac{24}{\text{Re}_k} \left(1 + 0.15 \text{Re}_k^{0.687} \right)$$
; $\text{Re}_k = \frac{\rho_g \varepsilon_g |\vec{v}_g - \vec{v}_s| d_p}{\mu_g}$
 $\text{Re} \ge 1000$; $C_{D0} = 0.44$

(j) Johnson and Jackson boundary conditions Velocity of solid particle phase at the wall ($\vec{v}_{t,W}$)

$$\vec{v}_{t,W} = -\frac{6\mu_s \varepsilon_{smax}}{\pi \phi \rho_s \varepsilon_s g_0 \sqrt{3\theta}} \frac{\partial \vec{v}_{s,W}}{\partial \vec{n}}$$
(16)

Granular temperature at the wall (θ_W)

$$\theta_{W} = -\frac{\kappa_{s}\theta}{\gamma_{W}} \frac{\partial \theta_{W}}{\partial \vec{n}} + \frac{\sqrt{3}\pi\phi \rho_{s}\varepsilon_{s}\vec{v}_{s,slip}^{2}g_{0}\theta^{\frac{3}{2}}}{6\varepsilon_{s,max}\gamma_{W}}$$

$$(17)$$

with
$$\gamma_W=rac{\sqrt{3}\pi\left(1-e_W^2\right)\epsilon_s
ho_sg_0\theta^{3/2}}{4\epsilon_{s,max}}$$

where e_W is the restitution coefficient between the solid particle and wall, ϕ is the specularity coefficient, γ_W is the collisional dissipation of solid fluctuating energy at the wall, $\vec{v}_{s,slip}$ is the slip velocity of a solid particle phase at the wall, $\vec{v}_{s,W}$ is the velocity of the solid particle phase at the wall and \vec{n} is the unit vector.

large amount of fine solid particles because these small particles will leave the system. However, in the present CFDS, the results with the uniform single sized solid particles matched those results from the experimental system with the unimodal size distributed solid particles. This is because the particles employed in the experimental system had a narrow normally distributed size range (Boonprasob et al., 2013), and they were also Geldart group B solid particles. Accordingly, the obtained experimental phenomena do not differ much from those found in the CFDS (Basu, 2006).

(ii) The gas inlet velocity range in the CFDS was varied between 0.25 and 25.00 m/s, while in the experimental measurements it was only between 0.25 and 10.00 m/s (i.e. no 25 m/s set up). This is because the experimental system

could not be operated in the extremely high gas inlet velocity of 25.00 m/s. However, a new gas-solid particle phenomenon was found inside the system by the CFDS at a 25.00 m/s gas inlet velocity. In the results section, for each fluidization regime the result from one representative gas inlet velocity was selected for presentation and discussion.

4. Results and discussion

4.1. Qualitative comparison

Fig. 2 illustrates the instantaneous photo snapshots of solid particles inside the CFBR riser at five different gas inlet velocities ($v_{\rm g}$ inlet) or fluidization regimes. The solid particle distributions were

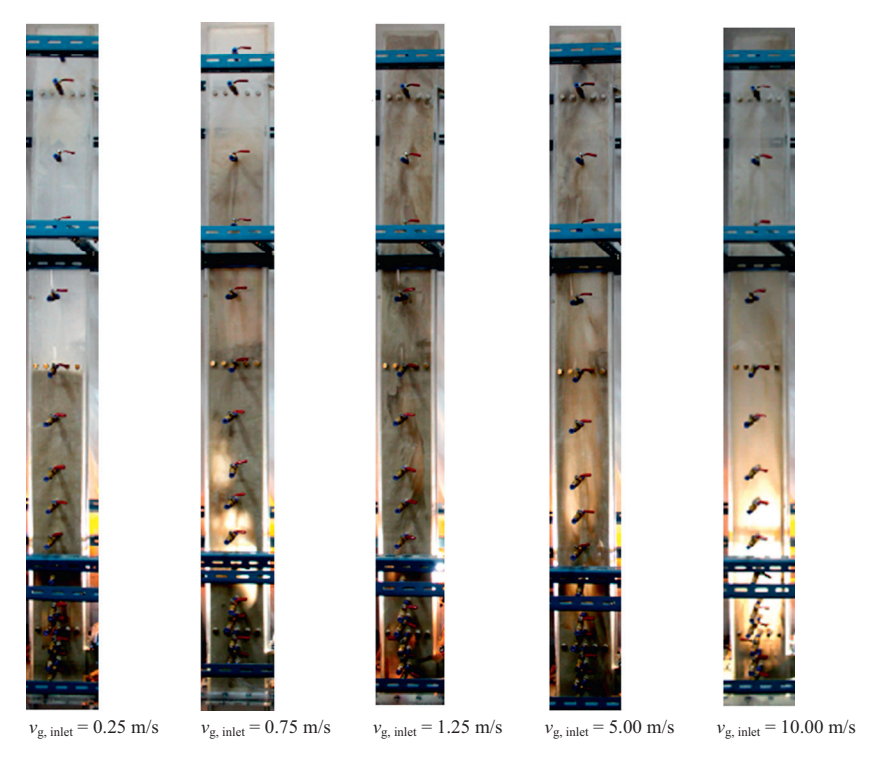


Fig. 2. The instantaneous photo snapshots of solid particles inside the CFBR riser with five different fluidization regimes obtained by different gas inlet velocities (vg. inlet).

clearly seen as the brown colored silica sand against the transparent column where no solid particles were noticed. The instantaneous contours of the particle SVF and the vectors of the solid particle velocity inside the CFBR riser with six different gas inlet velocities ($v_{\rm g,\ inlet}$) or fluidization regimes are displayed in Fig. 3. The results from Figs. 2 and 3 were captured after the system had reached the quasi-steady state condition, and so the system does not change with the simulation time. The results from the CFDS and experimental measurement were mostly consistent with each other when using the same gas inlet velocities. The CFDS captured all the fluidization phenomena observed in the experimental system, including the bubble formation and solid particle clustering, which supports the accuracy of the developed CFDS model.

The bubbling fluidization regime was found at the lowest employed gas inlet velocity (0.25 m/s). The main characteristic of this fluidization regime is the occurrence of gas bubbles inside the system (Basu, 2006). Above the system distributor, the input gas starts to coalescence as a gas bubble and as it moves along the CFBR riser the gas bubble propagates and grows. However, the gas bubble was not clearly seen at a gas inlet velocity of 0.25 m/s because it was too low. Increasing the gas inlet velocity to 0.75 m/s yielded a turbulent fluidization regime, where the gas bubble inside the system is larger at the bottom section of the CFBR riser (Yang, 2003). At the top section of the riser the solid particle bed surface had disappeared due to the breakage of the gas bubbles. The solid particles at the roof of a gas bubble are then pushed up as individual particles. The maximum height of individual solid particles obtained from the CFDS was slightly lower than that from the experimental system, which is because of the attrition or fragmentation of the solid particles.

At a 1.25 m/s gas inlet velocity the unconventional CTFB regime was observed, with no transparent column area being evident in the experimental system. This means that the uniformly dense solid particle system is scattered throughout the column or a more uniformly dense solid particle system is obtained. However, the CFDS-derived SVF profile revealed that the SVF at the wall region was slightly higher than that at the center region. With a 5.00 m/s

gas inlet velocity a fast fluidization regime was observed, where a high solid particle concentration was found at the wall region, and a low solid particle distribution at the center region. This is the unique characteristic of a fast fluidization regime, a coreannulus flow structure, in a generally low solid particle density system (Kunii and Levenspiel, 1991). At the top of the CFBR riser, solid particles accumulated due to the system outlet configuration.

Further increasing the gas inlet velocity to 10.00 m/s yielded a dilute-phase fluidization regime, where a more dilute solid particle distribution was observed in both the experimental and CFDS systems. The difference in the solid particle concentration between the wall and center region was less pronounced. The main characteristic of a dilute-phase fluidization regime is the uniformly dilute solid particle distribution (Das et al., 2004). Finally, at a 25.00 m/s gas inlet velocity a dense suspension bypassing fluidization regime was found in the CFDS, which is the second unconventional fluidization regime observed. From the SVF contours, the solid particles moved up half the column height near the solid particle inlet from the CFBR downer while the gas moved up in the other half of the column. The effect of system outlet configuration was also slightly evident, and is due to the high gas inlet velocity condition.

4.2. Quantitative comparison

For the quantitative comparison, the axial distribution of the absolute pressure was selected. The different gauge pressures in the same system have previously been validated (Chalermsinsuwan et al., 2014a). After the validation, the time-averaged SVFs were obtained from the CFDS to further explain the observed experimental measurement.

Fig. 4 shows the vertical distributions of the time-averaged absolute pressure and SVF with different gas inlet velocities ($v_{\rm g}$, $i_{\rm nlet}$), selected to represent the different fluidization regimes. All the absolute pressures from the CFDS and experimental systems were consistent with each other. When considering on the qualitative results, one gas inlet velocity for each distinct system hydrodynamics was discussed.

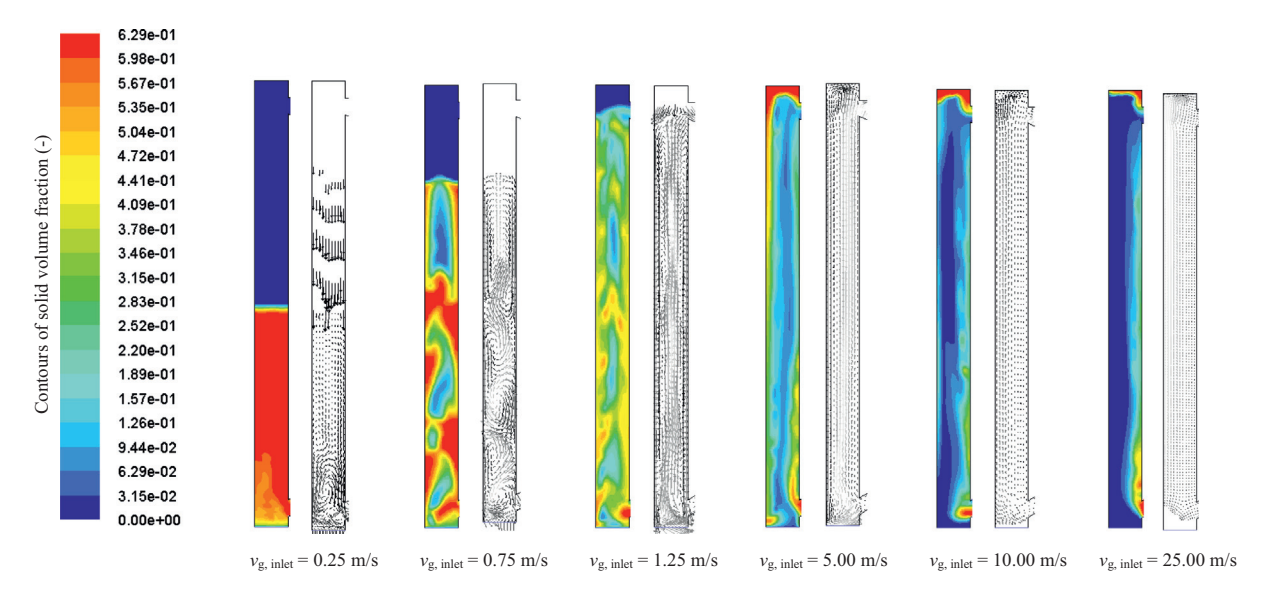


Fig. 3. The instantaneous contours of the particle SVF and vectors of the solid particle velocity inside the CFBR riser with six different fluidization regimes obtained with different gas inlet velocities ($v_{g, inlet}$). The red and blue contour colors represent the high and low SVFs, respectively.

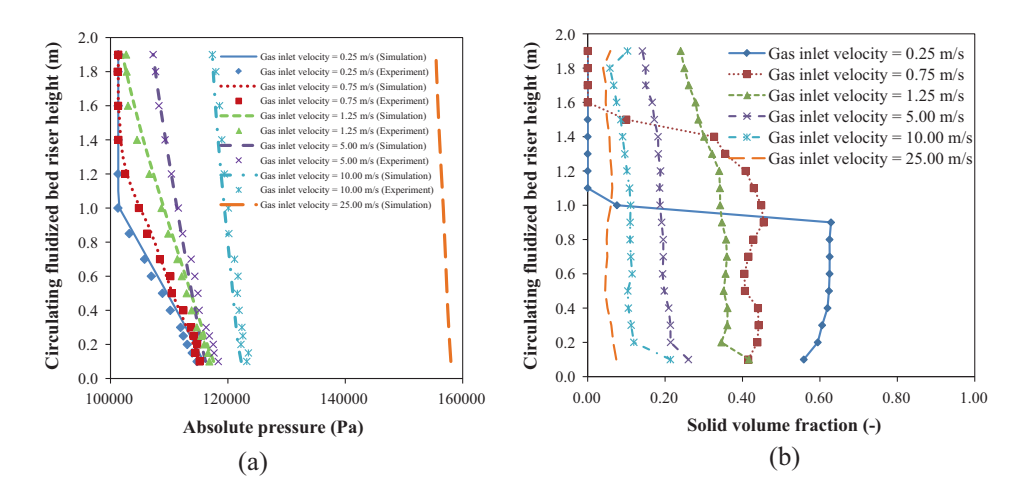


Fig. 4. The vertical distributions of the time-averaged (a) experimentally- and CFDS-derived absolute pressure and (b) the CFDS-derived SVF for the six different fluidization regimes obtained with different representative gas inlet velocities ($v_{g, inlet}$). In (a), the symbol and line represent the experimental measurement and simulation results, respectively, while in (b), the symbol with a line represents the simulation results.

For the bubbling fluidization regime (0.25 m/s gas inlet velocity), the profile could be divided into two zones. At the bottom zone, the absolute pressure increased steadily with an increasing height of the CFBR riser, which is because of the constant quantity of solid particles at the bottom reactor region. At the top zone, the absolute pressure profile was constant at atmospheric pressure, explaining why only a small amount of solid particles was observed in that reactor region. The surface of the solid particle bed was at a height of approximately 1.00 m in the CFBR riser. The vector of the solid particle velocity (Fig. 3) also confirmed this observed system characteristic, where a high system recirculation occurred at the bottom zone. Above the solid particle bed surface, the solid particle velocities had a negative value, since at this low gas inlet velocity the solid particles had insufficient translation force to move out and fall back to the bottom zone.

For the turbulent fluidization regime (0.75 m/s gas inlet velocity), the obtained absolute pressure profile also had two zones. However, the slope was lower than that in the bubbling fluidization regime (0.25 m/s gas inlet velocity), which was consistent with the obtained SVF. At the top zone, the absolute pressure

profile was at atmospheric pressure, but the solid particle bed surface was at a height of approximately 1.40 m in the CFBR riser, which was higher than that with a 0.25 m/s gas inlet velocity. From the vector profile (Fig. 3), the recirculation zone was enlarged towards the upper area of the CFBR. Above the solid particle bed surface the solid particles had a fountain-like trajectory, which is due to the force balance inside the system (Gao et al., 2012). At the center and wall regions of the riser, positive and negative solid particle velocities were found, respectively.

With the CTFB regime (1.25 m/s gas inlet velocity), different results from the previous two fluidization regimes were evident, with only a single pattern along the CFBR riser height being found. Therefore, the unconventional CTFB regime was verified. The absolute pressure decreased with increasing CFBR height, but a slightly constant profile was still observed at the top zone, which reflects the uniform distribution of solid particles along the CFBR riser. The SVF did not vary over the reactor column. From the solid particle velocity vectors (Fig. 3), mixing or turbulence inside the system was observed throughout the system, which is because of the high solid particle quantity and relatively low gas inlet velocity

operating condition. The surface of the solid particle bed was located at the outlet of the CFBR riser, reflecting that the uplift force inside the system had reached the minimum level required to lift the solid particles up to the CFBR downer. In the radial direction, the solid particles exhibited a mild core–annulus flow structure similar to that in the general fast fluidization regime (Rhodes, 2008; Chalermsinsuwan et al., 2009).

In the fast fluidization regime (5.00 m/s gas inlet velocity), the absolute pressure decreased throughout the CFBR riser. Compared to the CTFB regime (1.25 m/s gas inlet velocity, the decreasing rate or slope of the absolute pressure was lower in the fast fluidization regime, which infers a low SVF. In addition, a slightly increasing SVF at the top and bottom zones was found due to the recirculation of solid particles from the CFBR downer. No solid particle bed surface was observed due to the continuous system operation. From the solid particle velocity vectors, the general core–annulus profile in a low solid particle density system was observed (Rhodes et al., 1998; Almuttahar and Taghipour, 2008; Rhodes, 2008), with turbulence inside the system at the top and bottom zones.

For the dilute-phase fluidization regime (10.00 m/s gas inlet velocity), the absolute pressure at the top of the CFBR riser was high due to the relatively high gas velocity and low SVF inside the riser. The SVF profile supported this notion, with a lower SVF compared to that in the other fluidization regimes at lower gas inlet velocities. At the top and bottom zones, the high solid particle concentrations were consistent with the absolute pressure profiles. No solid particle bed surface was observed, but the solid particle velocity had an asymmetric profile and was highest near one side of the system wall. Inside the system, the flow pattern was a mild core–annulus. This profile matched that previously reported for a dilute-phase fluidization regime (Grace et al., 1997; Rabinovich and Kalman, 2011).

Finally, with a 25.00 m/s gas inlet velocity the second unconventional fluidization regime of a dense suspension bypassing fluidization regime was observed in the CFDS. However, the experimental measurement could not be conducted at this gas inlet velocity due to the limitation of the current experimental apparatus, and so this result lacks experimental data for support. Nevertheless, from the CFDS the highest absolute pressure was observed throughout the CFBR riser and the difference between the absolute pressure at the top and the bottom zones was the lowest, which is due to the low SVF inside the system (Fig. 4(b)). Indeed, the low SVF and high gas inlet velocity gave a uniform solid particle distribution in the axial direction. Similar to the two previous fluidization regimes (at a gas inlet velocity of 5.0 and 10.0 m/s), the system did not show a clear solid particle bed surface. With respect to the solid particle velocity vectors, all the solid particle velocities moved upwards at one side of the riser only, which is the unique hydrodynamics of this fluidization regime compared to the other fluidization regimes.

Both the qualitative and quantitative comparisons supported the occurrence of two unconventional fluidization regimes inside the high solid particle concentration CFBR; namely the CTFB and dense suspension bypassing fluidization regimes, which were similar to that reported in an experimental 3D CFBR (Mei et al., 2007; Zhu and Zhu, 2008; Qi et al., 2012a). Subsequently, the specific fluidization regime was evaluated using the three statistical parameters of the ASVF and the SD of the horizontal and vertical SVFs.

4.3. Fluidization regime explanation

Fig. 5 shows the horizontal distributions of the averaged SVFs obtained from the CFDSs with six different gas inlet velocities, one representative per different fluidization regime. The results were averaged over the heights of the CFBR riser. For the bubbling fluidization regime (0.25 m/s gas inlet velocity), the horizontal

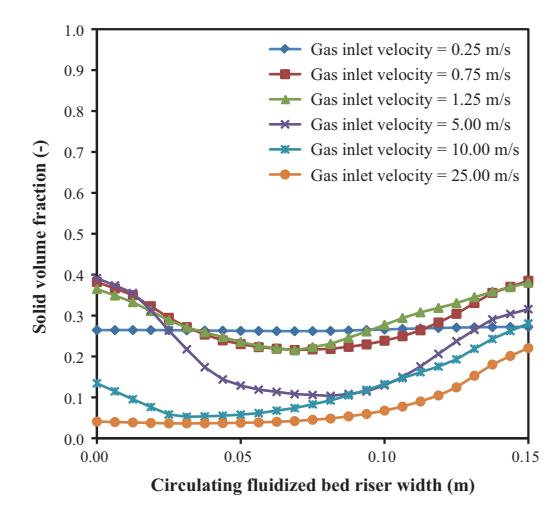


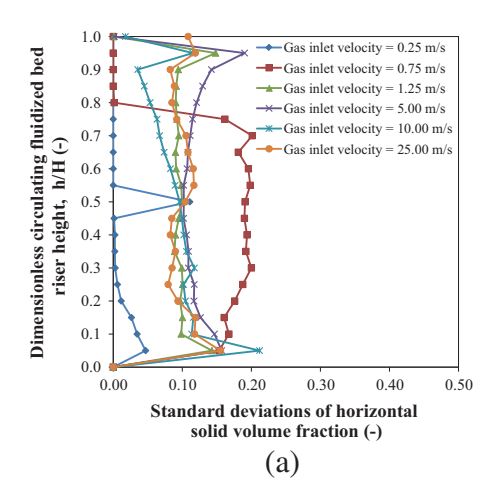
Fig. 5. The horizontal distributions of the time-averaged SVF obtained from the CFDS for the six different fluidization regimes obtained with different representative gas inlet velocities.

profile of the SVF was constant at approximately 0.27, which can be explained by the low gas inlet velocity in this system. Actually, the SVF inside the solid particle bed was higher than 0.27, but no solid particles were found at the top zone.

With the turbulent fluidization and CTFB regimes (gas inlet velocities of 0.75 and 1.25 m/s, respectively), the obtained profiles were somewhat similar, where low and high SVFs were found at the center and wall regions, respectively. Still, the overall SVF values across the width of the CFBR riser were higher than 0.20, which reflects the high solid particle concentration system condition (Issangya et al., 1999). For the fast fluidization regime (5.00 m/s gas inlet velocity), the core–annulus flow structure was observed, which was consistent with the solid particle velocity vectors, and a difference in the SVFs at the center and the wall regions was clearly observed.

For the 10 and 25 m/s gas inlet velocities, the SVFs inside the system were low compared to those in the fluidization regimes obtained with lower gas inlet velocities. With a dilute-phase fluidization regime (10.00 m/s gas inlet velocity), the flow structure was a mild asymmetric core–annulus flow, which was consistent with the obtained solid particle velocity. For the 25.00 m/s gas inlet velocity (dense suspension bypassing fluidization regime), the SVFs were high and low at the opposite wall regions, respectively. The high SVF occurred near the wall at which the solid particles were recirculated from the CFBR downer. The flow pattern inside this unconventional fluidization regime was, therefore, found to have unique system characteristics.

The SD of the SVF values inside the high solid particle density CFBR riser were used in this study to reflect the distribution of the solid particles along the vertical and horizontal directions, and to imply the quality of mixing inside the system. High and low SDs imply a non-uniform and uniform SVF, respectively. The vertical distributions of the SD of the horizontal SVF with the six different gas inlet velocities that are each representative of a different fluidization regime, are shown in Fig. 6(a). With a 0.25 m/s gas inlet velocity (bubbling fluidization regime), the SD was high at the bottom zone because of the low gas inlet velocity. In addition, a high mixing level was observed near the solid particle bed surface. At a 0.75 m/s gas inlet velocity (turbulent fluidization regime), the highest SD values across the solid particle bed were observed, which is the unique characteristic of this fluidization regime and implies the highest horizontal mixing level inside the system. This is also consistent with previous reports that bubble agglomeration and breakage occurred in this fluidization regime (Yang, 2003).



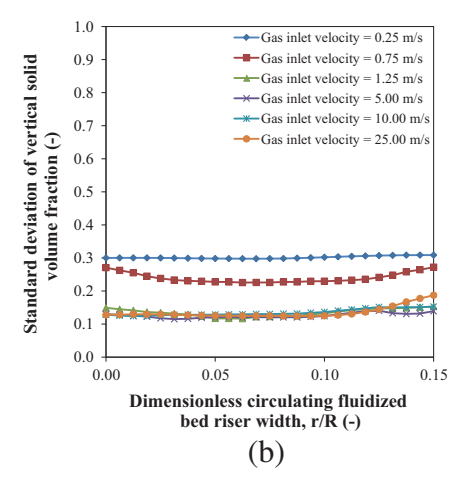


Fig. 6. The (a) vertical and (b) horizontal distributions of the SD of the (a) horizontal and (b) vertical SVFs for the six different fluidization regimes obtained with different representative gas inlet velocities.

Less solid particles were observed above the surface of solid particle bed.

In the CTFB regime (1.25 m/s gas inlet velocity), the system radial mixing was homogeneous throughout the riser, which is presumably due to the uniform system hydrodynamics and is the advantage of this fluidization regime. With a 5.00 m/s gas inlet velocity (fast fluidization regime), high SD values were found at the top and bottom zones of the CFBR riser due to the inlet and outlet configurations, whilst in the dilute-phase fluidization regime (10.00 m/s gas inlet velocity), high and low SD values were observed at the bottom and top zones, respectively, which is due to the alteration in the SVFs inside the system (Fig. 3). Finally, in the dense suspension bypassing fluidization regime (25.00 m/s gas inlet velocity), the horizontal mixing was constant throughout the riser, as seen in the CTFB regime, but different between these two unconventional fluidization regimes differed in the high and low averaged SVFs (Fig. 4).

The horizontal distributions of the SD of the vertical SVF was uniform throughout the CFBR riser in all six different fluidization regimes, as shown for the representative gas inlet velocities in Fig. 6(b). At a 0.25 m/s gas inlet velocity (bubbling fluidization regime), the constant observed profile was similar to that seen in the vertical distribution and the highest non-uniform SVF was found. With a 0.75 m/s gas inlet velocity (turbulent fluidization regime), a high variation in the SD values was still obtained, but the values were lower than that for the bubbling fluidization regime. The SD near the wall region was slightly higher than that near the center region, which infers that the system fluctuation was higher near the wall region. For the gas inlet velocities of 1.25, 5.00 and 10.00 m/s gas, the profiles were constant over the width of the CFBR riser, but the obtained SD values were lower than the two fluidization regimes obtained with the lower (0.25 and 0.75 m/s) gas inlet velocities. This implies a lower level of system fluctuation inside these fluidization regimes. For the 25.00 m/s gas inlet velocity (dense suspension bypassing fluidization regime), the SD at one side wall (near the solid particle inlet from the CFBR downer) was slightly higher than the one on the other side, which is due to the recirculating solid particles.

4.4. Fluidization regime mapping

The effect of the particle Reynolds number $(Re_p = \rho_g d_p V | \mu_g)$, where V is the gas inlet velocity) on the horizontal and vertical SD of the SVF for each fluidization regime are shown for representative examples in Fig. 7 along with those for the ASVF for comparison. These three statistical parameters were used to

deduce a suitable system operating condition. The ASVF had a maximum value of about 0.30 at a 1.25 m/s gas inlet velocity (CTFB regime). For the 0.25 m/s (bubbling fluidization regime) and 0.75 m/s (turbulent fluidization regime) gas inlet velocities, the average SVF increased with increasing gas inlet velocities, which can be explained by the batch fluidization system hydrodynamics. The solid particles then recirculate inside the system. The solid particle bed surfaces were observed below the exit to the CFBR downer, giving a low ASVF.

For the 5.00 m/s (fast fluidization regime), 10.00 m/s (dilutephase fluidization regime) and 25.00 m/s (dense suspension bypassing fluidization regime) gas inlet velocities, the ASVF dramatically decreased with an increasing gas inlet velocity, as the higher gas volumetric flow rate makes the system more dilute.

With respect to the SD of the horizontal SVF, the lowest value was found in the 0.25 m/s gas inlet velocity (bubbling fluidization regime), due to this gas inlet velocity only just providing sufficient uplift force to slightly move some of the solid particles. The highest SD of the horizontal SVF was observed at a 0.75 m/s gas inlet velocity (turbulent fluidization regime), which is because of the high fluctuation in the system hydrodynamics. For the other gas inlet velocities, the SDs of the horizontal SVF were approximately constant, and so less particle movement was observed in the horizontal direction for these gas inlet velocities and the main flow direction was vertical. The highest SD of the vertical SVF was

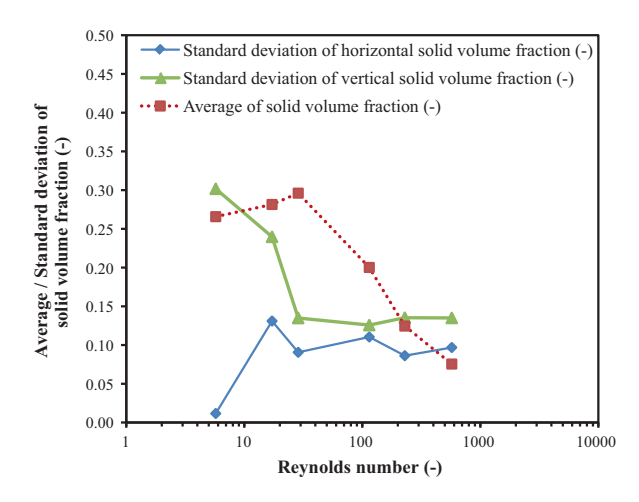
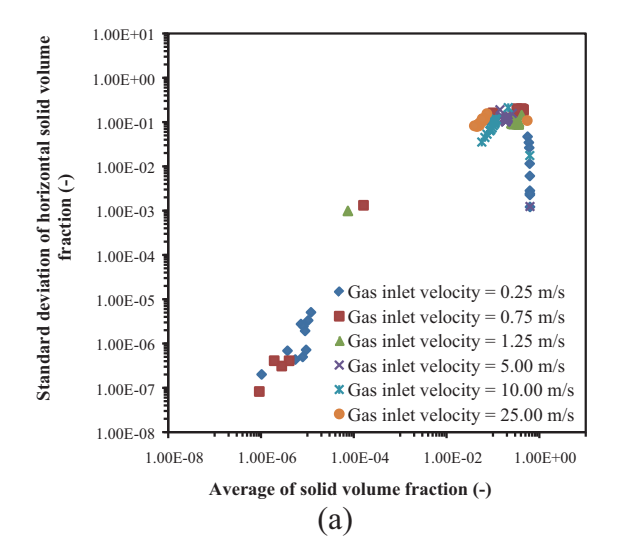


Fig. 7. The effect of the particle Reynolds number on the ASVFs and the SD of the horizontal and vertical SVFs.

observed with a 0.25 m/s gas inlet velocity (bubbling fluidization regime), which can be explained by the solid particle distribution in the vertical direction as already explained. As the gas inlet velocity increased, the SDs of the vertical SVF initially decreased with a 0.75 m/s gas inlet velocity and then approached a constant value of 0.13 for the 1.25, 5.00, 10.00 and 25.00 m/s gas inlet velocities. This near constant value was obtained because the same flow structure was obtained with each of these higher gas inlet velocities. From all the results, the CTFB regime will likely be the more optimal fluidization regime for applications that need a high contact surface area, while the dense suspension bypassing fluidization regime will be more suitable for applications that need to transport a high quantity of solid particles.

The effect of the ASVF on the horizontal and vertical SDs of the SVF revealed a clear trend between the AVSF and horizontal SD of the SVF (Fig. 8). The maximum value was obtained at a moderate ASVF, where the solid particles inside the system could move as a single particles or clusters, resulting in the high SD of the SVF. At a low ASVF a small amount of solid particles resided in the system and they only moved as individual particles giving a lower system fluctuation, whereas at a high ASVF the solid particles were packed or agglomerated together and so restricted in their movement, which also led to a low system fluctuation.

With respect to the effect of the ASVF on the vertical SD of the SVF, an overall trend of an increasing vertical SD of the SVF was



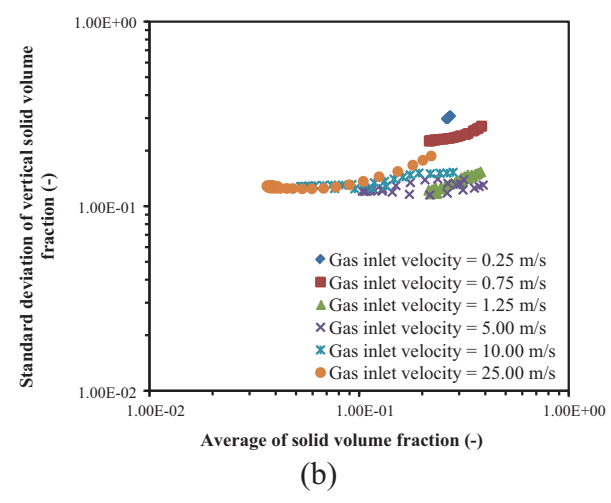


Fig. 8. The effect of the ASVF on the SDs of the (a) horizontal and (b) vertical SVFs.

observed in all the fluidization regimes. As the solid particle concentration became denser, the system fluctuation inside the system increased. Comparing between the different fluidization regimes, the bubbling and turbulent fluidization regimes gave a higher SD of the axial SVF, as discussed above, while the other fluidization regimes had SD values of the axial SVF in the same order of magnitude. In conclusion, a general simplified fluidization regime mapping was summarized using the equations for calculating the minimum gas inlet velocity shown in Table 3 and obtained from previous reports (Grace et al., 1997; Basu, 2006; Rabinovich and Kalman, 2011; Jaiboon et al., 2013b). The six different fluidization regimes observed in the CFBR riser with a high solid particle concentration are shown in Fig. 9 in terms of the dimensionless velocity (V^*) and Archimedes number (Ar), as calculated from Eq. (18).

$$V^* = \left[\frac{\rho_g^2}{g\mu_g(\rho_s - \rho_g)}\right]^{1/3} \left[V - \frac{G_s \varepsilon}{\rho_s (1 - \varepsilon)}\right],\tag{18}$$

where ε is the void fraction. The graph for each conventional fluidization regime was plotted as the minimum fluidization velocity (u_{mf}) , minimum turbulent fluidization velocities (u_c, u_k) , minimum transport velocity (u_{mp}) derived from the gas inlet velocity. The minimum terminal velocity (u_t) , where the terminal velocity is the equilibrium velocity at which the buoyancy force and the fluid drag balance the effect of gravity, is also shown. Below the minimum terminal velocity, the solid particles are generally retained within a certain bed height and there is no large scale migration of solid particles. Above the minimum terminal velocity, there is large-scale migration of solid

Table 3 A summary of the minimum gas inlet velocity equations.

Description	Equation
Minimum fluidization velocity	$\frac{\rho_{\rm g} d_{\rm p} u_{\rm mf}}{\mu_{\rm g}} = \left[27.2^2 + 0.0408 Ar\right]^{0.5} - 27.2$
Minimum turbulent fluidization velocity	$\frac{\rho_{\rm g} d_{\rm p} u_{\rm c}}{\mu_{\rm g}} = 0.565 A r^{0.461}$
Minimum turbulent fluidization velocity	$\frac{\rho_{\rm g} d_{\rm p} u_{\rm k}}{\mu_{\rm g}} = 1.310 A r^{0.450}$
Minimum transport velocity	$rac{ ho_g d_p u_{tr}}{\mu_g} = 2.28 A r^{0.419}$
Minimum pneumatic transport fluidization velocity	$u_{mp} \approx 20 \mathrm{u_t}$
Minimum terminal velocity	$\frac{\rho_{\rm g} d_{\rm p} u_{\rm t}}{\mu_{\rm g}} = \left(\frac{\rm Ar}{7.5}\right)^{0.666}$

where Archimedes number(Ar) = $\frac{\rho_g(\rho_s - \rho_g)gd_p^3}{\mu_g^2}$.

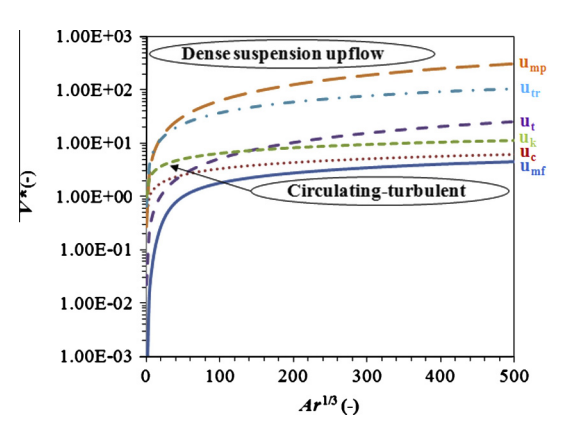


Fig. 9. Summary of the six different fluidization regimes observed in the CFBR riser with a high solid particle density.

particles out of the system. Because the difference between the turbulent fluidization and CTFB regimes lies in the elutriation of solid particles, the novel CTFB regime should be positioned at the intersection region above the minimum turbulent and terminal velocities and below the minimum transport velocity. For the dense suspension bypassing fluidization regime, it should occur above the minimum pneumatic transport velocity.

5. Conclusions

In this study, the system hydrodynamics inside a high solid particle concentration CFBR were conducted using CFDS and experimental measurements. The appropriate CFDS model, as well as the initial and boundary conditions, were successfully developed and confirmed by qualitative and quantitative comparisons with the experimentally derived data. For the qualitative comparison, the photo snapshots of the solid particle distribution inside the CFBR riser were used to compare with the SVF contours obtained from the CFDS. For the quantitative comparison, the axial distributions of the absolute pressure inside the CFBR riser were evaluated. Then, further fluidization regime explanation and mapping were concluded and the results were summarized in terms of the ASVF and the SDs of the horizontal and vertical SVFs. The ASVF had a maximum value in the CTFB regime (1.25 m/s gas inlet velocity), while the SD of the horizontal and vertical SVFs had minimum and maximum values in the bubbling fluidization regime (0.25 m/s gas inlet velocity), respectively. As the gas inlet velocity increased, the SDs of the SVF tended to approach a constant value, which is because of the constant flow structure throughout the CFBR riser at a high gas inlet velocity. For the CTFB and dense suspension bypassing fluidization regimes, a constant system mixing was obtained throughout the CFBR riser, but the difference between these two unconventional fluidization regimes was the high and low ASVFs, respectively. The CTFB regime will be more optimal for applications that need a high contact surface area, while the dense suspension bypassing fluidization regime will be more suitable for applications that need to transport a high quantity of solid particles. Moreover, the maximum SD of the horizontal SVF was found at a moderate ASVF, while the SD of the vertical SVF increased with an increasing ASVF in all six fluidization regimes. Finally, the positions of the two unconventional fluidization regimes (using only primary gas injection) on a general simplified fluidization regime mapping were summarized.

Acknowledgements

This study was financially supported by the Grants from the National Research University Project, Office of Higher Education Commission (WCU-044-CC-57), from the Thailand Research Fund for fiscal year 2014–2016 (TRG5780205), from the Chulalongkorn University (Ratchadaphiseksomphot Endowment Fund), from the Faculty of Science of Chulalongkorn University, from the Graduate School of Chulalongkorn University (Research Assistant Scholarship: GCUGE1725560004D) and from the Center of Excellence on Petrochemical and Materials Technology, Chulalongkorn University. In addition, the silica sand was donated by the Quality Sand Corporation Ltd.

References

- Almuttahar, A., Taghipour, F., 2008. Computational fluid dynamics of a circulating fluidized bed under various fluidization conditions. Chem. Eng. Sci. 63, 1696–1709.
- Bai, D., Kato, K., 1999. Quantitative estimation of solids holdups at dense and dilute regions of circulating fluidized beds. Powder Technol. 101, 183–190.

- Bastos, J.C.S.C., Rosa, L.M., Mori, M., Marini, F., Martignoni, W.P., 2008. Modelling and simulation of a gas-solids dispersion flow in a high-flux circulating fluidized bed (HFCFB) riser. Catal. Today 130, 462–470.
- Basu, P., 2006. Combustion and Gasification in Fluidized Beds. CRC Press, New York. Basu, P., Fraser, S.A., 1991. Circulating Fluidized Bed Boiler: Design and Operations. Butterworth-Heinemann, Stoneham.
- Bi, H.T., Grace, J.R., 1995. Flow regime diagrams for gas-solid fluidization and upward transport. Int. J. Multiphas. Flow 21, 1229–1236.
- Bi, H., Zhu, J., 1993. Static instability analysis of circulating fluidized beds and concept of high-density risers. AIChE J. (8), 1272–1280.
- Boonprasob, S., Chalermsinsuwan, B., Piumsomboon, P., 2013. Studying freeboard's velocity of turbulent fluidization in 2 dimensional fluidization reactor. The 4rd National Research Symposium on Petroleum, Petrochemicals, and Advanced Materials, Bangkok, Thailand.
- Chalermsinsuwan, B., Piumsomboon, P., 2011. Computation of the mass transfer coefficient of FCC particles in a thin bubbling fluidized bed using two-and three-dimensional CFD simulation. Chem. Eng. Sci. 66, 5602–5613.
- Chalermsinsuwan, B., Piumsomboon, P., Gidaspow, D., 2009. Kinetic theory based computation of PSRI riser: part I estimate of mass transfer coefficient. Chem. Eng. Sci. 64, 1195–1211.
- Chalermsinsuwan, B., Kuchonthara, P., Piumsomboon, P., 2010a. CFD modeling of tapered circulating fluidized bed reactor risers: hydrodynamic descriptions and chemical reaction responses. Chem. Eng. Process. 49, 1144–1160.
- Chalermsinsuwan, B., Piumsomboon, P., Gidaspow, D., 2010b. A computational fluid dynamics design of a carbon dioxide sorption circulating fluidized bed. AIChE J. 56, 2805–2824.
- Chalermsinsuwan, B., Gidaspow, D., Piumsomboon, P., 2013. Comparisons of particle cluster diameter and concentration in circulating fluidized bed riser and downer by using CFD simulations. KIChE J. 30, 963–975.
- Chalermsinsuwan, B., Gidaspow, D., Piumsomboon, P., 2014a. In-depth system parameters of transition flow pattern between turbulent and fast fluidization regimes in high solid particle density circulating fluidized bed reactor. Powder Technol. 253, 522–536.
- Chalermsinsuwan, B., Thummakul, T., Gidaspow, D., Piumsomboon, P., 2014b. Characterization of fluidization regime in circulating fluidized bed reactor with high solid particle concentration using computational fluid dynamics. KIChE J. 31, 350–363
- Chew, J.W., Hays, R., Findlay, J.G., Knowlton, T.M., Karri, S.B.R., Cocco, R.A., Hrenya, C.M., 2011. Impact of material property and operating conditions on mass flux profiles of monodisperse and polydisperse Group B particles in a CFB riser. Powder Technol. 214, 89–98.
- Cody, G.D., Johri, J., Goldfarb, D., 2008. Dependence of particle fluctuation velocity on gas flow, and particle diameter in gas fluidized beds for mono dispersed spheres in the Geldart B and A fluidization regimes. Powder Technol. 182, 146–170.
- da Silva, F.R.G.B., de Souza, M., de Souza da Costa, A.M., de Matos Jorge, L.M., Paraíso, P.R., 2012. Experimental and numerical analysis of soybean meal drying in fluidized bed. Powder Technol. 229, 61–70.
- Das, A.K., De Wilde, J., Heynderickx, G.J., Marin, G.B., Vierendeels, J., Dick, E., 2004. CFD simulation of dilute phase gas-solid riser reactors: part I a new solution method and flow model validation. Chem. Eng. Sci. 59, 167–186.
- Dubrawski, K., Tebianian, S., Bi, H.T., Chaouki, J., Ellis, N., Gerspacher, R., Jafari, R., Kantzas, A., Lim, C., Patience, G.S., Pugsley, T., Qi, M.Z., Zhu, J.X., Grace, J.R., 2013. Traveling column for comparison of invasive and non-invasive fluidization voidage measurement techniques. Powder Technol. 235, 203–220.
- Gao, X., Wu, C., Cheng, Y.W., Wang, L.J., Li, X., 2012. Experimental and numerical investigation of solid behavior in a gas-solid turbulent fluidized bed. Powder Technol. 228, 1–13.
- Gidaspow, D., 1994. Multiphase Flow and Fluidization: Continuum and Kinetic Theory Description. Academic Press, Boston.
- Gidaspow, D., Jiradilok, V., 2010. Computational Techniques: The Multiphase CFD Approach to Fluidization and Green Energy Technologies. Nova Science Publishers Inc., New York
- Grace, J.R., 2000. Reflections on turbulent fluidization and dense suspension upflow. Powder Technol. 113, 242–248.
- Grace, J.R., Avidan, A.A., Knowlton, T.M., 1997. Circulating Fluidized Beds. Blackie Academic and Professional, London.
- Hou, Q.F., Zhou, Z.Y., Yu, A.B., 2012. Micromechanical modeling and analysis of different flow regimes in gas fluidization. Chem. Eng. Sci. 84, 449–468.
- Issangya, A.S., Bai, D., Bi, H.T., Lim, K.S., Zhu, J., Grace, J.R., 1999. Suspension densities in a high-density circulating fluidized bed riser. Chem. Eng. Sci. 54, 5451–5460.
- Issangya, A.S., Grace, J.R., Bai, D., Zhu, J., 2000. Further measurements of flow dynamics in a high-density circulating fluidized bed riser. Powder Technol. 111, 104–113.
- Jaiboon, O., Chalermsinsuwan, B., Mekasut, L., Piumsomboon, P., 2013a. Effect of flow patterns/regimes on CO_2 capture using K_2CO_3 solid sorbent in fluidized bed/circulating fluidized bed. Chem. Eng. J. 219, 262–272.
- Jaiboon, O., Chalermsinsuwan, B., Mekasut, L., Piumsomboon, P., 2013b. Effect of flow pattern on power spectral density of pressure fluctuation in various fluidization regimes. Powder Technol. 233, 215–226.
- Johnson, P.C., Jackson, R., 1987. Frictional-collisional constitutive relations for granular materials, with application to plane shearing. J. Fluid Mech. 176, 67–93.
- Johnsson, F., Zijerveld, R.C., Schouten, J.C., van den Bleek, C.M., Leckner, B., 2000. Characterization of fluidization regimes by time-series analysis of pressure fluctuations. Int. J. Multiphas. Flow 26, 663–715.

- Kim, S.W., Kirbas, G., Bi, H., Lim, C.J., Grace, J.R., 2004. Flow behavior and regime transition in a high-density circulating fluidized bed riser. Chem. Eng. Sci. 59, 3955–3963.
- Kim, J.S., Tachino, R., Tsutsumi, A., 2008. Effects of solids feeder and riser exit configuration on establishing high density circulating fluidized beds. Powder Technol. 187, 37–45.
- Kunii, D., Levenspiel, O., 1991. Fluidization Engineering. Butterworth-Heinemann, Boston.
- Li, Z.Q., Wu, C.N., Wei, F., Jin, Y., 2004. Experimental study of high-density gas-solids flow in a new coupled circulating fluidized bed. Powder Technol. 139, 214–220.
- Li, L., Zhao, N., Wei, W., Sun, Y., 2011. A review of research progress on CO₂ capture, storage, and utilization in Chinese Academy of Sciences. Fuel, Accepted Manuscript
- Lim, K.S., Zhu, J.X., Grace, J.R., 1995. Hydrodynamics of gas-solid fluidization. Int. J. Multiphas. Flow 21, 141–193.
- Llauró, F.X., Llop, M.F., 2006. Characterization and classification of fluidization regimes by non-linear analysis of pressure fluctuations. Int. J. Multiphas. Flow 32, 1397–1404.
- Makkawi, Y.T., Wright, P.C., 2002. Fluidization regimes in a conventional fluidized bed characterized by means of electrical capacitance tomography. Chem. Eng. Sci. 57, 2411–2437.
- Malvern Instruments Ltd., 2013. Mastersizer 2000. Resource Center.
- Manyele, S.V., Pärssinen, J.H., Zhu, J.X., 2002. Characterizing particle aggregates in a high-density and high-flux CFB riser. Chem. Eng. J. 88, 151–161.
- Manyele, S.V., Zhu, J.X., Khayat, R.E., Pärssinen, J.H., 2006. Analysis of the chaotic dynamics of a high-flux CFB riser using solids concentration measurements. China Particuol. 4, 136–146.
- Masuda, H., Higashitani, K., Yoshida, H., 2006. Powder Technology: Handling and Operations, Process Instrumentation, and Working Hazards. CRC Press, Boca Raton.
- Mei, J., Shadle, L.J., Yue, P.C., Monazam, E.R., 2007. Flow regime study in a high density circulating fluidized bed riser with an abrupt exit. ECI Conference on the 12th International Conference on Fluidization-New Horizons in Fluidization Engineering, Vancouver, Canada.
- Qi, M., Zhu, J., Barghi, S., 2012a. Particle velocity and flux distribution in a high solids concentration circulating turbulent fluidized bed. Chem. Eng. Sci. 84, 437–448.

- Qi, M., Barghi, S., Zhu, J., 2012b. Detailed hydrodynamics of high flux gas-solid flow in a circulating turbulent fluidized bed. Chem. Eng. J. 209, 633–644.
- Rabinovich, E., Kalman, H., 2011. Flow regime diagram for vertical pneumatic conveying and fluidized bed systems. Powder Technol. 207, 119–133.
- Rhodes, M., 2008. Introduction to Particle Technology. John Wiley & Sons Ltd., West
- Rhodes, M.J., Sollaart, M., Wang, X.S., 1998. Flow structure in a fast fluid bed. Powder Technol. 99, 194–200.
- Salvaterra, A., Geldart, D., Ocone, R., 2005. Solid flux in a circulating fluidized bed riser. Chem. Eng. Res. Des. 83, 24–29.
- Tamadondar, M.R., Azizpour, H., Zarghami, R., Mostoufi, N., Chaouki, J., 2012. Using particle trajectory for determining the fluidization regime in gas–solid fluidized beds. Adv. Powder Technol. 23, 349–351.
- Tatemoto, Y., Yano, S., Mawatari, Y., Noda, K., Komatsu, N., 2007. Drying characteristics of porous material immersed in a bed of glass beads fluidized by superheated steam under reduced pressure. Chem. Eng. Sci. 62, 471–480.
- Wang, C., Zhu, J., Barghi, S., Li, C., 2014. Axial and radial development of solids holdup in a high flux/density gas-solids circulating fluidized bed. Chem. Eng. Sci. 108, 233–243.
- Wei, F., Lin, H., Cheng, Y., Wang, Z., Jin, Y., 1998. Profiles of particle velocity and solids fraction in a high-density riser. Powder Technol. 100, 183–189.
- Yang, W.C., 2003. Handbook of Fluidization and Fluid-Particle Systems. Marcel Dekker Inc., New York.
- You, C., Li, Y., 2013. Population balance for CFB-FGD systems. Powder Technol. 235, 859–865.
- Zhu, J., 2010. Circulating turbulent fluidization a new fluidization regime or just a transitional phenomenon. Particuology 8, 640–644.
- Transitional phenomenon. Particuology 8, 640–644.

 Zhu, H., Zhu, J., 2008. Comparative study of flow structures in a circulating-turbulent fluidized bed. Chem. Eng. Sci. 63, 2920–2927.
- Zhu, X., Yang, C., Li, C., Liu, Y., Wang, L., Li, T., Geng, Q., 2013. Comparative study of gas-solids flow patterns inside novel multi-regime riser and conventional riser. Chem. Eng. J. 215–216, 188–201.
- Zijerveld, R.C., Johnsson, F., Marzocchella, A., Schouten, J.C., van den Bleek, C.M., 1998. Fluidization regimes and transitions from fixed bed to dilute transport flow. Powder Technol. 95, 185–204.

This article was downloaded by: [1.10.206.41]

On: 13 November 2014, At: 04:21

Publisher: Taylor & Francis

Informa Ltd Registered in England and Wales Registered Number: 1072954 Registered office: Mortimer House,

37-41 Mortimer Street, London W1T 3JH, UK



Chemical Engineering Communications

Publication details, including instructions for authors and subscription information: http://www.tandfonline.com/loi/gcec20

Effect of Regeneration Temperature on the Composition and Carbon Dioxide Sorption Ability of a K₂CO₃/Al₂O₃ Solid Sorbent in a Bubbling Fluidized Bed Reactor

Or-Ampai Jaiboon $^{\rm a}$, Benjapon Chalermsinsuwan $^{\rm a\ b}$, Lursuang Mekasut $^{\rm a\ b}$ & Pornpote Piumsomboon $^{\rm a\ b}$

Accepted author version posted online: 12 May 2014. Published online: 01 Oct 2014.

To cite this article: Or-Ampai Jaiboon , Benjapon Chalermsinsuwan , Lursuang Mekasut & Pornpote Piumsomboon (2015) Effect of Regeneration Temperature on the Composition and Carbon Dioxide Sorption Ability of a K_2CO_3/AI_2O_3 Solid Sorbent in a Bubbling Fluidized Bed Reactor, Chemical Engineering Communications, 202:3, 361-365, DOI: 10.1080/00986445.2013.838163

To link to this article: http://dx.doi.org/10.1080/00986445.2013.838163

PLEASE SCROLL DOWN FOR ARTICLE

Taylor & Francis makes every effort to ensure the accuracy of all the information (the "Content") contained in the publications on our platform. However, Taylor & Francis, our agents, and our licensors make no representations or warranties whatsoever as to the accuracy, completeness, or suitability for any purpose of the Content. Any opinions and views expressed in this publication are the opinions and views of the authors, and are not the views of or endorsed by Taylor & Francis. The accuracy of the Content should not be relied upon and should be independently verified with primary sources of information. Taylor and Francis shall not be liable for any losses, actions, claims, proceedings, demands, costs, expenses, damages, and other liabilities whatsoever or howsoever caused arising directly or indirectly in connection with, in relation to or arising out of the use of the Content.

This article may be used for research, teaching, and private study purposes. Any substantial or systematic reproduction, redistribution, reselling, loan, sub-licensing, systematic supply, or distribution in any form to anyone is expressly forbidden. Terms & Conditions of access and use can be found at http://www.tandfonline.com/page/terms-and-conditions

^a Fuels Research Center, Department of Chemical Technology, Faculty of Science , Chulalongkorn University , Bangkok , Thailand

^b Center of Excellence on Petrochemical and Material Technology , Chulalongkorn University , Bangkok , Thailand

DOI: 10.1080/00986445.2013.838163



Effect of Regeneration Temperature on the Composition and Carbon Dioxide Sorption Ability of a K₂CO₃/Al₂O₃ Solid Sorbent in a Bubbling Fluidized Bed Reactor

OR-AMPAI JAIBOON¹, BENJAPON CHALERMSINSUWAN^{1,2}, LURSUANG MEKASUT^{1,2}, and PORNPOTE PIUMSOMBOON^{1,2}

¹Fuels Research Center, Department of Chemical Technology, Faculty of Science, Chulalongkorn University, Bangkok, Thailand ²Center of Excellence on Petrochemical and Material Technology, Chulalongkorn University, Bangkok, Thailand

The effect of the regeneration temperature (150°, 250°, and 350°C) during multiple CO₂ cyclic sorption-regeneration cycles of a K₂CO₃/Al₂O₃ solid sorbent in a bubbling fluidized bed reactor was evaluated in terms of the CO₂ capture capacity and chemical composition of the solid sorbent. The CO₂ capture capacity after regeneration at 150° and 250°C decreased with increasing cycle numbers, reaching approximately 57 and 78%, respectively, and 19.0 and 39.3%, respectively, of the original capacity after one and five regeneration cycles. This decline in the CO₂ capture capacity was due to the accumulation of KHCO₃ (at 150°C) and KAI (CO₃)₂(OH)₂ (150° and 250°C) from their incomplete degradation back to the K₂CO₃/Al₂O₃ solid sorbent. When regenerated at 350°C, the CO₂ capture capacity remained essentially constant in each cycle number because of complete desorption (no residual KHCO₃ and KAl(CO₃)₂(OH)₂). The formation mechanism of complex structure occurred similar to the one in a fixed bed reactor/thermogravimetric analyzer with lower regeneration temperature. The general operation conditions for K₂CO₃/Al₂O₃ solid sorbents are summarized.

Keywords: Adsorption; CO₂ capture; Fluidized bed; Regeneration; Solid sorbent; Sorption

Introduction

Nowadays, carbon dioxide (CO₂) is the principal gas released into the atmosphere from the use of fossil fuels, such as for electricity generation (Huang and Shen, 2013). With the increasing rate of use of fossil fuels compounded by the reduced rate of photosynthetic fixation of CO₂ (largely due to mass deforestation), this net increase in the global CO2 level plays an important role in the global warming problem. Reduction in CO₂ emission levels is, therefore, a major global concern in preventing deleterious or adverse world climate changes. To reduce CO₂ emission levels, CO₂ capture options have become of interest.

For the flue gas from fossil fuel-burning power plants, various methods to capture its CO₂ have been investigated, such as chemical-looping, membrane separation, cryogenic separation, and others. Chemical sorption with dry alkali metal-based solid sorbents inside a chemical-looping system is one promising technology for CO₂ capture (Adanez et al., 2012). This is because dry solid sorbents have several advantages over other methods, such as ease of material handling and safety for the

Address correspondence to Pornpote Piumsomboon, Fuels Research Center, Department of Chemical Technology, Faculty of Science, Chulalongkorn University, 254 Phayathai Road, Patumwan, Bangkok 10330, Thailand. E-mail: pornpote.p@ chula.ac.th

local environment (Liang and Harrison, 2004). CO₂ has been shown to be effectively adsorbed on alkaline carbonate solid sorbents (Hayashi et al., 1998; Liang and Harrison, 2004). However, in contrast to aqueous NaOH, the rate of reaction between CO₂ and Na₂CO₃ is too slow to be effective (commercially viable). Among various dry alkaline carbonates, K₂CO₃ has been found to provide the best results for the sorption of CO₂ over a suitable temperature range (Lee and Kim, 2007; Lee et al., 2006a, 2006b, 2008; Xiao et al., 2011). The principal (important) chemical reaction involved in reversible CO_2 capture/release with a K_2CO_3 solid sorbent is:

$$K_2CO_3 + CO_2 + H_2O \longleftrightarrow 2KHCO_3 + heat$$
 (1)

where sorption (left to right) proceeds at low temperatures and regeneration (right to left) proceeds at high temperatures.

Most research has focused on the improvement of the sorption performance of dry K₂CO₃-based sorbents by modifying the solid sorbent. Lee and Kim (2007) improved alkalinebased solid sorbent characteristics by pretreatment with water, which enhanced the CO₂ capture capacity in a fixed bed reactor. The effect of supporting materials, such as activated carbon, Al₂O₃, CaO, TiO₂, MgO, NaX, SiO₂, and zeolites, on the sorption characteristic was extensively explored by thermogravimetric analysis (TGA) and in fixed and (batch or bubbling) fluidized bed reactors (FBRs) (Lee and Kim, 2007; Lee at al., 2004, 2006a, 2006b, 2008, 2009). The use of 362 O.-A. Jaiboon et al.

Table I. Summary of literature studies on regeneration and multi-cycle performance of K₂CO₃-basedsolid sorbents

Reference	Reactor	New findings
Lee et al., 2006a Lee and Kim, 2007	Fixed-bed reactor Fixed-bed reactor	The K ₂ CO ₃ /TiO ₂ and K ₂ CO ₃ /Al ₂ O ₃ sorbents showed excellent multi-cycle sorption/regeneration performance at regeneration temperatures of 150° and 400°C, respectively.
		The formation of stable complex crystal structure was the explanation for the poor regeneration characteristic at low temperature.
Lee et al., 2009	Fixed-bed reactor	A new alumina-modified potassium-based sorbent (K ₂ CO ₃ /ZrO ₂) was
Lee et al., 2011	Thermogravimetric analyzer/fixed-bed reactor	developed for CO ₂ capture with regeneration temperature at 130°C.
Zhao et al., 2012a	Thermogravimetric analyzer	The effects of operation conditions, including the regeneration temperature, gas composition, and heating rate on the regeneration process of K_2CO_3/A_1O_3 were studied.
Lee et al., 2014	Fixed-bed reactor	The K ₂ CO ₃ /ZrO ₂ sorbent showed high thermal stability for multi-cycle sorption/regeneration CO ₂ capture regardless of calcination temperature.

K₂CO₃ supported on Al₂O₃ (K₂CO₃/Al₂O₃) was reported to offer the best potential for use in a large-scale operation unit (Lee et al., 2006a, 2008; Xiao et al., 2011; Zhao et al., 2012a). In addition, the effects of the sorption temperature, CO₂ concentration, and H₂O concentration on the system efficiency were explored (Zhao et al., 2010, 2012b). However, evaluation of the regeneration and multi-cycle performance of K₂CO₃based solid sorbents is limited, as summarized in Table I. Lee et al. (2006a), Lee and Kim (2007), and Zhao et al. (2012a) found that the CO₂ capture capacity of K₂CO₃ with various supporting materials (MgO and Al₂O₃) was decreased at regeneration temperatures lower than 200°C. Although a durable solid sorbent that could be regenerated at below 200°C was reported (Lee et al., 2009, 2011, 2014), this has the drawback of high manufacturing cost. Although the effect of gas composition on the regeneration process was found to not be significant (Zhao et al., 2012a), the operation in a continuous fluidization regime has not been extensively explored (Jaiboon et al., 2013). The previous studies were mainly performed in fixed bed reactor/TGAs.

This study evaluated the effect of the regeneration temperature on a K_2CO_3/Al_2O_3 solid sorbent for cyclic CO_2 sorption-regeneration in a bubbling FBR. The CO_2 capture capacity of the sorbent was evaluated at three different regeneration temperatures (150°, 250°, and 350°C) in a multiple continuous sorbent-regeneration cycle system. The continuous system will have an advantage over the batch system for industrial-scale applications. The explanation for the obtained CO_2 capture capacity was clarified using temperature programmed desorption (TPD) and X-ray diffraction (XRD) analysis. Then, the results were extrapolated to the general operation conditions for the use of a K_2CO_3/Al_2O_3 solid sorbent in other continuous fluidization regimes.

Materials and Experimental Methods

Preparation of K₂CO₃IAl₂O₃ Solid Sorbents

The potassium-based solid sorbents used in this study were prepared by the conventional impregnation of K_2CO_3 onto a γ -Al₂O₃ porous support. First, 5 g of γ -Al₂O₃ were added

to an aqueous solution containing 5 g of anhydrous K_2CO_3 in 25 mL of deionized water and mixed using a solution shaker at room temperature for 24 h. After mixing, the mixture was dried in a vacuum oven at 105° C. The dried samples were ground and sieved to select solid sorbent particles in the size range of $75-150\,\mu m$. Then, the samples were calcined in a furnace for 4 h at 300° C with a heating (ramp) rate of 3° C/min. The amount of alkaline metal impregnated on the γ -Al₂O₃ support was determined by atomic absorption spectrometry using a Shimadzu AA 6800 instrument, while the surface area was determined by Brunauer-Emmett-Teller (BET) analysis using the ASAP 2020 surface area analyzer. The properties of the as-prepared K_2CO_3/γ -Al₂O₃ solid sorbent are presented in Table II.

Experimental Apparatus and Procedure

A cylindrical glass FBR of 25 cm internal diameter and 0.80 m height was used, into which 60 g of the K_2CO_3/γ - Al_2O_3 solid sorbent was placed with a bottom gas inlet velocity of 0.20 m/s. At this gas inlet velocity, the reactor system operated in the bubbling fluidization regime (Jaiboon et al., 2013). The reactor was heated and cooled by heating tape. For cyclic CO_2 sorption-regeneration, a constant sorption temperature of 60° C was used for 60 min, while three different regeneration temperatures (150°, 250°, and 350°C) were employed for 60 min. After regeneration with 99.999 vol.% N_2 , the regenerated solid sorbent was adsorbed under a crudely simulated flue gas of 12% (v/v, dry basis) CO_2 with 18.4% H_2O using a bubbler for a new sorption cycle for 60 min. The K_2CO_3/Al_2O_3 solid sorbents readsorbed CO_2

Table II. Properties of the K₂CO₃/Al₂O₃ solid sorbent

Solid sorbent property	Value
BET surface area (m ² /g)	80.92
Actual weight of K ₂ CO ₃ impregnated	35
on Al_2O_3 (wt.%)	
Diameter (μm)	75–150
Density (kg/m^3)	3,900

Table III. Experimental conditions for CO_2 adsorption and regeneration of the K_2CO_3/Al_2O_3 solid sorbent

Operating condition	Sorption	Regeneration
Temperature (°C)	60	150, 250, and 300
Pressure (atm) Gas inlet velocity (m/s) Solid sorbent loading (g) Gas composition (vol.%)	1 0.20 60 CO ₂ : 12 dry basis with H ₂ O: 18.4, N ₂ : balance	1 0.20 60 N ₂ : 99.999

for a total of five cycles. Table III summarizes the experimental conditions for the sorption and regeneration of the K_2CO_3/Al_2O_3 solid sorbent.

The CO_2 capture capacity of the K_2CO_3/Al_2O_3 sorbent was computed by integration of the area under the breakthrough curves of the weight of CO₂ adsorbed by K₂CO₃ and time. This parameter implies the amount of CO₂ (mg) adsorbed per 1 kg of K₂CO₃ in the saturated solid sorbent. The solid sorbent was characterized for its crystalline structure (composition) using XRD (Rigaku XRD system equipped with a RINT 2000 wide-angle goniometer employing $CU_{K\alpha}$ radiation ($\lambda = 1.54 \,\text{Å}$) and an X-ray power of 40 kV/30 mA). In addition, TPD analysis was used to investigate the desorption temperature of the K₂CO₃/Al₂O₃ solid sorbent. The K₂CO₃/Al₂O₃ solid sorbents were conditioned in a U-shaped quartz reactor under an Ar flow rate of 40 cm³/min at 60°C for 1 h. After pretreatment, the K₂CO₃/ Al₂O₃ solid sorbents were cooled to room temperature, argon was introduced at a flow rate of 40 cm³/min, and the solid sorbent was heated to 500°C at a constant rate of 10°C/min. A thermal conductivity detector (TCD) was employed to determine the amount of desorbed CO_2 .

Results and Discussion

Figure 1 illustrates the CO_2 capture capacity over five sorption-regeneration cycles at the three different regeneration temperatures. When regenerated at 150° and 250° C

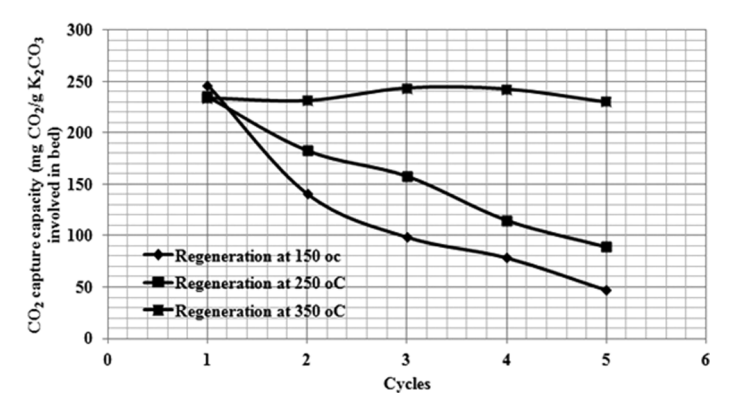


Fig. 1. Multi-cycle CO₂ capture capacity of K₂CO₃/Al₂O₃ solid sorbent over five sorption-regeneration cycles with regeneration at 150°, 250°, and 350°C.

the CO₂ capture capacity decreased significantly with increasing regeneration cycle numbers, falling to approximately 57% and 78%, respectively, of the initial level after one cycle and then declining steadily thereafter to approximately 19% and 39%, respectively, after five regeneration cycles. The implication is that the K₂CO₃/Al₂O₃ solid sorbent was not completely regenerated at 150° or 250°C. However, with regeneration at 350°C the CO₂ capture capacity was essentially the same over all five cycles assayed, suggesting that the spent K₂CO₃/Al₂O₃ solid sorbent can be entirely regenerated at 350°C. This regeneration temperature in the continuous condition was lower than the one in batch condition (Lee et al., 2006a; Lee and Kim, 2007). The high contacting surface area/system mixing in the bubbling fluidization regime is the explanation for the observed phenomenon.

In order to confirm the degree of regeneration of the K₂CO₃/Al₂O₃ solid sorbent at the different regeneration temperatures, the used K₂CO₃/Al₂O₃ solid sorbent was subject to TPD analysis after regeneration (Figure 2). When regenerated at 150°C, two extra peaks other than those for K₂CO₃ were observed, which correspond to KHCO₃ at 120°C and KAl(CO₃)₂(OH)₂ at 300°C (see XRD analysis below for support). The CO₂ capture capacity of the K₂CO₃/Al₂O₃ solid sorbent after regeneration at 150°C is then likely to have decreased due to the incomplete degradation of the formed KHCO3 and KAl(CO3)2(OH)2 to K₂CO₃/Al₂O₃. For the regeneration at 250°C, only the extra peak of KAl(CO₃)₂(OH)₂ was found (at 300°C), which implies the complete degradation of KHCO₃ but that the capture capacity had decreased because of the incomplete degeneration of KAl(CO₃)₂(OH)₂, which instead accumulated to a higher amount. However, with regeneration at 350°C no extra peaks were observed, suggesting the complete regeneration of the K₂CO₃/Al₂O₃ solid sorbent. The formation mechanism of complex structure occurred similar to the one in a fixed bed reactor/TGA with lower regeneration temperature (Lee and Kim, 2007).

To confirm the TPD results, XRD analysis of the regenerated K₂CO₃/Al₂O₃ solid sorbents after regeneration was undertaken. The XRD patterns of the fresh and solid sorbents regenerated at 150°, 250°, or 350°C in N₂ are shown in

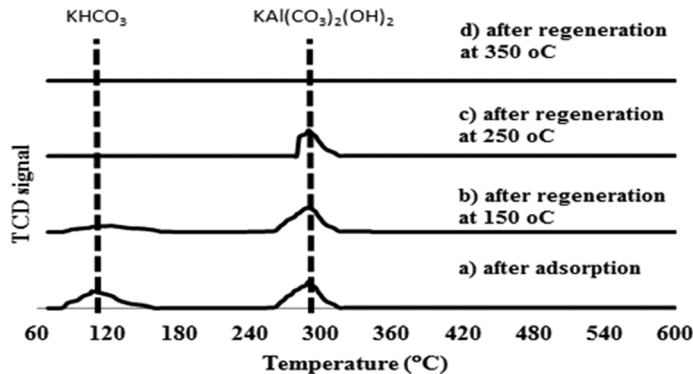


Fig. 2. TPD results of the K_2CO_3/Al_2O_3 solid sorbent directly after (a) sorption and (b)–(d) regeneration at (b) 150°C, (c) 250°C, and (d) 350°C.

364 O.-A. Jaiboon et al.

Figure 3. The XRD analysis of the fresh sorbent showed two structure phases, K₂CO₃ and KAl(CO₃)₂(OH)₂. The KAl (CO₃)₂(OH)₂ was formed by the reaction of the Al₂O₃ support with K₂CO₃ during calcination at 300°C (Lee et al., 2006a, 2006b). After the solid sorbent was used, the XRD patterns changed to show the structure phase of KHCO₃, along with the increasing $KAl(CO_3)_2(OH)_2$ peak intensity as a result of its higher concentration. For the solid sorbent after regeneration at 150°C, these three structures were still observed. Thus, after regeneration at 150°C the CO₂ capture capacity of the solid sorbent decreased due to the reduced amount of available K₂CO₃ following the incomplete conversion of $KAl(CO_3)_2(OH)_2$ and $KHCO_3$ back to K_2CO_3 . For the solid sorbent after regeneration at 250°C, the KHCO₃ phase was absent, supporting its regeneration back to K₂CO₃, but the CO2 capture capacity was still decreased (albeit at a lower magnitude than at 150°C) because of the thermal stability of KAl(CO₃)₂(OH)₂ at this temperature. When regenerated at 350°C the KAl(CO₃)₂(OH)₂ phase as well as the KHCO₃ was absent and the K₂CO₃ peaks were larger, consistent with the complete regeneration of K₂CO₃. These results are consistent with the TPD results mentioned earlier.

Thus, a regeneration temperature of 350°C is preferred in the CO₂ sorption-regeneration cycles with a K₂CO₃/Al₂O₃ solid sorbent for bubbling fluidization regime or continuous system. In previous studies, the CO₂ caption-regeneration system was performed by TGA or fixed bed reactor. Therefore, higher regeneration temperature was required for complete recovery of solid sorbent in those systems. To apply this concept in all remaining fluidization regimes or in a chemical-looping system, a high regeneration temperature would be required to prevent solid sorbent deactivation, although those systems have a lower residence time (Jaiboon et al., 2013). Otherwise, costly preparation to modify the solid sorbent to be able to perform regeneration at a low temperature would be required (Lee et al., 2009, 2011, 2014). However, the decreased operating cost for a low regeneration temperature solid sorbent is replaced by the increased material preparation cost compared to that for a high regeneration temperature solid sorbent (Lee et al., 2011).

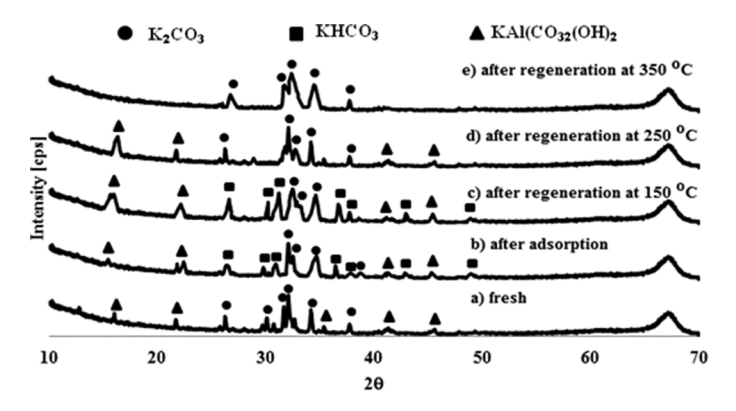


Fig. 3. XRD patterns of the K_2CO_3/Al_2O_3 solid sorbent for (a) fresh and (b) after sorption, plus (c)–(e) after regeneration at (c) 150°C, (d) 250°C, and (e) 350°C.

Conclusion

For the K₂CO₃/Al₂O₃ solid sorbent, the CO₂ capture capacity decreased with increasing cycle numbers when regenerated at 150°C or 250°C due to the failure to degrade KHCO₃ (150°C) and KAl(CO₃)₂(OH)₂ (150° and 250°C) back to K₂CO₃. In contrast, when regenerated at 350°C the CO₂ capture capacity did not decline during at least five sorption-regeneration cycles due to the complete desorption of both KHCO₃ and KAl(CO₃)₂(OH)₂. The formation mechanism of complex structure occurred similar to the one in a fixed bed reactor/TGA with lower regeneration temperature. Therefore, in order to use the K₂CO₃/Al₂O₃ solid sorbent repeatedly, the solid sorbent should be regenerated at 350°C for all fluidization regimes. Otherwise, a method for modifying the solid sorbent with a low regeneration temperature will be required.

Funding

The authors are grateful to the Grants from the National Research University Project, Office of Higher Education Commission (WCU-044-CC-57), the Thailand Research Fund for fiscal year 2014–2016 (TRG5780205), the NRCT, the EPPO of Ministry of Energy (Thailand) and the PET-ROMAT for their financial support.

Nomenclature

- λ wavelength of the incident X-ray beam (Å)
- θ angle of incident X-ray beam (°)

References

Adanez, J., Abad, A., Garcia-Labiano, F., Gayan, P., and de Diego, L. F. (2012). Progress in chemical-looping combustion and reforming technologies, *Prog. Energy Combust.*, 38, 215–282.

Hayashi, H., Taniuchi, J., Furuyashiki, N., Sugiyama, S., Hirano, S., Shigemoto, N., and Nonaka, T. (1998). Efficient recovery of carbon dioxide from flue gases of coal-fired power plants by cyclic fixed-bed operations over K₂CO₃-on-carbon, *Ind. Eng. Chem. Res.*, 37, 185–191.

Huang, C. C., and Shen, S.-C. (2013). Adsorption of CO₂ on chitosan modified CMK-3 at ambient temperature, J. Taiwan Inst. Chem. Eng., 44, 89–94.

Jaiboon, O. A., Chalermsinsuwan, B., Mekasut, L., and Piumsomboon, P. (2013). Effect of flow patterns/regimes on CO₂ capture using K₂CO₃ solid sorbent in fluidized bed/circulating fluidized bed, *Chem. Eng. J.*, 219, 262–272.

Lee, S. C., Chae, H. J., Lee, S. J., Choi, B. Y., Yi, C. K., Lee, J. B., Ryu, C. K., and Kim, J. C. (2008). Development of regenerable MgO-based sorbent promoted with K₂CO₃ for CO₂ capture at low temperatures, *Environ. Sci. Technol.*, 42, 2736–2741.

Lee, S. C., Chae, H. J., Lee, S. J., Park, Y. H., Ryu, C. K., and Yi, C. K. (2009). Novel regenerable potassium-based dry sorbents for CO₂ capture at low temperatures, *J. Mol. Catal. B: Enzym.*, **56**(2–3), 179–184.

Lee, S. C., Choi, B. Y., Lee, S. J., Jung, S. Y., Ryu, C. K., and Kim, J. C. (2004). CO₂ absorption and regeneration using Na and K based sorbents, Stud. Surf. Sci. Catal. Today, 153, 527–530.

Lee, S. C., Choi, B. Y., Lee, T. J., Ryu, C. K., Soo, Y. S., and Kim, J. C. (2006a). CO₂ absorption and regeneration of alkali metal-based solid sorbents, *Catal. Today*, 111, 385–390.

Lee, S. C., Choi, B. Y., Ryu, C. K., Ahn, Y. S., Lee, T. J., and Kim, J. C. (2006b). The effect of water on the activation and the CO₂ captive

- capacities of alkali metal-based sorbents, *Korean J. Chem. Eng.*, 23, 374–379.
- Lee, S. C., and Kim, J. C. (2007). Dry potassium-based sorbents for CO₂ capture, *Catal. Surveys Asia*, 11, 171–185.
- Lee, S. C., Kwon, Y. M., Jung, S. Y., Lee, J. B., Ryu, C. K., and Kim, J. C. (2014). Excellent thermal stability of potassium-based sorbent using ZrO₂ for post combustion CO₂ capture, *Fuel*, **115**, 97–100.
- Lee, S. C., Kwon, Y. M., Ryu, C. Y., Chae, H. J., Ragupathy, D., Jung, S. Y., Lee, J. B., Ryu, C. K., and Kim, J. C. (2011). Development of new alumina-modified sorbents for CO₂ sorption and regeneration at temperatures below 200°C, Fuel, 90, 1465–1470.
- Liang, Y., and Harrison, D. P. (2004). Carbon dioxide capture using dry sodium-based sorbents, *Energy Fuels*, **18**, 569–575.

- Xiao, G., Singh, R., Chaffee, A., and Webley, P. (2011). Advanced adsorbents based on MgO and K₂CO₃ for capture of CO₂ at elevated temperatures, *Int. J. Greenhouse Gas Control*, **5**, 634–639.
- Zhao, C., Chen, X., and Zhao, C. (2010). Multiple-cycles behavior of K₂CO₃/Al₂O₃ for CO₂ capture in a fluidized-bed reactor, *Energy Fuels*, **24**, 1009–1012.
- Zhao, C., Chen, X., and Zhao, C. (2012a). K₂CO₃/Al₂O₃ for capturing CO₂ in flue gas from power plants. Part 2: Regeneration behaviors of K₂CO₃/Al₂O₃, *Energy Fuels*, **26**, 1406–1411.
- Zhao, C., Chen, X., Zhao, C., Wu, Y., and Wei, D. (2012b). K₂CO₃/Al₂O₃ for capturing CO₂ in flue gas from power plants. Part 3: CO₂ capture behaviors of K₂CO₃/Al₂O₃ in a bubbling fluidized-bed reactor, *Energy Fuels*, **26**, 3062–3068.

Thermogravimetric Analysis and Chemical Kinetic for Regeneration of Sodium Carbonate Solid Sorbent

Submitted: 06.01.2015

Accepted: 07.01.2015

Pilaiwan Chaiwang^{1,a}, Benjapon Chalermsinsuwan^{1,2,b}, Pornpote Piumsomboon^{1,2,c}

¹Fuels Research Center, Department of Chemical Technology, Faculty of Science, Chulalongkorn University, 254 Phayathai Road, Patumwan, Bangkok 10330, Thailand

²Center of Excellence on Petrochemical and Materials Technology, Chulalongkorn University, 254, Phayathai Road, Patumwan, Bangkok 10330, Thailand

^apilaiwan.c@student.chula.ac.th, ^bbenjapon.c@chula.ac.th, ^cpornpote.p@chula.ac.th

Keywords: Chemical kinetic, Thermogravimetric analysis, Decomposition, Regeneration, Sodium Carbonate

Abstract. In this study, non-isothermal kinetic methods for the decomposition of the adsorbed CO_2 on pure sodium hydrogen carbonate (NaHCO₃) were investigated by a thermogravimetric analysis (TG) and differential thermogravimetry (DTG). Four different heating rates were measured to calculate the order of reaction (n), the pre-exponential factor (A) and activation energy (E_a) using three different models: Kissinger-Akahira-Sunose Method (KAS), Flynn-Wall-Ozawa (FWO) and analytical method. The results showed that KAS and FWO methods gave similar values due to the approximation of employed equation whereas the analytical method gave different values. The obtained parameters from those three methods then were used to calculate the chemical reaction conversion versus temperature and their R^2 . The results showed that analytical method provided the most accurate results comparing with KAS and FWO methods.

Introduction

Nowadays, the major greenhouse gas which causes large effects to the atmosphere is carbon dioxide (CO₂). The emission and reduction processes of CO₂ by primary production can naturally occur [1]. Since the industrial revolution, the CO₂ emission is dramatically increasing due to human activities such as coal and fossil fuel combustions, power generation and transportation. The ratio of world total energy production was enlarging according to population growth [2]. Many research studies have been performed to find the methods for capturing CO₂ whether physical, chemical or biological [3,4]. A dry alkali-metal solid sorbent is an effective method in term of cost and energy consumption [5-8]. However, the kinetic for regeneration of solid sorbents is still lacking in the literature. The regeneration reaction scheme is considered as an irreversible first-order of thermal decomposition. This assumption works well with the solid state compound. For the rate constant, it depends on the temperature providing by the Arrhenius equation.

In this study, non-isothermal kinetic methods of the decomposition of the adsorbed CO_2 on pure sodium hydrogen carbonate (NaHCO₃) were investigated by the thermogravimetric analysis (TG). Three different models, which were Kissinger-Akahira-Sunose Method (KAS), Flynn-Wall-Ozawa (FWO) and analytical methods, were used to calculate the order of reaction (n), the pre-exponential factor (A) and activation energy (E_a).

Kinetic Study: Theory. The expression of the rate law for non-isothermal decomposition criteria can be clarified from the single-step kinetic equation of solid state decomposition:

$$\frac{d\alpha}{dt} = k(T)f(\alpha) \tag{1}$$

where $f(\alpha)$ is the reaction model of the conversion mechanism expressing on the dependence of the reaction rate which can take in the various forms. The temperature-dependence of the rate constant can provide in term of k(T) with the Arrhenius equation,

$$\frac{d\alpha}{dt} = k(T)f(\alpha) = A \exp\left(\frac{-E_a}{RT}\right)f(\alpha) \tag{2}$$

For the non-isothermal conversion, the heating rate of sample is constant. The $d\alpha/dt$ term in Eq. 2 is converted into β ($d\alpha/dT$), where β is the heating rate,

$$\frac{d\alpha}{dT} = \frac{k(T)}{\beta} f(\alpha) = \frac{A}{\beta} exp\left(\frac{-E_a}{RT}\right) f(\alpha) \rightarrow g(\alpha) = \int_0^\alpha \frac{d\alpha}{f(\alpha)} = \frac{A}{\beta} \int_0^T exp\left(\frac{-E_a}{RT}\right) dT$$
 (3)

Substituted $x \cong E_a/RT$ in Eq. 3,

$$g(\alpha) = \frac{AE_a}{\beta R} \int_{-\infty}^{\infty} \frac{exp^{-x}}{x^2} dx = \frac{AE_a}{\beta R} p(x)$$
 (4)

where p(x) is the temperature integral which can not define the exact solution. However, the temperature integral can be estimated from an empirical interpolation equations presented by many literature researchers [9].

Kissinger-Akahira-Sunose (KAS) Method. This method was developed by Kissinger-Akahira-Sunose [10,11]. They used $p(x) \cong e^{-x}/x^2$, for $20 \le x \le 50$;

$$\ln \frac{\beta}{T^2} = \ln \frac{AR}{E_a g(\alpha)} - \frac{E_a}{RT} \tag{5}$$

The calculation of the order of reaction, n, using the shape index factor, S, determined by Kissinger index [10,12] which measures the absolute value of the ratio of slope of the inflecting tangent point at the left (a) and the right (b) of the TG curves.

$$n = 1.26\sqrt{a/b} \tag{6}$$

Flynn-Wall-Ozawa (FWO) Method. Flynn-Wall-Ozawa [13,14] proposed the method using Doyle's approximation [15,16] for the thermal decomposition of octamethylcyclotetrasiloxane and polytetrafluoroethylene powders. The order of reaction, n, is calculated by the same method as KAS method. They used $\log p(x) \cong -2.315 - 0.4567x$ for $20 \le x \le 60$.

$$\log \beta = \log \frac{AE_a}{g(\alpha)R} - 2.315 - 0.457 \frac{E_a}{RT}$$
 (7)

Analytical Method. This method is derived from the expression for the reaction rate of the combustion process. The relationship between the weight loss with temperature can be written in the term of the activation energy and the frequency factor. It can be calculated by the following equation, when $n \ne 1$;

$$\alpha = 1 - \left\{ 1 - \left(n - 1 \right) \left(\frac{ART^2}{\beta E_a} \right) \left(1 - \frac{2RT}{E_a} \right) \exp \left(\frac{E_a}{RT} \right) \right\}^{\frac{1}{1 - n}}$$
(8)

Experiment

Sodium hydrogen carbonate (NaHCO₃) AR grade from Ajex Finechem Pty Ltd was heated by using the Pyris Diamond Perkin Elmer thermogravimetric analyzer apparatus. The average size and density of NaHCO₃ particles is 300 µm and 2,160 kg/m³, respectively. Constant flow rate of 50

ml/min N_2 was used as an inert gas throughout the experiment in order to maintain the thermal decomposition. An approximate weight of sample to test per one experiment was 10-30 mg. All sample conditions started with initial temperature and final temperature of 40 and 600°C, respectively. Four different heating rates, 5, 10, 20 and 40 °C/min under N_2 atmosphere, were used to carry out TG and DTG data.

Results and Discussion

Thermogravimetric Analysis. As stated in the experimental section, NaHCO₃ particles were heated from 40°C to maximum temperature of 600°C. TG and DTG curves corresponding to a chemical reaction studied using four different heating rates are shown in Fig. 1. TG and DTG are the parameters which displayed in the term of a fraction of weight loss and rate of weight loss, respectively. The weight loss or TG is shown by the left-hand axis. For the chemical reaction characteristic, NaHCO₃ particles began to decompose at temperature of 100°C and terminated in the narrow range between 150°C to 250°C. This is because the pure bicarbonate particles are employed. A heating rate of 5°C provided the maximum slope of weight loss and the slope gradually decreased when increasing the heating rate. This is due to the beginning of the decomposition temperature of NaHCO₃ at 5°C and the range of decomposed is narrower than the others. The rate of fraction of weight loss or DTG is shown in the right-hand axis of Fig. 1. There observed one region peak representing the decomposition temperature for each heating rate. The TG and DTA graphs were found to be consistent because when the decomposition temperature increased, the rate of fraction of weight loss increased accordingly. At heating rate of 40°C/min, both TG and DTG gave similar trends which were sharply decomposed at the highest temperature. As can be seen from Fig. 1, when particles reached the decomposition temperature, CO₂ was released to the atmosphere which decreased a fraction of weight loss. Moreover, the increasing of heating rate shifted the highest fraction of weight loss of higher temperature due to the difference between the environment and the system temperature [17].

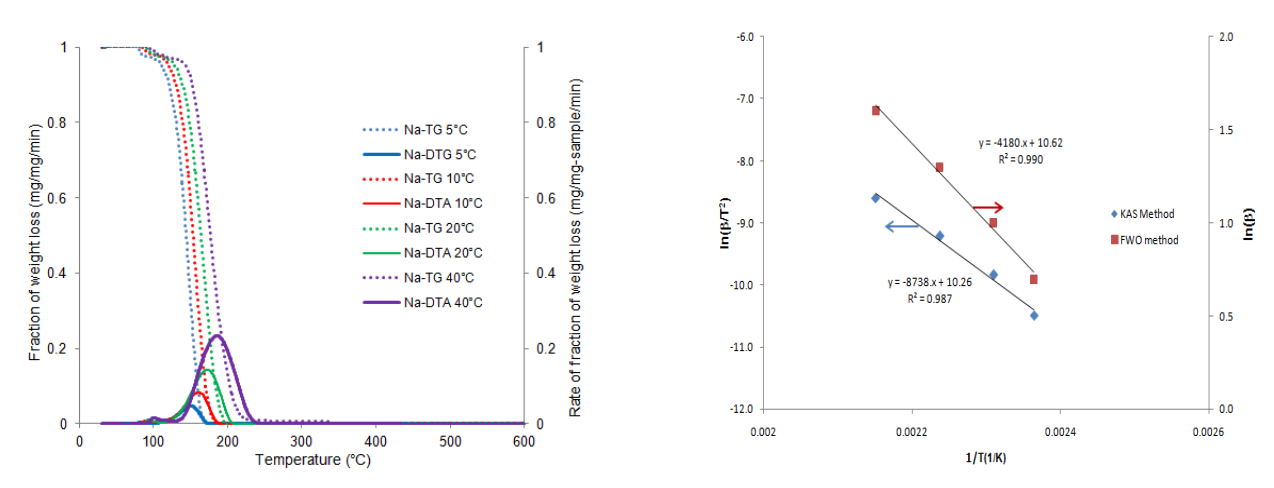


Fig. 1.TG (left) and DTG (right) curves corresponding Fig. 2. The plots of KAS method in Eq. 5 to a reaction studied using four different heating rates. and FWO method in Eq. 7.

Kinetic Parameter Analysis. The kinetic parameters were calculated from the results acquiring from thermogravimetric analysis. Four maximum weight loss peaks from Fig. 1 were measured to calculate the kinetic parameters in Eq. 3. As stated above, the order of the reaction (n) is obtained from the average ratio of both sides of the width between the slope of the DTG for each heating rate in Fig.1. The activation energy (E_a) and the pre-exponential factor (A) were determined using Kissinger-Akahira-Sunose (KAS) and Flynn-Wall-Ozawa (FWO) methods. The plot between $\ln(\beta/T^2)$ versus temperature using KAS and the plot between $\log(\beta)$ versus temperature using FWO

is displayed in Fig. 2. The linear regressions and the correlation coefficients (\mathbb{R}^2) are also shown in Fig. 2. The activation energy (E_a) and the pre-exponential factor (A) can derive from the slope and intercept of linear regression plot, respectively.

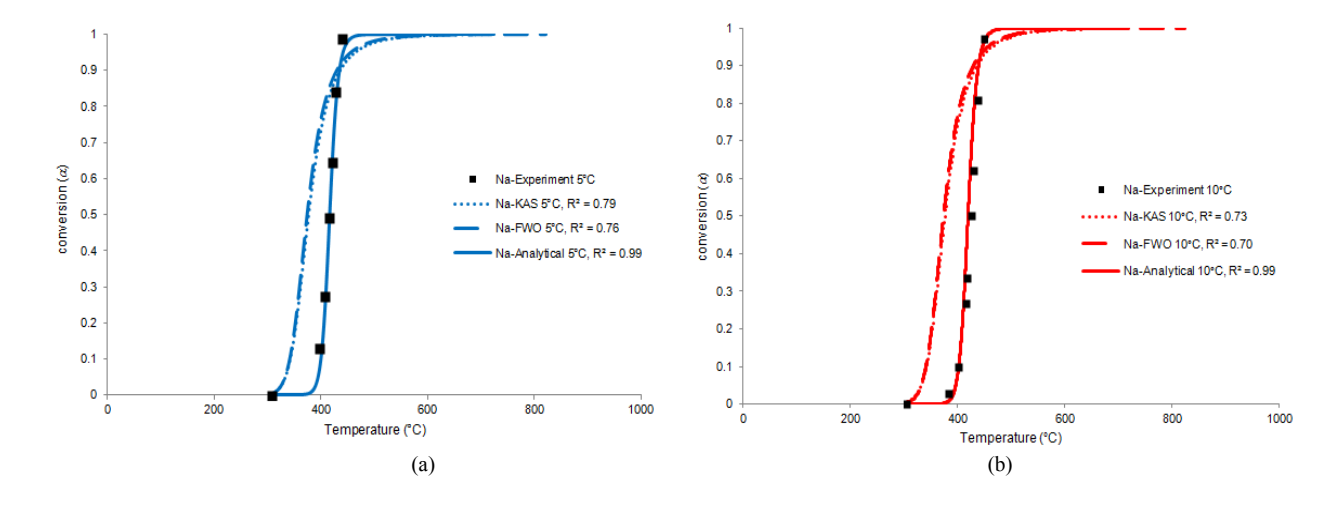
The kinetic parameters of the analytical method in Eq. 8 were determined using MATLAB. Table 1 shows the results of n, A and E_a of NaHCO₃ obtained by KAS, FWO and analytical methods. It can be seen that, the obtained n values of KAS and FWO methods were the same and A and E_a were quite similar. Due to these two methods being derived from the origin, Eq. 2, they are developed in terms of temperature integral function, p(x), which is an approximate solution. However, the computation results obtained from the analytical method was different because it is calculated directly from the single decomposition equation.

The parameters in Table 1 were substituted back in Eq. 8 which $n\neq 1$ to find the reaction conversion (α). The conversion versus temperature of KAS, FWO and analytical methods with their R^2 values are display in Fig. 3(a) to 3(d). Comparing the experiments with heating rates of 5, 10, 20 and 40°C/min, Fig. 3(a) to 3(d) presented that the results from analytical method were highly fitted to the experimental data. Their R^2 were rather than 0.95 for all heating rates. Nevertheless, the KAS and FWO method were slightly far off from the experimental data especially during the decomposition reaction. From the previous study, the intrinsic first order kinetic parameters of 125 μ m NaHCO₃ particle using TG experimental data could calculate E_a equal to 102 kJ/mol [18]. With Avrami-Erofeev equation which is one of the $f(\alpha)$, the E_a under N_2 atmosphere were in range of 90 to 119 kJ/mol [19]. The kinetic parameter from the analytical method then was consistent to the literature experimental data.

Table 1: The results of n, A and E_a of NaHCO₃ obtained by KAS, FWO and analytical methods.

Method	n	A	E_a
KAS	1.51	3.73E+08	72.65
FWO	1.51	1.40E+09	76.10
Analytical	1.94	1.38E+20	163.70

The deviation values from KAS and FWO calculation methods can be occurred by measuring of the slope from the TG curves. Besides, using Doyle's approximation which was arranged in the integral function terms, p(x), can cause the obtained values to be lower than the actual value. In addition, the analytical method was derived directly from the single decomposition equation. After this calculation, the results of n, A and E_a will be applied as kinetic parameters to simulate the chemical reaction and to use for the chemical reaction model optimization.



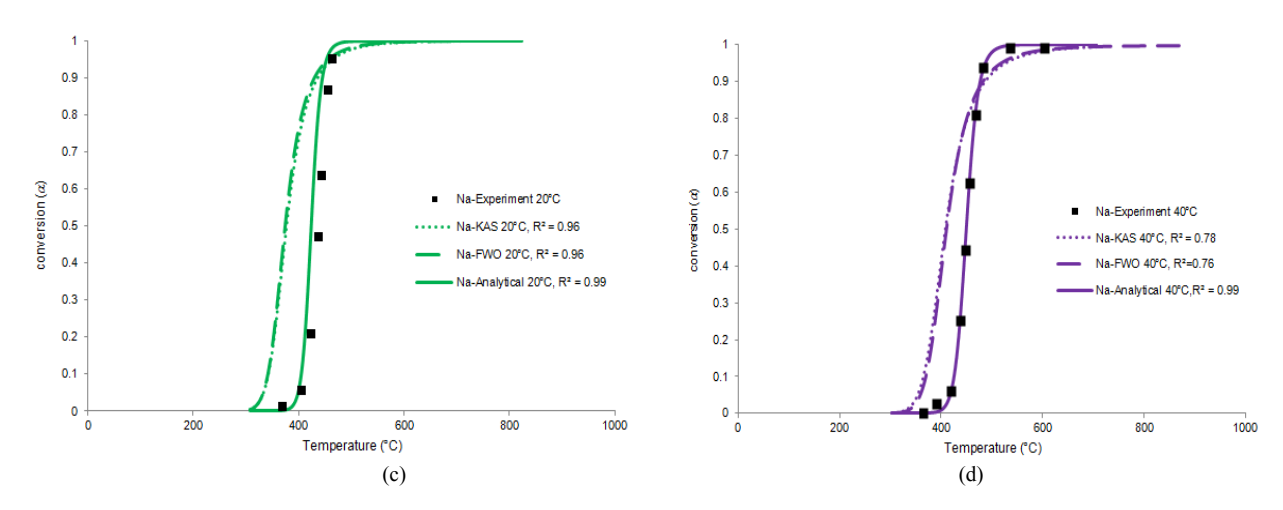


Fig. 3. The conversion versus temperature of KAS, FWO and analytical methods with R² at heating rate of (a) 5, (b) 10, (c) 20 and (d) 40°C/min comparing with the experiments.

Conclusion

In this study, non-isothermal kinetic methods of the decomposition of the adsorbed CO_2 on pure sodium hydrogen carbonate (NaHCO₃) were investigated by a thermogravimetric analysis (TG) and Differential thermogravimetry (DTG). Four different heating rates were measured to calculate the order of reaction (n), the pre-exponential factor (A) and activation energy (E_a) using three different models: Kissinger-Akahira-Sunose Method (KAS), Flynn-Wall-Ozawa (FWO) and analytical method. The results showed that analytical method provided the most accurate results comparing with KAS and FWO methods. The order of the decomposition reaction of NaHCO₃ was approximately 2. Comparing to the experimental data, the R^2 for analytical method were higher than 0.95 for all the heating rates.

Notati	ion		
Symbo	ols		
TG	Thermogravimetry analysis	T	Temperature [°C]
DTG	Differential thermogravimetry	$f(\alpha)$	Reaction model [-]
n	Reaction order [-]	$g(\alpha)$	Integrated reaction model [-]
E_a	Activation energy [kJ mol ⁻¹]		
A	Pre-exponential factor [s ⁻¹]	Greek	k symbols
k	Reaction rate constant [s ⁻¹]	α	Conversion [-]
R	Gas constant [J mol ⁻¹ K ⁻¹]	β	Heating rate [°C min ⁻¹]
t	Time [s]		

Acknowledgement

This research has been supported by National Research University Project, Office of Higher Education Commission (WCU-044-CC-57). In addition, the authors thank the Thailand Research Fund for partial support through the Royal Golden Jubilee Ph.D. Program (Grant No. PHD/0356/2551) and the Thailand Research Fund for fiscal year 2014–2016 (TRG5780205).

References

- [1] P. J. Kramer, Carbon dioxide concentration, photosynthesis, and dry matter production. BioScience. 31 (1981) 29-33.
- [2] R. C. Duncan, World energy production, population growth, and the road to the Olduvai Gorge. Popul. Environ. 22 (2000) 503-522.
- [3] M. Olaizola, T. Bridges, S. Flores, L. Griswold, J. Morency and T. Nakamura, Microalgal removal of CO₂ from flue gases: CO₂ capture from a coal combustor Third Annual Conference on Carbon Capture and Sequestration Alexandria, VA 2004.

- [4] A. Yokozeki, M. B. Shiflett, C. P. Junk, L. M. Grieco and T. Foo, Physical and chemical absorptions of carbon dioxide in room-temperature ionic liquids. J. Phys. Chem. B. 112 (2008)16654-16663.
- [5] C. Zhao, X. Chen and C. Zhao, Multiple-cycles behavior of K₂CO₃/Al₂O₃ for CO₂ capture in a fluidized-bed reactor. Energy Fuels. 24 (2010) 1009-1012.
- [6] S.W. Park, D. H. Sung, B. S. Choi, J. W. Lee and H. Kumazawa, Carbonation kinetics of potassium carbonate by carbon dioxide. J. Ind. Eng. Chem. 12 (2006) 522-530.
- [7] P. Behr, A. Maun, K. Deutgen, A. Tunnat, G. Oeljeklaus and K. Görner, Kinetic study on promoted potassium carbonate solutions for CO₂ capture from flue gas. Energy Procedia. 4 (2011) 85-92.
- [8] Y. Liang, D. Harrison, R. Gupta, D. Green and W. McMichael, Carbon dioxide capture using dry sodium-based sorbents. Energy Fuels. 18 (2004) 569-575.
- [9] J. E. White, W. J. Catallo and B. L. Legendre, Biomass pyrolysis kinetics: a comparative critical review with relevant agricultural residue case studies. J. Anal. Appl. Pyrolysis. 91 (2011) 1-33.
- [10] H. E. Kissinger, Reaction kinetics in differential thermal analysis. Anal. Chem. 29 (1957) 1702-1706.
- [11] T. Akahira, T. Sunose, Method of determining activation deterioration constant of electrical insulating materials. Res. Rep. Chiba. Inst. Technol. 16 (1971) 22-31.
- [12] C. P. Lin, Y. M. Chang, J. P. Gupta and C. M. Shu, Comparisons of TGA and DSC approaches to evaluate nitrocellulose thermal degradation energy and stabilizer efficiencies. Process. Saf. Environ. 88 (2010) 413-419.
- [13] J. H. Flynn, L. A. Wall, General treatment of the thermogravimetry of polymers. J. Res. Natl. Bur. Stand.70 (1966) 487-523.
- [14] T. Ozawa, A new method of analyzing thermogravimetric data. Chem. Soc. Jpn. 38 (1965)1881-1886.
- [15] C. Doyle, Doyle CD. Kinetic analysis of thermogravimetric data. J. Appl. Polym. Sci. 5 (1961) 285-292.
- [16] C. Doyle, Estimating isothermal life from thermogravimetric data. J. Appl. Polym. Sci. 6 (1962) 639-642.
- [17] H. Yang, R. Yan, T. Chin, D. T. Liang, H. Chen and C. Zheng, Thermogravimetric analysis-Fourier transform infrared analysis of palm oil waste pyrolysis. Energy Fuels. 18 (2004) 1814-1821.
- [18] W. Hu, J. Smith, T. Dogu and G. Dogu, Kinetics of sodium bicarbonate decomposition. AIChE J. 32 (1986) 1483-1490.
- [19] P. K. Heda, D. Dollimore, K. S. Alexander, D. Chen, E. Law and P. Bicknell, A method of assessing solid state reactivity illustrated by thermal decomposition experiments on sodium bicarbonate. Thermochim. Acta. 255 (1995) 255-272.

Article history

TBA

Jurnal Teknologi

CO₂ SORPTION USING NA₂CO₃/AL₂O₃ SORBENT WITH VARIOUS FLOW PATTERNS OF FIXED/FLUIDIZED BED REACTORS

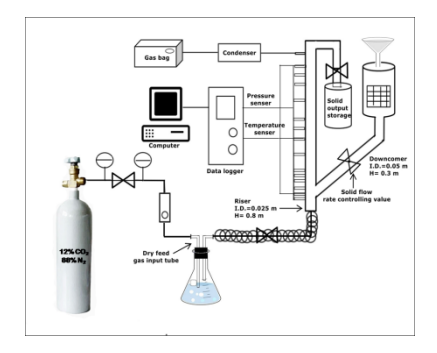
Received TBA Received in revised form TBA Accepted

Nathphatsorn Jongartklang¹, Ratchanon Piemjaiswang¹, Pornpote Piumsomboon¹, Benjapon Chalermsinsuwan^{1,2,*}

*Corresponding author benjapon.c@chula.ac.th

- ¹ Department of Chemical Technology, Faculty of Science, Chulalongkorn University, 254 Phayathai Road, Patumwan, Bangkok 10330, Thailand
- ² Center of Excellence on Petrochemical and Materials Technology, Chulalongkorn University, 254, Phayathai Road, Patumwan, Bangkok 10330, Thailand

Graphical abstract



Abstract

In this study, the carbon dioxide sorption using solid sorbent (sodium carbonate supported on alumina) in fixed and fluidized bed reactors was investigated. The key objective was to examine the carbon dioxide concentration profile or breakthrough curve (as well as capture capacity) and carbon dioxide sorption kinetic parameters with various flow regimes/flow patterns. The basic information for the sorption kinetic parameter computation was the breakthrough curve under different flow operating conditions. From the results, all the breakthrough curves were constant at the beginning stage then it decreased with the sorption time. The fixed bed gave longest sorption time. All the carbon dioxide gas was not captured in the fast fluidization flow regime. The turbulent fluidization flow regime exhibited highest carbon dioxide capture capacity. In addition, the employed deactivation kinetic model fitted well with the obtained experimental information. The initial sorption and deactivation reaction rate constants were the highest at the turbulent fluidization flow regime.

Keywords: Breakthrough curve; carbon dioxide; deactivation model; flow regimes/patterns; sodium carbonate.

© 2015 Penerbit UTM Press. All rights reserved

1.0 INTRODUCTION

Carbon dioxide (CO₂) is known as a major cause of global warming problem due to their ability to maintain the heat inside the earth atmosphere [1]. Recently, the fluidization technology using dry solid sorbent has been considered as an alternative for reducing CO₂ release [2-4]. For conventional gas-solid particle flow, the flow operating condition can be divided into five different regimes/patterns with the increasing of gas inlet velocity [5]. Each regime has its

own distinct characteristic [6]. Sodium carbonate (Na_2CO_3) is promisingly proposed to use as a solid sorbent because it can easily adsorb and regenerate using low temperature and economically employed when comparing to the other solid sorbents [7]. The fundamental theory about adsorption of CO_2 on Na_2CO_3 can be found in the previous studies [7-11]. From the literature, the research study about CO_2 sorption using solid sorbents has paid attention on two topics: solid sorbent development and process system improvement [8-9]. For the solid sorbent development,

 Na_2CO_3 was performed as the active component of the solid sorbent [7]. To improve the sorption efficiency and the attrition resistance of the solid sorbent, Na_2CO_3 was prepared on various supporting materials, such as activated carbon, silica, vermiculite and alumina [10-11]. For the process system improvement, the CO_2 capture performance with various system variables such as gaseous composition, operating pressure and operating temperature were mainly evaluated in fixed bed reactor [12-14]. However, there are still many problems that need to be solved. The understanding of CO_2 capture behavior and CO_2 sorption kinetic parameters will help engineers and technologists to better design the commercial chemical reactor.

About the reaction kinetic study, the deactivation model was effectively used to illustrate the decreasing in activity of alkali-metal carbonate during chemical reaction of various alkali-metal carbonates with CO₂ when comparing to the other chemical kinetic models, the homogeneous model and the shrinkingcore model [15-18]. Though, most reaction kinetic studies on the CO₂ capture using alkaline-metal performed carbonate were mainly thermogravimetric analyzer which then encountered the mass transfer limitation effect. Recently, Lee et al. [19] and Guo et al. [20] investigated the carbonation reaction kinetic behaviors of alkaline-metal carbonate aenerated by calcination of alkaline-metal bicarbonate with a pressurized thermogravimetric and fixed bed apparatus, respectively.

The deactivation model was therefore selected to calculate the kinetic parameters of carbonation reaction for sodium carbonate supported on alumina (Na_2CO_3/Al_2O_3) in fixed and fluidized bed reactors. In addition, the effect of flow regimes/flow patterns on the CO_2 capture behavior and CO_2 sorption kinetic parameters was discussed based on the system hydrodynamics.

2.0 EXPERIMENTAL

2.1 Solid sorbent preparation

In this study, the pure Na₂CO₃ was impregnated on porous alumina support (Al₂O₃) for using as the solid sorbents. The aqueous solution containing five grams of Na₂CO₃ in 25 ml of de-ionized water was added with five grams of support. Then, the solution was mixed in an orbital-shaker for 24 hours at room temperature. After the mixing, the obtained solution was dried at 105°C in a vacuum oven and calcined at 300°C with the ramping temperature rate of 3°C/min in a furnace for 4 hours. The surface area of solid sorbent was determined using Micromentics 2020 apparatus (BET) while the quantity of alkaline metal impregnated was quantified by using Energy Dispersive X-Ray Fluorescence Spectrometer (EDX). The other physical properties of Na₂CO₃/Al₂O₃ solid sorbent are sum up in Table 1.

2.2 Apparatus

The CO₂ sorption was experimented in a laboratory scale fixed bed and fluidized bed reactors as displayed in Figure 1. The riser section, made from glass, had 0.025 m inside diameter and 0.80 m height while the downcomer section, made from polyvinylchloride (PVC), had 0.050 m inside diameter and 0.30 m height. The solid sorbent storage was employed to collect entrained solid sorbents above the riser section. The controlling valve was employed to regulate the feeding or returning flow of solid sorbents to the riser section. The temperature and pressure taps were placed along the riser height to evaluate the system temperature and pressure, respectively. The solid sorbent flow regimes/flow patterns were explored by considering the solid concentration or volume fraction (ε_s) along the riser height. The ε_s was determined using the obtained pressure drop, ΔP , measuring at the mounted pressure taps. By discarding the acceleration flow contribution effect and wall friction effect, the relationship $\Delta P = \rho_s(\varepsilon_s)gH$ then valid (where g and H being the gravitational force acceleration and the length between two successive pressure taps, respectively).

Table 1 Prepared Na₂CO₃/Al₂O₃ solid sorbent physical properties.

Solid sorbent property	Value
Surface area of solid sorbent (m²/g)	105.4
Actual weight of Na_2CO_3 impregnated on Al_2O_3 (wt%)	10
Diameter of solid sorbent (d_p , μ m)	150
Density of solid sorbent (ρ_s , kg/m³)	2,545

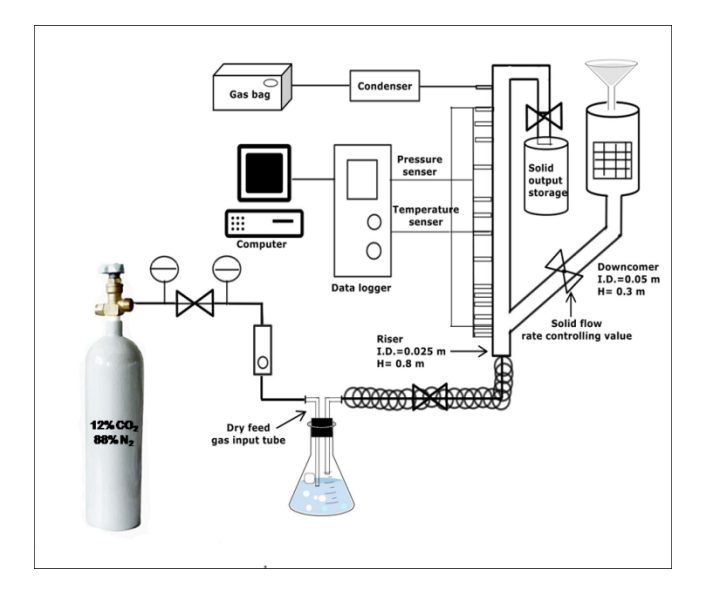


Figure 1 The reactor system used in this study.

2.3 Flow regime/pattern characterization

The wide range of gas velocities from 0.02 to 2.30 m/s was investigated in this study. Five different flow regimes/patterns with the increasing of gas velocity were operated. These include two different operations which are the circulating operation system and the non-circulating operation system. The non-circulating operation system was consisting of four unique flow regimes/flow patterns: fixed bed, bubbling fluidized bed, slugging fluidized bed and turbulent fluidized bed. However, the small amount of bed material was circulated in the turbulent fluidized bed or fluidization regime. The circulating operation system was run in fast fluidized bed or fluidization regime. All the used flow regimes/flow patterns were previously verified the system hydrodynamics in our preceding study [21]. Table 2 presents the operating conditions with different gas velocities.

2.4 CO₂ sorption procedure

For the CO₂ sorption study, the 40 g and 200 g of Na₂CO₃/Al₂O₃ solid sorbent were placed into the riser section for non-circulating and circulating operation systems, respectively. The inlet gas composition, which was measured by online sensor, was prepared as the simulated flue gas composition. The other experimental conditions of flow regimes/patterns in fixed and fluidized bed reactors are shown in Table 3. After the sorption, the gas at the top of the riser section was sampling to measure the quantity of CO₂ in mixture gas using gas chromatography column (GC).

2.5 Kinetic parameters calculation

As stated in the introduction, the deactivation model was used. In this model, the diffusion resistance creating from the occurrence of the product deposition on the reactant is the reason for a decreasing in the rate of chemical reaction. The considerable changes in the surface area, the pore structure and the activity of solid reactant are then arisen. All the changes are included in a deactivation model. When the deactivation of the solid sorbent is specified to be first-order with respect to the concentration of CO_2 gas and the solid active sites, after solving iterative procedure of the obtained equation as described and derived by Park et al. [16], it can be found that:

$$\frac{C}{C_o} = exp \left[I - \frac{exp \left(\frac{k_o W}{Q_s} (I - exp(-k_d t)) \right)}{I - exp(-k_d t)} \right] exp(-k_d t)$$
(1)

where t is time, Q_0 is gas flow rate, W is weight of solid sorbent, C is CO_2 outlet concentration and C_0 is CO_2 inlet concentration. Therefore, the two kinetic parameters of k_0 (initial sorption rate constant) and k_d (deactivation rate constant) are then calculated from the CO_2 concentration profile.

Table 2 The operations of flow regimes/patterns.

Fluidization operation system	Solid sorbent loading (g)	Flow regime / flow pattern	Inlet gas velocity (m/s)
Non- circulating	40	Fixed bed	0.02
		Bubbling	0.18
		Slugging	0.32
		Turbulent	0.84
Circulating	200	Fast fluidization	2.30

Table 3 The experimental conditions of CO₂ sorption in fixed bed and fluidized bed reactors.

Condition	CO ₂ sorption
System temperature (°C)	60
System pressure (atm)	1
Gas composition (vol.%)	CO ₂ : 12, H ₂ O: 19.5, N ₂ : balance
Mole fraction of H_2O (water vapor) to CO_2 (-)	1.60

3.0 RESULTS AND DISCUSSION

3.1 Carbonation behaviors

The flow regimes/flow patterns effect on CO_2 breakthrough curves of Na_2CO_3/Al_2O_3 solid sorbent in fixed bed and fluidized bed reactors at system temperature of 60°C and system pressure of 1 atm in 12 vol.% of CO_2 and 19.5 vol.% of H_2O is shown in Figure 2.

For the CO₂ concentration profile under fixed bed flow pattern, the CO₂ breakthrough curve was constant at the beginning stage then it progressively decreased with the sorption time. For bubbling fluidization regime, the trend of CO₂ concentration curve was comparable to the one with fixed bed flow pattern. However, the constant period of CO₂ breakthrough curve in bubbling fluidized bed flow regime was less than the one in fixed bed flow pattern. This is because the inlet gas velocity of bubbling fluidized bed is higher than that of fixed bed. For slugging and turbulent fluidization regimes, the CO₂ breakthrough curve increased sharply from the beginning stage with the increasing of sorption time because the system residence time through the bed is inadequate for the reactant gas to transfer onto the surface of solid sorbents. Although the system residence time in turbulent fluidization flow regime was lower than the slugging fluidization flow regime, the CO₂ sorption under turbulent fluidization flow regime was higher. The large contacting surface area of gassolid sorbent inside the turbulent fluidized bed flow regime is the reason for the obtained phenomenon. When the solid sorbents were performed in fast fluidization flow regime, the solid sorbents were

elutriated by the high inlet gas velocity and returned to the feeding section at the bottom of the riser. It took 6 min for all 200 grams of solid sorbent to pass through the riser section. During first sorption cycle or 0 to 6 min, the fresh solid sorbent adsorbed about 80 percent ($C_A/C_{A0} \approx 0.20$) of CO_2 in the feed because the extremely high operating gas velocity. The competition between the effect of gas-solid sorbent contacting surface area and system residence time (or solid sorbent elutriation) on CO_2 capture is found in this flow regime. After 6 min, the sorption reaction of Na₂CO₃/Al₂O₃ solid sorbents gradually decreased or the CO_2 concentration gradually increased due to the returning of employed solid sorbents.

Figure 3 shows the CO₂ capture capacity (the ratio of the overall amount of CO₂ sorption per the amount of active component on solid sorbent) at different flow regimes of Na₂CO₃/Al₂O₃ solid sorbent in fixed and fluidized bed reactors at system temperature of 60°C and system pressure of 1 atm in 12 vol.% of CO₂ and 19.5 vol.% of H₂O. The fixed bed, slugging and fast fluidizations showed poor CO₂ capture capacity at about 97-158 mg CO₂/g Na₂CO₃ while the turbulent and bubbling fluidizations showed good CO₂ capture capacity at about 190-194 mg CO₂/g Na₂CO₃. When considering the CO₂ breakthrough curve or CO₂ concentration profile as shown in Figure 2, the fixed bed flow pattern gave the highest sorption time. However, the achieved CO₂ capture capacity was not the highest in this flow pattern. The reason is because the solid sorbent packing among each other causes the active site loss of the solid sorbent. In bubbling fluidization regime, the CO₂ capture capacity of solid sorbents showed that higher gas-solid sorbent contacting surface area will give better the CO₂ capture capacity of solid sorbents. For the remaining fluidization flow regimes, the solid sorbents could not capture all the CO₂ gas even at the early

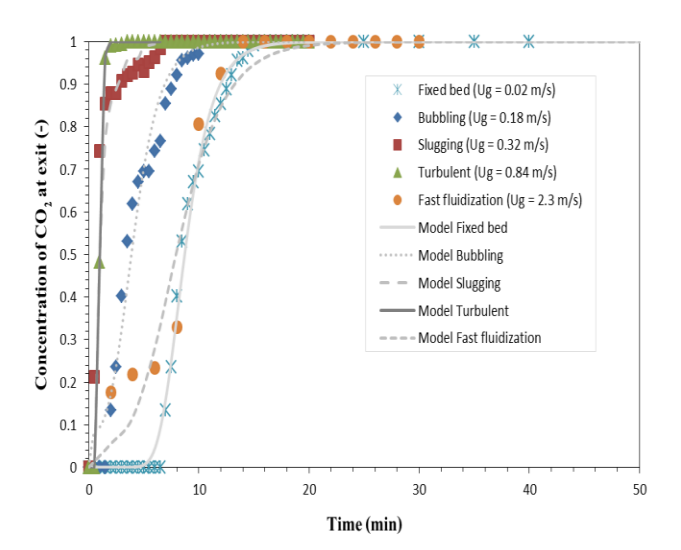


Figure 2 The effect of various flow regimes/flow patterns on breakthrough curve of CO₂ concentration at system temperature of 60°C and system pressure of 1 atm in 12 vol.% of CO₂ and 19.5 vol.% of H₂O.

stage. Considering the CO₂ capture capacity of solid sorbents, the slugging and fast fluidization flow regimes showed lowest capture capacity of solid sorbents because the large gas bubble forming in the slugging fluidization regime and low system residence time in the fast fluidization regime. The turbulent fluidization regime reflected the promising CO₂ capture capacity. The proper solid sorbent elutriation and system backmixing are the explanation for this situation [5].

3.2 Carbonation chemical reaction kinetics

To obtain chemical reaction kinetic parameters (k_0 and k_d), the regression fitting was performed using Equation (1) with non-linear least square technique [16]. Figure 2 also displays the regression results of the real experimental data by the deactivation model. The selected deactivation model could precisely predict the breakthrough behaviors for all the reaction of Na₂CO₃/Al₂O₃ and CO₂. Table 4 summarizes the kinetic parameters for all flow regimes/patterns of Na₂CO₃/Al₂O₃ solid sorbent in fixed and fluidized bed reactors at system temperature of 60°C and system pressure of 1 atm in 12 vol.% of CO₂ and 19.5 vol.% of H₂O. As can be seen from the results, the sorption kinetic parameters were greatly depending on the flow regime/pattern performing inside the system. In general, the chemical reaction kinetic parameters are those that describe the reaction rate and they then should be the same irrespective of the reactor type. However, the kinetic models in this study were the overall or simplified kinetic models including mass transfer and chemical reaction resistances. Because the obtained kinetic parameters were different in each type of fluidization flow regime, it can be concluded that mass transfer resistance occurred and governed these systems.

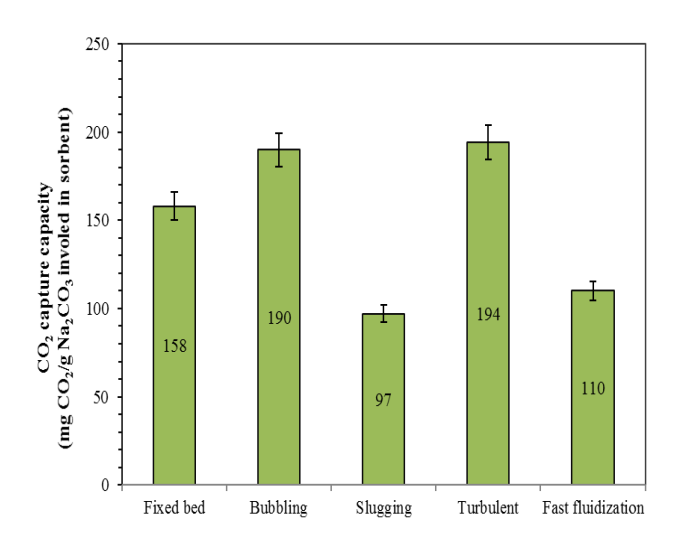
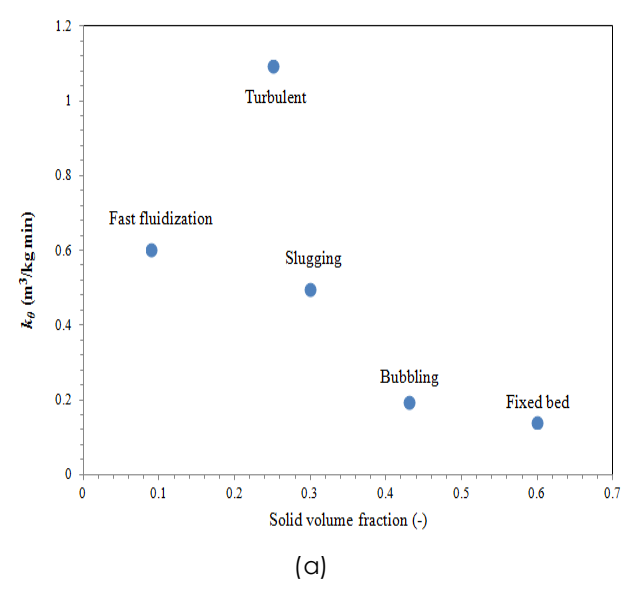


Figure 3 The effect of various flow regimes/flow patterns on CO_2 capture capacity at system temperature of 60°C and system pressure of 1 atm in 12 vol.% of CO_2 and 19.5 vol.% of H_2O .

Although the fixed bed flow pattern gave the longest sorption result, the obtained value of k_0 was very low. The solid sorbent packing among each other slows the speed of reaction rate. In bubbling fluidization regime, the value of k_0 was slightly higher which is because of the high gas-solid sorbent mixing behavior. Considering the values of k_0 for slugging and fast fluidization flow regimes, the similar k_0 value range was observed due to the large bubble formation and low system residence time, respectively. The turbulent fluidization flow regime provided the highest value of k_0 because of both the suitable residence time and system back-mixing [21]. In addition, the value of k_d or the deactivation rate constant had the same trend similar to the value of k_0 the initial sorption rate. For all the flow pattern/regimes, the k_d values were extremely lower than k_0 values. This implies the low solid sorbent deactivation in all fluidization flow pattern/regimes causing by the solid sorbent properties and system hydrodynamics.

Finally, the solid volume fraction effect on the $\rm CO_2$ sorption kinetic parameters was illustrated as shown in Figure 4. From the result in the figure, the highest kinetic parameters for the turbulent fluidization flow regime can be clarified using the appropriate solid sorbent concentration or volume fraction behavior inside the system. The highest kinetic parameter was obtained at the moderate value of the solid concentration or volume fraction. At the low value, the solid particles were diluted and distributed across the column. At the high value, the solid particles were too dense inside the system and blocked the active surface area. Both the solid volume fraction behaviors then gave a negative effect on the sorption reaction rate.

To confirm the assumption for the derivation of the deactivation model, Figure 5 shows the SEM image taken at the magnification of x10000 (a) before and (b) after CO₂ sorption of Na₂CO₃/Al₂O₃ solid sorbent in the turbulent fluidized bed. The surface image of the sorption product was distinctively different from the one of the reactant. After the CO₂ sorption, the layer of product over the solid sorbent was found.



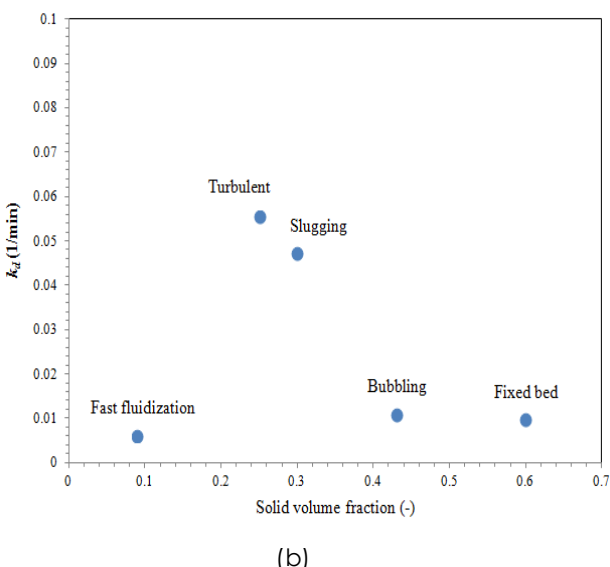
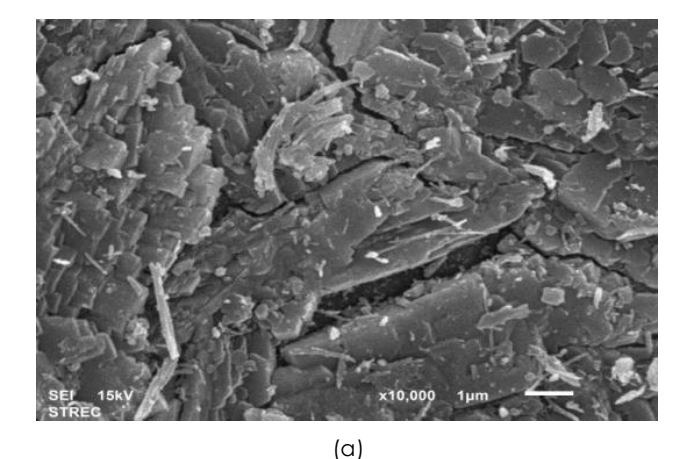


Figure 4 The effect of the solid volume fraction on (a) k_0 and (b) k_d .

Table 4 The effect of various flow regimes/flow patterns on initial sorption rate and deactivation rate at system temperature of 60°C and system pressure of 1 atm in 12 vol.% of CO₂ and 19.5 vol.% of H₂O.

Flow regime / flow pattern	w (g)	k₀ (m³/kg⋅min)	<i>k</i> _d (1/min)	Solid volume fraction (-)
Fixed bed	40	0.1408	0.0098	0.60
Bubbling	40	0.1950	0.0108	0.43
Slugging	40	0.4979	0.0471	0.30
Turbulent	40	1.0934	0.0554	0.25
Fast fluidization	200	0.6020	0.0061	0.09



(b)

Figure 5 SEM image taken at the magnification of x10000 (a) before and (b) after CO₂ sorption of Na₂CO₃/Al₂O₃ solid sorbent in the turbulent fluidization regime at system temperature of 60°C and system pressure of 1 atm in 12 vol.% of CO₂ and 19.5 vol.% of H_2O .

4.0 CONCLUSION

The carbon dioxide sorption behavior and sorption kinetic parameters using deactivation kinetic model with sodium carbonate supported on alumina solid sorbent in fixed and fluidized bed reactors had been successfully investigated under different regimes/patterns. All the breakthrough curves were constant at the beginning stage then it decreased with the sorption time. The fixed bed flow pattern gave longest sorption time while the fast fluidized bed flow regime could not capture all the carbon dioxide concentration. The turbulent fluidized bed regime exhibited the highest value on carbon dioxide capture capacity. This can be explained by the sorption reaction rate constants were highest at moderate solid volume fraction value due to the suitable system hydrodynamics including appropriate gas-solid sorbent contacting area and system residence time or solid sorbent elutriation.

It was found that the employed deactivation kinetic model was validated and fitted well with the obtained experimental data.

Acknowledgement

The 90th Anniversary of Chulalongkorn University Fund, the Ratchadaphiseksomphot Endowment Fund 2015 of Chulalongkorn University (CU-58-059-CC), the Faculty of Science of Chulalongkorn University and the Thailand Research Fund (TRG5780205) are acknowledged in this study.

References

Bandyopadhyay, A. 2014. Carbon Capture and Storage: CO₂ Management Technologies, CRC Press.

Chalermsinsuwan, B., Piumsomboon, P. and Gidaspow, D. 2010. A computational fluid dynamics design of a carbon dioxide sorption circulating fluidized bed. AIChE Journal 56: 2805-2824.

2805–2824. Zhao, C., Chen, X. Wu, Y. and Dong, W., 2012. K_2CO_3/Al_2O_3 for capturing CO_2 in flue gas from power plants. Part 3: CO_2 capture behaviors of K_2CO_3/Al_2O_3 in a bubbling fluidized-bed reactor. Energy & Fuels 26: 3062-3068. Chaiw ang, P., Chalermsinsuwan, B., Piumsomboon, P. and Gidaspow, D. 2014. CFD design of a sorber for CO_2 capture with 75 and 375 micron particles. Chemical Engineering Science 105: 32–45. Jaiboon, O.A., Chalermsinsuwan, B., Mekasut, L. and Piumsomboon, P. 2013. Effect of flow patterns/regimes on CO_2 capture using K_2CO_3 solid sorbent in fluidized bed/circulating fluidized bed. Chemical Engineering bed/circulating fluidized bed. Chemical Engineering Journal 219: 262–272.

Kunii, D., and Levenspiel, O. 1991. Fluidization engineering.

Butterworth-Heinemann.

Dong, W., Wu, Y., Zhao, C. and Liu C.L. 2012. Carbonation characteristics of dry sodium-based sorbents for CO₂ capture. Energy & Fues 26: 6040–6046. Zhao, C., Chen, X., Zhao, C. 2010. Carbonation behavior of

[8] Zhao, C., Chen, X., Zhao, C. 2010. Carbonation behavior of K₂CO₃ with different microstructure used as an active component of dry sorbents for CO₂ capture. *Industrial & Engineering Chemistry Research* 49: 12212–12216.
[9] Khongprom, P. and Gidaspow, D. 2010. Compact fluidized bed sorber for CO₂ capture. *Particuology* 8(6):531–535.
[10] Lee, S.C., Choi, B.Y., Lee, T.J., Ryu, C.K., Ahn, Y.S. and Kim, J.C. 2006. CO₂ absorption and regeneration of alkali metal-based solid sorbents. *Cat alysis Today* 111: 385–390.
[11] Dong, W., Chen, X., Yu, F. and Wu, Y. 2015. Na₂CO₃/M gO/Al₂O₃ solid sorbents for low temperature CO₂ capture. *Energy & Fuels* 29(2): 968–973.

Na₂CO₃/M gO/Al₂O₃ solid sorbents for low-femperature CO₂ capture. Energy & Fuels 29 (2): 968–973.
[12] Liang, Y., Harrison, D.P., Gupta, R.P., Green, D.A. and McMichael, W.J. 2004. Carbon dioxide capture using dry sodium-based sorbents. Energy & Fuels 18(2): 569–575.
[13] Arunkumar, S., Zhao, A., George K.H.S., Partha, S. and Rajender, G. 2012. Post-combustion CO₂ capture using solid sorbents: A review. Industrial & Engineering Chemistry Pagarach 51(4): 1433–1443.

Research 51 (4): 1438–1463.

[14] Seo, Y., S.H., Ryu, H.J., Bae, H.D. and Yi, C.K. 2007. Effect of water pretreatment on CO₂ capture using a potassium-based solid sorbent in a bubbling fluidized bed reactor. Chemical Engineering Journal 24:457–460.

[15] Park, S.W., Sung, D.H., Choi, B.S., Lee, J.W. and Kumazawa, J. 2004. Carbonstian kingling of partarisism carbonata by

[13] Falk, S.W., Sung, D.H., Choi, B.S., Lee, J.W. and Kumazawa, H. 2006. Carbonation kinetics of potassium carbonate by carbon dioxide. Journal of Industrial and Engineering Chemistry 12(4): 522–330.
[16] Park, S.W., Sung, D.H., Choi, B.S., Oh, K.J. and Moon, K.H. 2006. Sorption of carbon dioxide onto sodium carbonate. Separation Science and Technology 41: 2665–2684.
[17] Park S.W., Sung, D.H., Choi, B.S., Loo, L.W., and Kumazawa.

Park, S.W., Sung, D.H., Choi, B.S., Lee, J.W. and Kumazawa, H. 2009. Carbonation kinetics of potassium carbonate by carbon dioxide. Korean Journal of Chemical Engineering 26(5): 1383-1388.

[18] Zhao, C., Chen X. and Zhao, C. 2012. Carbonation behavior and the reaction kinetic of a new dry potassium-

behavior and the reaction kinetic of a new dry potassium-based sorbent for CO₂ capture. Industrial & Engineering Chemistry Research 51: 14361–14366.

[19] Lee, D.K., Young, D.M., Seo, H., Kang, N.Y., Choit, W.C. and Park, Y.K. 2013. Kinetic Expression for the carbonation reaction of K₂CO₃/ZrO₂ sorbent for CO₂ capture. Industrial & Engineering Chemistry Research 52(26): 9323–9329.

[20] Guo, Y., Zhao, C. and Li, C. 2015. Thermogravimetric analysis of kinetic characteristics of K₂CO₃-impregnated mesoporous silicas in low-concentration CO₂. Journal of

mesoporous silicas in low-concentration CO₂. Journal of Thermal Analysis and Calorimetry 121: 1393–1402

Jaiboon, O.A., Chalemsinsuwan, B., Mekasut, L. and Piumsomboon, P. 2013. Effect of flow pattern on power spectral density of pressure fluctuation in various fluidization regimes. Powder Technology 233: 215-226.



Contents lists available at ScienceDirect

Advances in Engineering Software

journal homepage: www.elsevier.com/locate/advengsoft



Integration of computational fluid dynamics simulation and statistical factorial experimental design of thick-wall crude oil pipeline with heat loss



Wanwisa Rukthong ^a, Wichapun Weerapakkaroon ^b, Ungkana Wongsiriwan ^b, Pornpote Piumsomboon ^{a,c}, Benjapon Chalermsinsuwan ^{a,c,*}

- ^a Fuels Research Center, Department of Chemical Technology, Faculty of Science, Chulalongkorn University, 254 Phayathai Road, Patumwan, Bangkok 10330, Thailand
- b PTT Research & Technology Institute, PTT Public Company Limited, 555 Vibhavadi Rangsit Road, Chatuchak, Bangkok 10900, Thailand
- ^c Center of Excellence on Petrochemical and Materials Technology, Chulalongkorn University, 254 Phayathai Road, Patumwan, Bangkok 10330, Thailand

ARTICLE INFO

Article history: Received 5 November 2014 Received in revised form 31 March 2015 Accepted 12 April 2015 Available online 22 April 2015

Keywords:
Thick-wall
Pipeline
Crude oil
Wax appearance distance
Experimental design
Computational fluid dynamics

ABSTRACT

The aim of this study was to explore the heat transfer behavior between convection and conduction in the thick wall crude oil pipeline with laminar unsteady state flow using integration of developed computational fluid dynamics model and statistical experimental design. The governing equations were employed to investigate the effects of wall thickness, wall thermal conductivity, surrounding heat transfer coefficient and ambient temperature on transport profile using statistical experimental design and to locate an origin point where wax precipitate in the pipeline (wax appearance distance) by using response surface methodology (RSM). A good agreement between the model and literature experimental data suggests that the proposed numerical scheme is suitable for simulating the transport profile in pipeline and predicting the phenomena for any other conditions. From the statistical analysis, it was found that, surrounding heat transfer coefficient and ambient temperature were the major effect parameters on the wax appearance distance.

© 2015 Elsevier Ltd. All rights reserved.

1. Introduction

Transportation of crude oil by pipelines is the general process in petroleum industry. Generally, pipelines are made of various materials which have different ability to conduct heat. Consequently, the heat affects the transport properties of the crude oil leading to operational efficiency. The proper selection of materials for the pipeline brings the effective production system [1]. Stainless steel has the thermal conductivity of 15.1 W/m K while copper has the very high thermal conductivity of 401.0 W/m K [2]. This variety of thermal conductivity affects the performance of a heat exchanger between crude oil and surrounding outside the pipe [3]. In this study, the conjugated heat transfer coupling between wall convection and conduction were concerned [4]. The analysis of this problem was carried out to study the effect of parameters which related to thick-wall problem such as wall thickness, pipe thermal conductivity, surrounding heat transfer

E-mail address: benjapon.c@chula.ac.th (B. Chalermsinsuwan).

coefficient and ambient temperature on the hydrodynamics changing in transport profile inside the pipeline. All these parameters have an important role in designing the pipeline system.

The heat and mass transfers of crude oil through pipelines are very complicated process because there are many factors which affect transport profile [5]. The knowledge in computational fluid dynamics (CFD) is therefore required for better understanding the flow behavior and for predicting the phenomena inside pipeline. Wang et al. [6] determined an optimized pigging frequency using experimental method and wax deposition model. Zhu et al. [7] investigated the thermal influential factors affecting the crude oil temperature in double pipelines system using the computational fluid dynamics methodology. However, in most of previous studies focusing on convective heat transfer, wall conduction was ignored because of the assumption of extremely thin wall. This may distort crude oil transport profile at the wall boundary condition. Thus, besides the heat convection, the heat conduction through the pipe wall should also be considered.

The aim of this study was to develop the computational fluid dynamics model for investigating the effect of thick-wall pipeline on the transport profile using statistical experimental design. In the literature, the experimental results on integration of

^{*} Corresponding author at: Fuels Research Center, Department of Chemical Technology, Faculty of Science, Chulalongkorn University, 254 Phayathai Road, Patumwan, Bangkok 10330. Thailand.

Nomenclature Symbols time (s) wall thickness/coded factor of wall thickness (-) Α Τ temperature (°C) В pipe thermal conductivity/coded factor of pipe thermal и x-velocity (m/s)conductivity (-) y-velocity (m/s) ν С surrounding heat transfer coefficient/coded factor of *x*-direction surrounding heat transfer coefficient (-) wall thickness (m) Δχ D ambient temperature/coded factor of ambient tempera*y*-direction ture (-) wax appearance distance (m) pipe diameter (m) D_{pipe} heat transfer coefficient (kW/m² °C) h Greek symbols h_i inner wall heat transfer coefficient (kW/m² °C) dependent variable h_o outer wall heat transfer coefficient (kW/m² °C) density (kg/m³) thermal conductivity (kW/m °C) k_p diffusion coefficient L pipe length (m) inner wall radius (m) r_i Subscript outer wall radius (m) r_o ambient а heat resistance (m² °C/kW) R fluid/crude oil f S_{ϕ} source term

computational fluid dynamics simulation and statistical experimental design were limited. This analysis will be helpful for preventing and solving real problems which may emerge during the crude oil transportation such as precipitation of wax.

2. Methodology

2.1. Computational fluid dynamics model

The fluid flow problem can be solved by using computational fluid dynamics (CFD) technique. CFD is a very powerful tool for analyzing the system involving fluid flow, heat transfer, mass transfer and other special phenomena such as chemical reaction [8,9] by solving the mathematical equations which govern these processes using numerical methods. To develop the CFD model, governing equations which are in partial differential form are transformed to algebraic form using finite volume numerical solution techniques [10]. Crude oil was considered as incompressible fluids. The generalized conservation equation for two-dimensional flow system where the dependent variable is denoted by ϕ can be written as:

$$\frac{\partial(\rho\phi)}{\partial t} + \frac{\partial(\rho u\phi)}{\partial x} + \frac{\partial(\rho v\phi)}{\partial y} = \frac{\partial}{\partial x} \left(\Gamma \frac{\partial\phi}{\partial x}\right) + \frac{\partial}{\partial x} \left(\Gamma \frac{\partial\phi}{\partial y}\right) + S_{\phi}$$
(1)

The two-dimensional Cartesian co-ordinates were employed as an approximation for the cylindrical pipeline system. In Eq. (1), there are the transient and the convective terms in x and y directions on the left hand side and the conductive term in x and y directions and the source term on the right hand side. Eq. (1) will turn into the continuity equation by replacing ϕ with 1. In addition, when ϕ is substituted by u, v and v, Eq. (1) will become the conservation of momentum in v and v directions and the conservation of energy, respectively.

2.2. Boundary conditions and properties

The problem was analyzed to investigate the heat exchange among surrounding, pipe wall and crude oil [11]. The schematic drawing of the thick-wall pipe problem is shown in Fig. 1. This crude oil pipeline was chosen from the real crude oil pipeline in the literature information. The flow had Peclet number of 16,300 and Biot number of 0.07–22.00 depending on the condition. Because the Peclet number is high, convection is important

to flow in this system. In addition, this study Biot numbers vary from the condition that conduction inside the pipeline is unimportant to important. Heat flows from crude oil to the surrounding through a two-dimensional Cartesian thick-wall pipe with conductive heat coefficient of k_p in the wall and convective heat coefficient of h_i and h_o at the inner and outer surfaces of the wall pipe, respectively. Inner wall convection coefficient is determined from Nusselt number. The Nusselt number in laminar flow of circular tube is 3.66 [2]. The heat resistance (R) through a thick-wall pipe is

$$R = (1/h_i) + (\Delta x/k_p) + (1/h_o)$$
(2)

The wall thickness is the difference between the radiuses of outer and inner walls ($\Delta x = r_o - r_i$). The formula was added as an additional source term in the energy conservation equation at the wall boundary condition.

2.3. Numerical solution

To compute the solution of governing equations for each control volume on the staggered grid arrangement, SIMPLE (Semi Implicit Method Pressure-Linked Equation) algorithm was employed [9]. First order upwind differencing scheme and Tri-Diagonal Matrix Algorithm (TDMA) were applied to solve the interface problem and to calculate the results of linear algebraic equations, respectively. All of developed equations and CFD procedure were then written as standalone computer program code. The developed CFD program can handle both symmetry and non-symmetry boundary conditions. Parameters used in CFD simulation are listed

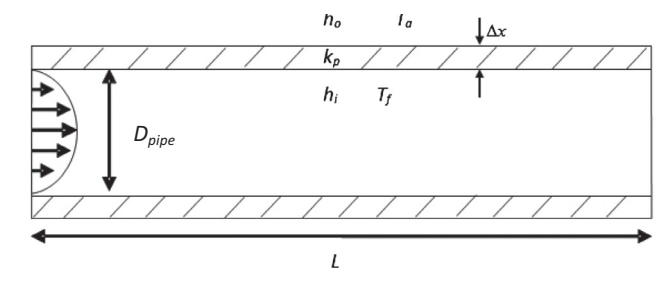


Fig. 1. The schematic drawing of a thick-wall straight pipe model.

Table 1Parameters used in CFD simulation [12,13].

Description	Value	Unit
Pipe inner diameter	0.15	m
Pipe length	3000	m
Crude oil inlet temperature	50	°C
Crude oil inlet velocity	0.01	m/s
Operating time	3600	s
Crude oil density	822.3	kg/m ³
Crude oil thermal conductivity	0.0002	kW/m °C
Crude oil heat capacity	2.008	kJ/kg °C
Crude oil viscosity	$[19.54674 - 1.36857(T - 38) + 0.07271(T - 38)^2 - 0.00163(T - 38)^3]/1000$	kg/ms

in Table 1. The correlation between the crude oil viscosity and temperature (*T*) by Guozhong and Gang [12] was employed in this study which links the fluid flow and heat transfer. The numerical simulations have been done under unsteady state laminar flow conditions (Reynolds number < 2000) with single phase liquid flow and used under-relaxation factor to ensure stability of the SIMPLE process [9]. After the grid independency testing, the straight pipe model was composed of a 30,000 mesh. The simulation tests were performed until reaching the steady state condition (operation time less than 3600 s). The results from developed CFD simulation program were validated with the literature experimental study by Guozhong and Gang [12].

2.4. Design of experiments

In this study, the factorial experimental design analysis was used to investigate the main effects and interactions of the parameters related to a thick-wall pipe problem. Two levels of the following four varying parameters which were the wall thickness (A), pipe thermal conductivity (B) surrounding heat transfer coefficient (C) and ambient temperature (D) were considered as shown in Table 2. In this study, the parameters and their levels were selected based on the available literature and some experiments of OH crude oil which is a type of crude oil in China [12]. In general, pipe thermal conductivity depends on type of pipe material. We selected carbon steel and stainless steel as the pipe material which have the thermal conductivity of 0.0625 and 0.0151 kW/m °C, respectively. For the wall thickness, the range from the real system from Petroleum Company and from the literature information [13] were selected. Two values of surrounding heat transfer coefficient (h_0) were chosen from the range of air speed which correspond to natural or low air velocity (0.005 kW/ m² °C) and force or high air velocity (0.1 kW/m² °C) convection conditions [2]. The lowest and highest values of each factor are coded as -1 and +1 numbers, respectively. The location of wax appearance represented by wax appearance distance was chosen as the response, based on the wax appearance temperature for QH crude oil at 47 °C. The wax appearance distance was separated in two positions, near the pipe wall and the pipe center. Design of experiment with three factors, orthogonal array, was designed and the single replicate response data was then obtained as also shown in Table 2.

3. Results and discussion

3.1. Transport profile in crude oil pipeline

As stated above, all 16 simulation cases were carried out based on the 2⁴ factorial experimental design in order to obtain 16 flow patterns of crude oil inside the pipeline. The results showed that those all 16 profiles had quite similar flow patterns. The difference between each profile was the decreasing rate of crude oil temperature. Examples of crude oil temperature and velocity profiles are shown in Figs. 2 and 3, respectively.

It can be seen in Fig. 2(a) that crude oil temperature decreased along pipeline length and continuously dropped with the time because there was the heat loss of crude oil to environment [12]. In the same time, temperature of crude oil near the pipe center had the highest value then decreased along the radial direction of the pipe until reaching the pipe wall where the temperature was the same as the surrounding temperature as shown in Fig. 2(b). As for the velocity profile, Fig. 3(a) shows that the crude oil velocity in the pipeline was quite constant along the pipeline length due to the constant cross-section area of the pipeline. Because the viscosity is depended on the temperature, the

Table 2 The 2^4 factorial experimental design with the CFD simulation results.

Run	Wall thickness (m) A Pipe thermal		Surrounding heat transfer	Ambient temperature (°C) D	Wax appearance distance (m)	
		conductivity (kW/m °C) B	coefficient (kW/m ² °C) C		Near pipe wall	Near pipe center
1	0.0880	0.0151	0.100	35	220.0	2157.0
2	0.0880	0.0625	0.100	25	121.0	1672.0
3	0.0012	0.0625	0.100	35	218.5	2153.0
4	0.0880	0.0625	0.005	35	247.5	2240.0
5	0.0012	0.0151	0.100	35	218.5	2153.0
6	0.0012	0.0151	0.005	35	247.0	2239.0
7	0.0880	0.0151	0.005	25	136.5	1732.0
8	0.0012	0.0625	0.005	35	247.5	2236.0
9	0.0880	0.0151	0.005	35	248.0	2238.0
10	0.0012	0.0151	0.100	25	121.0	1671.0
11	0.0012	0.0151	0.005	25	136.0	1731.0
12	0.0880	0.0151	0.100	25	121.0	1673.0
13	0.0880	0.0625	0.005	25	136.5	1733.0
14	0.0880	0.0625	0.100	35	219.0	2154.0
15	0.0012	0.0625	0.100	25	121.0	1669.0
16	0.0012	0.0625	0.005	25	136.0	1732.0

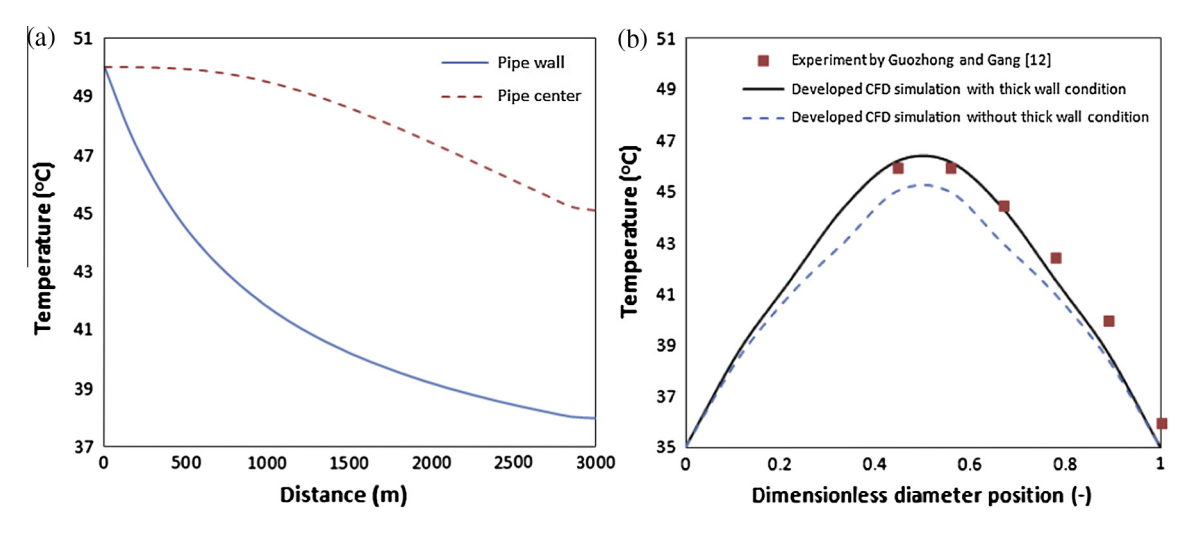


Fig. 2. Temperature profile of crude oil (a) along the pipeline length and (b) along the diameter of pipe at the system outlet.

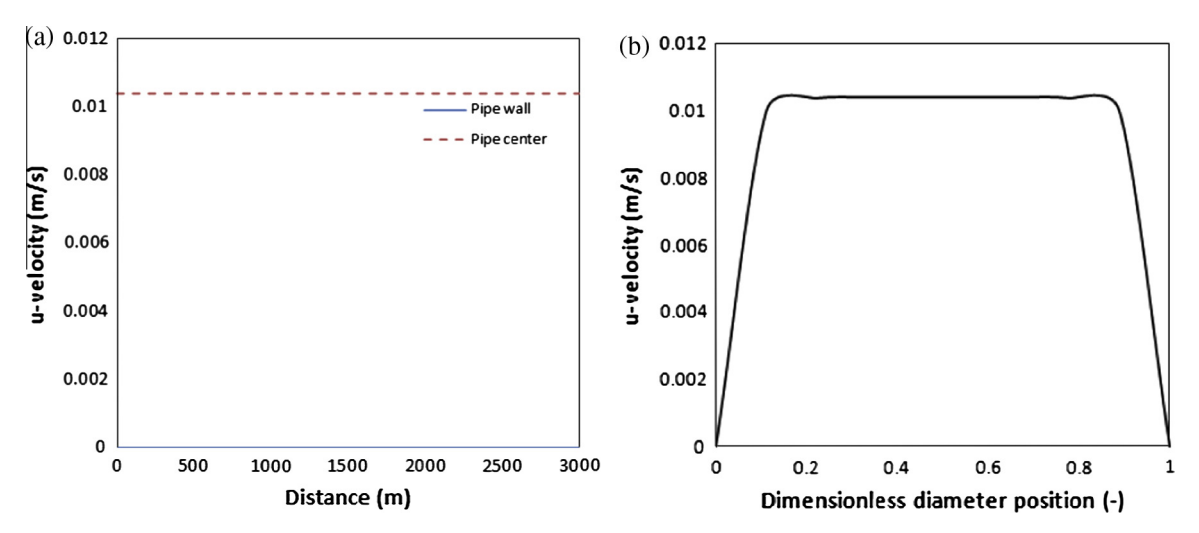


Fig. 3. U-velocity profile of crude oil (a) along the pipeline length and (b) along the diameter of pipe at the system outlet.

obtained velocity profile at the wall region then should lower than the obtained velocity profile at the center region. On the other hand, Fig. 3(b) shows dropping of crude oil velocity along the pipe diameter direction due to rapid increase of the crude oil viscosity near the pipe wall caused by the decreasing of crude oil temperature near the pipe wall. These results agreed well with previously reported trends [14].

The steady state temperature profiles in crude oil pipeline obtained from developed CFD simulation code then were compared with the experimental data by Guozhong and Gang [12] as displayed in Fig. 2(b). Using the quite similar operating conditions as used in this study, the obtained results then can be compared. It is found that the obtained profiles were quite similar. The small difference near the pipe wall is because the unknown properties of pipeline in the literature information [12]. Therefore, the model accuracy and correctness was proved. In Fig. 2(b), the result without thick-wall condition is also shown. The profile was different and lower from the one with thick-wall pipeline which confirmed the assumption of this study about the importance of thick-wall condition. The heat transfer resistance inside the wall slightly made the crude oil temperature near the wall for the thick-walled pipeline to be higher than the thin-walled pipeline. In addition, the result trend was compared with the one from commercial software, ANSYS FLUENT, the obtained results from both simulation codes also had a similar trend [15].

3.2. The 2⁴ factorial experimental design analysis

The response results from the 2^4 factorial experimental design analysis with a single replicate were shown in Table 2. The ANOVA statistical analysis of the results obtaining with a confidence level of 95% or p-value equals to 0.05 were summarized in Tables 3 and 4 for the wax appearance distance near the pipe wall and the pipe center, respectively. The p-values provide a cut-off beyond which we assert that the findings are statistically significant. From the results in Table 3, it is found that surrounding heat transfer coefficient (C), ambient temperature (D) and their interaction (CD) had significant effect on the response. In addition, it can be seen in Table 4 that surrounding heat transfer coefficient (C) ambient temperature (D) were the effect parameters on the wax appearance distance near the pipe center. These were indicated by the low p-value of 0.05.

Fig. 4 illustrates the plots of the main and interaction effects for each significant response variable. From both the results, near the wall and center regions, the parameters had the same effects on the responses. A negative effect of surrounding heat transfer

Table 3The analysis of variance when the response variable was the wax appearance distance near pipe wall.

Source	Sum of squares	Degree of freedom (DF)	Mean square	F-value	P-value
Model C D CD Residual Cor Total	5.10759E-05 2.08029E-06 4.88429E-05 1.52609E-07 2.37535E-09 5.10783E-05	3 1 1 1 12 15	1.702E-05 2.080E-06 4.884E-05 1.526E-07 1.979E-10	86009.89 10509.37 246749.3 770.9659	<0.0001 <0.0001 <0.0001 <0.0001

Table 4The analysis of variance when the response variable was the wax appearance distance near pipe center.

Source	Sum of squares	Degree of freedom (DF)	Mean Square	F-value	P-value
Model C D Residual Cor Total	7.157E-08 1.475E-09 7.009E-08 1.491E-11 7.158E-08	2 1 1 13 15	3.578E-08 1.475E-09 7.009E-08 1.147E-12	31194.04 1286.057 61102.01	<0.0001 <0.0001 <0.0001

coefficient (C) on wax appearance distance was observed. When the surrounding heat transfer coefficient (C) is increased, the wax appearance distance decreases due to the increase of heat transfer rate from crude oil to environment outside the pipe [16]. Meanwhile, the ambient temperature (D) had a positive effect on wax appearance distance, the wax appearance distance increases with increasing of ambient temperature. This is because a higher ambient temperature causes a lower heat transfer rate from crude oil to surrounding and results in slower wax appearance distance [17]. In Fig. 4(b), the negative interaction effects between surrounding heat transfer coefficient and ambient temperature were also illustrated. In fact, the wall thickness and pipe thermal conductivity had an effect on the response variable but had less significant when comparing to the surrounding heat convection transfer coefficient and ambient temperature using 95% confidence interval. The reason is because the response variable in this study is the wax appearance distance which directly depending on the surrounding heat convection transfer coefficient and ambient temperature. The pipe thermal conductivity and wall thickness may have an effect on the temperature especially at near the pipe wall. Comparing between the responses variables, there was higher temperature drop near the wall than the pipe center, the reason is that the crude oil near the pipe wall receives the influence of heat transfer directly from the conduction through the wall and convection from the surrounding environment outside of the pipeline.

The obtained mathematical models for the wax appearance distance are as follow;

Near the pipe wall:

$$1/z = 0.00605 + 0.00036 * C - 0.00175 * D - 0.000098 * C * D$$
(3)

Near the pipe center:

$$1/z = 0.000522 + 0.0000096 * C - 0.000066 * D$$
 (4)

where z is the wax appearance distance, C and D are the coded factors of surrounding heat transfer coefficient and ambient temperature, respectively. As stated in the methodology section, the coded factors represent the dimensionless values of each factor ranging from the lowest (or -1) to highest (or +1) ones as summarized in Table 2. For surrounding heat transfer coefficient, the -1 and +1coded values show the surrounding heat transfer coefficient of 0.005 and 0.100 kW/m² °C, respectively, while for ambient temperature, the -1 and +1 coded values show the ambient temperature of 25 and 35 °C, respectively. After substituting the values of code factors, the obtained mathematical models can be used to predict the wax appearance distance near the pipe wall and pipe center [18]. From statistical experimental design theory, the obtained equation can be used for any other systems which have the similar dimensionless conditions. For the other cases, those equations can explain the result trend. About the models, there is an interaction effect near the pipe wall and no interaction effect near the pipe center. In addition, response surface methodology (RSM) which is the mathematical and statistical techniques was used to locate the origin point of the wax appearance distance from the obtained models [18]. As can be seen in Fig. 5, the wax appearance distance will be longer at low surrounding heat transfer coefficient and high ambient temperature. Therefore, crude oil transportation should operate with this condition to avoid or reduce the wax appearance. Surrounding heat transfer coefficient generally depends on fluid properties and velocity while the ambient temperature depends on weather, season and duration time of the day. It can be seen that these parameters mostly depend on the natural environment where the pipeline is located. However, there are some indirect ways to control or manage the effect of these parameters such as coating the pipeline with organic substance to decrease heat transfer rate or adding the thermal insulation apparatus to attenuate the effect of the surrounding temperature [19].

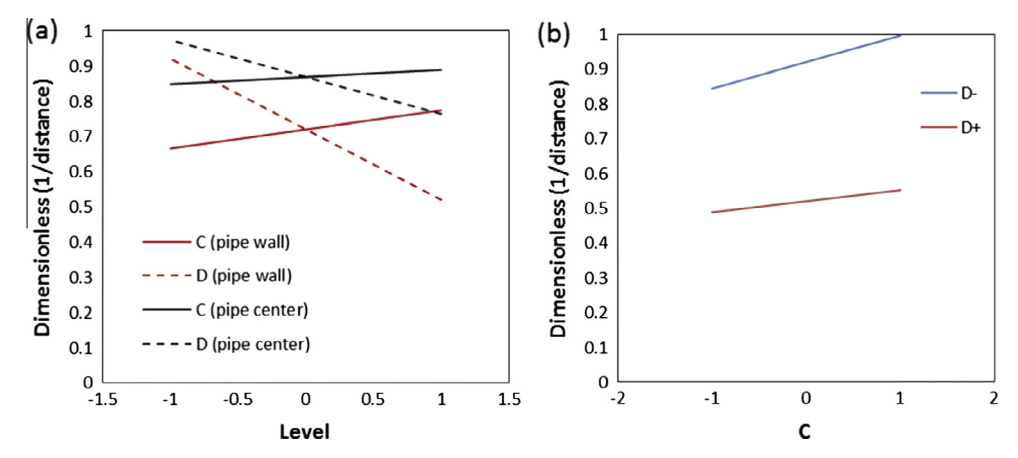


Fig. 4. The (a) main and (b) interaction (for pipe center) effect plots of the dimensionless wax appearance distance.

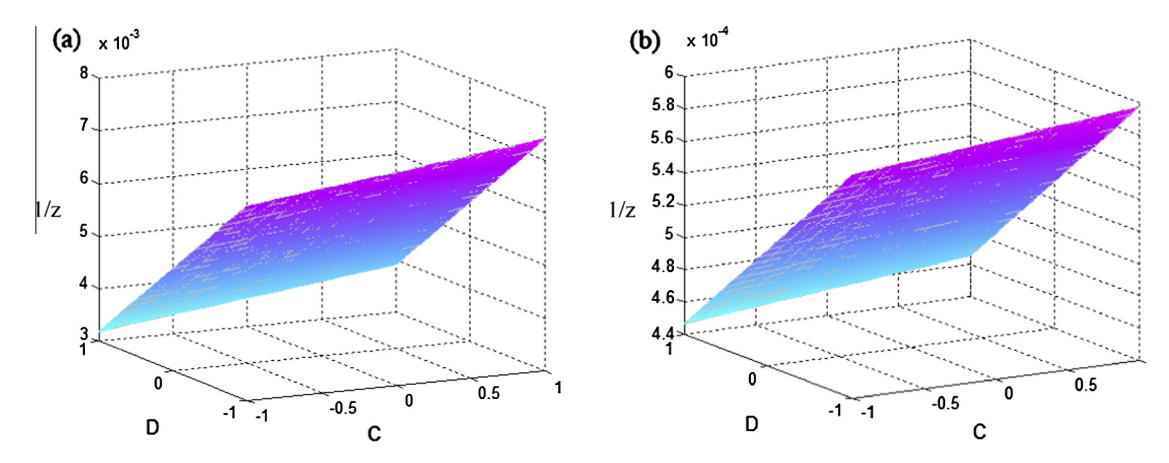


Fig. 5. Response surface plots of the wax appearance distance (a) near pipe wall and (b) near pipe center.

4. Conclusions

Computational fluid dynamics model was developed to investigate the effect of the parameters related to the thick-wall pipe (wall thickness, pipe thermal conductivity, surrounding heat transfer coefficient and ambient temperature) on the transport profile of crude oil inside pipeline. It is found that all the obtained flow patterns from the developed CFD simulation program were quite similar. These results had good agreement with the information in the previous literatures. The profile without thick-wall pipeline was different from the one with thick-wall pipeline which confirmed the importance of thick-wall condition. The influences of various parameters on transport profile were analyzed using statistical experimental design. The result showed that surrounding heat transfer coefficient (C), ambient temperature (D) and their interaction (CD) had significant effect on the wax appearance distance near the pipe wall while the parameters that affected on the wax appearance distance near the pipe center were surrounding heat transfer coefficient (C) and ambient temperature (D). In addition, the obtained mathematical model can be used for optimizing the system problem. To apply this knowledge in real situation, pipeline system should be carefully designed based on the prevention of the occurrence of wax inside the pipeline.

Acknowledgements

The Scholarship from the Graduate School, the Chulalongkorn University graduate scholarship to commemorate the 72nd anniversary of his Majesty King Bhumibol Adulyadej Grant, and the CU Graduate School Thesis Grant, as well as, the Grant from Thailand Research Fund (IRG5780001/TRG5780205), PETROMAT and PTT Public Company Limited are gratefully acknowledged for financial support of this study.

References

[1] Jin H. Design and construction of a large-diameter crude oil pipeline in Northeastern China: a special issue on permafrost pipeline. Cold Reg Sci Technol 2010;64(3):209–12.

- [2] Frank IP, David PD, Theodore LB, Adrienne SL. Fundamentals of heat and mass transfer. 6th ed. United States: John Wiley; 2007. p. A3–6.
- [3] Li G, Sheng Y, Jin H, Ma W, Qi J, Wen Z, et al. Forecasting the oil temperatures along the proposed China-Russia Crude Oil Pipeline using quasi 3-D transient heat conduction model. Cold Reg Sci Technol 2010;64(3):209–12.
- [4] Adelaja AO, Dirker J, Meyer JP. Effects of the thick walled pipes with convective boundaries on laminar flow heat transfer. Appl Energy 2014;130(1):838–45.
- [5] Lu T, Wang K. Numerical analysis of the heat transfer associated with freezing/ solidifying phase changes for a pipeline filled with crude oil in soil saturated with water during pipeline shutdown in winter. J Petrol Sci Eng 2008;62(1– 2):52–5.
- [6] Wang W, Huang Q. Prediction for wax deposition in oil pipelines validated by field pigging. J Energy Inst 2014;87(3):196–207.
- [7] Zhu H, Yang X, Li J, Li N. Simulation analysis of thermal influential factors on crude oil temperature when double pipelines are laid in one ditch. Adv Eng Softw 2013;65:23–31.
- [8] Patankar SV. Numerical heat transfer and fluid flow, Series in computational methods in mechanics and thermal sciences. New York: McGraw-Hill; 1980. p. 11, 2
- [9] Verstreeg HK, Malalasekera W. An introduction to computational fluid dynamics: the finite volume method. 2nd ed. England: Longman; 2007. p. 1–2.
- [10] Jeong W, Seong J. Comparison of effects on technical variances of computational fluid dynamics (CFD) software based on finite element and finite volume methods. Int J Mech Sci 2014;78:19–26.
- [11] Alboudwarej H, Huo Z, Kempton E. Flow-assurance aspects of subsea systems design for production of waxy crude oils, Society of petroleum engineers. In: SPE annual technical conference and exhibition. San Antonio, Texas, USA; 2006, 24–27 September.
- [12] Guozhong Z, Gang L. Study on the wax deposition of waxy crude in pipelines and its application. J Petrol Sci Eng 2010;70(1-2):1-9.
- [13] Hec AY. Heavy crude oils: from geology to upgrading an overview. Paris: Technip; 2011. p. 209–14.
- [14] Tavakoli1 A, Baktash M. Numerical approach for temperature development of horizontal pipe flow with thermal leakage to ambient. Int J Modern Eng Res 2012;2:3784–94.
- [15] Rukthong W, Weerapakkaroon W, Wongsiriwan U, Piumsomboon P, Chalermsinsuwan B. Effect of thick wall on transport profile inside pipeline using computational fluid dynamics simulation. In: Proceedings of the international conference on chemical and material engineering, China; 2014.
- [16] Nouri-Borujerdi A, Ziaei-Rad M. Simulation of compressible flow in high pressure buried gas pipelines. Int J Heat Mass Transf 2009;52(25–26):5751–8.
- [17] Valinejad R, Nazar ARS. An experimental design approach for investigating the effects of operating factors on the wax deposition in pipelines. Fuel 2013;106:843–50.
- [18] Montogomery DC. Design and analysis of experiments. 7th ed. United State: John Wiley & Sons; 2009. p. 417–20.
- [19] Diodijo MRT, Belec L, Aragon E, Perrin FX, Bonnaudet M, Lanarde L, et al. Numerical modelling of pipe internal stresses induced during the coating process – influence of pipe geometric characteristics on stress state. Mater Des 2013;52:429–40.

ENGINEERING JOURNAL

Article

Computation of Biomass Combustion Characteristic and Kinetic Parameters by using Thermogravimetric Analysis

Wanwisa Rukthong¹, Phattharanid Thanatawee¹, Sasithorn Sunphorka¹, Pornpote Piumsomboon^{1,2}, and Benjapon Chalermsinsuwan^{1,2,*}

- ¹ Fuels Research Center, Department of Chemical Technology, Faculty of Science, Chulalongkorn University, 254 Phayathai Road, Patumwan, Bangkok 10330, Thailand
- 2 Center of Excellence on Petrochemical and Material Technology, Chulalongkorn University, 254 Phayathai Road, Patumwan, Bangkok 10330, Thailand
- *E-mail: benjapon.c@chula.ac.th (Corresponding author)

Abstract. In this study, the response surface methodology and simplex-lattice design were applied to investigate the effect of biomass constituents on the kinetics of biomass combustion, important information for process design. The synthetic biomass made from pure cellulose, xylan and Organosolv lignin was used instead of real biomass for this purpose. The combustion process was employed using thermogravimetric analyzer. The results obtained from three different kinetic models including Kissinger-Akahira-Sunose, Ozawa-Flynn-Wall and Analytical Method were provided and compared. According to the analysis of variances (ANOVA), the higher cellulose and hemicellulose fraction provided greater activation energy and frequency factor. The proposed regression models with high R² coefficient indicated that the predicted kinetic values and experimental data agreed very well. The contour plots generated from the proposed models were also provided in this study. They were used to observe the influence of biomass components on each kinetic parameter.

Keywords: Biomass, combustion, kinetic parameters, response surface methodology, TGA.

ENGINEERING JOURNAL Volume 19 Issue 2

Received 5 August 2014 Accepted 24 November 2014 Published 30 April 2015 Online at http://www.engj.org/ DOI:10.4186/ej.2015.19.2.41

1. Introduction

The energy crisis has been issued and driven to research and utilize renewable resources. Biomass is considered for energy purposes by partially substitution of coal and petroleum. The thermochemical conversion processes of biomass including pyrolysis, combustion and gasification are alternative ways for biomass conversion. Oxidation is the major technology for bioenergy production [1]. The biomass oxidation involves several simultaneous physical and chemical processes such as elimination of water, the release of volatile, fixed carbon production, dissociation of volatile matter into oil and gases, oxidation of produced gases and fixed carbon, and decarbonation [2]. However, the complexity in reaction mechanism and biomass structure leads to difficulty in prediction of behavior of biomass oxidation. The understanding in biomass oxidation process and estimation of kinetic parameters such as the activation energy, frequency factor and reaction order is very important for simulation and optimization of reactors. The appropriate models that achieve a better understanding of this process have been studied and many literatures proposed the mathematical models for kinetic modeling and decomposition profile of biomass oxidation [3–7].

Among the lab-scale apparatus, the thermogravimetric analysis (TGA) is a common technique to study the fundamental kinetic characteristics of biomass pyrolysis and oxidation. Therefore, some of literatures studied the behavior of biomass combustion in TGA. The kinetic parameters were then obtained from TGA data by using various methods, such as analytical, differential, and integral methods [8–12]. Chen *et al.* investigated the combustion behavior of *Chlorella vulgaris* microalgae by using TGA in O₂/N₂ atmospheres [11]. The activation energy of microalgae combustion at different oxygen concentration was calculated by iso-conversional methods including Ozawa–Flynn–Wall (OFW) and Kissinger–Akahira–Sunose (KAS) methods. By using FWO and KAS, the values of activation energy were 134.03–241.04 kJ/mol⁻¹ and 134.53–242.33 kJ/mol⁻¹, respectively. Idris *et al.* calculated the kinetic values for the oxidation of palm kernel shell, palm mesocarp fibre and empty fruit bunches from TGA data using model-free kinetics developed by Vyazovkin and Sbirrazzuoli [12]. The average apparent activation energies for the combustion of these biomasses were 139, 118 and 105 kJ/mol, respectively.

The prediction of kinetic parameters from biomass composition has also been focused in many literatures [8, 13–15]. López-González *et al.* investigated the combustion characteristics of biomass main components and three real biomasses [13]. The authors reported that the biomass oxidation behavior was influenced by its composition. Biomass with higher cellulose content shifted the devolatilization stage to lower temperatures and increased the decomposition rate whilst the lignin content affect the behavior of char oxidation stage. Conesa and Domene studied the decomposition of five biomasses in TGA and proposed global kinetic models [15]. The proposed model, derived under the assumption of simultaneous parallel decomposition reactions of three different organic fractions, provided a good agreement between predicted values and experimental values. From this point of view, the development of simplified kinetic model which can potentially predict the combustion behavior and kinetic values is still attractive.

Recently, the statistical techniques have been applied to investigate the relationship between input parameters and desired responses. The process information involving physical or chemical mechanism does not required in these techniques. The response surface methodology (RSM) is one of the mathematical and statistical techniques. It was commonly used to evaluate the effect of the individual factors on the desired output [16–20]. Among the several experimental design methods, the simplex-lattice design (SLD) was chosen to investigate the influence of correlated three factors. Therefore, it is suitable for applying to biomass process since the biomass has three main compositions: cellulose, hemicellulose and lignin (under dry, ash-free basis). In case of pyrolysis, Liu *et al.* used SLD to determine the interaction between the biomass components [18] whilst Yang *et al.* also employed the SLD to examine the relationship between biomass composition and weight loss during pyrolysis [20]. The effect of main biomass constituents on the weight loss profile was identified and the effect of their interactions on weight loss rate was observed. However, in case of combustion process, the application of this kind of mathematical and statistical model to this research field is still scarce.

In the present study, the effect of main biomass constituents and their interactions was screened and the simplified models for the prediction of kinetic values for biomass oxidation were developed using The RSM based on SLD. The synthetic biomass oxidation was observed in TGA. The kinetic values were then calculated using iso-conversional methods and analytical method. Finally, the relationship between biomass components and kinetic values were expressed in terms of cubic models. The statistical results and proposed models obtained from several kinetic methods were compared. In addition, contour plots were provided in this study and described in detail.

2. Materials and Methods

2.1. Materials

The synthesized biomass used in this work consisted of pure α -cellulose, hemicellulose (xylan), Organosolv lignin and their mixtures. Cellulose, hemicellulose, and lignin were purchased from Sigma Aldrich.

2.2. Experimental Design based on Simplex-lattice Design

The influences of cellulose, hemicellulose and lignin on decomposition behavior of biomass under oxidative atmosphere were studied using RSM with SLD. The kinetic parameters including activation energy (E_a), frequency factor (A) and reaction order (n) represented the decomposition behavior and used to simulate the decomposition profiles. With respect to SLD, the three-component system was designed as shown in Fig. 1. This figure also shows the ratios of each component. Thirteen combinations composed of three pure components, six points of two-component mixtures and four points of three-component mixtures. The summation between mass fraction of cellulose (X_t), mass fraction of hemicellulose (X_t) and mass fraction of lignin (X_t) must be one. For each combination, the experiments were performed using four constant heating rates with two replicates.

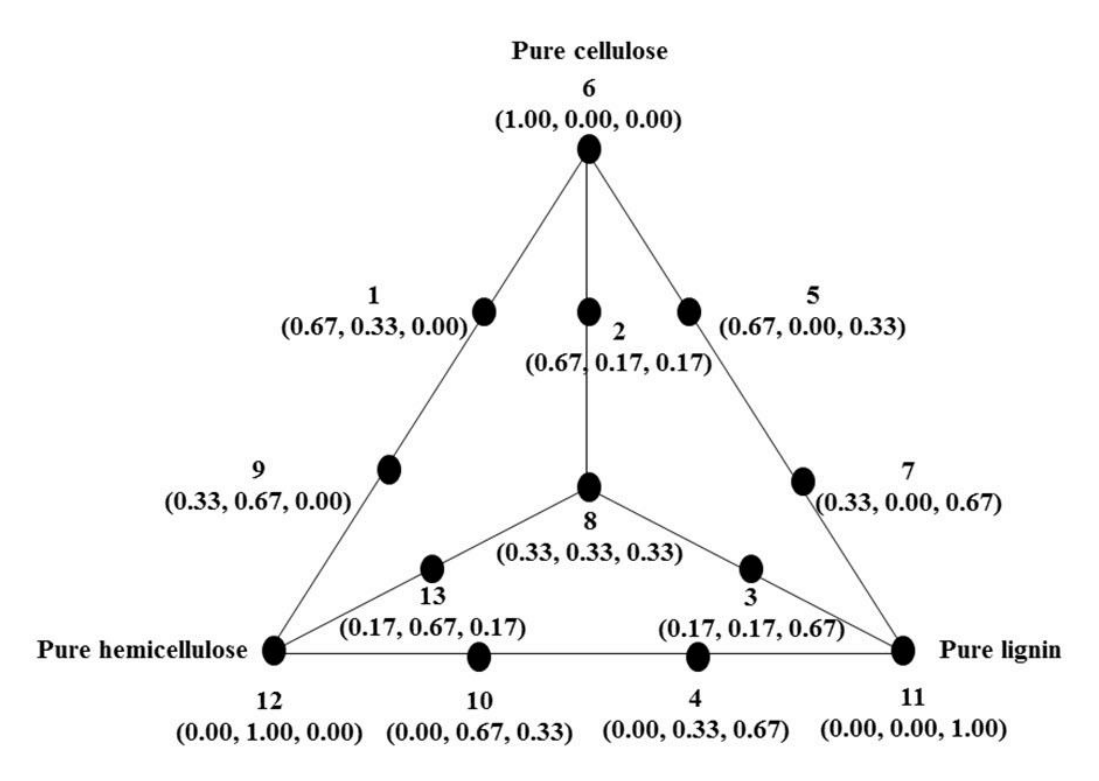


Fig. 1. 13 points augmented simplex lattice design. (Numbers in parenthesis represents mass fraction of cellulose, hemicellulose and lignin, respectively).

2.3. Thermogravimetric Analysis (TGA)

The weight loss and differential weight loss of synthesized biomass and real biomass oxidation as functions of temperature and time was observed using thermogravimetric/ differential thermal analyzer (Perkin Elmer TG/DTA Analyzer) under air atmosphere. The flow rate of air was 50 mL min⁻¹. Approximately 3.0 mg of sample was placed into an aluminium pan and then heated from 30 to 1000 °C at four linear heating rates (5, 10, 20 and 40 °C min⁻¹).

2.4. Derivation of Kinetic Parameters from TGA Data

For the non-isothermal system, the sample mass was recorded as a function of temperature and time. The rate of decomposition $(d\alpha/dt)$ can be expressed as:

$$\frac{d\alpha}{dt} = k(T)f(\alpha) \tag{1}$$

where a is the fraction of convertible part of biomass decomposed at any time t which is defined by Eq. (2) and k(T) is the rate constant given by Arrhenius equation. The function $f(\alpha)$ depends on the decomposition mechanism.

$$\alpha = \frac{W_0 - W}{W_0 - W_{ash}} \tag{2}$$

By applying Arrhenius equation and the constant heating rate ($\beta = dT/dt$), Eq. (1) can be written as Eq. (3).

$$\frac{d\alpha}{f(\alpha)} = \frac{A}{\beta} \exp\left(-\frac{E_a}{RT}\right) dT \tag{3}$$

where A is the frequency factor (s⁻¹), E_a is the activation energy (kJ/kmol), R is a gas constant (8.314 kJ/kmol.K) and T is the reaction temperature (K).

To simplify the equation, single step decomposition reaction was assumed. Therefore, function $f(\alpha)$ is defined as $(1-\alpha)^n$. Then, the integrated form of Eq. (3) for 1^{st} order and n^{th} order of reaction can be written as Eqs. (4) and (5), respectively.

For 1st order of reaction

$$\alpha = 1 - \exp\left\{-\frac{ART^2}{\beta E_a} \left(1 - \frac{2RT}{E_a}\right) \exp\left(-\frac{E_a}{RT}\right)\right\}$$
 (4)

For nth order of reaction

$$\alpha = 1 - \left\{ 1 - \left(n - 1 \right) \left(-\frac{ART^2}{\beta E_a} \right) \left(1 - \frac{2RT}{E_a} \right) \exp \left(-\frac{E_a}{RT} \right) \right\}^{\frac{1}{1 - n}}$$
 (5)

Hereafter, Eqs. (4) and (5) were called as analytical models. To calculate the kinetic parameters, the TGA curves were fitted with the analytical models by means of maximizing the regression coefficient (R²). Then, a set of kinetic values those shows the better fit to the TGA data will be chosen for developing the correlation between biomass compositions and kinetic parameters.

In this study, other well-known kinetic models including Kissinger-Akahira-Sunose Model (KAS) and Ozawa-Flynn-Wall (OFW) were also applied for the calculation. These iso-conversional methods also consider the single step decomposition reaction as analytical models [21]. Eq. (3) was rearranged and function $g(\alpha)$ was given as Eq. (6).

$$g(\alpha) = \int_0^\alpha \frac{d\alpha}{f(\alpha)} = \int_0^\alpha \frac{A}{\beta} \exp\left(-\frac{E_a}{RT}\right) dT = \frac{AE_a}{\beta R} p\left(\frac{E_a}{RT}\right)$$
 (6)

where the term $p(E_a/RT)$ is the temperature integral. The difference of KAS and OFW methods is due to the approximation for solving the equation. In case of KAS, the approximation is proposed to be [22–24]:

$$p\left(\frac{E_a}{RT}\right) = \exp\left(-\frac{E_a}{RT}\right) \times \left(\frac{E_a}{RT}\right)^{-2} \tag{7}$$

Substitutes Eq. (7) into Eq.(6) and takes logarithm. Then, Eq. (6) becomes:

$$\ln\left(\frac{\beta}{T^2}\right) = \ln\left(\frac{AE_a}{Rg(\alpha)}\right) - \frac{E_a}{RT} \tag{8}$$

The E_a and A can be calculated by plotting curve of $\ln(\beta/T^2)$ against 1/T.

In case of OFW, The approximation of this model is based on Doyle's approximation [22, 25–27]. Therefore, Eq. (6) becomes:

$$\log \beta = \log \left(A \frac{E_a}{Rg(\alpha)} \right) - 2.315 - 0.457 \left(\frac{E_a}{RT} \right) \tag{9}$$

The E_a and A can be calculated by plotting curve of log (β) against 1/T. In case of any order n of KAS and OFW methods, n was calculated by Kissinger index of shape equation using differential thermal analysis (DTA) curves [23, 28]. The $g(\alpha)$ is equal to $-\ln(1-\alpha)$ for first-order kinetics and $(n-1)^{-1}(1-\alpha)^{(1-n)}$ for any order n.

2.5. Statistical Analysis and Mathematical Model

A statistical test called ANOVA (analysis of variance) and response surface methodology (RSM) were used to evaluate the effect of each biomass constituent, determine the most significant factor on the desired response (E_a , A or n obtained from various methods) and also generate the statistical models for predicting the kinetic parameters. The values of each response were transformed by taking natural logarithm previous to the statistical analysis in order to satisfy assumptions of linearity and homogeneity of variance. The ANOVA tables of response surface model for each response were provided to summarize the test performed. The Model p-value below 0.05 implies the model is significant.

Since the response was the function of mass fraction of cellulose, hemicellulose and lignin, the behavior of the response could be explained by the following cubic equation (Eq. (10)) [17, 19].

$$\ln Y = a_1 X_1 + a_2 X_2 + a_3 X_3 + a_{12} X_1 X_2 + a_{13} X_1 X_3 + a_{23} X_2 X_3 + a_{123} X_1 X_2 X_3 + a_{1-2} X_1 X_2 (X_1 - X_2) + a_{1-3} X_1 X_3 (X_1 - X_3) + a_{2-3} X_2 X_3 (X_2 - X_3)$$
(10)

where $\ln Y$ is natural logarithm of estimated response. The a_1 , a_2 , a_3 , a_{12} , a_{13} , a_{123} , a_{1-2} , a_{1-3} and a_{2-3} are constant coefficients for linear and non-linear (interaction) terms. The models were also used to generate the ternary contour plots in order to observe the influence of biomass compositions on E_a , A and n. The models and ternary contour plots for estimated kinetic values obtained from different kinetic models were produced to observe the individual effects of the selected factors and interactions between them. Moreover, these generated models and ternary plots were compared to each other as well.

3. Results and Discussion

3.1. Combustion of Main Chemical Compositions of Biomass and Their Mixtures

Combustion of the main chemical compositions of biomass including cellulose, hemicelluloses, lignin and their blends were studied using a TGA analyzer. Fig. 2 shows the weight loss profiles and rate of weight loss curves as a function of temperature at a heating rate of 5 °C/min.

It could be found that significant variations between different compositions existed due to differences in their chemical compositions. From Fig. 2(a), two decomposition zones were observed for both cellulose and hemicellulose combustion. The first decomposition zone was taken account to the pyrolytic reactions of biomass components. The degradation reaction is accompanied by the release of water, gaseous products and eventual formation of char [8]. During combustion reaction, with a presence of oxygen, the char residues underwent ignition resulting in an appearance of the second decomposition zone. Compared to hemicellulose combustion, the weight loss of cellulose started at higher temperature and finished at lower temperature. This behavior is attributed to the fact that the cellulose composes of only one simple repeating unit, cellubiose. Therefore, cellulose decomposes through a rapid depolymerization process by cleavage of glycosidic bonds during the combustion process [29]. In contrast, xylan, which was used as hemicellulose model in this work, was the least thermally stable component of biomass. The onset temperature of xylan combustion was lower than that of cellulose. Fig. 2(d) also illustrated that the maximum of weight loss in case of xylan combustion occurred at lower temperature than that of cellulose combustion. For the blending of cellulose and hemicellulose, as shown in Fig. 2(a) and 2(d), TG and DTG curves of the blends laid between those of the individual biomass components. At higher blending ratio of hemicellulose (xylan), more volatiles of polypentose was released which shifted the volatile release onset temperature to lower value.

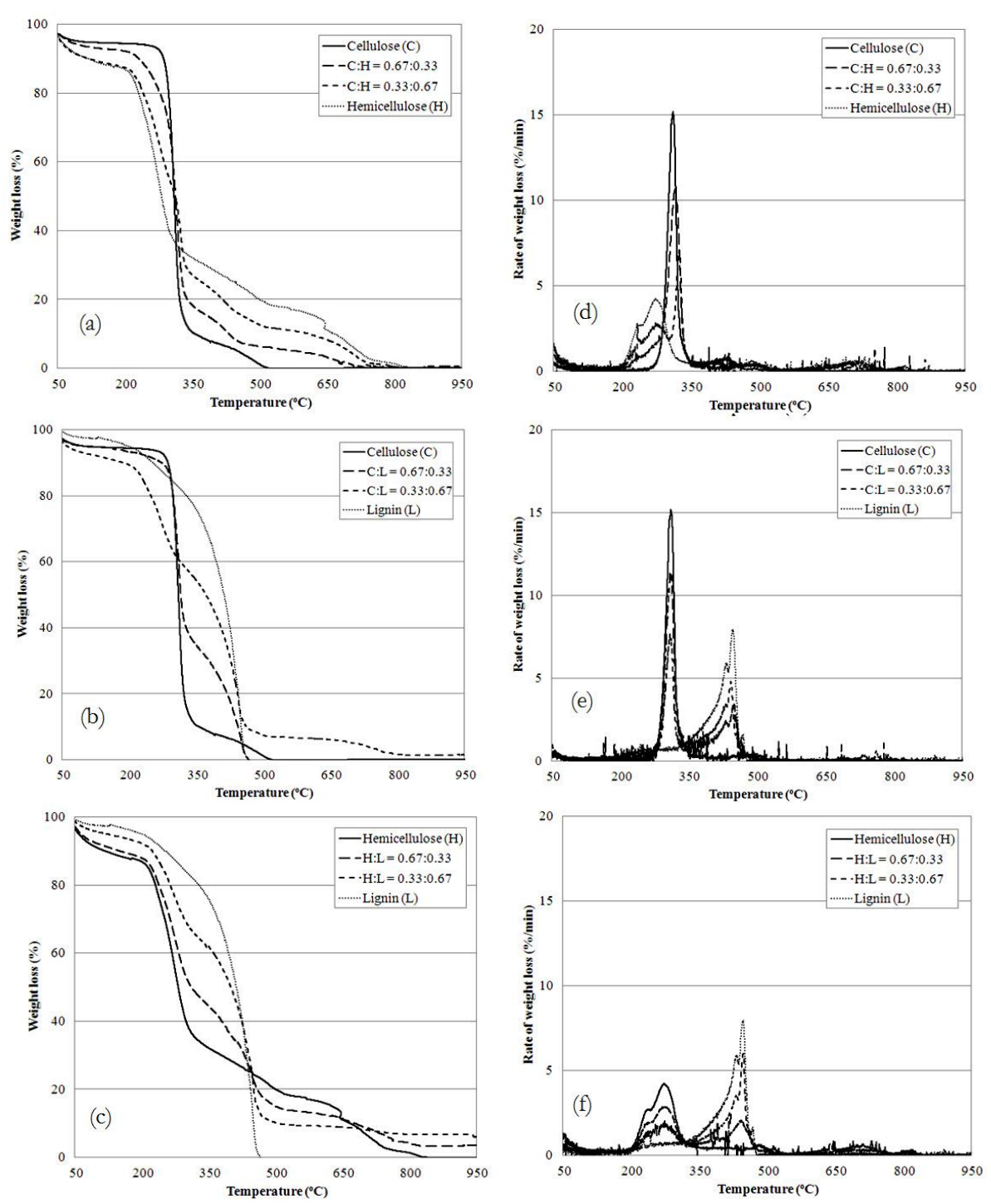


Fig. 2. TGA data for the combustion of cellulose/hemicellulose (a), cellulose/lignin (b) and hemicellulose/lignin (c) and DTG data for the combustion of cellulose/hemicellulose (d), cellulose/lignin (e) and hemicellulose/lignin (f).

Fig. 2(b) and 2(c) shows the comparison of TGA data between lignin combustion and other components. It could be seen that lignin shows a gradual decomposition over a broad temperature range. It started to decomposition at lower temperature compared to cellulose whilst its final decomposition temperature was higher than that of hemicellulose since it makes of aromatic compounds that have numerous branches and heavily cross linked. The complicated interconnected structure provided high thermal stability to lignin. The maximum weight loss rate of lignin thus appeared at the highest temperature. From Fig. 2(e) and 2(f), the numbers of DTG peaks corresponded to the main decompositions. In case of

blending, the magnitude of peaks related to the blending ratios and laid between those of the individual biomass components.

3.2. Evaluation of Kinetic Values

The kinetic values of synthetic biomass combustion calculated from KAS, OFW and Analytical methods are presented in Table 1(a), 1(b) and 1(c), respectively. The combustion of each synthetic biomass blending ratio were conducted at 4 heating rates with 2 replicates. The results demonstrated that kinetic values calculated from KAS (Table 1(a)) were comparable to those calculated from OFW (Table 1(b)) since they were developed from the same procedure, excepting an approximation of temperature integral term. For KAS and OFW methods, it should be noted that the values of E_a calculated from first-order and any-order kinetics had the same values. The E_a was calculated from the slope of linear plots without any influence of other parameters whilst the A and n were calculated from the intercept of linear plots. In addition, the values of n calculated from both KAS and OFW methods were equal because they were calculated from the same DTA curve.

From Table 1(a) and 1(b), the E_a and A were about 88 – 141 kJ/mol and 1E+5 – 8E+12 min⁻¹ whilst n were approximately 1.2 – 1.7. It could be observed that synthetic biomass with high lignin blending ratios (Sample code 3, 4 and 7) and pure lignin (Sample code 11) gave relatively low E_a and A. It was because of the complexity of lignin structure as mention earlier. The decomposition of lignin composes of several chemical reactions, including the cleavage of α - and β -aryl-aryl-ether linkages, splitting of aliphatic side chains from the aromatic rings and cleavage of carbon-carbon linkage between lignin units [30], which occurs simultaneously. Coincidentally, oxygen in air promoted the formation of volatiles and gasified the residue. In cases of cellulose and xylan combustion, the decomposition of these components occurred faster than lignin since they have much simpler repeating unit. Therefore, the E_a and A provided from these cases were higher than a case of lignin combustion. However, the results exhibited that the values of E_a and A obtained from the blends cannot be calculated from the arithmetic method, indicating the interaction between each component.

Considering the Analytical method, the calculated E_a and \mathcal{A} (for both cases of first-order kinetic and any-order kinetics) values were higher than those obtained from other cases. Moreover, the relationship between kinetic values calculated from this method and biomass composition was not obviously observed, especially a case of first-order kinetic.

Table 1. Predicted kinetic values obtained from different kinetic models.

(a)	KAS

Sample	n=1	1	1	n≠1	
code	$E_a(\mathrm{kJ/mol})$	A (min-1)	$E_a(\mathrm{kJ/mol})$	A (min-1)	n
1	101.2	1.4E+08	101.2	2.3E+08	1.6
2	138.6	2.8E+11	138.6	4.2E+11	1.4
3	86.2	1.5E + 05	86.2	2.3E+05	1.5
4	88.4	2.4E + 05	88.4	4.4E+05	1.7
5	119.1	5.0E+09	119.1	9.3E+09	1.6
6	103.8	3.6E + 08	103.8	6.4E + 08	1.6
7	88.2	2.6E + 05	88.2	3.0E + 05	1.2
8	113.9	1.7E + 09	113.9	2.4E+09	1.4
9	119.1	5.0E+09	119.1	9.3E+09	1.6
10	137.2	2.9E+12	137.2	4.6E+12	1.5
11	98.2	1.3E+06	98.2	2.0E+06	1.5
12	121.4	9.5E+10	121.4	1.5E+11	1.5
13	120.5	6.9E+09	120.5	1.4E+10	1.7

(b) OFW

Sample	n=	1	1	n≠1	
code	$E_a(\mathrm{kJ/mol})$	A (min-1)	$E_a(\mathrm{kJ/mol})$	A (min-1)	n
1	106.0	5.1E+08	106.0	8.7E+08	1.6
2	141.5	5.7E+11	141.5	8.4E+11	1.4
3	94.1	1.2E+06	94.1	1.8E+06	1.5
4	96.1	1.7E + 06	96.1	3.2E + 06	1.7
5	132.0	1.6E+11	132.0	2.5E+11	1.5
6	108.4	1.3E+09	108.4	2.2E+09	1.6
7	95.9	1.9E+06	95.9	2.2E + 06	1.2
8	118.2	5.1E+09	118.2	7.3E+09	1.4
9	123.1	1.4E+10	123.1	2.6E+10	1.6
10	139.5	5.2E+12	139.5	8.1E+12	1.5
11	105.5	7.6E + 06	105.5	1.2E + 07	1.5
12	124.4	2.1E+11	124.4	3.4E+11	1.5
13	124.4	1.9E+10	124.4	3.7E+10	1.7

(c) Analytical models

Sample	n=1	1		n≠1	
code	$E_a(\mathrm{kJ/mol})$	A (min-1)	$E_a(\mathrm{kJ/mol})$	A (min-1)	n
1	127.9	5.1E+08	114.8	8.7E+08	1.4
2	159.6	2.8E+11	145.0	3.6E+11	1.4
3	152.0	1.5E+09	117.5	2.3E + 08	1.3
4	149.9	1.0E+09	100.0	2.8E + 07	1.3
5	154.2	6.9E+10	127.7	2.0E+10	1.3
6	123.7	3.6E + 08	116.7	6.4E + 08	1.6
7	151.0	2.6E + 08	100.0	2.4E+08	1.2
8	139.5	2.2E + 09	113.2	2.4E+09	1.2
9	140.5	1.4E+10	113.7	2.6E+10	1.2
10	167.5	2.8E+12	134.6	5.0E + 12	1.1
11	155.2	8.3E + 08	107.6	4.0E + 07	1.4
12	174.4	5.2E+12	114.8	2.4E+11	1.2
13	143.9	1.5E+10	114.4	1.8E+10	1.1

The difference between Analytical method and the others occurred because this method attempted to fit the model with experimental data without considering the combustion behavior. The apparent kinetic values provided by this method came from the average of 8 individual experiments (4 heating rates with 2 replicates) whilst iso-conversional method, KAS and OFW methods, approximated the reaction order from DTA data and calculate other kinetic values from larger information (simultaneously calculated the E_a and A from 4 heating rates and progress of conversion). However, Analytical method for any-order kinetic provided more comparable kinetic values to iso-conversional method. As can be seen in Fig. 3, the conversion curve obtained from a case of any-order kinetic showed the better fit to an experimental data and gave very high R^2 (0.98) compared to that obtained from a case of first-order kinetic (0.94). Therefore, an apparent reaction order of biomass combustion was greater than one.

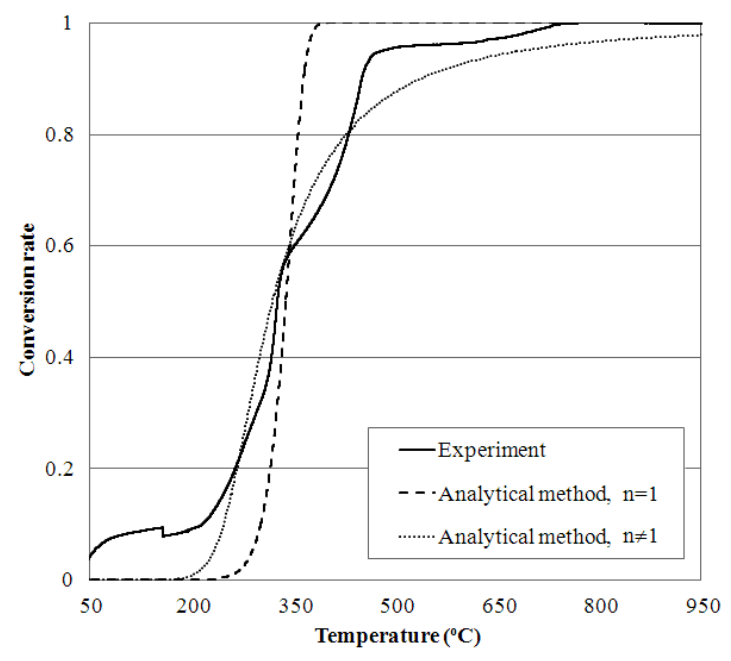


Fig. 3. Relationship between temperature and conversion (wt./wt.) of biomass pyrolysis obtained from Analytical methods for first-order kinetics and any-order kinetics.

3.3. Statistical Analysis and Modeling

3.3.1. Analysis of variance

After transforming the data by applying natural logarithm, the effects for all model terms were calculated. The statistical values such as F-value and p-value were used for indicating the factors those had significant effect on the response. ANOVA results for kinetic values obtained from KAS, OFW and Analytical methods have been summarized in Table 2(a), 2(b) and 2(c), respectively. The very low probability values (<0.05) indicated that all the linear terms of individual biomass components (X_1 , X_2 and X_3) were statistically significant for frequency factor estimated by using KAS and OFW methods. In addition, in case of OFW method, an interaction term between mass fraction of cellulose and lignin, $X_1X_3(X_1 - X_3)$, had significant effect on frequency factor and activation energy as well. However, the statistical results showed that none of cubic terms was the prominent factor that had significant effect on reaction order obtained by using KAS and OFW methods.

In case of Analytical method, the linear terms were found to have remarkable effects on activation energy (first-order kinetic) and reaction order. Moreover, some interaction terms such as X_1X_3 , $X_1X_2(X_1 - X_2)$ and $X_2X_3(X_2 - X_3)$ also had significant effect on reaction order whilst the other factors were not significantly influential (P > 0.05). To show the interactions between mass and the kinetic values, the regression models were generated and contour plots were profiled as discussed further down.

Table 2. The analysis of variance (ANOVA) for biomass oxidation kinetics obtained from different methods.

(a) KAS

	DF		Sum of	Sum of Squares			Mean	Mean Square			F-Value	alue			p-valu	p-value > F	
Source		E	A (first order)	A (any order)	u	E	A (first order)	(any order)	u	E_{s}	A (first order)	(any order)	u	E	A (first order)	(any order)	u
Linear	2	0.12	203.61	209.65	0.02	90.0	101.80	104.83	0.01	6.18	11.73	13.04	1.42	0.09	0.04*	0.03*	0.37
X,X2	-	<0.01	4.57	4.35	<0.01	< 0.01	4.57	4.35	<0.01	0.05	0.53	0.54	60.0	0.83	0.52	0.52	0.78
X_iX_j	-	<0.01	1.27	0.99	0.01	<0.01	1.27	0.99	0.01	0.12	0.15	0.12	1.47	0.75	0.73	0.75	0.31
ζ_{X_3}	-	<0.01	0.19	0.32	0.01	<0.01	0.19	0.32	0.01	0.01	0.02	0.04	0.79	0.94	0.89	0.85	0.44
$X_1X_2X_3$	-	<0.01	2.71	2.43	<0.01	<0.01	2.71	2.43	<0.01	0.46	0.31	0.30	0.21	0.54	0.62	0.62	0.68
$X_1X_2(X_1-X_2)$	-	<0.01	2.92	2.17	0.02	<0.01	2.92	2.17	0.02	0.03	0.34	0.27	2.44	0.86	09.0	0.64	0.22
$X_iX_j(X_i-X_j)$	-	0.07	51.06	54.58	0.03	0.07	51.06	54.58	0.03	7.43	5.88	6.79	3.84	0.07	60.0	0.08	0.14
$X_2X_3(X_2-X_3)$	_	0.05	59.46	57.51	0.01	0.05	59.46	57.51	0.01	5.57	6.85	7.15	06.0	0.10	0.08	0.08	0.41
otal	12	0.03	26.04	24.12	0.02												

(b) OFW

	DF		Sum of	Sum of Squares			Mean	Mean Square			F-Value	lue			p-value > F	e > F	Œ.
Source		E	A	A	u	$E_{\rm s}$	Ą	¥	u	E	A	Ą	u	$E_{\rm s}$	¥	¥	и
			(first	(any			(first	(any			(first	(any			(first	(any	
			order)	order)			order)	order)			order)	order)			order)	order)	
Linear	7	0.07	160.99	166.85	0.02	0.04	80.49	83.42	0.01	5.80	13.05	14.59	2.19	60.0	0.03*	0.03*	0.26
Mixture																	
X_1X_2	-	<0.01	4.35	4.10	<0.01	<0.01	4.35	4.10	<0.01	90.0	0.70	0.72	0.16	0.83	0.46	0.46	0.72
X_iX_j	H	<0.01	5.15	4.31	0.02	<0.01	5.15	4.31	0.02	0.73	0.83	0.75	3.58	0.45	0.43	0.45	0.15
X_2X_3	-	<0.01	0.29	0.44	0.01	<0.01	0.29	0.44	0.01	<0.01	0.05	0.08	0.98	0.98	0.84	0.80	0.40
$X_iX_2X_3$	-	<0.01	89.0	0.59	<0.01	<0.01	0.68	0.59	<0.01	0.23	0.11	0.10	0.07	99.0	0.76	0.77	0.81
$X_iX_2(X_i-X_2)$	-	<0.01	1.31	0.88	0.02	<0.01	1.31	0.88	0.02	<0.01	0.21	0.15	2.69	0.98	0.68	0.72	0.20
$X_iX_j(X_i-X_j)$	-	0.08	60.95	63.61	0.02	0.08	60.95	63.61	0.02	11.71	9.88	11.12	2.99	0.04*	0.05*	0.04*	0.18
$X_2X_3(X_2-X_3)$	-	0.04	47.45	45.88	0.01	0.04	47.45	45.88	0.01	5.97	7.69	8.02	1.09	60.0	0.07	0.07	0.37
Total	12	0.24	331.53	335.26	0.11												

50

(c) Analytical method

	DF		Su	Sum of Squares	nares			Mea	Mean Square	e e			H	F-Value				I	p-value > F	> F	
Source	8	E_{s}	$E_{\rm s}$	A	Ą	и	E	E,	Ą	¥	п	E	E_{s}	A	Ą	и	E_s	E	A	¥	п
		(first	(any	(first	(any			(any		(any		(first	(any	(first	(any		(first	(any	(first	(any	
		order)	order)	order)	order)			order)	order)	order)		order)	orde	order)	order)		order)			order)	8
Linear	7	0.05	0.04	203.16	75.40	90.0	0.02	0.02	101.58 37.70	37.70	0.03	4.61	1.2	11.69	4.40	149.01	0.12	0.41	0.04*	0.13	<0.01*
Mixture																					
X_iX_j	, ,	0.01	<0.01	4.60	1.34	< 0.01	0.01	<0.01	4.60	1.34	<0.01	1.65	0.04	0.53	0.16	5.20	0.29	0.85	0.52	0.72	0.11
X_iX_j		0.01	<0.01	1.33	10.79	0.02	0.01	<0.01	1.33	10.79	0.02	2.44	0.08	0.15	1.26	105.85	0.22	0.80	0.72	0.34	<0.01*
X_2X_3	-	<0.01	< 0.01	0.16	1.03	< 0.01	<0.01	<0.01	0.16	1.03	< 0.01	0.42	0.10	0.02	0.12	1.33	0.56	0.78	06.0	0.75	0.33
$X_iX_2X_3$	-	<0.01	< 0.01	2.75	0.08	< 0.01	<0.01	<0.01	2.75	80.0	< 0.01	0.05	0.13	0.32	0.01	2.28	0.84	0.74	0.61	0.93	0.23
$X_tX_2(X_t-X_2)$	-	0.01	0.01	2.89	2.67	<0.01	0.01	0.01	2.89	2.67	< 0.01	1.24	0.46	0.33	0.31	11.60	0.35	0.54	09.0	0.62	0.04*
$X_tX_3(X_t-X_3)$	Н	0.01	0.02	51.07	10.09	<0.01	0.01	0.02	51.07	10.09	< 0.01	1.95	1.37	5.88	1.18	0.13	0.26	0.33	60.0	0.36	0.75
$X_2X_3(X_2-X_3)$	-	<0.01	0.01	59.61	24.19	0.01	<0.01	0.01	59.61	24.19	0.01	90.0	0.77	98.9	2.82	27.97	0.82	0.44	0.08	0.19	0.01*
Total	12	0.11	0.13	380.68	163.86	0.10															

3.3.2. Modeling and ternary contour plot

Generally, the model terms in the cubic equation were calculated after elimination of some insignificant variables and their interactions which have the low p-value (<0.05). However, in this study, all terms were included in the models to maximize the accuracy, in terms of R^2), of models. The generated regression models for kinetic values obtained from KAS, OFW and Analytical methods have been summarized in Table 3. For KAS and OFW methods, the regression models with high R^2 values (varied from 0.91 – 0.95) for predicting E_a and A (6 models) are obtained. These high R^2 coefficients ensured a fitting of the cubic models to the experimental data. Therefore, these models could be used to predict the E_a and A values from mass fractions of biomass compositions. However, in case of n, the R^2 values were relatively low (0.80 for KAS method and 0.84 for OFW method) but they were probably acceptable. Therefore, these proposed models were accurately employed for predicting kinetic parameters of synthetic biomass combustion. In case of Analytical method, R^2 coefficients indicated that the proposed regression models provided quite lower accurate kinetic values, excepted n. As mentioned earlier, this method was used to calculate the apparent kinetic values by forced fitting the model to TGA curve. The calculated kinetic values were quite poorly used to describe the biomass combustion behavior and also the relationship between biomass components.

Table 3. The regression models for biomass pyrolysis kinetics obtained from different methods.

Response		Regression models in terms of actual factors	\mathbb{R}^2	SD
KAS	E_a	$\operatorname{Ln} E_a = 4.64X_1 + 4.81X_2 + 4.59X_3 - 0.10X_1X_2 + 0.15X_1X_3 - 0.04X_2X_3 + 1.97X_1X_2X_3$	0.91	0.10
		$+ 0.16X_1X_2(X_1 - X_2) + 2.30X_1X_3(X_1 - X_3) + 2.00X_2X_3(X_2 - X_3)$		
	A (first	$\operatorname{Ln} A = 19.55X_1 + 25.46X_2 + 14.02X_3 - 9.54X_1X_2 + 5.04X_1X_3 + 1.94X_2X_3$	0.93	2.95
	order)	$+47.95X_1X_2X_3+14.60X_1X_2(X_1-X_2)+60.87X_1X_3(X_1-X_3)$		
		$+65.70X_2X_3(X_2-X_3)$		
	A (any	$\operatorname{Ln} A = 20.14X_1 + 25.91X_2 + 14.43X_3 - 9.31X_1X_2 + 4.45X_1X_3 + 2.53X_2X_3$	0.94	2.84
	order)	$+45.41X_1X_2X_3+12.58X_1X_2(X_1-X_2)+62.93X_1X_3(X_1-X_3)$		
		$+64.61X_2X_3(X_2-X_3)$		
	n	Ln $n = 0.48X_1 + 0.41X_2 + 0.37X_3 + 0.12X_1X_2 - 0.47X_1X_3 + 0.35X_2X_3 - 1.17X_1X_2X_3$	0.80	0.09
		$-1.17X_1X_2(X_{1^{-}}X_2) + 1.46X_1X_3(X_{1^{-}}X_3) - 0.71X_2X_3(X_{2^{-}}X_3)$		
OFW	E_a	Ln $E_a = 4.68X_1 + 4.83X_2 + 4.66X_3 - 0.09X_1X_2 + 0.31X_1X_3 - 0.01X_2X_3 + 1.12X_1X_2X_3$	0.92	0.08
		$+0.01X_1X_2(X_1-X_2) + 2.34X_1X_3(X_1-X_3) + 1.67X_2X_3(X_2-X_3)$		
	A (first	Ln $A = 20.85X_1 + 26.23X_2 + 15.77X_3 - 9.30X_1X_2 + 10.12X_1X_3 + 2.38X_2X_3$	0.94	2.48
	order)	$+23.93X_{1}X_{2}X_{3}+9.79X_{1}X_{2}(X_{1}-X_{2})+66.71X_{1}X_{3}(X_{1}-X_{3})$		
	•	$+58.86X_2X_3(X_2-X_3)$		
	A (any	$\operatorname{Ln} A = 21.43X_1 + 26.70X_2 + 16.18X_3 - 9.04X_1X_2 + 9.26X_1X_3 + 2.94X_2X_3$	0.95	2.39
	order)	$+22.38X_1X_2X_3+8.01X_1X_2(X_1-X_2)+68.15X_1X_3(X_1-X_3)$		
		$+ 57.88X_2X_3(X_2-X_3)$		
	n	Ln $n = 0.48X_1 + 0.41X_2 + 0.37X_3 + 0.13X_1X_2 - 0.64X_1X_3 + 0.33X_2X_3 - 0.59X_1X_2X_3$	0.84	0.08
		$-1.05X_1X_2(X_{1^{-}}X_2) + 1.11X_1X_3(X_{1^{-}}X_3) - 0.67X_2X_3(X_{2^{-}}X_3)$		
Analytical	E_a (first	$\operatorname{Ln} E_a = 4.82X_1 + 5.17X_2 + 5.05X_3 - 0.41X_1X_2 + 0.50X_1X_3 - 0.21X_2X_3 - 0.46X_1X_2X_3$	0.86	0.07
method	order)	$+ 0.68X_1X_2(X_1-X_2) + 0.85X_1X_3(X_1-X_3) + 0.15X_2X_3(X_2-X_3)$		
	E_a (any	$\operatorname{Ln} E_a = 4.76X_1 + 4.76X_2 + 4.68X_3 - 0.12X_1X_2 + 0.15X_1X_3 + 0.17X_2X_3 + 1.32X_1X_2X_3$	0.64	0.13
	order)	$+0.73X_1X_2(X_1-X_2)+1.26X_1X_3(X_1-X_3)+0.94X_2X_3(X_2-X_3)$		
	A (first	$\operatorname{Ln} A = 19.56X_1 + 25.46X_2 + 14.02X_3 - 9.57X_1X_2 + 5.15X_1X_3 + 1.77X_2X_3$	0.93	2.95
	order)	$+48.20 X_1X_2X_3 + 14.53X_1X_2(X_1-X_2) + 61.06 X_1X_3(X_1-X_3)$		
		$+65.98 X_2X_3(X_2-X_3)$		
	A (any	$\operatorname{Ln} A = 20.26X_1 + 26.47X_2 + 17.53X_3 - 5.17X_1X_2 + 14.66X_1X_3 + 4.52X_2X_3$	0.84	2.93
	order)	$-8.23X_{1}X_{2}X_{3} + 13.96X_{1}X_{2}(X_{1}-X_{2}) + 27.14X_{1}X_{3}(X_{1}-X_{3})$		
		$+42.03 X_2 X_3 (X_2 - X_3)$		
	n	$\operatorname{Ln} n = 0.44X_1 + 0.14X_2 + 0.30X_3 - 0.15X_1X_2 - 0.68X_1X_3 - 0.08X_2X_3 + 0.65X_1X_2X_3$	0.99	0.01
		$+ 0.43X_1X_2(X_1-X_2) + 0.04X_1X_3(X_1-X_3) - 0.66X_2X_3(X_2-X_3)$		

The contour plots in Fig. 4–6 show the effects of mass fraction of cellulose, hemicellulose and lignin on activation energy, frequency factor and reaction order obtained from different methods. Fig. 4(a), 4(b) and 4(d) illustrate that the synthetic biomass with high cellulose-hemicellulose content and low lignin content requires high E_a for combustion process. Fig. 5 confirmed again the influence of biomass composition on the variation of A. The higher cellulose-hemicellulose blend provided higher value of A. Fig. 6 shows the influence of biomass composition on variation of n. It could be difficult to observe the

trend. However, Fig. 6(c) which was obtained from Analytical method suggested that higher cellulose content provided higher reaction order whilst higher hemicellulose content provided lower value.

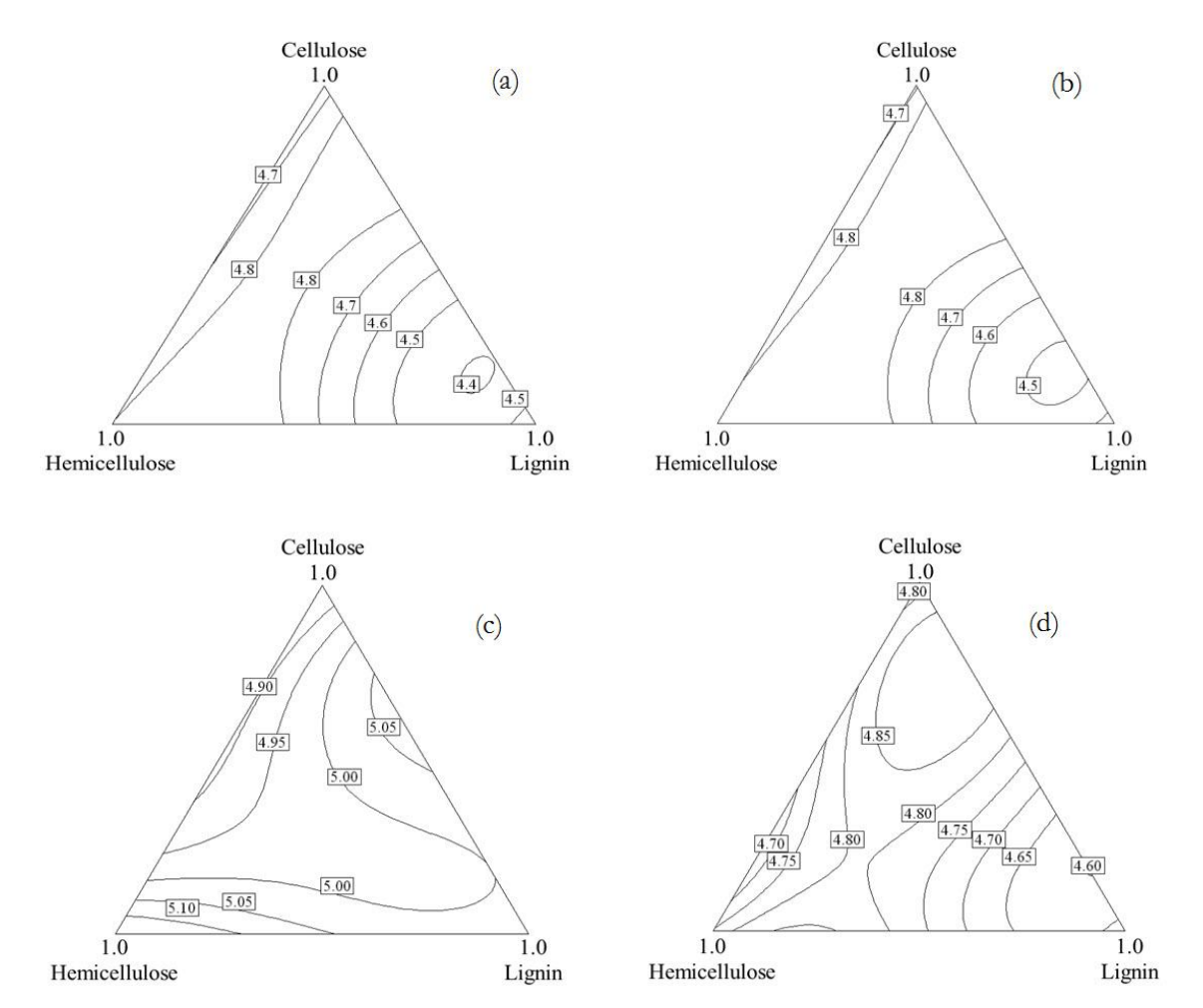


Fig. 4. Contour plots of predicted $\ln E_a$ for synthetic biomass combustion obtained from KAS method (a), OFW method (b), Analytical method for first-order kinetics (c) and Analytical method for any-order kinetics (d).

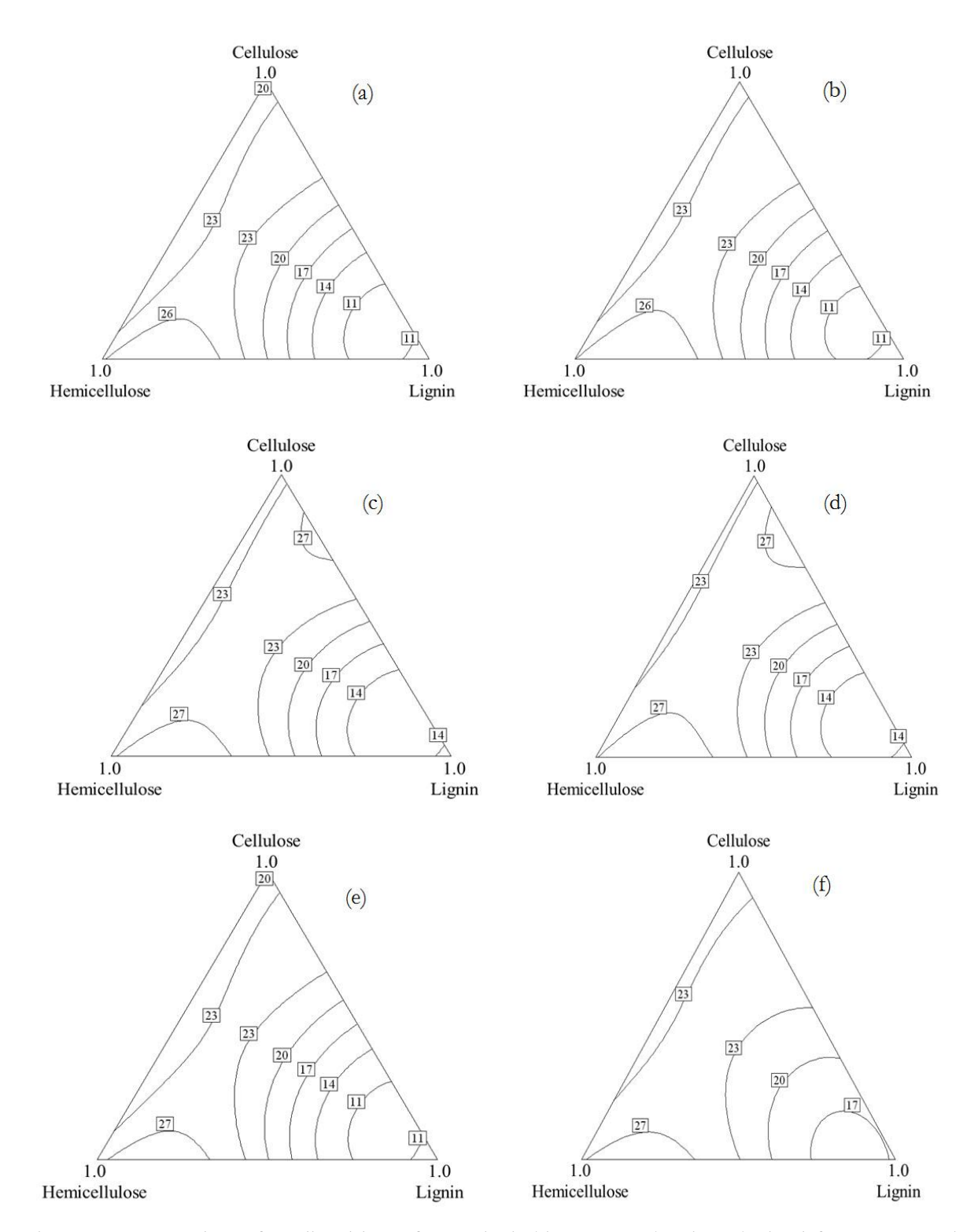


Fig. 5. Contour plots of predicted ln A for synthetic biomass combustion obtained from KAS method for first-order kinetics (a), KAS method for any-order kinetics (b), OFW method for first-order kinetics (c), OFW method for any-order kinetics (d), Analytical method for first-order kinetics (e) and Analytical method for any-order kinetics (f).

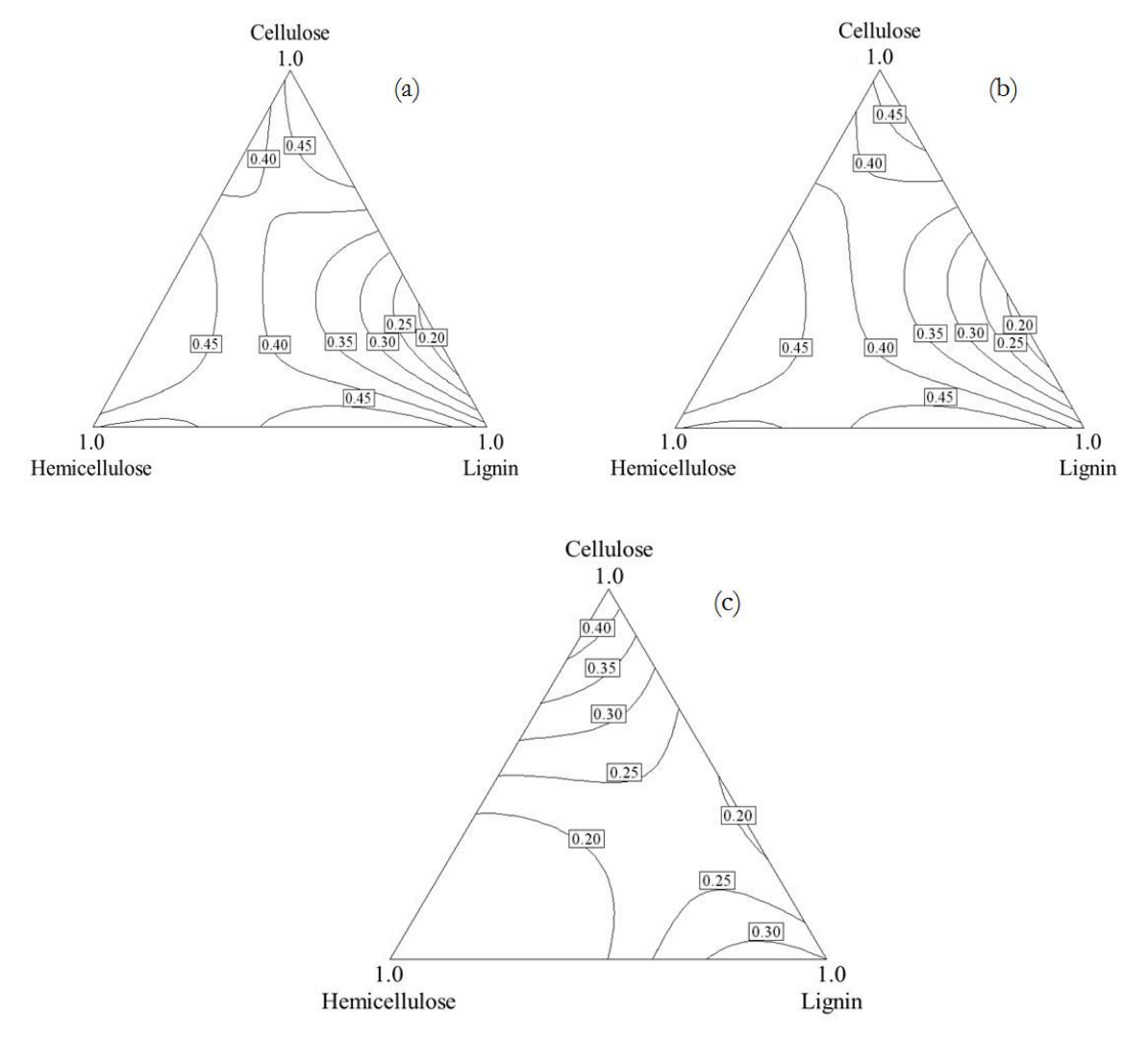


Fig. 6. Contour plots of predicted ln *n* for synthetic biomass combustion obtained from KAS method (a), OFW method (b) and Analytical method (c).

4. Conclusions

The effect of biomass composition on kinetic values for biomass combustion process was investigated. Based upon the experiments which were designed by using Simplex-lattice design, the RSM was used to observe the effect of cellulose, hemicellulose and lignin content and indicate the factors those have significant effect on the kinetic values. The results showed that the kinetic values calculated from KAS and OFW methods provided more reliable values compared to those calculated from Analytical method. The higher cellulose and hemicellulose fraction led to higher activation energy and frequency factor. By applying RSM, the statistical analysis also confirmed that all main variables could be considered significant. The proposed regression models with very high R² coefficients demonstrated that experimental data were in close agreement with the predicted values. The RSM with Simplex-lattice design provided good information about the prediction of apparent kinetic values for biomass combustion.

Acknowledgement

This study was financially supported by the Grants from the Thailand Research Fund for fiscal year 2014–2016 (TRG5780205), the Grant for Development of New Faculty Staff (Ratchadaphisek Somphot Endowment Fund) of Chulalongkorn University, the Grant from Faculty of Science of Chulalongkorn University and the Center of Excellence on Petrochemical and Materials Technology, Chulalongkorn

University. In addition, the authors would like to express their thanks to the Graduate School, Chulalongkorn University for partial financial support.

References

- [1] J. Koppejan and S. V. Loo, *The Handbook of Biomass Combustion and Co-firing*. London, UK: Earthscan, 2008.
- [2] M. A. B. Zanoni, H. Massard, and M. Ferreira Martins, "Formulating and optimizing a combustion pathways for oil shale and its semi-coke," *Combustion and Flame*, vol.159, pp. 3224–3234, 2012.
- [3] M. Amutio, G. Lopez, R. Aguado, M. Artetxe, J. Bilbao, and M. Olazar, "Kinetic study of lignocellulosic biomass oxidative pyrolysis," *Fuel*, vol.95, pp. 305–311, 2012.
- [4] E. Ranzi, M. Corbetta, F. Manenti, and S. Pierucci, "Kinetic modeling of the thermal degradation and combustion of biomass," *Chemical Engineering Science*, vol.110, pp. 2–12, 2013.
- [5] R. Mehrabian, A. Shiehnejadhesar, R. Scharler, and I. Obernberger, "Multi-physics modelling of packed bed biomass combustion," *Fuel*, vol.122, pp. 164–178, 2014.
- [6] M. V. Gil, D. Casal, C. Pevida, J. J. Pis, and F. Rubiera, "Thermal behaviour and kinetics of coal/biomass blends during co-combustion," *Bioresource Technology*, vol.101, pp. 5601–5608, 2010.
- [7] G. Várhegyi, E. Mészáros, M. J. Antal, J. Bourke, and E. Jakab, "Combustion kinetics of corncob charcoal and partially demineralized corncob charcoal in the kinetic regime," *Industrial & Engineering Chemistry Research*, vol.45, pp. 4962–4970, 2006.
- [8] K. Cheng, W. T. Winter, and A. J. Stipanovic, "A modulated-TGA approach to the kinetics of lignocellulosic biomass pyrolysis/combustion," *Polymer Degradation and Stability*, vol.97, pp. 1606–1615, 2012.
- [9] X. Fang, L. Jia, and L. Yin, "A weighted average global process model based on two-stage kinetic scheme for biomass combustion," *Biomass and Bioenergy*, vol.48, pp. 43–50, 2013.
- [10] D. Shen, J. Ye, R. Xiao, and H. Zhang, "TG-MS analysis for thermal decomposition of cellulose under different atmospheres," *Carbohydrate Polymers*, vol.98, pp. 514–521, 2013.
- [11] C. Chen, X. Ma, and K. Liu, "Thermogravimetric analysis of microalgae combustion under different oxygen supply concentrations," *Applied Energy*, vol.88, pp. 3189–3196, 2011.
- [12] S. S. Idris, N. A. Rahman, and K. Ismail, "Combustion characteristics of Malaysian oil palm biomass, sub-bituminous coal and their respective blends via thermogravimetric analysis (TGA)," *Bioresource Technology*, vol.123, pp. 581–591, 2012.
- [13] D. López-González, M. Fernandez-Lopez, J. L. Valverde, and L. Sanchez-Silva, "Thermogravimetric-mass spectrometric analysis on combustion of lignocellulosic biomass," *Bioresource Technology*, vol.143, pp. 562–574, 2013.
- [14] M. Othman, Y.-H. Park, T. Ngo, S.-S. Kim, J. Kim, and K. Lee, "Thermogravimetric characteristics and pyrolysis kinetics of Giheung Respia sewage sludge," *Korean Journal of Chemical Engineering*, vol. 27, pp. 163–167, 2010.
- [15] J. A. Conesa and A. Domene, "Biomasses pyrolysis and combustion kinetics through n-th order parallel reactions," *Thermochimica Acta*, vol. 523, pp. 176–181, 2011.
- [16] S. Azevedo, L. M. Cunha, P. V. Mahajan, and S. C. Fonseca, "Application of simplex lattice design for development of moisture absorber for oyster mushrooms," *Procedia Food Science*, vol. 1, pp. 184–189, 2011.
- [17] P. V. Rao and S. S. Baral, "Experimental design of mixture for the anaerobic co-digestion of sewage sludge," *Chemical Engineering Journal*, vol.172, pp. 977–986, 2011.
- [18] Q. Liu, Z. Zhong, S. Wang, and Z. Luo, "Interactions of biomass components during pyrolysis: A TG-FTIR study," *Journal of Analytical and Applied Pyrolysis*, vol.90, pp. 213–218, 2011.
 [19] S. Karaman, M. T. Yilmaz, and A. Kayacier, "Simplex lattice mixture design approach on the
- [19] S. Karaman, M. T. Yilmaz, and A. Kayacier, "Simplex lattice mixture design approach on the rheological behavior of glucomannan based salep-honey drink mixtures: An optimization study based on the sensory properties," *Food Hydrocolloids*, vol.25, pp. 1319–1326, 2011.
- [20] H. Yang, R. Yan, H. Chen, C. Zheng, D. H. Lee, and D. T. Liang, "In-depth investigation of biomass pyrolysis based on three major components: hemicellulose, cellulose and lignin," *Energy & Fuels*, vol. 20, pp. 388–393, 2005.
- [21] T. Damartzis, D. Vamvuka, S. Sfakiotakis, and A. Zabaniotou, "Thermal degradation studies and kinetic modeling of cardoon (Cynara cardunculus) pyrolysis using thermogravimetric analysis (TGA)," *Bioresource Technology*, vol. 102, pp. 6230–6238, 2011.

- [22] J. E. White, W. J. Catallo, and B. L. Legendre, "Biomass pyrolysis kinetics: A comparative critical review with relevant agricultural residue case studies," *Journal of Analytical and Applied Pyrolysis*, vol. 91, pp. 1–33, 2011.
- [23] H. E. Kissinger, "Reaction Kinetics in Differential Thermal Analysis," *Analytical Chemistry*, vol. 29, pp. 1702–1706, 1957.
- [24] T. Akahira and T. Sunose, "Method of determining activation deterioration constant of electrical insulating materials," *Research Report of Chiba Institute of Technology*, vol. 16, pp. 22–31, 1971.
- [25] T. Ozawa, "Kinetic analysis of derive curves in thermal analysis," *Journal of Thermal Analysis*, vol.2, pp. 301–324, 1970.
- [26] J. H. Flynn, "The Temperature Integral'—Its use and abuse," *Thermochimica Acta*, vol. 300, pp. 83–92, 1997.
- [27] C. D. Doyle, "Series approximations to the equations of thermogravimetric data," *Nature*, vol. 207, pp. 290–291, 1965.
- [28] C.-P. Lin, Y.-M. Chang, J. P. Gupta, and C.-M. Shu, "Comparisons of TGA and DSC approaches to evaluate nitrocellulose thermal degradation energy and stabilizer efficiencies," *Process Safety and Environmental Protection*, vol.88, pp. 413–419, 2010.
- [29] V. Pasangulapati, K. D. Ramachandriya, A. Kumar, M. R. Wilkins, C. L. Jones, and R. L. Huhnke, "Effects of cellulose, hemicellulose and lignin on thermochemical conversion characteristics of the selected biomass," *Bioresource Technology*, vol.114, pp. 663–669, 2012.
- [30] T. Faravelli, A. Frassoldati, G. Migliavacca, and E. Ranzi, "Detailed kinetic modeling of the thermal degradation of lignins," *Biomass and Bioenergy*, vol.34, pp. 290–301, 2010.

using simplex lattice design

Sasiporn Chayaporn*, Panusit Sungsuk*, Sasithorn Sunphorka*, Prapan Kuchonthara*,**,
Pornpote Piumsomboon*,**, and Benjapon Chalermsinsuwan*,**,

*Fuels Research Center, Department of Chemical Technology, Faculty of Science, Chulalongkorn University, 254 Phayathai Road, Patumwan, Bangkok 10330, Thailand

**Center of Excellence on Petrochemical and Material Technology, Chulalongkorn University, 254 Phayathai Road, Patumwan, Bangkok 10330, Thailand

(Received 7 June 2014 • accepted 2 October 2014)

Abstract—We evaluated the correlation between the biomass constituents and their kinetic values. To simplify the models and indicate the effect of each constituent, pure biomass components and their mixtures were used as biomass model. The experiments were set up based on simplex-lattice design. The pyrolysis of synthesized biomass was performed by non-isothermal thermogravimetric analyzer. Several kinetic models in the literature, including Kissinger-Akahira-Sunose, Ozawa-Flynn-Wall and analytical method were used to determine kinetic values for each experiment. The generated regression models and predicted kinetic values from those methods were compared. The results obtained from analytical model (for $n \neq 1$) showed a good agreement ($R^2 > 0.95$) with those obtained from experiments. This study also provide contour plots for all cases in order to observe the behavior of biomass pyrolysis at different component ratio.

Keywords: Simplex-lattice Design, Biomass, Pyrolysis, Model, Kinetics

INTRODUCTION

Biomass is an interesting resource that can potentially replace fossil fuel since it can be used in short cycle. It has the potential to contribute to the future energy and it is suitable for agricultural countries. Thermal decomposition such as pyrolysis, combustion and gasification is a conversion process for transformation of biomass into biofuel [1]. Pyrolysis is the well-known process for biomass conversion to energy under an absence of oxygen. It is the initial step of all thermochemical conversion processes [2,3]. In addition, pyrolysis is the simplest and easiest to set up compared to gasification [4,5].

The kinetics of biomass decomposition is the key to understanding the mechanism and designing a suitable conversion process. Non-isothermal thermogravimetric analysis (TGA) is one of the best methods for the study of the kinetics of pyrolysis. Several kinetic methods were used to calculate kinetic parameters including the activation energy, frequency factor and reaction order from TGA data with various factor effects [3,6-12]. Among several kinetic models, the iso-conversional methods such as The Kissinger - Akahira - Sunose (KAS) method and Ozawa-Flynn-Wall (OFW) method are the most commonly accepted for computational calculation based on TGA and successfully used to simulate the pyrolysis behavior of biomass [3,13-15]. These kinetic models were developed from single-step pyrolysis. They calculate the kinetic parameters with a

[†]To whom correspondence should be addressed. E-mail: benjapon.c@chula.ac.th Copyright by The Korean Institute of Chemical Engineers. progress of conversion and temperature without considering the reaction mechanism [16]. The previous literature study reported that KAS and OFW methods are reliable enough for calculating activation energy of cardoon pyrolysis from TGA data [3]. Besides these two kinetic models, the analytical model, which is derived from single-step decomposition kinetics, was also selected [7,10,11]. The analytical model derived by an assumption of $n^{\rm th}$ -order kinetics is reported to be acquirable, representative, and reliable for biomass pyrolysis [7]. The calculated kinetic values obtained from all models revealed that pyrolysis of biomass were complex and multistep kinetics.

pISSN: 0256-1115

eISSN: 1975-7220

To simplify the calculation of kinetic parameters, the prediction of kinetic parameters from biomass composition has been explored [17-21]. The correlations between main biomass components and each kinetic parameter were proposed instead of a calculation from TGA data. The previous study described the thermal degradation of pistachio shells by a detailed reaction mechanism [20]. The results indicated that the expected mass loss during pistachio shell pyrolysis derived from reaction mechanisms and discrete particle method agreed well with experimental data. However, the major advantage of the developed model is that it could employ the pyrolysis mechanism, but the model is very complex. Moreover, some studies detected the differences between predicted values and experimental data which were probably due to the interactions between compounds and extractives [19,21]. Therefore, the development of simply and accurate models which can potentially predict the thermal behavior and kinetic values is still attractive.

Besides the development of models from reaction mechanisms, many studies attempted to use the mathematical and statistical meth-

ods for finding the correlation between biomass main components and kinetic parameters. Response surface methodology (RSM), based on simplex-lattice design, was chosen and demonstrated as a suitable method for examining the effect of correlated three input components on the output data [22,23]. It is suitable for investigating the biomass system since biomass' three main components and summation of three proportions might be assumed to one. The previous study used simplex-lattice design (SLD) to determine the interaction between the biomass components during synthesized biomass pyrolysis [23]. The effect of each component and its interactions on mass loss rate could be observed. However, this study did not provide the other kinetic values.

However, there is a lack of applying this kind of model to this research field. Therefore, the aim of this study was to develop a simplified model for predicting kinetic values for biomass pyrolysis from its main components. The correlations between mass fractions of cellulose, hemicellulose and lignin were the input data, while output data were activation energy, pre-exponential factor and reaction order. The RSM based on SLD was chosen as a tool for this purpose. For each point of experimental design, the synthesized biomass was prepared at the desired ratio. The kinetic values were evaluated from TGA data using the isoconversional methods, including KAS and OFW methods, and also analytical method (in cases of first-order kinetics and n^{th} -order kinetics). The calculated kinetic parameters obtained from three kinetic models (six cases) were compared. The statistical analyses were also provided for all six cases. The effect of pure biomass components and their interactions were identified for each case and discussed. The regression models and contour plots for predicted kinetic parameters were also provided in this study to observe the interactions of biomass components.

MATERIALS AND METHODS

1. Materials

Pure a-cellulose, xylan (a model of hemicellulose), and organosolv lignin were purchased from Sigma Aldrich. The real biomass, *Leucaena Leucocephala*, was used to check the accuracy of the model. The lignin content was analyzed by Tappi T222om-98 [24]. The holocellulose content (cellulose and hemicellulose) was analyzed by the Browning method of wood chemistry [25], whilst the a-cellulose content was analyzed by Tappi T203om-88 [26]. The *Leucaena Leucocephala* was ground by biomass grinder and filtered into particle sizes of 150-250 micron. The synthesized biomass and real biomass were dried at 110 °C for 24 h before use.

2. Experimental Design

The simplex-lattice design (SLD) was used to determine the number of experiments and evaluate the effect of mass fraction of cellulose (X_1) , mass fraction of hemicellulose (X_2) and mass fraction of lignin (X_3) on kinetic parameters including activation energy (E_a) , frequency factor (A) and reaction order (n). The samples were prepared by physical mixing of the three pure components at different ratios. Based on SLD, summation of mass fractions $(X_1 + X_2 + X_3)$ is unity. The sample codes for total 13 combinations and the mass fraction of each experimental design point are presented in Table 1. The 13 experimental points were three single-component

Table 1. Sample code and mass fractions of cellulose, hemicellulose and lignin

Sample code		Mass fraction				
Sample code	Cellulose	Hemicellulose	Lignin			
1	1.00	0.00	0.00			
2	0.00	1.00	0.00			
3	0.00	0.00	1.00			
4	0.00	0.33	0.67			
5	0.00	0.67	0.33			
6	0.17	0.17	0.67			
7	0.17	0.67	0.17			
8	0.33	0.00	0.67			
9	0.33	0.33	0.33			
10	0.33	0.67	0.00			
11	0.67	0.00	0.33			
12	0.67	0.17	0.17			
13	0.67	0.33	0.00			

treatments (Nos. 1, 2 and 3), six two-component mixtures (Nos. 4, 5, 8, 10, 11 and 13) and four three-component mixtures (Nos. 6, 7, 9 and 12). For each mixture, the experiments were performed at four linear heating rates (5, 10, 20 and 40 °C min⁻¹) with replicates.

3. Thermogravimetric Analysis (TGA)

At each experimental run based on SLD, the weight loss and differential weight loss of synthesized and real biomass pyrolysis were observed by thermogravimetric/differential thermal analyzer (Mettler Toledo TG Analyzer) under nitrogen atmosphere. The flow rate of nitrogen gas was 50 mL min $^{-1}$. Approximately 3.0 mg of sample was placed into an aluminum pan. The sample was heated from 30 to 1,000 $^{\circ}\mathrm{C}$ at four linear heating rates.

4. Kinetic Models

The values of kinetic parameters were calculated by data interpretation of thermogravimetric analysis (TGA) and differential thermal analysis (DTA) curves, since they present the overall weight loss rate of biomass pyrolysis. The biomass pyrolysis can be described by three kinetic models, including Kissinger-Akahira-Sunose (KAS), Ozawa-Flynn-Wall (OFW) and analytical model. These methods are based on the assumptions that the reaction rate at constant extent of conversion is only a function of temperature [27], and they take into consideration the one-step process decomposition [3]. This study's apparent kinetic ignores the effect of particle size (heat and mass transfers) since the real pyrolysis process might be operated by using different particle sizes of biomass.

The general reaction rate is expressed as

$$\frac{\mathrm{d}\alpha}{\mathrm{d}t} = k(T)f(\alpha) \tag{1}$$

where α is the conversion of convertible part of biomass and calculated from $\alpha = (W_o - W)/(W_o - W_{ash})$; W_o is the original weight, W is the weight at any time t and W_{ash} is the ash content in the sample. The function k(T) is the rate constant given by Arrhenius equation, while the function $f(\alpha)$ depends on the decomposition mechanism.

By combining the constant heating rate (β =dT/dt) and Arrhe-

nius equation, Eq. (1) can be shown as Eq. (2).

$$\frac{d\alpha}{f(\alpha)} = \frac{A}{\beta} \exp\left(-\frac{E_a}{RT}\right) dT$$
 (2)

Gives

$$g(\alpha) = \int_{0}^{\alpha} \frac{d\alpha}{f(\alpha)} = \int_{0}^{\alpha} \frac{A}{\beta} \exp\left(-\frac{E_{a}}{RT}\right) dT = \frac{AE_{a}}{\beta R} p\left(\frac{E_{a}}{RT}\right)$$
(3)

where E_a is the activation energy (kJ/kmol), R is a gas constant (8.314 kJ/kmol·K) and T is the reaction temperature (K). The term $p(E_a/RT)$ is the temperature integral. The difference of iso-conventional methods is due to the approximation for solving the equation. 4-1. Kissinger-Akahira-Sunose Model (KAS) [27-29]

The approximation is proposed to be:

$$p\left(\frac{E_a}{RT}\right) = \exp\left(-\frac{E_a}{RT}\right) \times \left(\frac{E_a}{RT}\right)^{-2}$$
(4)

Substitutes Eq. (4) into Eq. (3) and takes logarithm. Then, Eq. (3) becomes:

$$\ln\left(\frac{\beta}{T^2}\right) = \ln\left(\frac{AE_a}{Rg(\alpha)}\right) - \frac{E_a}{RT}$$
 (5)

 E_a and A can be calculated by plotting curve of $\ln(\beta/T^2)$ versus 1/T. In this study, the $g(\alpha)$ is equal to $-\ln(1-\alpha)$ for first-order kinetics and $(n-1)^{-1}(1-\alpha)^{(1-n)}$ for any order n.

4-2. Ozawa-Flynn-Wall (OFW) [27,30,31]

The approximation of this model is based on Doyle's approximation [32]. Therefore, Eq. (3) becomes:

$$\log \beta = \log \left(A \frac{E_a}{Rg(\alpha)} \right) - 2.315 - 0.457 \left(\frac{E_a}{RT} \right)$$
 (6)

 E_a and A can be calculated by plotting curve of $\log(\beta)$ versus 1/T. The function $g(\alpha)$ is the same as indicating in Section 2.4.1.

4-3. Analytical Model

This model is derived based on single step decomposition process. Therefore, the function $f(\alpha)$ in Eq. (2) is equal to $(1-\alpha)^n$. Then, Eq. (2) becomes:

$$\frac{\mathrm{d}\alpha}{\mathrm{dT}} = \frac{\mathrm{A}}{\beta} \exp\left(-\frac{\mathrm{E}_a}{\mathrm{RT}}\right) (1-\alpha)^n \tag{7}$$

After solving the equation, the equations for analytical method are given below:

for first-order kinetics:

$$\alpha = 1 - \exp\left\{-\frac{ART^{2}}{\beta E_{a}} \left(1 - \frac{2RT}{E_{a}}\right) \exp\left(-\frac{E_{a}}{RT}\right)\right\}$$
 (8)

for n^{th} -order kinetics:

$$\alpha = 1 - \left\{ 1 - (n-1) \left(-\frac{ART^2}{\beta E_a} \right) \left(1 - \frac{2RT}{E_a} \right) \exp\left(-\frac{E_a}{RT} \right) \right\}^{\frac{1}{1-n}}$$
(9)

To calculate the kinetic parameters including E_a and A, the TGA curves were fitted with analytical models (Eqs. (8) and (9)) by means of maximizing the regression coefficient (R^2). In case of any order n of all methods, n was calculated by Kissinger index of shape equation. The shape index is defined as the absolute value of the ratio

of the slope of tangents to the curve at inflection points of differential thermal analysis (DTA) curves [28,33].

The pyrolysis of real example biomass, *Leucaena Leucocephala*, was also performed. The kinetic parameters were calculated from the proposed models. Then, the conversion curves obtained from kinetic values of different methods were compared to that obtained from experiment.

5. Statistical Analysis and Modeling

An analysis of variance (ANOVA) and response surface methodology (RSM) were used to evaluate the effect of each biomass constituent, determine the most significant factor on the desired response and also generate the statistical models for predicting the kinetic parameters. The model is expressed in terms of cubic equation (Eq. (10)) [22,34].

$$Y=a_{1}X_{1}+a_{2}X_{2}+a_{3}X_{3}+a_{12}X_{1} X_{2}+a_{13}X_{1} X_{3}+a_{23}X_{2} X_{3}$$

$$+a_{1-2}X_{1}X_{2} (X_{1}-X_{2})+a_{1-3}X_{1}X_{3} (X_{1}-X_{3})+a_{2-3}X_{2}X_{3} (X_{2}-X_{3})$$

$$(10)$$

where Y is an estimated response ($E_{a\nu}$ A or n). The a_1 , a_2 , a_3 , a_{12} , a_{13} , a_{23} , a_{1-2} , a_{1-3} and a_{2-3} are constant coefficients for linear and nonlinear (interaction) terms. The direction and magnitude of coefficients can illustrate the effect of each term on the desired response. The models were also used to generate the ternary contour plots in order to observe the influence of biomass compositions on $E_{a\nu}$ A and n. The models and ternary contour plots for estimated kinetic values obtained from different kinetic models were produced and compared to each other.

RESULTS AND DISCUSSION

1. Evaluation of Kinetic Values from Different Kinetic Models

Table 2 presents the E_a and A calculated from different kinetic models based on first-order kinetics. The results were averaged from eight replicates (four heating rates with two replicates per each). Both values calculated from KAS and OFW have the same trend and comparable values, because both methods are developed from the same assumption with different approximations of $p(E_a/RT)$. The results obtained from both methods indicated that pure lignin gave the highest E_a (~200 kJ/mol), while pure hemicellulose and hemicellulose: lignin mixture at 0.33:0.67 wt:wt gave the lowest E_a (~120-130 kJ/mol). However, in case of mixtures, a different trend was observed. Mixtures with high cellulose and hemicellulose proportion gave higher E_a compared to those with high lignin proportion. Moreover, the values of E_a and A in cases of mixtures cannot be calculated from the arithmetic method (e.g., summation of mass fractions multiplied by E_a and A of pure components). It might be due to the interaction between each component.

Considering the case of analytical method, some differences occurred. The calculated E_a and A values were much lower than those obtained from KAS and OFW methods in many cases. The large differences were probably because the analytical method attempts to fit the model with experimental data without considering the pyrolysis behavior, while the isoconversional method approximates the reaction order from DTA data and calculates other kinetic values from larger information (simultaneously calculated from different heating rates and progress of conversion). Anyway, the accuracy of models was tested and is discussed further down.

Table 2. Predicted kinetic values obtained from different decomposition models

Sample	KA	KAS		W	Analytical method		
code	E _a (kJ/mol)	A (min ⁻¹)	E _a (kJ/mol)	A (min ⁻¹)	E _a (kJ/mol)	A (min ⁻¹)	
1	145.0	1.0E+12	147.6	2.0E+12	143.2	3.7E+12	
2	123.0	9.7E+10	126.0	2.2E+11	90.0	1.8E+06	
3	199.8	2.3E+16	199.9	2.4E+16	103.4	4.4E+05	
4	120.8	4.0E+10	124.0	8.2E+10	103.9	2.8E+06	
5	164.5	2.7E+14	165.5	7.1E+10	69.3	6.7E+05	
6	142.0	2.6E+11	145.0	5.3E+11	104.8	1.7E+06	
7	165.8	8.8E+14	166.6	1.2E+15	95.5	1.8E+06	
8	179.9	1.0E+15	181.0	1.2E+15	108.2	1.6E+07	
9	141.2	1.8E+11	144.3	3.7E+11	103.9	2.1E+06	
10	164.4	6.2E+14	165.3	8.0E+14	104.5	1.8E+07	
11	142.0	2.6E+11	134.9	4.9E+11	93.9	2.5E+07	
12	169.7	3.5E+15	171.5	3.9E+15	86.1	6.0E+04	
13	183.6	6.3E+13	184.7	2.5E+15	90.7	6.4E+05	
Biomass	178.6	1.0E+15	179.5	1.3E+15	100.4	1.7E+06	

The highest E_a and A values, in this case, were obtained from a case of pure cellulose while the lowest E_a was obtained from a case of hemicellulose: lignin mixture at 0.67:0.33 wt:wt (Sample no. 5). In addition, the mixtures with high cellulose proportion gave lower E_a , while the mixtures with higher lignin proportion gave higher E_a , excepting sample 5. This phenomenon was also reported in the literature [21]. The previous study demonstrated that higher E_a is required to decompose woody biomass, which has higher lignin content. It is because the complex aromatic structure of lignin. The interactions were also observed in this case. The differences of results obtained from the former methods and those obtained from analytical method were probably due to different assumptions of reaction mechanism in forms of function $f(\alpha)$ as mentioned in Section 2.4.

Table 3 provides the values of E_a , A and n calculated from different kinetic models based on n^{th} -order kinetics. The results were

also averaged from eight replicates. It should be noted that the E_a calculated from cases of first-order (Table 2) and $n^{\rm th}$ -order kinetics (Table 3) for both KAS and OFW had the same values, because they were calculated from the slope of linear plots which do not involve the calculation of n. The A and n were calculated from the intercept of linear plots. However, even though the calculated A obtained from cases of first-order and $n^{\rm th}$ -order kinetics were different, the trend was still the same.

Considering the calculated n, Table 3 shows that the apparent reaction orders of biomass pyrolysis are larger than one, especially in the case of using the analytical method. KAS and OFW gave the same n values since they were calculated from the same DTA curve. It can be seen that reaction order obtained from pure components was lower than those obtained from mixtures. When the different compound was added to other compounds, the several decomposition reactions were parallel occurring due to the decom-

Table 3. Predicted kinetic values obtained from different decomposition models for n≠1

Sample		KAS			OFW		Anal	ytical method	
code	E _a (kJ/mol)	A (min ⁻¹)	n (-)	E _a (kJ/mol)	A (min ⁻¹)	n (-)	E _a (kJ/mol)	A (min ⁻¹)	n (-)
1	145.0	1.50E+12	1.4	147.6	2.80E+12	1.4	178.1	9.38E+13	1.6
2	123.0	1.60E+11	1.5	126.0	5.00E+12	1.5	83.6	7.60E+07	1.1
3	199.8	2.50E+16	1.2	199.9	2.20E+12	1.2	68.3	1.82E+05	1.1
4	120.8	5.00E+10	1.3	124.0	1.20E+11	1.3	74.3	4.00E+04	6.2
5	164.5	4.80E+14	1.6	165.5	7.80E+14	1.6	72	1.10E+05	6.5
6	142.0	5.20E+11	1.8	145.0	1.10E+12	1.8	74.5	3.60E+04	5.9
7	165.8	1.40E+15	1.5	166.6	3.50E+12	1.5	82.1	3.80E+07	6.4
8	179.9	1.70E+15	1.6	181.0	2.10E+15	1.6	117.6	6.40E+08	7.1
9	141.2	3.10E+11	1.6	144.3	4.90E+12	1.6	89	2.10E+06	6.5
10	164.4	1.20E+15	1.6	165.3	1.50E+15	1.6	84.7	6.80E+07	5.8
11	142.0	3.90E+11	1.5	134.9	8.60E+11	1.5	127.6	1.10E+09	5.9
12	169.7	5.20E+15	1.5	171.5	3.10E+12	1.5	118.9	6.40E+08	5.6
13	183.6	4.40E+15	1.7	184.7	5.10E+15	1.7	81.3	9.80E+05	4.8
Biomass	178.6	3.10E+15	2	179.5	3.80E+15	2	125.1	9.70E+09	1.4

position of the added compounds and also interactions between all components. Multiple reactions including several parallel first-order reactions can be expressed by an apparent n^{th} -order reaction [35]. The calculated n was thus increased in case of mixture.

In case of using analytical method, n values for pyrolysis of the mixtures were much higher than those obtained from KAS and OFW. Higher lignin content gave higher n values. Besides the n, the trends of E_a and A were different from those obtained from other isoconversional methods. The highest E_a was obtained in a case of pure cellulose, higher than a case of pure lignin. Higher cellulose content needed higher E_a during pyrolysis based on these results.

Besides the pyrolysis of synthesized biomass, real biomass pyrolysis, *Leucaena Leucocephala*, was performed. The kinetic values of biomass pyrolysis are presented in Tables 2 and 3 as well. The n obtained from this method was very large compared to that obtained from other models, indicating very complex reactions occurred. Fig. 1(a) and (b) show the conversion curves obtained from calculated kinetic values. Fig. 1(a) presents the conversion curves for case of first-order kinetics, and Fig. 1(b) presents the curves for *n*th-order kinetics. The regression coefficients (R²) for each case are shown in Table 4. The conversion rate of Fig. 1(a) and 1(b) was calculated by Eq. (1) with the initial and final temperatures of 100 °C and 700 °C, respectively. This temperature range ignores the weight change due to the evaporation of moisture and focuses mainly on the decomposition or pyrolysis step of biomass. The pyrolysis of biomass com-

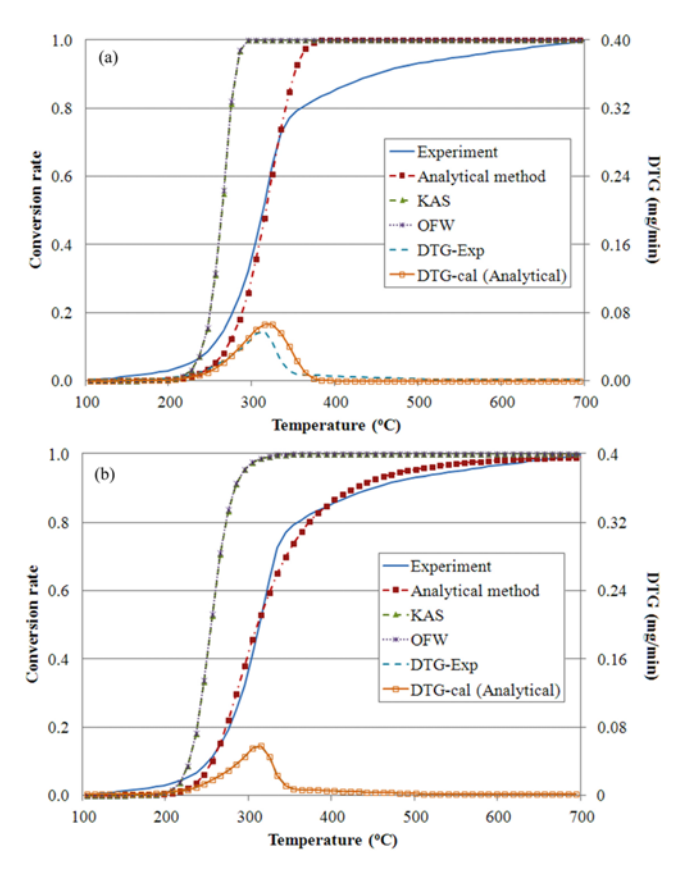


Fig. 1. Relation between temperature and conversion (wt/wt) of biomass pyrolysis obtained from different methods for first-order kinetics (a) and any-order kinetics (b).

Table 4. Regression coefficients of the decomposition curves generated from KAS, OFW and analytical method for biomass pyrolysis

Method	Regression co	efficients (R ²)
	n=1	n≠1
KAS	0.77	0.73
OFW	0.76	0.73
Analytical method	0.98	1.00

monly occurs in this temperature range [3,8,10,11,37]. Conversion curves obtained from the analytical model showed the best fit to experimental data, possibly because the analytical method was fitted to experimental data directly to calculate the kinetic parameters, resulting in the highest R². However, differences were observed between experimental and predicted data at relatively low temperature and high temperature. It was due to the assumption of the kinetic model since the kinetic model was developed based on single-step decomposition. In fact, the biomass pyrolysis involves multi-step degradation. At low temperature, the conversion is due to the moisture evaporation, while the conversion at high temperature is due to lignin degradation. Therefore, the deviation of predicted values from experimental values was sometimes observed at these steps. However, the predicted conversion rate was highly accurate at the session in which mostly decomposition occurred.

In case of isoconversional methods, they also simulate the biomass pyrolysis as a one-step process and neglect the physical and chemical nature of the pyrolysis process. The details in diffusion, adsorption, desorption and other occurring phenomena as well as the whole reaction scheme are not considered [3]. The errors in the calculated values obtained from KAS and OFW were probably due to the assumption of f(a) and $g(\alpha)$. The other reaction models including nucleation or diffusional model might be applied instead.

2. Statistical Analysis and Modeling

2-1. Analysis of Variance for First-order Kinetics

To evaluate the effect of cellulose, hemicellulose and lignin on the kinetic parameters and understand the interaction between them, the simplex-lattice design was used. Based on this experimental design, the synthesized biomass was prepared as described in Section 2.2. Then ANOVA was applied to analyze the effect of response as described in Section 2.5. The p-value indicates the probability of kinetic parameters affected from each term of model. The terms which have p-value less than 0.05 have an important effect on the kinetic parameters during biomass pyrolysis. All analysis results are shown in Appendix A (Table A.1). For the case of using the KAS model, the results demonstrated that the interaction terms including quadratic term between cellulose and hemicellulose (X₁X₂) and cubic term between hemicellulose and lignin $(X_2X_3(X_2-X_3))$ had a statistically significant effect on E_a . By the same way, the results indicated that the linear terms, interaction terms including X₁X₃, X_2X_3 , $X_1X_3(X_1-X_3)$ and $X_2X_3(X_2-X_3)$, had a statistically significant effect on A. In case of using OFW, the important factors which have significant effect on both parameters were almost the same as the case of using KAS, excepting the $X_1X_2X_3$ term. As mentioned above, both KAS and OFW were developed by the same way excepting

an approximation of $g(\alpha)$. Therefore, the calculated kinetic values and also ANOVA for both cases were comparable.

For the analytical method, the analysis results were different. The statistical analysis results presented that the linear terms and interaction including X_1X_2 and $X_1X_2(X_1-X_2)$ had a significant effect on E_a while all terms excluding X_2X_3 and $X_2X_3(X_2-X_3)$ had significant effect on A. The effect of each component was unclear in case of E_a . However, in case of A, it seems that the cellulose proportion was the dominant factor since all terms containing X₁ had a significant effect on A. This result differs from other models. Considering the trend of conversion curves in Fig. 1 and R2 values in Table 4, the calculated kinetic parameters obtained from analytical method provided higher R². Therefore, the analysis results obtained from this model must be concerned. The cellulose pyrolysis has higher decomposition rate due to its simple ordered repeating unit, cellobiose. The TGA data (not shown here) indicated that cellulose decomposes rapidly in a narrow temperature range, resulting in high reaction rate, while lignin decomposes at wider temperature range. This observation was consistent with other previous studies [36,37]. The cellulose pyrolysis thus influenced the decomposition rate for all synthesized biomass which contain cellulose in their composition. 2-2. Analysis of Variance for nth-order Kinetics

The statistical analysis results are shown in Appendix A (Table A.2). In this section, only the analysis results for case of using analytical method (Table A.2(g)-(i)) are discussed. The results indicated that linear terms and interaction between cellulose and hemicellulose (X_1X_2) had a significant effect on E_a . No interaction effect was observed. In case of A, the effluent factors were the same as the case of first-order kinetics, which confirmed that cellulose acts as the dominant factor on decomposition rate of biomass pyrolysis. For n, the two quadratic terms and interactions between all pure components ($X_1X_2X_3$) were indicated as the important factors. The interactions between all pure components were obviously seen since the n values of pure components were below two (Table 3) and dramatically increased by mixing together. The several components contain in hemicellulose and lignin provided parallel n^{th} -order reaction, leading to higher n.

The ANOVA analysis for KAS and OFW methods is also provided in Table A.2. As expected, the results for E_a and n obtained from both methods are similar. However, the case of A was different. It is difficult to determine what makes the large difference on statistical analysis between these methods. Table 3 shows that the calculated values of A were almost equal and comparable. In addition, the only one thing which is different from each other is the approximation of $g(\alpha)$ term.

2-3. Modeling and Ternary Contour Plot

To predict and observe the variation of $E_{a\nu}$ A and n at different biomass compositions, the regression models and contour plots were also generated. The regression models for predicting kinetic parameters based on analytical method are shown in Appendix B (Eqs. (B.1)-(B.5)). Considering the coefficient of each term, it provided an insight into ranking the importance of each term correspondence with the ANOVA analysis. The positive coefficient indicated that an increase in term magnitude increased the kinetic values, while the negative coefficient indicated the opposite effect. The R^2 values of all models were above 0.95, which revealed very

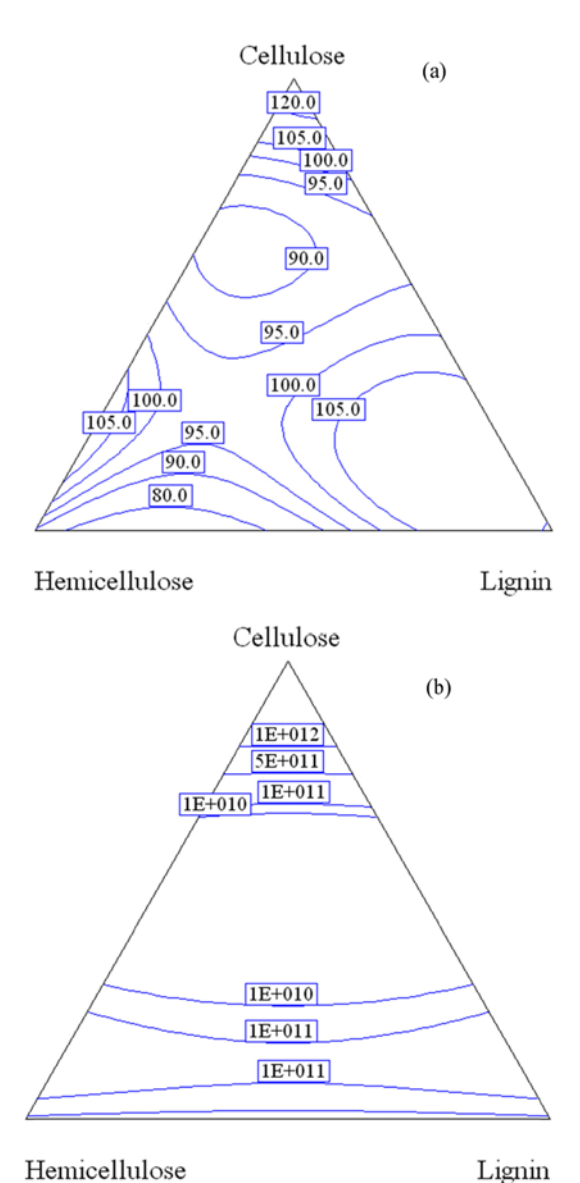


Fig. 2. Ternary contour plots of predicted activation energy (a) and pre-exponential factor (b) obtained from analytical method for first-order kinetics.

good agreement of predicted values from regression models and experiments.

The response of each kinetic parameter was graphically represented as ternary contour plot (Figs. 2 and 3). Based on SLD, all 13 points of experiments are located inside the triangle. It means that the sum of proportions of cellulose, hemicellulose and lignin was always unity. Fig. 2 shows the contour plots of E_a and A for first-order kinetics and Fig. 3 shows the plots for n^{th} -order kinetics, with respect to the regression models. The interactions between biomass components were obviously seen. The variation in biomass composition was the important key to predict the kinetic of its pyrolysis and observe the thermal behavior as well.

Regression models and ternary contour plots for predicting kinetic parameters based on KAS and OFW methods were also provided in Appendices B and C, respectively. All regression models, exclud-

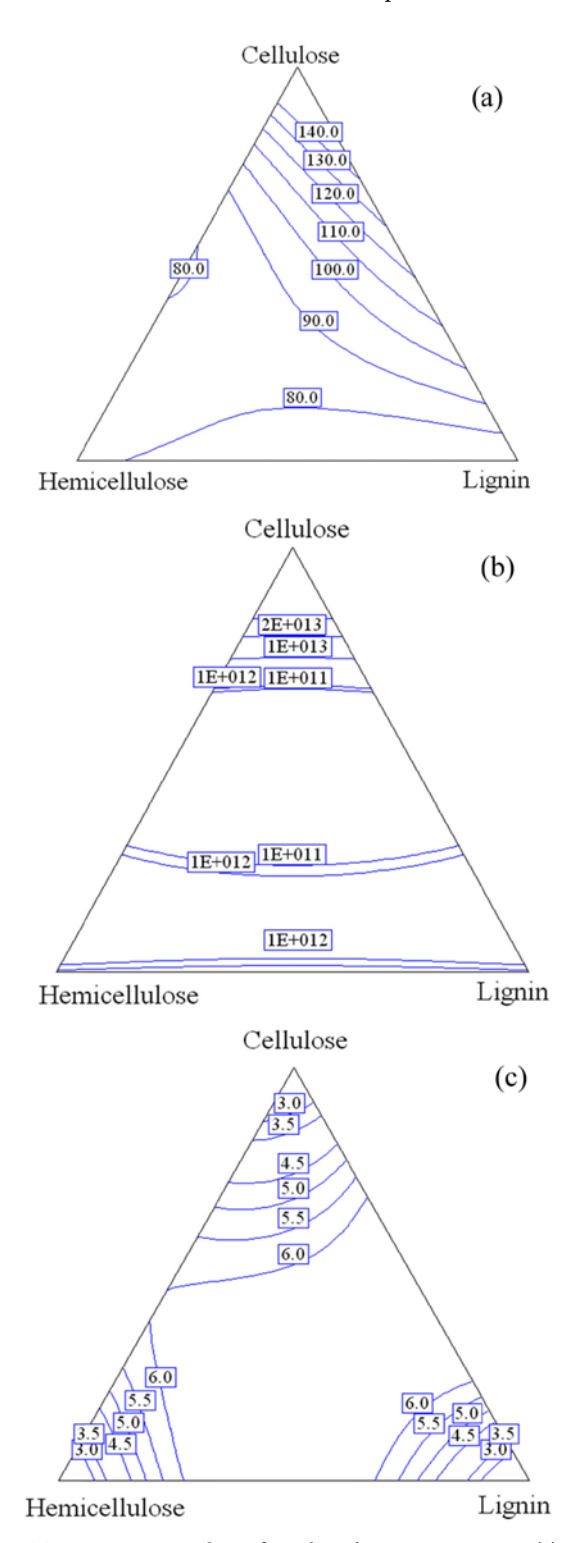


Fig. 3. Ternary contour plots of predicted activation energy (a), preexponential factor (b) and reaction order (c) obtained from analytical method for n^{th} -order kinetics.

ing the case of n, had high R². The relatively low R² of regression model for n revealed that the model could not be used to predict the accurate values for those kinetic models. On the other hand, the model generated from SLD might not do enough to predict the values of n obtained from Kissinger index of shape equation.

CONCLUSIONS

The variation of biomass composition plays an important role in its thermal behavior. The calculated kinetic values from three kinetic models showed the different results and trend. Compared to the conversion curve of real biomass, the conversion curve generated from analytical method showed the best fit compared to that obtained from other kinetic models. Based on SLD and analytical model, cellulose proportion was the most important factor influencing the A and n. The proposed regression models showed very high R² values, almost equal to unity. The generated contour plots could be used to observe the variation of kinetic parameters at different biomass composition.

ACKNOWLEDGEMENT

This study was financially supported by grants from the Thailand Research Fund for fiscal year 2014-2016 (TRG5780205), the grant for Development of New Faculty Staff (Ratchadaphisek Somphot Endowment Fund) of Chulalongkorn University, the grant from Faculty of Science of Chulalongkorn University and the Center of Excellence on Petrochemical and Materials Technology, Chulalongkorn University. In addition, the authors would like to express their thanks to the Graduate School, Chulalongkorn University for partial financial support.

REFERENCES

- 1. N. Choobuathong, *Effects of chemical composition of biomass on pyrolysis and combustion*, Department of Chemical Technology, Chulalongkorn University, Bangkok (2007).
- 2. J. Jones, Chem. Eng., 85, 87 (1978).
- T. Damartzis, D. Vamvuka, S. Sfakiotakis and A. Zabaniotou, *Biore-sour. Technol.*, 102, 6230 (2011).
- 4. J. M. Encinar, J. F. Gonzalez and J. Gonzalez, *Fuel Process. Technol.*, **68**, 209 (2000).
- 5. E. Mura, O. Debono, A. Villot and F. Paviet, *Biomass Bioenergy*, **59**, 187 (2013).
- 6. Y. F. Huang, P. T. Chiueh, W. H. Kuan and S. L. Lo, *Appl. Energy*, **110**, 1 (2013).
- 7. Y. F. Huang, W. H. Kuan, P. T. Chiueh and S. L. Lo, *Bioresour. Technol.*, **102**, 9241 (2011).
- 8. S. Hu, A. Jess and M. Xu, Fuel, 86, 2778 (2007).
- A. Meng, H. Zhou, L. Qin, Y. Zhang and Q. Li, J. Anal. Appl. Pyrol., 104, 28 (2013).
- 10. S. Ren, H. Lei, L. Wang, Q. Bu, S. Chen and J. Wu, *Biosystems Eng.*, **116**, 420 (2013).
- 11. S. Singh, C. Wu and P. T. Williams, *J. Anal. Appl. Pyrol.*, **94**, 99 (2012).
- 12. J. Chattopadhyay, C. Kim, R. Kim and D. Pak, *Korean J. Chem. Eng.*, **25**, 1047 (2008).
- 13. S. Unz, T. Wen and M. Beckmann, Characterization of biomass used in thermal processes with regard to the kinetic properties, 35th International Technical Conference on Clean Coal & Fuel Systems, Clearwater, Florida, USA (2010).
- 14. C. Chen, X. Ma and Y. He, Bioresour. Technol., 117, 264 (2012).

- 15. S. Ceylan and Y. Topcu, Bioresour. Technol., 156, 182 (2014).
- A. Khawam, Application of solid-state kinetics to desolvation reactions, Pharmacy, Graduate College of The University of Iowa, Iowa, USA (2007).
- 17. A. Garcia-Maraver, D. Salvachua, M. J. Martinez, L. F. Diaz and M. Zamorano, *Waste Manage.*, **33**, 2245 (2013).
- 18. A. Gani and I. Naruse, Renew. Energy, 32, 649 (2007).
- 19. C. Couhert, J.-M. Commandre and S. Salvador, Fuel, 88, 408 (2009).
- 20. B. Peters, Fuel Process. Technol., 92, 1993 (2011).
- L. Burhenne, J. Messmer, T. Aicher and M.-P. Laborie, *J. Anal. Appl. Pyrol.*, **101**, 177 (2013).
- 22. P. V. Rao and S. S. Baral, Chem. Eng. J., 172, 977 (2011).
- 23. Q. Liu, Z. Zhong, S. Wang and Z. Luo, *J. Anal. Appl. Pyrol.*, **90**, 213 (2011).
- TAPPI PRESS, Atlanta, USA. TAPPI Standard T-222 om-98, "Acidinsoluble lignin in wood and pulp, TAPPI Test Methods", TAPPI PRESS, Atlanta, USA (1998).
- 25. B. L. Browning, *Methods of wood chemistry*, Wiley Inter-Science Publishers, New York (1967).
- 26. TAPPI Official Test Method T 203 om-88, "Alpha-, Beta-, and Gamma-Cellulose in Pulp", the TAPPI Press, Atlanta, Georgia, revised 1988, correction 1992, pp. 1-3 (1988).
- 27. J. E. White, W. J. Catallo and B. L. Legendre, *J. Anal. Appl. Pyrol.*, **91**, 1 (2011).
- 28. H. E. Kissinger, Anal. Chem., 29, 1702 (1957).
- T. Akahira and T. Sunose, Research Report of Chiba Institute of Technology, 16, 22 (1971).
- 30. T. Ozawa, J. Therm. Anal., 2, 301 (1970).
- 31. J. H. Flynn, Thermochim. Acta, 300, 83 (1997).
- 32. C. D. Doyle, Nature, 207, 290 (1965).
- C.-P. Lin, Y.-M. Chang, J.P. Gupta and C.-M. Shu, *Process. Safe. Environ.*, 88, 413 (2010).
- 34. S. Karaman, M. T. Yilmaz and A. Kayacier, *Food Hydrocolloid.*, **25**, 1319 (2011).
- K. Hashimoto, I. Hasegawa, J. Hayashi and K. Mae, *Fuel*, 90, 104 (2011).
- 36. H. Zhou, Y. Long, A. Meng, Q. Li and Y. Zhang, *Thermochim. Acta*, **566**, 36 (2013).
- 37. H. Haykiri-Acma, S. Yaman and S. Kucukbayrak, Fuel Process. Technol., 91, 759 (2010).

APPENDIX A

ANOVA analysis of kinetic parameters from KAS, OFW and analytical method (first-order kinetics)

Table A.1. The analysis of variance (ANOVA) for first-order kinetic values of biomass pyrolysis

(a) Activation energy obtained from KAS method									
Source Sum of squares DF Mean square F value P-value>F									
Model	6,494.30	9	721.59	9.22	0.05				
Linear mixture	618.21	2	309.10	3.95	0.14				
X_1X_2	1,716.32	1	1,716.32	21.93	0.02^{a}				

Table A.1. Continued

(a) Activation energy obtained from KAS method								
Source	Sum of squares	DF	Mean square	F value	<i>P</i> -value>F			
X_1X_3	116.37	1	116.37	1.49	0.31			
X_2X_3	393.69	1	393.69	5.03	0.11			
$X_1X_2X_3$	147.75	1	147.75	1.89	0.26			
$X_1X_2(X_1-X_2)$	198.97	1	198.97	2.54	0.21			
$X_1X_3(X_1-X_3)$	100.62	1	100.62	1.29	0.34			
$X_2X_3(X_2-X_3)$	3,096.39	1	3,096.39	39.56	0.01^{a}			
Residual	234.82	3	78.27					
Total	6,729.13	12						

(b) Pre-exponential factor obtained from KAS method								
Source	Sum of squares	DF	Mean]square	F value	<i>P</i> -value>F			
Model	4.61E+32	9	5.12E+31	42.45	0.01 ^a			
Linear mixture	1.65E+32	2	8.26E+31	68.46	$> 0.00^{a}$			
X_1X_2	1.98E+29	1	1.98E+29	0.16	0.71			
X_1X_3	1.16E+32	1	1.16E+32	96.34	$> 0.00^{a}$			
X_2X_3	1.33E+32	1	1.33E+32	110.28	$> 0.00^{a}$			
$X_1X_2X_3$	1.09E+31	1	1.09E+31	9.06	0.06			
$X_1X_2(X_1-X_2)$	3.89E+29	1	3.89E+29	0.32	0.61			
$X_1X_3(X_1-X_3)$	3.70E+31	1	3.70E+31	30.68	0.01^{a}			
$X_2X_3(X_2-X_3)$	3.63E+31	1	3.63E+31	30.07	0.01^{a}			
Residual	3.62E+30	3	1.21E+30					
Total	4.65E+32	12						

Source	Sum of squares	DF	Mean square	F value	<i>P</i> -value>F
Model	6,230.46	9	692.27	6.68	0.07
Linear mixture	505.64	2	252.82	2.44	0.24
X_1X_2	1,591.80	1	1,591.80	15.35	0.03^{a}
X_1X_3	225.60	1	225.60	2.18	0.24
X_2X_3	389.62	1	389.62	3.76	0.15
$X_{1}X_{2}X_{3}$	70.14	1	70.14	0.68	0.47
$X_1X_2(X_1-X_2)$	251.16	1	251.16	2.42	0.22
$X_1X_3(X_1-X_3)$	230.81	1	230.81	2.23	0.23
$X_2X_3(X_2-X_3)$	2,863.61	1	2,863.61	27.61	0.01^{a}
Residual	311.13	3	103.71		
Total	6,541.59	12			

(d) Pre-exponential factor obtained from OFW method								
Source	Sum of squares	DF	Mean square	F value	<i>P</i> -value>F			
Model	5.13E+32	9	5.70E+31	112.31	>0.00 ^a			
Linear mixture	1.65E+32	2	8.25E+31	162.65	$>0.00^{a}$			
X_1X_2	3.16E+30	1	3.16E+30	6.23	0.09			
X_1X_3	1.31E+32	1	1.31E+32	257.40	$>0.00^{a}$			
X_2X_3	1.50E+32	1	1.50E+32	295.12	$>0.00^{a}$			
$X_{1}X_{2}X_{3}$	8.55E+30	1	8.55E+30	16.86	0.03^{a}			
$X_1X_2(X_1-X_2)$	3.60E+30	1	3.60E+30	7.09	0.08			
$X_1X_3(X_1-X_3)$	3.61E+31	1	3.61E+31	71.17	>0.00 ^a			

Table A.1. Continued

(d) Pre-exponential factor obtained from OFW method									
Source	Sum of squares	DF	Mean square	F value	<i>P</i> -value>F				
$X_2X_3(X_2-X_3)$	4.14E+31	1	4.14E+31	81.69	>0.00 ^a				
Residual	1.52E+30	3	5.07E+29						
Total	5.14E+32	12							

(e) Activation	energy	obtained	from	analytical	method

Source	Sum of squares	DF	Mean square	F value	<i>P</i> -value>F
Model	3,255.28	9	361.70	7.69	0.06
Linear mixture	995.56	2	497.78	10.58	0.04^{a}
X_1X_2	336.96	1	336.96	7.16	0.08
X_1X_3	559.88	1	559.88	11.90	0.04^{a}
X_2X_3	107.86	1	107.86	2.29	0.23
$X_{1}X_{2}X_{3}$	146.81	1	146.81	3.12	0.18
$X_1X_2(X_1-X_2)$	766.25	1	766.25	16.28	0.03^{a}
$X_1X_3(X_1-X_3)$	364.69	1	364.69	7.75	0.07
$X_2X_3(X_2-X_3)$	332.46	1	332.46	7.06	0.08
Residual	141.19	3	47.06		
Total	3,396.47	12			

(f) Pre-exponential factor obtained from analytical method

Source	Sum of squares	DF	Mean square	F value	<i>P</i> -value>F
Model	1.24E+25	9	1.38E+24	73.02	>0.00 ^a
Linear mixture	4.68E+24	2	2.34E+24	124.38	$> 0.00^{a}$
X_1X_2	3.41E+24	1	3.41E+24	181.25	$> 0.00^{a}$
X_1X_3	3.41E+24	1	3.41E+24	181.25	$> 0.00^{a}$
X_2X_3	5.22E+20	1	5.22E+20	0.03	0.88
$X_{1}X_{2}X_{3}$	2.20E+23	1	2.20E+23	11.67	0.04^{a}
$X_1X_2(X_1-X_2)$	7.98E+23	1	7.98E+23	42.39	0.01^{a}
$X_1X_3(X_1-X_3)$	7.98E+23	1	7.98E+23	42.39	0.01^{a}
$X_2X_3(X_2-X_3)$	0.00E+00	1	0.00E+00	0.00	1.00
Residual	5.65E+22	3	1.88E+22		
Total	1.24E+25	12			

^aSignificant F-values at the 95% confidence level (*p*-value≤0.05) DF=Degrees of freedom

ANOVA analysis of kinetic parameters from KAS, OFW and analytical method (n^{th} -order kinetics)

Table A.2. The analysis of variance (ANOVA) for n^{th} -order kinetic values of biomass pyrolysis

(a) Activation energy obtained from KAS method								
Source	Sum of squares	DF	Mean square	F value	<i>P</i> -value>F			
Model	6,494.30	9	721.59	9.22	0.05			
Linear mixture	618.21	2	309.10	3.95	0.14			
X_1X_2	1,716.32	1	1,716.32	21.93	0.02^{a}			
X_1X_3	116.37	1	116.37	1.49	0.31			

Table A.2. Continued

(a) Activation energy obtained from KAS method								
Source	Sum of squares	DF	Mean square	F value	<i>P</i> -value>F			
X_2X_3	393.69	1	393.69	5.03	0.11			
$X_{1}X_{2}X_{3}$	147.75	1	147.75	1.89	0.26			
$X_1X_2(X_1-X_2)$	198.97	1	198.97	2.54	0.21			
$X_1X_3(X_1-X_3)$	100.62	1	100.62	1.29	0.34			
$X_2X_3(X_2-X_3)$	3,096.39	1	3,096.39	39.56	0.01^{a}			
Residual	234.82	3	78.27					
Total	6,729.13	12						

(b) Pre-exponential factor obtained from KAS method

Source	Sum of squares	DF	Mean square	F value	<i>P</i> -value>F
Model	5.74E+32	9	6.38E+31	76.91	>0.00 ^a
Linear mixture	1.68E+32	2	8.42E+31	101.54	$>0.00^{a}$
X_1X_2	8.70E+30	1	8.70E+30	10.49	0.05
X_1X_3	1.41E+32	1	1.41E+32	170.22	$>0.00^{a}$
X_2X_3	1.62E+32	1	1.62E+32	195.14	$> 0.00^{a}$
$X_{1}X_{2}X_{3}$	6.50E+30	1	6.50E+30	7.84	0.07
$X_1X_2(X_1-X_2)$	1.00E+31	1	1.00E+31	12.11	0.04^{a}
$X_1X_3(X_1-X_3)$	3.77E+31	1	3.77E+31	45.51	0.01^{a}
$X_2X_3(X_2-X_3)$	5.25E+31	1	5.25E+31	63.31	$>0.00^{a}$
Residual	2.49E+30	3	8.29E+29		
Total	5.76E+32	12			

(c) Reaction order obtained from KAS method

Source	Sum of squares	DF	Mean square	F value	<i>P</i> -value>F
Model	0.27	9	0.03	1.23	0.48
Linear mixture	0.06	2	0.03	1.29	0.39
X_1X_2	0.03	1	0.03	1.33	0.33
X_1X_3	0.07	1	0.07	2.98	0.18
X_2X_3	0.01	1	0.01	0.34	0.60
$X_{1}X_{2}X_{3}$	0.00	1	0.00	0.00	0.98
$X_1X_2(X_1-X_2)$	0.01	1	0.01	0.55	0.51
$X_1X_3(X_1-X_3)$	0.08	1	0.08	3.19	0.17
$X_2X_3(X_2-X_3)$	0.00	1	0.00	0.01	0.94
Residual	0.07	3	0.02		
Total	0.34	12			

(d) Activation energy obtained from OFW method

Source	Sum of squares	DF	Mean square	F value	<i>P</i> -value>F
Model	6,230.46	9	692.27	6.68	0.07
Linear mixture	505.64	2	252.82	2.44	0.24
X_1X_2	1,591.80	1	1,591.80	15.35	0.03^{a}
X_1X_3	225.60	1	225.60	2.18	0.24
X_2X_3	389.62	1	389.62	3.76	0.15
$X_{1}X_{2}X_{3}$	70.14	1	70.14	0.68	0.47
$X_1X_2(X_1-X_2)$	251.16	1	251.16	2.42	0.22
$X_1X_3(X_1-X_3)$	230.81	1	230.81	2.23	0.23
$X_2X_3(X_2-X_3)$	2,863.61	1	2,863.61	27.61	0.01^{a}

Table A.2. Continued

(d) Activation energy obtained from OFW method								
Source	Sum of squares	DF	Mean square	F value	<i>P</i> -value>F			
Residual	311.13	3	103.71					
Total	6,541.59	12						

(e)	Pre-exponential	factor	obtained	from	OFW	method
-----	-----------------	--------	----------	------	-----	--------

Source	Sum of squares	DF	Mean square	F value	<i>P</i> -value>F
Model	2.48E+31	9	2.76E+30	5.46	0.09
Linear mixture	2.29E+30	2	1.14E+30	2.26	0.25
X_1X_2	1.08E+31	1	1.08E+31	21.45	0.02^{a}
X_1X_3	8.52E+29	1	8.52E+29	1.69	0.28
X_2X_3	2.39E+29	1	2.39E+29	0.47	0.54
$X_{1}X_{2}X_{3}$	6.62E+30	1	6.62E+30	13.12	0.04^{a}
$X_1X_2(X_1-X_2)$	5.09E+30	1	5.09E+30	10.07	0.05
$X_1X_3(X_1-X_3)$	4.04E+30	1	4.04E+30	8.01	0.07
$X_2X_3(X_2-X_3)$	7.02E+29	1	7.02E+29	1.39	0.32
Residual	1.51E+30	3	5.05E+29		
Total	2.63E+31	12			

(f) Reaction order obtained from OFW method

Source	Sum of squares	DF	Mean square	F value	<i>P</i> -value>F
Model	0.27	9	0.03	1.23	0.48
Linear mixture	0.06	2	0.03	1.29	0.39
X_1X_2	0.03	1	0.03	1.33	0.33
X_1X_3	0.07	1	0.07	2.98	0.18
X_2X_3	0.01	1	0.01	0.34	0.60
$X_{1}X_{2}X_{3}$	0.00	1	0.00	0.00	0.98
$X_1X_2(X_1-X_2)$	0.01	1	0.01	0.55	0.51
$X_1X_3(X_1-X_3)$	0.08	1	0.08	3.19	0.17
$X_2X_3(X_2-X_3)$	0.00	1	0.00	0.01	0.94
Residual	0.07	3	0.02		
Total	0.34	12			

(g) Activation energy obtained from analytical method

Source	Sum of squares	DF	Mean square	F value	<i>P</i> -value>F
Model	11,277.52	9	1253.06	8.05	0.07
Linear mixture	8,318.79	2	4159.39	26.71	0.01^{a}
X_1X_2	2,109.19	1	2109.19	13.54	0.03^{a}
X_1X_3	0.36	1	0.36	0.00	0.96
X_2X_3	28.79	1	28.79	0.18	0.70
$X_{1}X_{2}X_{3}$	12.28	1	12.28	0.08	0.80
$X_1X_2(X_1-X_2)$	421.30	1	421.30	2.71	0.20
$X_1X_3(X_1-X_3)$	58.00	1	58.00	0.37	0.58
$X_2X_3(X_2-X_3)$	0.31	1	0.31	0.00	0.97
Residual	467.23	3	155.74		
Total	11,744.76	12			

Table A.2. Continued

(h) Pre-exponential factor obtained from analytical method								
Source	Sum of squares	DF	Mean square	F value	<i>P</i> -value>F			
Model	8.1E+27	9	9.0E+26	73.0	>0.00 ^a			
Linear mixture	3.1E+27	2	1.5E+27	124.4	$>0.00^{a}$			
X_1X_2	2.2E+27	1	2.2E+27	181.3	$>0.00^{a}$			
X_1X_3	2.2E+27	1	2.2E+27	181.3	>0.00 ^a			
X_2X_3	3.4E+23	1	3.4E+23	0.0	0.88			
$X_{1}X_{2}X_{3}$	1.4E+26	1	1.4E+26	11.7	0.04^{a}			
$X_1X_2(X_1-X_2)$	5.2E+26	1	5.2E+26	42.4	0.01^{a}			
$X_1X_3(X_1-X_3)$	5.2E+26	1	5.2E+26	42.4	0.01^{a}			
$X_2X_3(X_2-X_3)$	0.0E+00	1	0.0E+00	0.0	1.00			
Residual	3.7E+25	3	1.2E+25					
Total	8.1E+27	12						

(i) Reaction order obtained from analytical method

Source	Sum of squares	DF	Mean square	F value	<i>P</i> -value>F
Model	56.22	9	6.25	34.53	0.01 ^a
Linear mixture	0.42	2	0.21	1.16	0.42
X_1X_2	16.67	1	16.67	92.17	$>0.00^{a}$
X_1X_3	27.05	1	27.05	149.51	$>0.00^{a}$
X_2X_3	27.42	1	27.42	151.56	$>0.00^{a}$
$X_{1}X_{2}X_{3}$	2.72	1	2.72	15.02	0.03^{a}
$X_1X_2(X_1-X_2)$	0.66	1	0.66	3.67	0.15
$X_1X_3(X_1-X_3)$	0.41	1	0.41	2.24	0.23
$X_2X_3(X_2-X_3)$	0.18	1	0.18	0.99	0.39
Residual	0.54	3	0.18		
Total	56.76	12			

^aSignificant F-values at the 95% confidence level (*p*-value≤0.05) DF=Degrees of freedom

APPENDIX B

Regression models of predicted kinetic parameters from analytical method

For first-order kinetics

Activation $142.8X_1 + 89.3 X_2 + 103.3 X_3 - 81.9 X_1 R^2 = 0.96$ (B.1) $X_2 - 105.6 \ X_1 \ X_3 - 46.3 \ X_2 \ X_3 + 352.43$ energy: $X_1 X_2 X_3 - 236.5 X_1 X_2 (X_1 - X_2) - 163.2$

 $X_1X_3(X_1-X_3)-155.8X_2X_3(X_2-X_3)$

Pre-exponential $(3.7E+12)X_1-(7.9E+09)X_2 R^2 = > 0.99$ (B.2) (7.9E+09) X₃-(8.2E+12) X₁ X₂factor:

> $(8.2E+12) X_1 X_3 - (1.0E+11) X_2$ $X_3+(1.4E+13) X_1 X_2 X_3-(7.6E+12)$ $X_1X_2(X_1-X_2)-(7.6E+12) X_1X_3(X_1 X_3$)-(2.9E+07) $X_2X_3(X_2-X_3)$

For nth-order kinetics

Activation $177.3X_1 + 83.5 X_2 + 68.9 X_3 - 204.9 X_1 R^2 = 0.96$ (B.3)

energy: $X_2 - 2.7 X_1 X_3 - 23.9 X_2 X_3 + 101.9 X_1$ $X_2 X_3 - 175.4 X_1 X_2 (X_1 - X_2) - 65.1$ $X_1X_3(X_1-X_3)+4.7 X_2X_3(X_2-X_3)$

Pre-exponential $(9.3E+13)X_1-(2.0E+11)X_2 R^2=>0.99$ (B.4)

factor: $(2.0E+11) X_3-(2.1E+14) X_1 X_2 (2.1E+14) X_1 X_3-(2.6E+12) X_2$

 $\begin{array}{l} \text{(2.1E+14)} \ X_1 \ X_3 - \text{(2.0E+12)} \ X_2 \\ X_3 + \text{(3.5E+14)} \ X_1 \ X_2 \ X_3 - \\ \text{(2.0E+14)} X_1 X_2 (X_1 - X_2) - \text{(2.0E+14)} \\ X_1 X_3 (X_1 - X_3) + \text{(2.6E+08)} \ X_2 X_3 (X_2 - X_3) \end{array}$

Reaction order: $1.6X_1+1.1 X_2+1.4 X_3+18.2 X_1$ $R^2=0.99$ (B.5)

$$\begin{split} &X_2 + 23.2 \ X_1 \ X_3 + 23.4 \ X_2 \ X_3 - 47.9 \ X_1 \\ &X_2 \ X_3 - 7.0 \ X_1 X_2 (X_1 - X_2) - 5.4 \\ &X_1 X_3 (X_1 - X_3) + 3.6 \ X_2 X_3 (X_2 - X_3) \end{split}$$

Regression models of predicted kinetic parameters from KAS

For first-order kinetics

Activation $145.3X_1+123.8 X_2+200.7 X_3+184.8 R^2=0.97$ (B.6)

energy: $X_1 X_2 - 48.1 X_1 X_3 - 88.5 X_2 X_3 - 353.5 X_1 X_2 X_3 + 120.5 X_1 X_2 (X_1 - X_2) - 85.7$

 $X_1X_2X_3 + 120.5X_1X_2(X_1-X_2) = 05.5$ $X_1X_3(X_1-X_3) + 475.5 X_2X_3(X_2-X_3)$

Pre-exponential $-(4.0E+13)X_1+(6.8E+13)$ $R^2=0.99$ (B.7)

factor: $X_2+(2.3E+16)X_3+(2.0E+15)X_1X_2-$

(4.8E+16) X₁ X₃-(5.1E+16) X₂ X₃+(9.6E+16) X₁ X₂ X₃+(5.3E+15) X₁X₂(X₁-X₂)+(5.2E+16) X₁X₃(X₁-X₃)+(5.1E+16) X₂X₃(X₂-X₃)

For nth-order kinetics

Activation $145.3X_1 + 123.8 X_2 + 200.7 X_3 + 184.8 R^2 = 0.97$ (B.8)

energy: $X_1 X_2 - 48.1 X_1 X_3 - 88.5 X_2 X_3 - 353.5$

X₁ X₂ X₃+120.5X₁X₂(X₁-X₂)-85.7 X₁X₃(X₁-X₃)+475.5 X₂X₃(X₂-X₃)

Pre-exponential $-(3.1E+12)X_1+(5.9E+13)$ $R^2=>0.99$ (B.9)

factor: $X_2+(2.5E+16) X_3+(1.3E+16) X_1 X_2-$ (5.3E+16) $X_1 X_3-(5.7E+16) X_2$

(5.3E+16) X₁ X₃-(5.7E+16) X₂ X₃+(7.4E+16) X₁ X₂ X₃+(2.7E+16) X₁X₂(X₁-X₂)+(5.2E+16) X₁X₃(X₁-X₃)+(6.2E+16) X₂X₃(X₂-X₃)

Reaction order: $1.4X_1+1.5 X_2+1.1 X_3+0.8 X_1 X_2+1.2 R^2=0.79$ (B.10)

 $X_1 X_3 + 0.4 X_2 X_3 + 0.1 X_1 X_2 X_3 + 1.0$ $X_1 X_2 (X_1 - X_2) - 2.4 X_1 X_3 (X_1 - X_3) - 0.1$

 $X_2X_3(X_2-X_3)$

Regression models of predicted kinetic parameters from OFW

For first-order kinetics

Activation $147.8X_1 + 126.8 X_2 + 200.8 X_3 + 178.0 R^2 = 0.95$ (B.11)

energy: $X_1 X_2 - 67.0 X_1 X_3 - 88.1 X_2 X_3 - 243.6$ $X_1 X_2 X_3 + 135.4 X_1 X_2 (X_1 - X_2) - 129.8$

 $X_1 X_2 X_3 + 135.4 X_1 X_2 (X_1 - X_2) - 129$ $X_1 X_3 (X_1 - X_3) + 457.3 X_2 X_3 (X_2 - X_3)$

Pre-exponential $-(1.1E+13)X_1+(4.2E+13)$ $R^2=>0.99$ (B.12)

factor: $X_2+(2.4E+16) X_3+(7.9E+15) X_1 X_2-$

 $(5.1E+16) X_1 X_3 - (5.5E+16) X_2$

X₃+(8.5E+16) X₁ X₂ X₃+(1.6E+16)X₁X₂(X₁-X₂)+(5.1E+16) X₁X₃(X₁-X₃)+(5.5E+16) X₂X₃(X₂-X₃)

For nth-order kinetics

Activation $147.8X_1 + 126.8 X_2 + 200.8 X_3 + 178.0 R^2 = 0.95 (B.13)$

energy: $X_1 X_2 - 67.0 X_1 X_3 - 88.1 X_2 X_3 - 243.6$ $X_1 X_2 X_3 + 135.4 X_1 X_2 (X_1 - X_2) - 129.8$

 $X_1 X_2 X_3 + 135.4 X_1 X_2 (X_1 - X_2) - 129.8$ $X_1 X_3 (X_1 - X_3) + 457.3 X_2 X_3 (X_2 - X_3)$

Pre-exponential $-(4.2E+12)X_1-(6.3E+13)X_2 R^2 = 0.94$ (B.14)

factor: $(4.3E+13) X_3+(1.5E+16) X_1$

 $X_2+(4.1E+15) X_1 X_3+(2.2E+15) X_2$

$$\begin{split} &X_3-(7.5E+16)\;X_1\;X_2\\ &X_3+(1.9E+16)X_1X_2(X_1-X_2)-\\ &(1.7E+16)\;X_1X_3(X_1-X_3)+(7.2E+15) \end{split}$$

 $X_2X_3(X_2-X_3)$

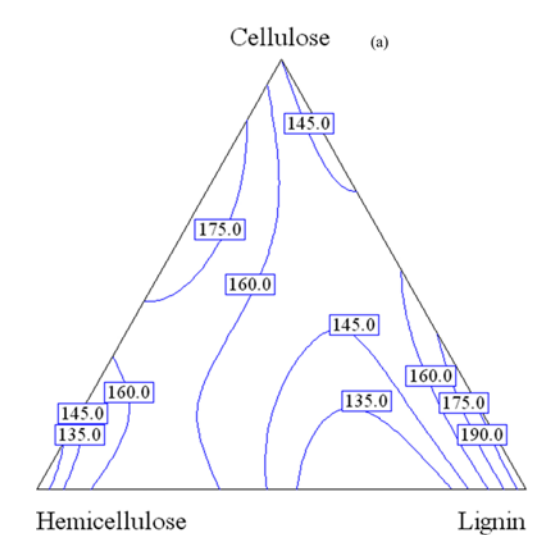
Reaction order: $1.4X_1 + 1.5 X_2 + 1.1 X_3 + 0.8 X_1 X_2 + 1.2 R^2 = 0.79$ (B.15)

 $\begin{array}{l} X_1 \; X_3 \! + \! 0.4 \; X_2 \; X_3 \! + \! 0.1 \; X_1 \; X_2 \\ X_3 \! + \! 1.0 X_1 X_2 (X_1 \! - \! X_2) \! - \! 2.4 \; X_1 X_3 (X_1 \! - \! X_2) \\ \end{array}$

 X_3) - 0.1 $X_2X_3(X_2-X_3)$

APPENDIX C

Contour plots of predicted kinetic parameters from KAS and OFW



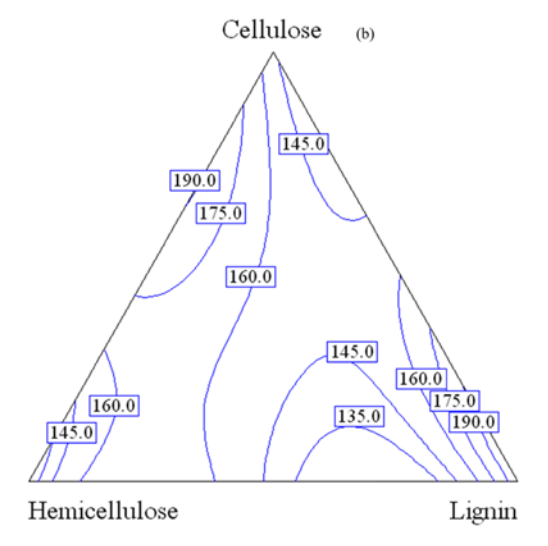


Fig. C.1. Ternary contour plots of predicted activation energy (for first-order kinetics) obtained from KAS (a) and OFW (b).

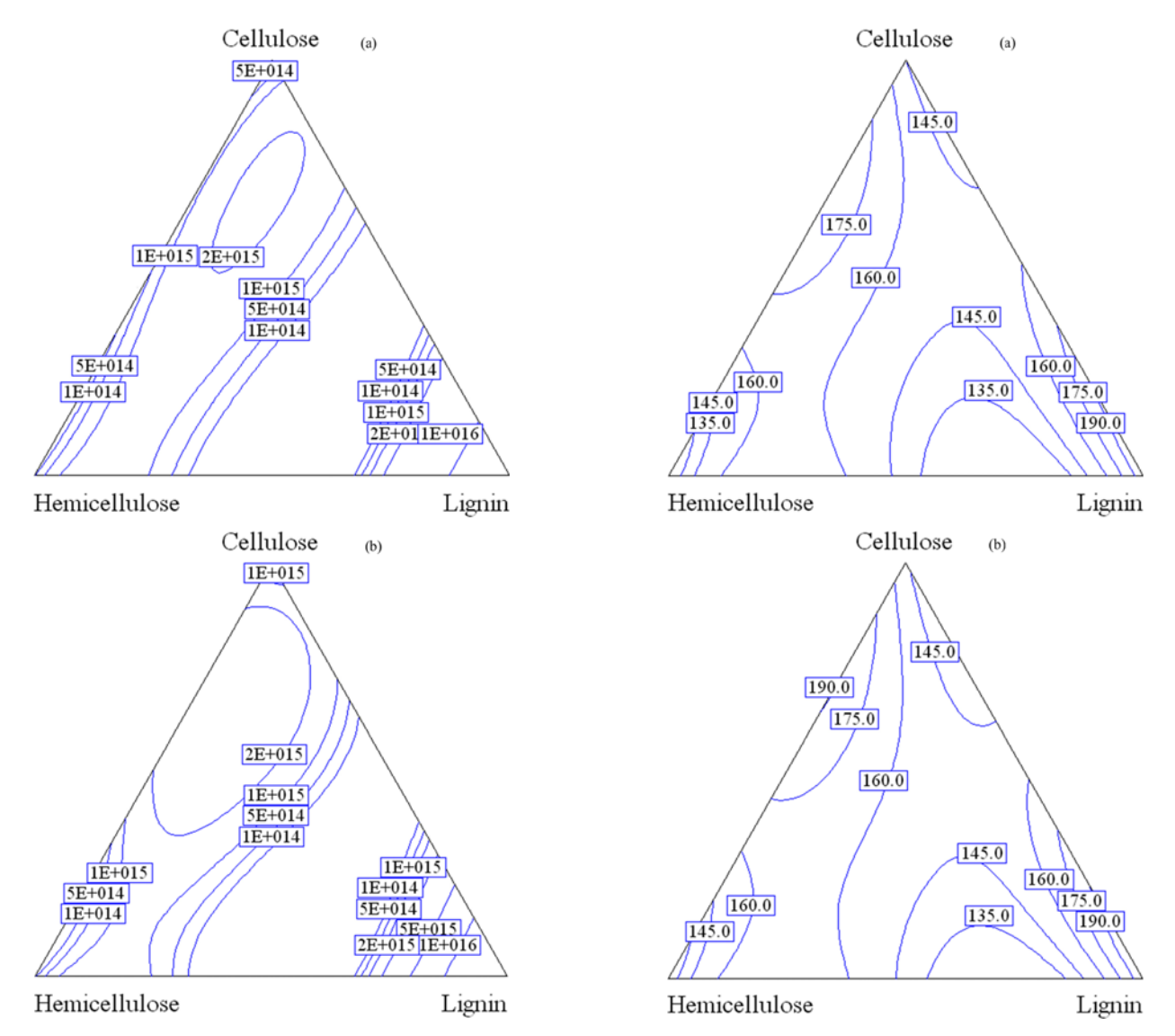


Fig. C.2. Ternary contour plots of predicted frequency factor (for first-order kinetics) obtained from KAS (a) and OFW (b).

Fig. C.3. Ternary contour plots of predicted activation energy (for any-order kinetics) obtained from KAS (a) and OFW (b).

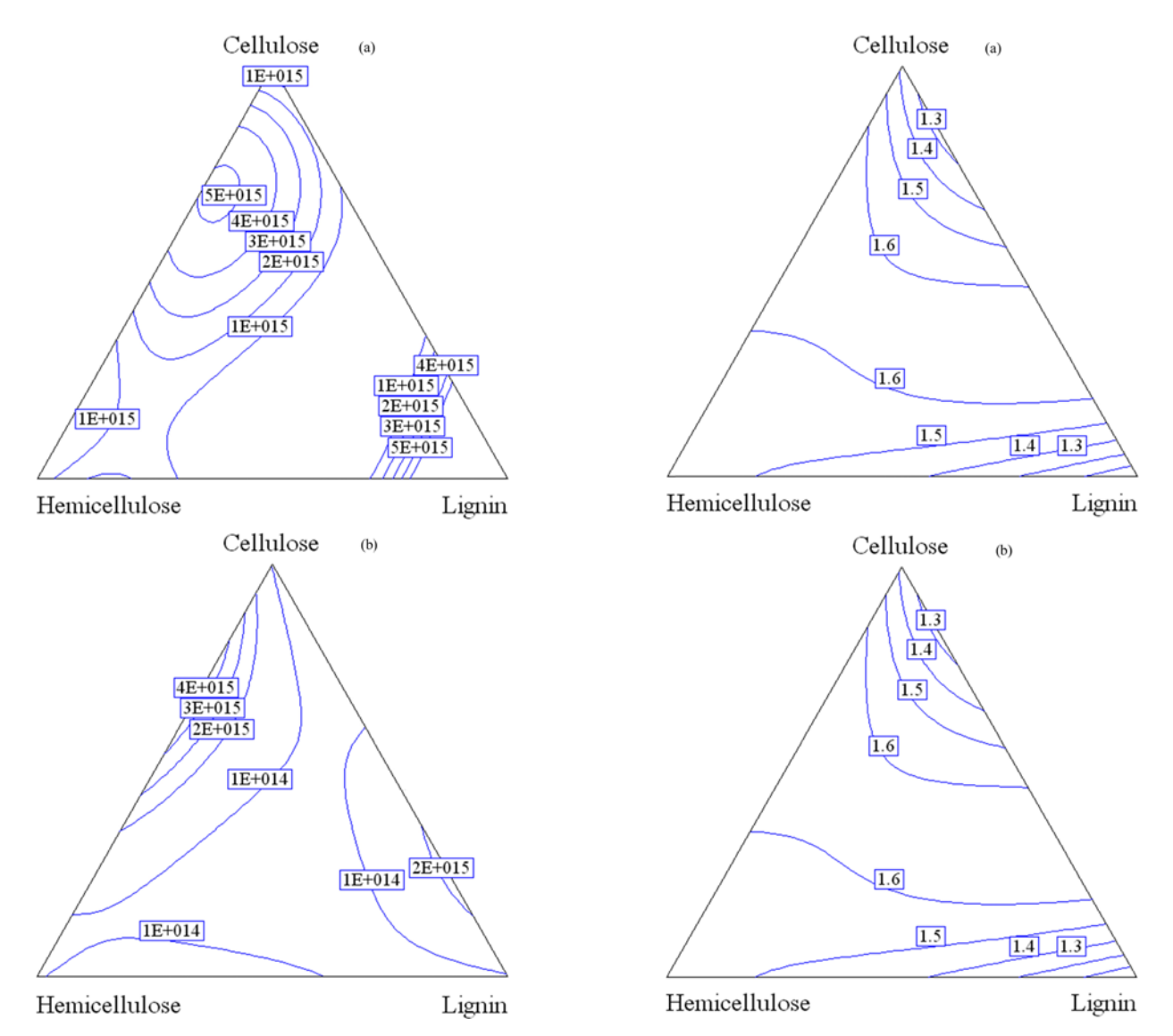


Fig. C.4. Ternary contour plots of predicted frequency factor (for any-order kinetics) obtained from KAS (a) and OFW (b).

Fig. C.5. Ternary contour plots of predicted reaction order (for anyorder kinetics) obtained from KAS (a) and OFW (b).



Chemical Engineering Communications



Date: 13 March 2016, At: 06:22

ISSN: 0098-6445 (Print) 1563-5201 (Online) Journal homepage: http://www.tandfonline.com/loi/gcec20

Thermogravimetric Analysis and Chemical Kinetics for Regeneration of Sodium and Potassium Carbonate Solid Sorbents

Pilaiwan Chaiwang, Benjapon Chalermsinsuwan & Pornpote Piumsomboon

To cite this article: Pilaiwan Chaiwang, Benjapon Chalermsinsuwan & Pornpote Piumsomboon (2016) Thermogravimetric Analysis and Chemical Kinetics for Regeneration of Sodium and Potassium Carbonate Solid Sorbents, Chemical Engineering Communications, 203:5, 581-588, DOI: 10.1080/00986445.2015.1078796

To link to this article: http://dx.doi.org/10.1080/00986445.2015.1078796

	Accepted author version posted online: 24 Aug 2015.
	Submit your article to this journal 🗷
ılıl	Article views: 26
Q ^L	View related articles 🗗
CrossMark	View Crossmark data 🗗

Full Terms & Conditions of access and use can be found at http://www.tandfonline.com/action/journalInformation?journalCode=gcec20

ISSN: 0098-6445 print/1563-5201 online DOI: 10.1080/00986445.2015.1078796



Thermogravimetric Analysis and Chemical Kinetics for Regeneration of Sodium and Potassium Carbonate Solid Sorbents

PILAIWAN CHAIWANG¹, BENJAPON CHALERMSINSUWAN^{1,2}, and PORNPOTE PIUMSOMBOON^{1,2}

In this study, nonisothermal kinetic methods for the decomposition of potassium hydrogen carbonate (KHCO₃) and sodium hydrogen carbonate (NaHCO₃) were investigated by thermogravimetry (TG) and derivative thermogravimetry (DTG). Four different heating rates were measured to calculate the order of reaction (n), preexponential factor (A), and activation energy (E_a) using four different models: Kissinger–Akahira–Sunose (KAS), Flynn–Wall–Ozawa (FWO), Kim–Park, and analytical methods. The results showed that the analytical method provided highly accurate results compared with the experimental data, whereas KAS, FWO, and Kim–Park methods gave less accurate results due to the approximation of employed equations. The order of the decomposition reaction of KHCO₃ and NaHCO₃ was approximately 2. The preexponential factor of KHCO₃ was slightly higher than NaHCO₃. The obtained kinetic parameters from those four methods then were used to calculate the chemical reaction conversion for further applications.

Keywords: Adsorption; Chemical Kinetics; Potassium hydrogen carbonate; Regeneration; Sodium hydrogen carbonate; Thermogravimetric analysis

Introduction

At this time, the major greenhouse gas affecting the atmosphere is carbon dioxide (CO₂). The emitting and reduction processes of CO2 by primary production take place naturally (Kramer, 1981). Since the industrial revolution, CO₂ emission has been dramatically increasing due to human activities such as coal and fossil fuel combustions, power generation, and transportation. The ratio of the world total energy production is increasing according to population growth (Duncan, 2001). Many research studies have found various methods for capturing CO₂ such as wet absorption (Yokozeki et al., 2008), adsorption such as solid sorbent, pressure swing adsorption (PSA) at high pressure (Kikkinides et al., 1993), chemical absorption, for example, amine solution (Saha et al., 1995), membrane separation, and cryogenic distillation or biological process from algae (Olaizola et al., 2004). Among these methods, dry alkali-metal solid sorbent has been considered to be an

Address correspondence to Pornpote Piumsomboon, Fuels Research Center, Department of Chemical Technology, Faculty of Science, Chulalongkorn University, 254 Phayathai Road, Patumwan, Bangkok 10330, Thailand. E-mail: pornpote.p@chula.ac.th

Color versions of one or more of the figures in the article can be found online at www.tandfonline.com/gcec.

effective method in terms of cost and energy consumption. The method is composed of two main processes: adsorption and regeneration. CO₂ and other gases from flue gas enter and make contact with solid sorbents in the adsorption reactor and then release clean gas into the atmosphere. After the adsorption, spent sorbents are transferred to the regeneration reactor to desorb rich CO₂ for carbon capture storage (CCS) by using thermal (Zhao et al., 2010) or vacuum approaches (Kongkitisupchai and Gidaspow, 2013). Zhao et al. (2010) found that potassium carbonate on alumina (K₂CO₃/Al₂O₃) sorbent had very capable sorption and regeneration abilities in a bubbling fluidized bed. The understanding of bicarbonates sorption chemical kinetics has been extensively studied (Park et al., 2006; Behr et al., 2011; Liang et al., 2004). After the adsorption process, it is necessary to understand kinetic parameters to maintain lower energy demand. However, the kinetics for regeneration of solid sorbents is still lacking in the literature. The regeneration reaction scheme is considered as an irreversible decomposition reaction. This assumption works well with the solid-state compound. The regeneration kinetic model depicts the conversion behavior, including the initial rate retardation (Lee et al., 2013).

In this study, nonisothermal kinetic methods of the decomposition of potassium hydrogen carbonate (KHCO₃) and sodium hydrogen carbonate (NaHCO₃) were investigated

¹Fuels Research Center, Department of Chemical Technology, Faculty of Science, Chulalongkorn University, Patumwan, Bangkok, Thailand

²Center of Excellence on Petrochemical and Materials Technology, Chulalongkorn University, Patumwan, Bangkok, Thailand

582 P. Chaiwang et al.

and compared by using thermogravimetry (TG) and derivative thermogravimetry (DTG). The sorption of these two solid sorbents was successfully explored in the literature. Four different models, which were Kissinger–Akahira–Sunose (KAS), Flynn–Wall–Ozawa (FWO), Kim–Park, and analytical methods, were used to calculate the order of reaction (n), the preexponential factor (A), and activation energy (E_a) . For the reaction rate constant, it depends on the temperature provided by the Arrhenius equation.

Kinetic Study: Theory

The expression of the rate law for nonisothermal decomposition criteria can be clarified from the single-step kinetic equation of solid-state decomposition as described in Equation (1):

$$\frac{\mathrm{d}\alpha}{\mathrm{d}t} = k(T)f(\alpha) \tag{1}$$

where $f(\alpha)$ is the reaction conversion mechanism model which can take place in various forms. The temperature dependence of the reaction rate constant is provided as k(T) according to the Arrhenius equation:

$$\frac{\mathrm{d}\alpha}{\mathrm{d}t} = k(T)f(\alpha) = A\exp\left(\frac{-E_a}{RT}\right)f(\alpha) \tag{2}$$

For nonisothermal conversion, the heating rate of the sample is constant. The $d\alpha/dt$ term in Equation (2) is converted into $\beta(d\alpha/dT)$ in Equation (3), where β is the heating rate:

$$\frac{\mathrm{d}\alpha}{\mathrm{d}T} = \frac{k(T)}{\beta}f(\alpha) = \frac{A}{\beta}\exp\left(\frac{-E_a}{RT}\right)f(\alpha) \tag{3}$$

$$g(\alpha) = \int_{0}^{\alpha} \frac{d\alpha}{f(\alpha)} = \frac{A}{\beta} \int_{0}^{T} \exp\left(\frac{-E_{a}}{RT}\right) dT$$
 (4)

Substituted $x \cong E_a/RT$ in Equation (4),

$$g(\alpha) = \frac{AE_a}{\beta R} \int_{\alpha}^{\infty} \frac{\exp^{-x}}{x^2} dx = \frac{AE_a}{\beta R} p(x)$$
 (5)

where p(x) in Equation (5) is the temperature integral which cannot generally define the exact solution. However, the temperature integral can be estimated from an empirical interpolation equation presented in a number of studies (White et al., 2011). There are two methods for analyzing nonisothermal solid-state kinetic data from TGA: model-fitting and model-free types. Both can determine isothermal and nonisothermal conditions (Slopiecka et al., 2012). The selected methods in this study covered all the methods mentioned in the literature.

Kissinger-Akahira-Sunose Method

This method was developed by Kissinger–Akahira–Sunose (Kissinger, 1957; Akahira and Sunose, 1971). They used $p(x) \cong e^{-x}/x^2$, for $20 \le x \le 50$, as shown in Equation (6):

$$\ln \frac{\beta}{T^2} = \ln \frac{AR}{E_a g(\alpha)} - \frac{E_a}{RT} \tag{6}$$

The calculation of the order of reaction, *n*, using the shape index factor, *S*, can be determined in Equations (7) and (8) by the Kissinger index (Kissinger, 1957; Lin et al., 2010), which measures the absolute value of the ratio of the slope from the inflecting point toward the left (a) and the right (b) of its TG tangent lines.

Table I. The solid-state reaction mechanisms in the general form

Reaction model	nodel $f(\alpha) = (1/k)(d\alpha / dt)$	
Reaction order		
Zero order	$(1-\alpha)^n$	α
First order	$\frac{(1-\alpha)^n}{(1-\alpha)^n}$	$-\ln(1-\alpha)$
<i>n</i> th order	$(1-\alpha)^n$	$-\ln(1-\alpha) \\ (n-1)^{-1}(1-\alpha)^{(1-n)}$
Nucleation		
Power law	$n(\alpha)^{(1-1/n)}$; $n = 2/3, 1, 2, 3, 4$	α^n ; $n = 3/2, 1, 1/2, 1/3, 1/4;$
Exponential law	ln α	α
Avrami–Erofeev (AE)	$n(1-\alpha)[-\ln(1-\alpha)]^{(1-1/n)}; n=1, 2, 3, 4$	$[-\ln(1-\alpha)]^{1/n}$; $n=1, 2, 3, 4$
Prout–Tompkins (PT)	$\alpha (1 - \alpha)$	$\ln[\alpha (1-\alpha)^{-1}] + C^{\underline{a}}$
Diffusional		
1-D	$1/2\alpha$	α^2
2-D	$[-\ln(1-\alpha)]^{-1}$	$(1 - \alpha)\ln(1 - \alpha) + \alpha$
3-D (Jander)	$3/2(1-\alpha)^{2/3}[1-(1-\alpha)^{1/3}]^{-1}$	$(1 - \alpha)\ln(1 - \alpha) + \alpha$ $[1 - (1 - \alpha)^{1/3}]^2$
3-D (Ginstling–Brounshtein)	$\begin{array}{l} [-\ln(1-\alpha)]^{-1} \\ 3/2(1-\alpha)^{2/3}[1-(1-\alpha)^{1/3}]^{-1} \\ 3/2[(1-\alpha)^{-1/3}-1]^{-1} \end{array}$	$1-2/3\alpha-(1-\alpha)^{2/3}$
Contracting geometry		, , , ,
Contracting area	$(1-\alpha)^{(1-1/n)}; n=2$	$1 - (1 - \alpha)^{1/n}; n = 2$
Contracting volume	$(1-\alpha)^{(1-1/n)}; n=3$	$1 - (1 - \alpha)^{1/n}; n = 3$

 $[\]underline{a}$ = Integration constant.

$$S = |a/b| \tag{7}$$

$$n = 1.26\sqrt{S} \tag{8}$$

Flynn-Wall-Ozawa Method

Flynn-Wall-Ozawa (Flynn and Wall, 1966; Ozawa, 1965) proposed the temperature integral function using Doyle's approximation obtained from the thermal decomposition of octamethylcyclotetrasiloxane and polytetrafluoroethylene powders in Equations (9) and (10) (Doyle 1961; Doyle 1962). The order of reaction, n, can be calculated by the same method as the KAS method in Equations (7) and (8).

$$\log \beta = \log \frac{AE_a}{g(\alpha)R} - 2.315 - 0.457 \frac{E_a}{RT}$$
 (9)

$$\log p(x) \cong -2.315 - 0.4567x$$
, for $20 \le x \le 60$ (10)

Kim-Park Method

Kim and Park (1995) developed a mathematical model that shows the relationship of heating rate and DTG curves as follows:

$$\ln \beta = \ln Z + \ln \left(\frac{E_a}{R}\right) + \ln \left[1 - n + \frac{n}{0.944}\right] - 5.3305 - 1.0516 \left(\frac{E_a}{RT_m}\right)$$
(11)

$$n = (E_a(1 - \alpha_m)/((RT_m^2)(d\alpha/dT)_m)))$$
 (12)

For this method, the order of reaction, n, is obtained by Equation (12) (Tang et al., 2004), where α_m , T_m , and $(d\alpha/dT)_m$ in Equations (11) and (12) are the maximum

conversion, maximum decomposition temperature, and maximum weight loss rate, respectively.

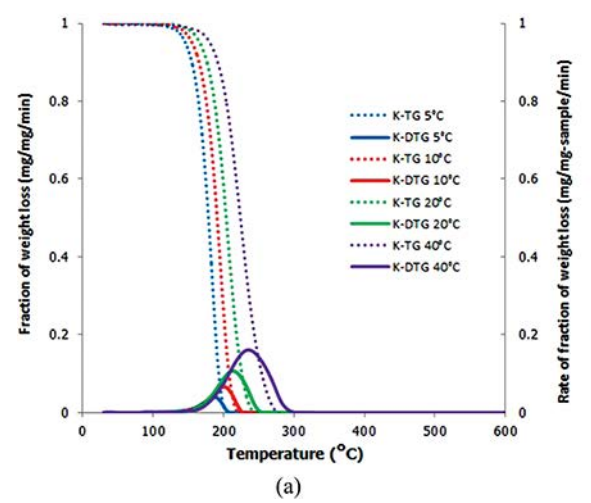
The Analytical Method

This method is generally derived from the expression of the reaction rate of the solid-state mechanism in Equation (3), where the reaction conversion $f(\alpha)$ is the *n*th reaction order from Table I. The relationship between weight loss and temperature can be written in terms of the activation energy and frequency factor. It can be calculated by Equation (13), when $n \neq 1$ (Zhu et al., 2012):

$$\alpha = 1 - \left\{ 1 - (n-1) \left(\frac{ART^2}{\beta E_a} \right) \left(1 - \frac{2RT}{E_a} \right) \right\}^{\frac{1}{1-n}} \exp \left(-\frac{E_a}{RT} \right) \right\}^{\frac{1}{1-n}}$$
(13)

Experiment

KHCO₃ and NaHCO₃ AR grade from Ajex Finechem Pty Ltd were investigated by using the Pyris Diamond Perkin Elmer thermogravimetric analyzer apparatus. The average size and density of KHCO₃ particles were 500 μ m and 2170 kg/m³, respectively, while the NaHCO₃ particles were 300 μ m and 2160 kg/m³, respectively. The sample solid sorbent weight for each run was 20 mg. Four different heating rates, 5, 10, 20 and 40°C/min under N₂ atmosphere, were used to carry out TG and DTG data. The constant inert gas flow rate of 50 ml N₂/min was used throughout the experiment. All sample conditions operated with initial and final temperatures of 40°C and 600°C, respectively. The conversion, α , can be determined in terms of weight loss as shown in Equation (14). Therefore, in this experiment, CO₂ gas and water vapor are decomposed:



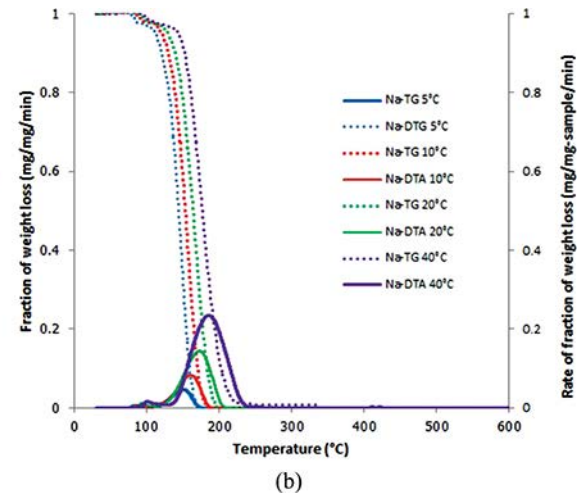


Fig. 1. (a) TG and DTG curves of KHCO₃ using four different heating rates. (b) TG and DTG curves of NaHCO₃ using four different heating rates.

P. Chaiwang et al.

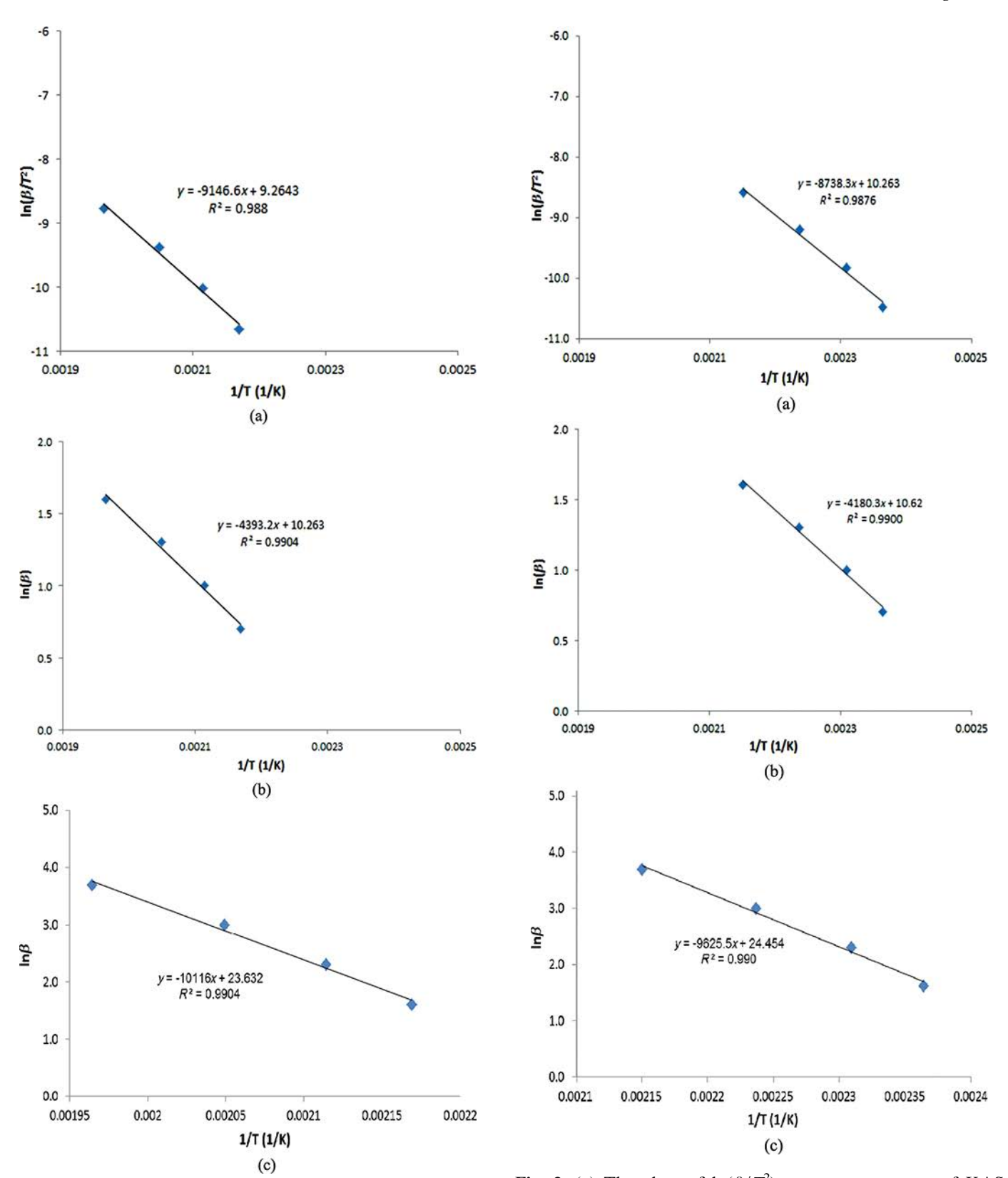


Fig. 2. (a) The plots of $\ln(\beta/T^2)$ versus temperature of KAS method in Equation (6) of KHCO₃. (b) The plots of $\ln(\beta)$ versus temperature of FWO method in Equation (9) of KHCO₃. (c) The plots of $\ln(\beta)$ versus temperature of Kim–Park method in Equation (11) of KHCO₃.

Fig. 3. (a) The plots of $\ln(\beta/T^2)$ versus temperature of KAS method in Equation (6) of NaHCO₃. (b) The plots of $\ln(\beta)$ versus temperature of FWO method in Equation (9) of NaHCO₃. (c) The plots of $\ln(\beta)$ versus temperature of Kim–Park method in Equation (11) of NaHCO₃.

		KHCO ₃			NaHCO ₃	
Method	n	A (min ⁻¹)	E_a (kJ/mol)	N	$A (\min^{-1})$	E_a (kJ/mol)
KAS	1.49	1.40E + 08	76.05	1.51	3.73E + 08	72.65
FWO	1.49	5.72E + 08	79.98	1.51	1.40E + 09	76.10
Kim-Park	1.46	3.90E + 08	79.98	1.53	9.87E + 08	76.31
Analytical	2.01	5.00E + 19	178.10	1.94	1.38E + 20	163.70

Table II. The results of n, A, and E_a obtained by KAS, FWO, Kim-Park, and analytical methods

$$\alpha = \frac{w_{initial} - w}{w_{initial} - w_{final}} \tag{14}$$

Results and Discussion

Thermogravimetric Analysis

As stated in the previous section, solid sorbent particles were heated from 40°C to maximum temperature of 600°C. TG and DTG curves of KHCO₃ and NaHCO₃ particles corresponding to a studied chemical reaction using four different heating rates are shown in Figure 1(a) and (b), respectively. TG is the parameter which displays weight loss fraction as

shown by the left-hand axis. For the chemical reaction characteristic, KHCO₃ particles began to decompose at a temperature of 120°C and terminated in the narrow range between 200°C and 300°C, while NaHCO₃ particles began to decompose at a temperature of 100°C and terminated in the range between 150°C and 250°C. This is because pure bicarbonate particles were employed in both cases. A heating rate of 5°C provided the maximum slope of weight loss, and the slope gradually decreased with the increase of heating rate. This is because the change of temperature is narrower than the others. While the system is heated, the temperature lag between apparatus and system is not much different. Solid sorbent particles then have time to absorb the heat and decompose earlier. The rate of fraction of

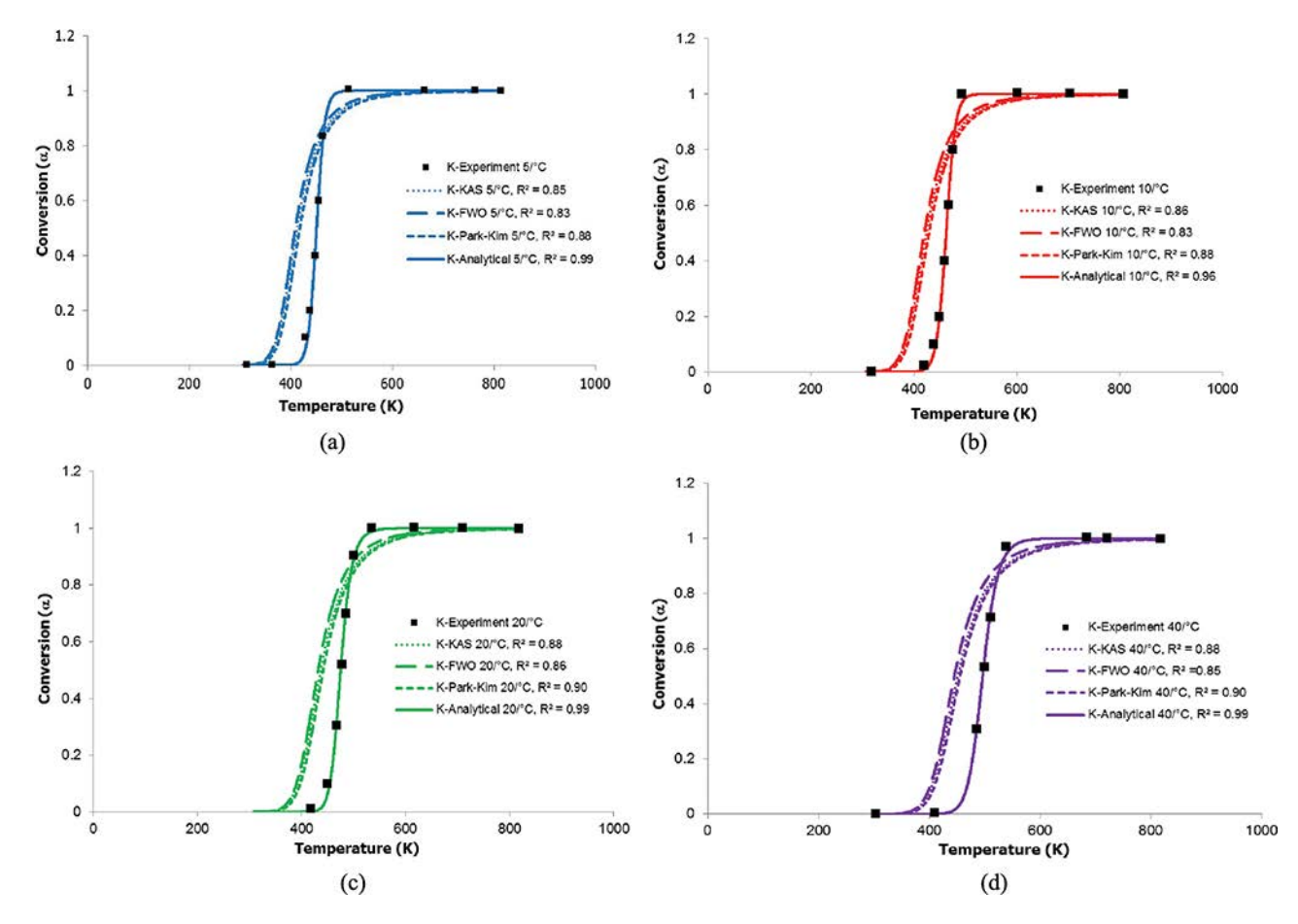


Fig. 4. The KHCO₃ conversion versus temperature of KAS, FWO, Kim–Park, and analytical methods for heating rate of (a) 5, (b) 10, (c) 20, and (d) 40°C/min comparing with the experiments.

586 P. Chaiwang et al.

weight loss or DTG is displayed in the right-hand axis of Figure 1. This shows one region peak representing the decomposition temperature for each heating rate. From the TG and DTG curves, when the decomposition temperature increased, the rate of weight loss fraction increased accordingly. At a heating rate of 40°C/min, both TG and DTG showed similar trends which were sharply decomposed at the highest temperature. When solid sorbent particles reached the decomposition temperature, CO₂ was released into the atmosphere which led to a weight loss fraction. Moreover, the increase of heating rate shifted the highest weight loss fraction to a higher temperature due to the temperature gradient inside the experimental system (Yang et al., 2004).

Kinetic Parameter Analysis

The kinetic parameters were calculated from the results acquired through thermogravimetric analysis. Four maximum weight loss peaks from Figure 1 were used to calculate the kinetic parameters in Equation (3). As stated above, the order of the reaction (n) for each heating rate was obtained from the absolute value of the ratio of the

slope from the inflecting point toward the left and the right of its TG tangent lines. The activation energy (E_a) and the preexponential factor (A) were determined using KAS, FWO, and Kim-Park methods. The KHCO₃ plot between $\ln(\beta/T^2)$ versus temperature of KAS method and the plot between $\log(\beta)$ versus inverse temperature of FWO and Kim-Park methods are displayed in Figure 2(a), (b), and (c), respectively. The NaHCO₃ plot between $\ln(\beta/T^2)$ versus temperature of KAS method and the plot between $\log(\beta)$ versus temperature of FWO method are displayed in Figure 3(a), (b), and (c), respectively. The linear regressions and the correlation coefficients (R^2) are also shown in these figures. The activation energy (E_a) and the preexponential factor (A) are derived from the slope and intercept of the linear regression plot, respectively.

The kinetic parameters of the analytical method in Equation (13) were determined using MATLAB. Table II shows the results of n, A, and E_a of KHCO₃ and NaHCO₃ obtained by KAS, FWO, Kim–Park, and analytical methods. Due to heat of regeneration, E_a of NaHCO₃ was lower than the ones of KHCO₃ which is consistent to the experimental data as NaHCO₃ began to decompose first (Chalermsinsuwan et al., 2010). While n of bicarbonates

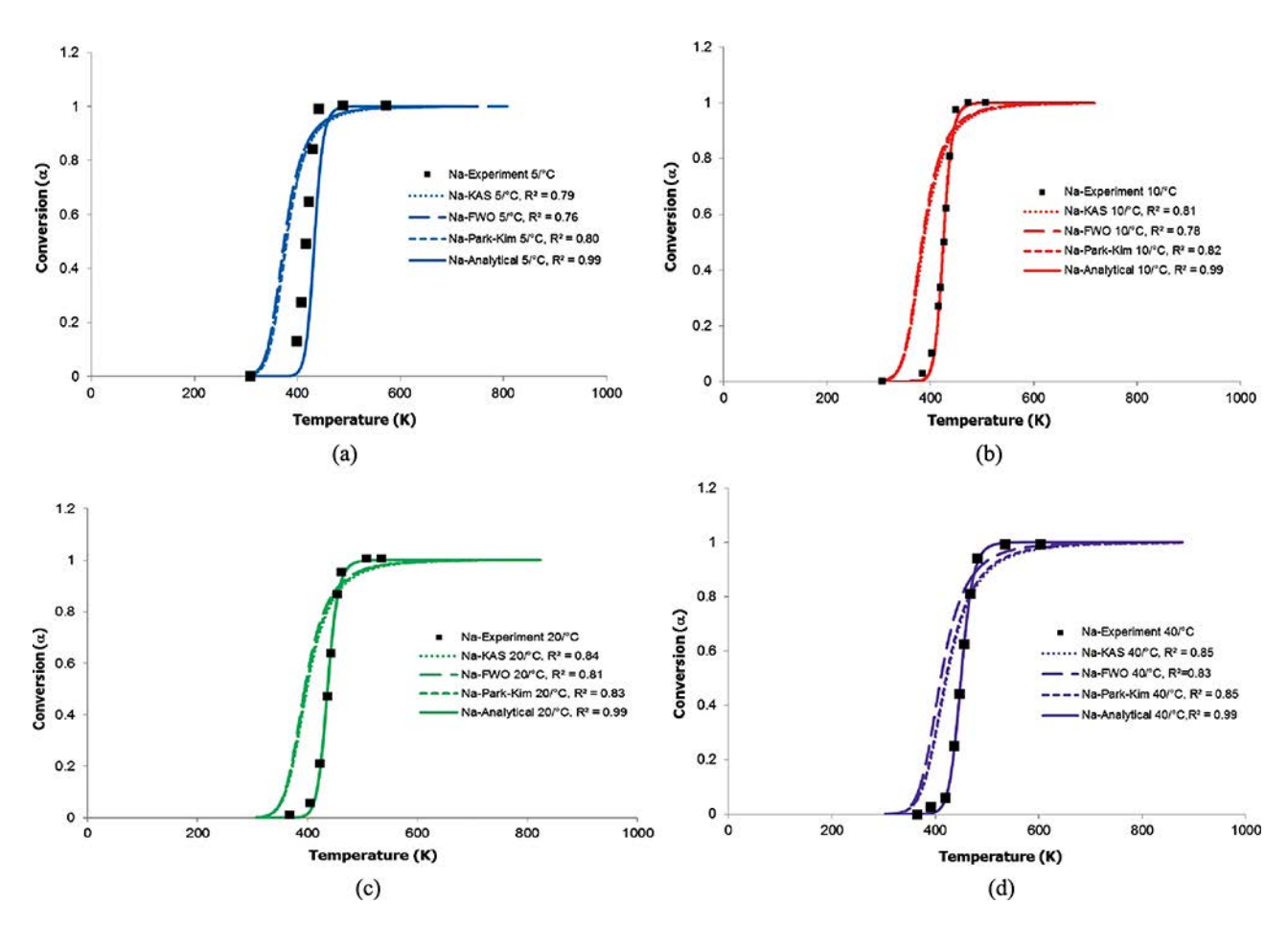


Fig. 5. The NaHCO₃ conversion versus temperature of KAS, FWO, Kim–Park, and analytical methods for heating rate of (a) 5, (b) 10, (c) 20, and (d) 40°C/min comparing with the experiments.

was close to 2, it can be seen that the obtained n values of KAS and FWO methods were similar, and A and E_a were quite similar since these two methods are derived from the same origin, Equation (2). Based on the literature about the decomposition of NaHCO₃, Koga et al. (2013) presented that the order of this reaction from the nonlinear least-square analysis optimization was second-order with the R^2 higher than 0.95, which was consistent with this experiment. In addition, since the equations of KHCO₃ and NaHCO₃ decomposition are an elementary bimolecular second-order reaction, the exact order of reaction in these equations should be 2. The analytical method used all of the raw data from an initial temperature to a final temperature; then, this was converted to conversion data (α) in following equation from TGA, whereas KAS, FWO, and Kim-Park methods used the range of data from the beginning of the decomposition temperature until the terminated temperature.

The kinetic parameters in Table II were substituted back in Equation (13), where $n \neq 1$ to find the reaction conversion (α). The conversion versus temperature of KAS, FWO, Kim-Park, and analytical methods of KHCO₃ particles with their R^2 values are displayed in Figure 4(a)–(d). Comparing the experiments with heating rates of 5, 10, 20. and 40°C/min, the results in Figure 4(a)–(d) show that the analytical method fits very well with the experimental data. Their R^2 were 0.95 for all heating rates. The results thus show that the best heating rate for regeneration of KHCO₃ and NaHCO₃ solid particles was 5°C/min due to the high heat transfer penetration. Nevertheless, the KAS and FWO methods were slightly different from the experimental data, especially during the decomposition reaction. Furthermore, the obtained results from the conversion versus temperature of KAS, FWO, and analytical methods of NaHCO₃ particles shown in Figure 5(a)-(d) are similar. From a previous study, the intrinsic first-order kinetic parameters of 125-µm NaHCO₃ particles using TG experimental data could calculate E_a equal to $102 \, \mathrm{kJ/mol}$ (Hu et al., 1986). With the Avrami–Erofeev equation with $f(\alpha)$, the E_a under N_2 atmosphere was in the range of 90-119 kJ/mol (Heda et al., 1995). The kinetic parameter from the analytical method then was consistent with the experimental data found in the literature.

There was deviation of the results obtained from the KAS and FWO calculation methods. The deviation depended on choosing the slope to compute the order of reaction from the inflecting point toward the left or the right of its TG of each heating rate. Meanwhile, the Kim-Park method used the maximum temperature values of DTG to calculate the order of reaction. These three methods used Doyle's approximation which was arranged in the integral function terms, p(x). This caused the obtained values to be lower than the actual value, while the analytical method was derived directly from the single decomposition equation. After this calculation, the results of n, A, and E_a will be applied as kinetic parameters in models to simulate the chemical reaction as well as be used for chemical reaction model optimization.

Conclusions

In this study, nonisothermal kinetic methods of the decomposition of KHCO₃ and NaHCO₃ were investigated by TG and DTG. Four different heating rates were used to calculate the order of reaction (n), preexponential factor (A), and activation energy (E_a) using four different models. The results showed that the analytical method provided the most accurate results compared with KAS, FWO, and Kim–Park methods. The activation energy of NaHCO₃ was lower than that of KHCO₃ due to heat of regeneration. The order of the decomposition reaction of KHCO₃ and NaHCO₃ was approximately 2. The preexponential factor of KHCO₃ was slightly higher than NaHCO₃. When compared to the experimental data, the R² for analytical method were higher than 0.95 for all the heating rates.

Funding

This research has been supported by the Ratchadaphisek-somphot Endowment Fund 2015 of Chulalongkorn University. In addition, the authors wish to thank the Thailand Research Fund for partial support through the Royal Golden Jubilee Ph.D. Program (Grant No. PHD/0356/2551) and Thailand Research Fund (Grant ID: TRG5780205).

References

Akahira, T., and Sunose, T. (1971). Method of determining activation deterioration constant of electrical insulating materials, Res. Rep. Chiba. Inst. Technol., 16, 22–31.

Behr, P., Maun, A., Deutgen, K., Tunnat, A., Oeljeklaus, G., and Görner, K. (2011). Kinetic study on promoted potassium carbonate solutions for CO₂ capture from flue gas, *Energy Proc.*, **4**, 85–92.

Chalermsinsuwan, B., Piumsomboon, P., and Gidaspow, D. (2010). A computational fluid dynamics design of a carbon dioxide sorption circulating fluidized bed, AIChE J., 56, 2805–2824.

Doyle, C. (1961). Kinetic analysis of thermogravimetric data, J. Appl. Polym. Sci., 5, 285–292.

Doyle, C. (1962). Estimating isothermal life from thermogravimetric data, J. Appl. Polym. Sci., 6, 639–642.

Duncan, R. C. (2001). World energy production, population growth, and the road to the Olduvai Gorge, *Popul. Environ.*, **22**, 503–522.

Flynn, J. H., and Wall, L. A. (1966). General treatment of the thermogravimetry of polymers, *J. Res. Natl. Bur. Stand.*, **70**, 487–523.

Heda, P. K., Dollimore, D., Alexander, K. S., Chen, D., Law, E., and Bicknell, P. (1995). A method of assessing solid state reactivity illustrated by thermal decomposition experiments on sodium bicarbonate, *Thermochim. Acta*, 255, 255–272.

Hu, W., Smith, J., Dogu, T., and Dogu, G. (1986). Kinetics of sodium bicarbonate decomposition, *AIChE J.*, **32**, 1483–1490.

Kikkinides, E. S., Yang, R. T., and Cho, S. H. (1993). Concentration and recovery of carbon dioxide from flue gas by pressure swing adsorption, *Ind. Eng. Chem. Res.*, 32, 2714–2720.

Kim, S., and Park, J. K. (1995). Characterization of thermal reaction by peak temperature and height of DTG curves, *Thermochim. Acta*, 264, 137–156.

Kissinger, H. E. (1957). Reaction kinetics in differential thermal analysis, Anal. Chem., 29, 1702–1706.

Kongkitisupchai, S., and Gidaspow, D. (2013). Carbon dioxide capture using solid sorbents in a fluidized bed with reduced pressure regeneration in a downer, AIChE J., 59, 4519–4537. 588 P. Chaiwang et al.

Koga, N., Goshi, Y., Yoshikawa, M., and Tatsuoka, T. (2013). Physico-geometrical kinetics of solid-state reactions in an undergraduate thermal analysis laboratory, J. Chem. Educ., 91, 239–245.

- Kramer, P. J. (1981). Carbon dioxide concentration, photosynthesis, and dry matter production, *BioScience*, 31, 29–33.
- Lee, D. K., Min, D. Y., Seo, H., Kang, N. Y., Choi, W. C., and Park, Y. K. (2013). Kinetic expression for the carbonation reaction of K2CO3/ZrO2 sorbent for CO2 capture, *Ind. Eng. Chem. Res.*, 52, 9323–9329.
- Liang, Y., Harrison, D., Gupta, R., Green, D., and McMichael, W. (2004). Carbon dioxide capture using dry sodium-based sorbents, *Energy Fuels.* 18, 569–575.
- Lin, C. P., Chang, Y. M., Gupta J. P., and Shu, C. M. (2010). Comparisons of TGA and DSC approaches to evaluate nitrocellulose thermal degradation energy and stabilizer efficiencies, *Process. Saf. Environ.*, 88, 413–419.
- Olaizola, M., Bridges, T., Flores, S., Griswold, L., Morency, J., and Nakamura, T. (2004). Microalgal removal of CO₂ from flue gases: CO₂ capture from a coal combustor, in: *Third Annual Conference on Carbon Capture and Sequestration*, May 3–6, 2004, Alexandria, VA.
- Ozawa, T. (1965). A new method of analyzing thermogravimetric data, Bull. Chem. Soc. Jpn., 38, 1881–1886.
- Park, S. W., Sung, D. H., Choi, B. S., Lee, J. W., and Kumazawa, H. (2006). Carbonation kinetics of potassium carbonate by carbon dioxide, *J. Ind. Eng. Chem.*, 12, 522–530.

Saha, A. K., Bandyopadhyay, S. S., and Biswas, A. K. (1995). Kinetics of absorption of CO₂ into aqueous solutions of 2-amino-2-methyl-1-propanol, *Chem. Eng. Sci.*, 50, 3587–3598.

- Slopiecka, K., Bartocci, P., and Fantozzi, F. (2012). Thermogravimetric analysis and kinetic study of poplar wood pyrolysis, *Appl. Energy*, 97, 491–497.
- Tang, W., Li, X. G., and Yan, D. (2004). Thermal decomposition kinetics of thermotropic copolyesters made from trans-p-hydroxycinnamic acid and p-hydroxybenzoic acid, *J. Appl. Polym. Sci.*, 91, 445–454.
- White, J. E., Catallo, W. J., and Legendre, B. L. (2011). Biomass pyrolysis kinetics: A comparative critical review with relevant agricultural residue case studies, *J. Anal. Appl. Pyrol.*, **91**, 1–33.
- Yang, H., Yan, R., Chin, T., Liang, D. T., Chen, H., and Zheng, C. (2004). Thermogravimetric analysis—Fourier transform infrared analysis of palm oil waste pyrolysis, *Energy Fuels*, 18, 1814–1821.
- Yokozeki, A., Shiflett, M. B., Junk, C. P., Grieco, L. M., and Foo, T. (2008). Physical and chemical absorptions of carbon dioxide in room-temperature ionic liquids, J. Phys. Chem. B., 112, 16654–16663.
- Zhao, C., Chen, X., and Zhao, C. (2010). Multiple-cycles behavior of K₂CO₃/Al₂O₃ for CO₂ capture in a fluidized-bed reactor, *Energy Fuels*, **24**, 1009–1012.
- Zhu, G., Zhu, X., Xiao, Z., and Yi, F. (2012). Study of cellulose pyrolysis using an in situ visualization technique and thermogravimetric analyzer, *J. Anal. Appl. Pyrol.*, **94**, 126–130.

FISEVIER

Contents lists available at ScienceDirect

Journal of Environmental Chemical Engineering

journal homepage: www.elsevier.com/locate/jece



Correlations of kinetic parameters with various system operating conditions for CO₂ sorption using K₂CO₃/Al₂O₃ solid sorbent in a fixed/fluidized bed reactor



Nathphatsorn Jongartklang^a, Saowaluck Chanchairoek^b, Pornpote Piumsomboon^a, Benjapon Chalermsinsuwan^{a,*}

- ^a Fuels Research Center, Department of Chemical Technology, Faculty of Science Chulalongkorn University, 254 Phayathai Road, Patumwan, Bangkok 10330, Thailand
- ^b Department of Chemistry, Faculty of Science and Technology, Phranakhon Rajabhat University, 9 Chaeng Watthana Road, Bangkhen, Bangkok 10220, Thailand

ARTICLE INFO

Article history: Received 26 November 2015 Received in revised form 10 January 2016 Accepted 10 March 2016 Available online 14 March 2016

Keywords:
Breakthrough curve
CO₂
Deactivation model
K₂CO₃
Sorbent
Sorption

ABSTRACT

The kinetic parameters for carbon dioxide sorption using potassium carbonate supported on an alumina oxide solid sorbent in a fixed/fluidized bed reactor were investigated using a deactivation kinetic model. The initial parameters of the deactivation model were explored by comparison of the obtained results with experimental data. Then, the effects of varying the three key system operating conditions (inlet gas velocity, sorption temperature and water vapor content) on the kinetic parameters were considered. The obtained breakthrough curves were used for calculation of the kinetic parameters. Finally, the relationship between the obtained kinetic parameters and the system operating conditions were summarized. The selected deactivation model was found to fit well with the experimental data. The reaction rate constant was highest in a turbulent fluidization flow pattern and the initial sorption and deactivation rate constant were dependent on the water vapor content except with excess water vapor content

© 2016 Elsevier Ltd. All rights reserved.

1. Introduction

Carbon dioxide (CO_2) is recognized as a major cause of global warming. The concentration of CO_2 in the atmosphere has increased progressively in the last ten years [7]. When analyzing the CO_2 release contributions, coal combustion in power plants accounts for approximately three-quarters of the total anthropogenic CO_2 emissions worldwide [2]. The U.S. Department of Energy states that more than 300 GW of coal-fired electricity generation currently in operation will increase the concentration of CO_2 in the atmosphere to nearly 450 ppm by 2030 [17]. To mitigate this CO_2 emission problem, methodology to capture or sequester CO_2 is required..

To date, several methods for capturing CO₂ from flue gas have been extensively explored such as solvent absorption, membrane separation and cryogenic fractionation. However, these methods have been restricted by either expensive operating cost or safety

* Corresponding author.

E-mail addresses: benjapon.c@chula.ac.th, benjapon.c@hotmail.com
(B. Chalermsinsuwan).

considerations. Sorption with dry alkali-metal-based solid sorbent is another promising technology for CO₂ capture. When compared to other solid sorbents, Potassium carbonate (K2CO3) is an interesting solid sorbent owing to easy handling and economic viability [29]. Therefore, solid sorbent development and sorption process improvement are considered to be important research topics. For the solid sorbent development, modifications of K₂CO₃ solid sorbent have been conducted to improve its performance. The effect of supporting materials on the sorption characteristic has been explored [11], and it has been concluded that the use of K₂CO₃ supported on Al₂O₃ (K₂CO₃/Al₂O₃) could be a potential solid sorbent for a large scale operation unit [25]. The calcined K₂CO₃ from KHCO₃ also showed excellent sorption capacity and a high reaction rate. When considering the process improvement, most of the recent studies that have focused on using K2CO3/Al2O3 as a solid sorbent were carried out in a thermogravimetric analyzer and fixed bed reactor [14,16,27]. The fixed and fluidized bed reactors were successfully used for various adsorption studies to remove contaminants [8,10,19,23,22,6]. The use of K_2CO_3/Al_2O_3 solid sorbents with fluidization technology has been proposed as a solution for reducing released CO₂ [1] since fluidization can

Nomenclature Activity of sorbent (-) а Initial activity of sorbent (–) a_0 Frequency factor (for $k_0 = m^3/kg \, min$; for $k_d = m^3/kg \, min$) Α Outlet concentration of CO₂ (% or kmol/m³) CInlet concentration of CO₂ (% or kmol/m³) C_0 Sorbent diameter (µm) $d_{\rm p}$ Activation energy (kJ/mol) $E_{\rm a}$ F Outlet CO₂ fraction (-) Inlet gas volumetric flow rate (m³/min) $F_{\rm input}$ Outlet gas volumetric flow rate (m³/min) $F_{ m output}$ Н Height (m) I.D. Internal diameter (m) Deactivation rate constant (1/min) $k_{\rm d}$ $k_{\rm o}$ Initial sorption rate constant (m³/kg min) Order of reaction with respect to sorbent active site m Order of reaction with respect to CO₂ concentration n (-)Time (min) Τ Sorption temperature (K) Q_o Volumetric flow rate (m³/min) Universal gas constant (J/mol K) R W Weight of sorbent (kg)

provide better heat and mass transfers inside a reactor. With this technology, the general flow patterns can be divided into four regimes based on the criterion of the increasing of gas inlet velocity [9]. Jaiboon et al. [9] found that the CO₂ capture capacity of solid sorbent varied in relation to the inlet gas velocity. In addition, the effects of system operating conditions on sorption efficiency were investigated such as sorption temperature, inlet gas composition and gaseous impurities [28].

Greek letters

ρ Sorbent density (kg/m³)

To design an efficient sorption unit, an understanding of the CO₂ sorption kinetics is important. For the gas-solid particle system, the mass transfer and reaction kinetics may have an effect on the chemical reaction. Recently, the shrinking-core, homogeneous, phenomenological and deactivation simplified models have been used for explaining the non-catalytic gas-solid particle reaction phenomena [15,16,12]. Comparing among these models, the deactivation model was the most successful in describing the decreasing activity of alkali-metal carbonate solid sorbents during the reaction with CO₂ in a thermogravimetric analyzer and in a fixed bed reactor. This can be explained by the changing solid sorbent structure throughout the chemical reaction. The formation of a dense product layer over the solid sorbent brings about additional diffusion resistance and a reduced chemical activity. However, the available data on the kinetic parameters in a fluidized bed reactor are still limited.

In this study, simplified kinetic models were first developed for CO_2 sorption using K_2CO_3/Al_2O_3 as the solid sorbent in both fixed and fluidized bed reactors. The deactivation model was successfully employed to compute the kinetic parameters. The obtained kinetic models were used as the input for mathematical modeling and computational fluid dynamics simulation programs with various system dimensions ranging from zero- to three-dimensions. The system operating conditions of the inlet gas velocity,

sorption temperature and water vapor (H_2O) content were investigated for their effects on the kinetic parameters of the deactivation model. In addition, the correlation between the obtained kinetic parameters and the system operating conditions were summarized.

2. Kinetic model development

The CO_2 sorption reaction using an anhydrous K_2CO_3/Al_2O_3 solid sorbent proceeds in the presence of H_2O to yield KHCO₃, as shown in Eq. (1),

$$K_2CO_{3(s)} + CO_{2(g)} + H_2O_{(g)} \Leftrightarrow 2KHCO_{3(s)}$$
 (1)

The sorption reaction is a heterogeneous gas-solid particle reaction [1]. As solute enters the bed, it contacts with the first layers of solid sorbent. Solute adsorbs and fills up some of the available sites. Then, it moves further by diffusing to the subsequent layers. This phenomenon takes place until each layer reaches its equilibrium. The simultaneous influence of both the chemical reaction and the transportation must take into account for a correct prediction of the reaction conversion as a function of time. In order to calculate the chemical kinetic of Eq. (1), the CO₂ breakthrough curve is employed in the deactivation model. The breakthrough curve shows the ratio of outlet solute concentration to inlet solute concentration as a function of time. It is a measure of the bulk or average reactor concentration. There are two important parameters related to the breakthrough curves, namely, breakthrough point (the point that the concentration ratio increases up to value higher than the initial one) and exhaust point (the point that the concentration ratio increases up to value about the final one). As stated in the introduction, this model is a proper choice for predicting the CO₂ sorption in a thermogravimetric analyzer and fixed bed reactor [15,16,26,27].

The development of the deactivation model is based on the diffusion resistance due to the formation of a product layer over the solid particle reactant [14,4]. This phenomenon then causes a drop in the chemical reaction rate with time. The effects of all the textural changes on the CO_2 sorption are combined with the reaction rate in terms of the activity (a). The following assumptions are made:

- The sorption reaction is operated under isothermal condition.
- The water vapor concentration is constant [28] found that the CO₂ sorption was similar at high water vapor concentration).

With the above assumptions, the pseudo-steady state species conservation equation without axial dispersion [20,14] is expressed as follows:

$$-Q_0 \frac{dC}{dW} - k_0 aC = 0 (2)$$

where a is the activity of the sorbent, W is the weight of sorbent, C is the outlet concentration of CO_2 , Q_o is the volumetric flow rate and k_o is the initial sorption rate constant.

This equation is derived based on the plug flow reactor model [5,13], which defines the solute flowing through the reactor as a series of infinitely thin coherent volume, each with a uniform composition [18]. The key assumption is that the solute is perfectly mixed in the radial direction but not in the axial direction. The plug flow reactor is the ideal reactor case for the real reactor cases, fixed and fluidized bed reactors. The key assumption for a plug flow reactor model then valids for the two reactors. This confirms the validity of using Eq. (2) for prediction of a kinetic parameter. This model has been used to simulate fixed and fluidized bed reactors in numerous studies [4,12]. The integrating of Eq. (2) is shown as the

following equation:

$$\int_{C_0}^{C} \frac{dC}{C} = \left(\frac{k_0 a}{Q_0}\right) \int_{0}^{W} dW \Rightarrow \ln\left(\frac{C}{C_0}\right) = -\left(\frac{k_0 a}{Q_0}\right) W \tag{3}$$

where C_0 is the inlet concentration of CO_2 . For the deactivation effect, the calculation of K_2CO_3/Al_2O_3 solid sorbent activity will depend on the hypothesis. If the first-order with respect to the solid active site and zeroth-order with respect to the concentration of CO_2 are assumed (m = 1, n = 0), the solid sorbent activity can then be described by the following equation [14]:

$$-\frac{da}{dt} = k_d C^n a^m \Rightarrow a = a_o \exp(-k_d t)$$
 (4)

where t is the time, k_d is the deactivation rate constant and a_0 is the initial activity of the solid sorbent. Combining Eqs. (3) and (4) with the initial activity of the solid sorbent as the unity, Eq. (5) can be expressed below.

$$\frac{C}{C_0} = \exp\left[-\frac{k_0 W}{Q_0} \exp(-k_d t)\right] \tag{5}$$

Arranging Eq. (5), the following equation is obtained:

$$\ln\left[\ln\left(\frac{C_0}{C}\right)\right] = \ln\left(\frac{k_0W}{Q_0}\right) - k_dt \tag{6}$$

Thus, the plot of $\ln[\ln(C_o/C)]$ versus time should give a linear line with $-k_d$ and $\ln(k_oW/Q_o)$ serving as the slope and the intercept, respectively. Thus, k_o can then be obtained.

On the other hand, the deactivation rate can be expected to be dominated by the CO_2 concentration. Therefore, if the first-order with respect to both the solid active site and the concentration of CO_2 reactant are assumed (m=1, n=1), an iterative procedure is required to solve the non-linear equation of solid sorbent activity. For the procedure, the zeroth order solution or Eq. (5) was substituted into Eq. (4). The first correction for the activity was obtained by the integration of this equation. Then, the corrected activity expression was substituted into Eq. (2), and the integration of this equation gave the first corrected solution. The detailed solution for the breakthrough curve with this hypothesis can be found in Park et al. [14].

$$a = \exp \left[\frac{1 - \exp\left(\frac{k_o W}{Q_o} (1 - \exp(-k_d t))\right)}{1 - \exp(-k_d t)} \exp(-k_d t) \right]$$
 (7)

Iterative solutions are most often implemented recursively until a defined criteria based were met. In this procedure, higher order terms in the series solutions of the integrals were neglected. The information on the conduct of the iterations and the assumption in this study can be found in [3]. Two kinetic parameters of k_o and k_d are then calculated from the $\rm CO_2$ breakthrough concentration profiles. More details about this deactivation model can be found in [4,14].

3. Materials and methodology

3.1. Solid sorbent

The solid sorbent was prepared by the impregnation of K_2CO_3 on a porous Al_2O_3 support. First, a solution containing 5 g of K_2CO_3 (Ajax Finechem Pty., Ltd.) in 25 mL of de-ionized water was mixed with 5 g of Al_2O_3 support (Sigma-Aldrich Co. LLC.) and shaken at room temperature for 24 h. The mixture was then dehydrated in a vacuum oven at 378 K and calcined in a furnace at 573 K with the temperature ramping rate of 3 K/min. The physical properties (surface area, pore volume and K_2CO_3 content on solid sorbent) of

Table 1The physical properties of employed K₂CO₃/Al₂O₃ solid sorbent.

Solid particle physical property	Value
Surface area (m ² /g)	80.92
Pore volume (cm ³ /g)	0.33
Actual weight of K ₂ CO ₃ impregnated on Al ₂ O ₃ (%wt)	35
Solid sorbent diameter $(d_p, \mu m)$	150
Solid sorbent density (ρ_s , kg/m ³)	3,900

solid sorbent were then determined using the atomic absorption spectrophotometer (AA) and the nitrogen physisorption (Brunauer-Emmett-Teller (BET) technique). The properties of the obtained K_2CO_3/Al_2O_3 solid sorbent are summarized in Table 1.

3.2. Reactor apparatus

In this study, the CO₂ sorption was investigated in a lab-scale semi-circulating fluidized bed reactor, as shown in Fig. 1. The riser column had a diameter of 25 mm and a height of 0.80 m, while the diameter and the height of the downer column were 50 mm and 0.30 m, respectively. The solid particle output storage was used to collect the solid sorbent elutriating out of the riser column. For the continuous operation, the solid sorbents were fed back to the downer column. A ball valve installed at the transfer line was used to adjust the solid particle flow between the downer and the riser columns. The gaseous reactant flow rate was manipulated using a rotameter. A gas bubbler with a pre-heating section was used to add the water vapor into the mixed reactant gas before entering the riser. The sorption temperature inside the riser column was controlled by heating tape. The outlet gas from the riser column was directly passed through the condensation unit and kept in the gas bag for measuring the CO₂ concentration by gas chromatography (GC). Then, the breakthrough curve was plotted. Pressure taps and a thermocouple were also installed along the height of the riser column.

3.3. CO₂ sorption methodology

The effects of varying the key system operating conditions (inlet gas velocity or flow pattern/regime, sorption temperature and water vapor content) on the kinetic parameters of the deactivation model were considered. The inlet gas velocities were explored from 0.01 to 2.64 m/s since these inlet gas velocities cover the four different flow patterns/regimes of a fixed bed, bubbling fluidization, turbulent fluidization and fast fluidization [9]. These flow patterns/regimes can be divided into the two different operating modes of non-circulating and circulating. The fixed bed, bubbling fluidization and turbulent fluidization flow patterns/regimes are non-circulating operations, while the fast fluidization flow pattern/regime is a circulating operation. The amount K₂CO₃/ Al₂O₃ solid sorbent in the riser column for the non-circulating and circulating operations was 60 and 300 g, respectively. However, at each operating time in the circulating operation the riser column would contain 60 g of solid sorbents. Table 2 presents the experimental operating conditions with different inlet gas velocities and the corresponding solid sorbent concentration (ε_s) for each flow pattern, which was calculated by processing the differential pressures measured from successive pressure taps. As in other studies, the sorption temperature was varied between 323 and 363 K. Also, the CO₂ concentration was selected to approximate the flue gas composition (10% vol. to 20% vol.). H₂O concentration was chosen to be consistent with the saturated water vapor at its corresponding sorption temperature [28]. Two experimental replications were performed for each operating condition. All the obtained data for each operating condition were qualitative

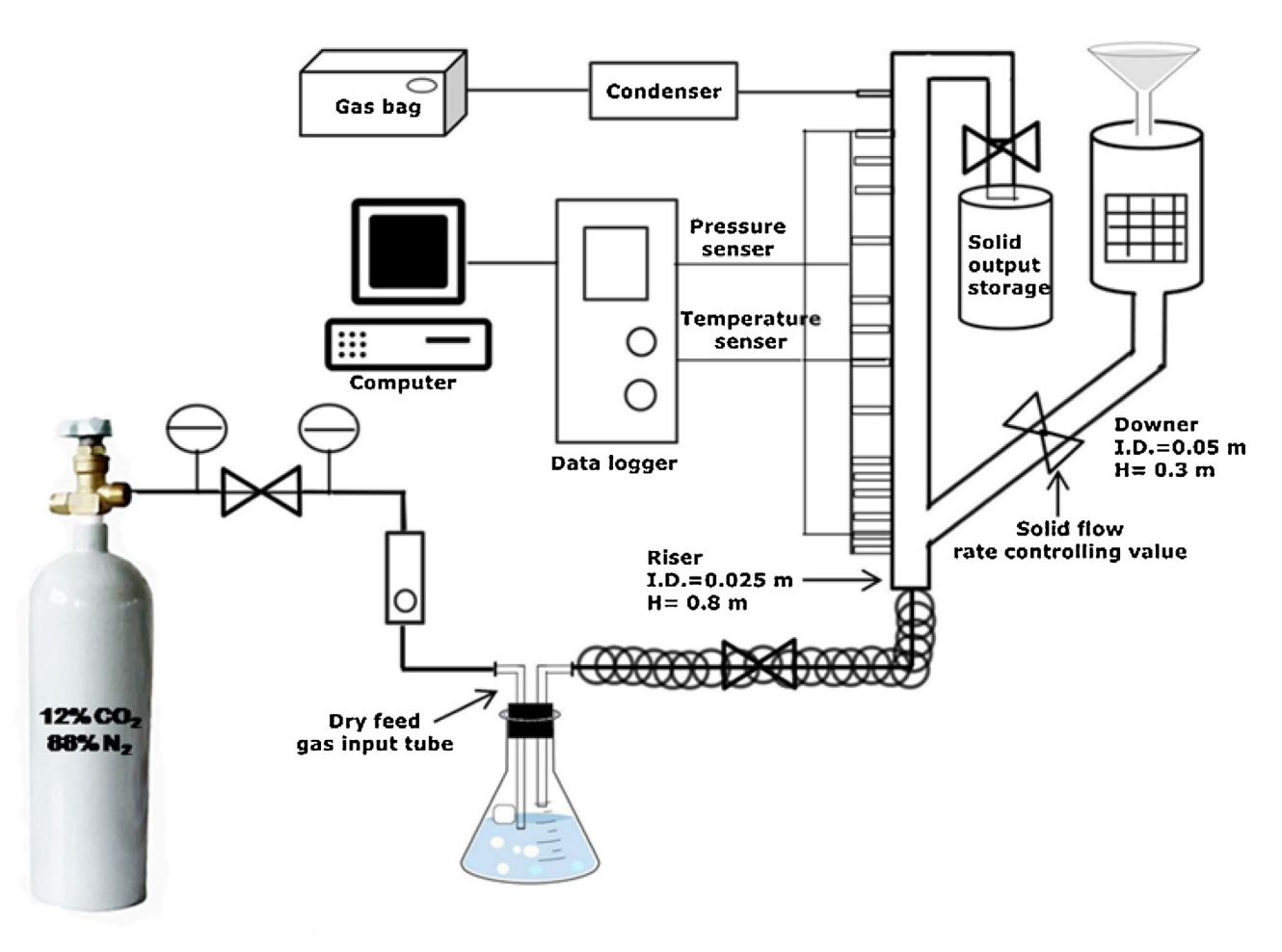


Fig. 1. Schematic diagram of the used semi-circulating fluidized bed reactor in this study.

Table 2Experimental operating conditions of used inlet gas velocity or flow pattern/regime for CO₂ sorption in semi-circulating fluidized bed reactor.

Fluidization system	Pressure (atm)	Solid Loading (g)	Flow pattern/regime	Inlet gas velocity (m/s)	Averaged solid volume fraction (–)
Non-circulating	1	60	Fixed bed	0.01	0.60
			Bubbling fluidization	0.20	0.52
			Turbulent fluidization	1.02	0.15
Circulating	1	300	Fast fluidization	2.64	0.09

and quantitative consistent within 10 percent deviation. Therefore, one of them was selected to represent the information. The reference simulated flue gas composition was selected to be 12.0% vol. CO₂ and 18.4% vol. H₂O with N₂ balance at a sorption

temperature of 333 K. In addition, three water vapor contents and four sorption temperatures were explored. The summary of experimental conditions for CO₂ sorption in the semi-circulating fluidized bed reactor is shown in Table 3. The sorption efficiency

Table 3Experimental operating conditions of used sorption temperature and water vapor content for CO₂ sorption in semi-circulating fluidized bed reactor.

Fluidization system	Pressure (atm)	Sorption temperature (K)	CO ₂ content (% vol. CO ₂)	Water vapor content (% vol. H ₂ O)	Mole fraction of water vapor to CO ₂ (–)
Non-circulating	1	323	12.0	18.4	1.53
Fixed bed		333	12.0	18.4	1.53
(0.01 m/s)		343	12.0	18.4	1.53
Solid loading 60 g		353	12.0	18.4	1.53
		363	12.0	18.4	1.53
Non-circulating	1	333	12.0	7.0	0.58
Fixed bed		333	12.0	13.5	1.13
(0.01 m/s)		333	12.0	18.4	1.53
Solid loading 60 g		333	12.0	22.5	1.88

was evaluated by inspecting the outlet CO_2 fraction (F) with the reaction time or breakthrough curve. The outlet CO_2 fraction [9] is calculated by:

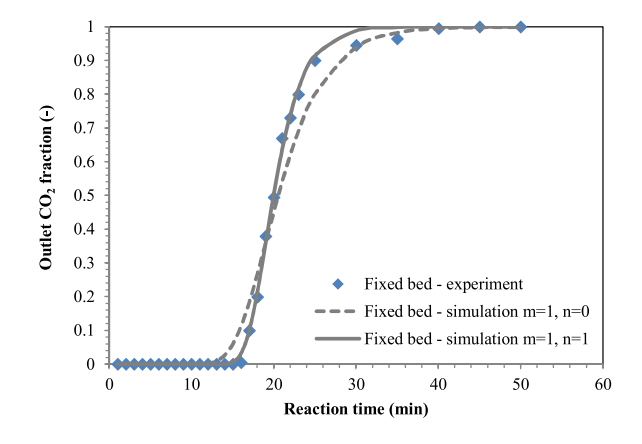
$$F = 1 - \frac{C_0 \cdot F_{input} - C \cdot F_{output}}{C_0 \cdot F_{input}}$$
(8)

where F_{input} is the inlet gas volumetric flow rate. Outlet gas volumetric flow rate (F_{output}) is calculated from the difference between F_{input} and the adsorbed CO_2 on solid sorbent.

4. Results and discussion

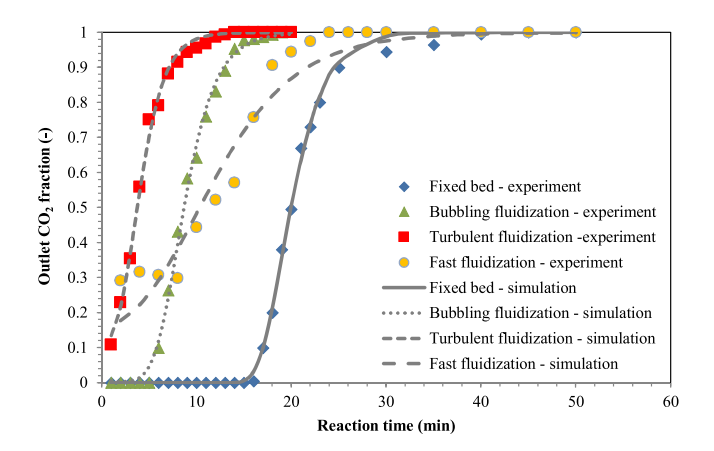
4.1. Evaluation of deactivation model

To test the agreement between the experimental data with the proposed models, two hypotheses were proposed. The first model was explored with the hypothesis of a first-order with respect to solid active site (m = 1) and a zero-order with respect to concentration of CO_2 reactant (n = 0). The second model was based upon both the first-order with respect to solid active site (m=1) and concentration of CO_2 reactant (n=1). The models were evaluated with an inlet gas velocity of 0.01 m/s or fixed bed flow pattern. The tuning of the reaction orders to match with the breakthrough experimental data is the generally used methodology in the Chemical Reaction Engineering's books [5,13]. The breakthrough experimental data of CO₂ are plotted in Fig. 2. The outlet CO₂ fraction increased with increasing reaction time due to the loss of solid sorbent active sites, as supported by previous scanning electron microscopy analysis [15], and the high initially reaction rate. The breakthrough time was after approximately 15 min. Then, the outlet CO₂ fraction reached its equilibrium at final values after approximately 35 min (exhaust time). Then, the kinetic parameters (k_0 and k_d) and their simulated breakthrough curve were calculated using all the experimental breakthrough data by a nonlinear least squares technique. The average and range of values were shown to express the slightly deviation between the obtained results. In the following section, the average values were then shown, only.



Hypothesis for deactivation model (-)	k_o $(m^3/\text{kg}\cdot\text{min})$	<i>k_d</i> (1/min)
m = 1, n = 0	2.107 ± 0.010	0.254 ± 0.017
m = 1, n = 1	0.301 ± 0.022	0.407 ± 0.002

Fig. 2. Effect of different deactivation model hypotheses on breakthrough curve of outlet CO_2 fraction and their corresponding kinetic parameters (with 333 K sorption temperature and 18.4% vol. H_2O).



Flow pattern/regime	$k_o \ ({ m m}^3/\ { m kg\cdot min})$	$\frac{k_d}{(1/\text{min})}$
Fixed bed	0.301	0.407
Bubbling fluidization	0.434	0.463
Turbulent fluidization	1.005	0.600
Fast fluidization	0.432	0.180

Fig. 3. Effect of different inlet gas velocities or flow patterns/regimes on breakthrough curve of outlet CO_2 fraction and their corresponding kinetic parameters (with m = 1, n = 1, 333 K sorption temperature and 18.4% vol. H_2O).

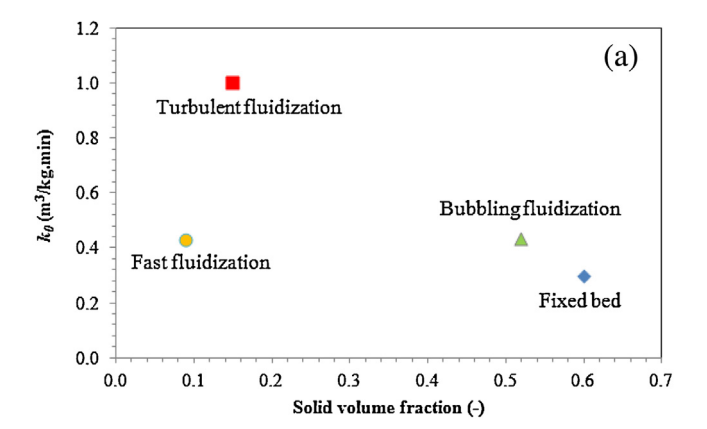
The simulated breakthrough curve was drawn from the obtained concentration profile as a function of the reaction time (Fig. 2). From the results, the calculated breakthrough curves and the breakthrough parameters (breakthrough and exhaust times) of CO_2 for the deactivation model with n = 0 did not fit well with the experimental data. Therefore, the model with n=0 was not appropriate for the sorption kinetics of CO₂ on K₂CO₃/Al₂O₃. However, the regression analysis of the breakthrough experimental data presented a very good agreement with the deactivation model with n=1 at high accuracy. Therefore, to explain the chemical mechanism of this gas-solid particle with a non-catalytic chemical reaction, the deactivation model with n=1 was more appropriate. The deactivation rate has been confirmed to be dependent on the CO₂ concentration [4] and so these results are in agreement with previous reports on the adequacy of the deactivation model compared with the other kinetic models. In the following sections, the deactivation model with m=1 and n = 1 was then employed.

4.2. Effect of inlet gas velocity

The effect of the inlet gas velocity on the CO₂ breakthrough curve of the K₂CO₃/Al₂O₃ solid sorbent in a semi-circulating fluidized bed reactor for the reference operating condition is shown in Fig. 3. The results strongly indicated that the maximum utilization of the solid sorbent depended on the operating condition. For the CO₂ capture capacity under the fixed bed flow pattern (0.01 m/s), the CO₂ breakthrough curve was constant at the beginning stage and then gradually decreased with an increasing reaction time. For the bubbling fluidization flow pattern (0.20 m/s), the CO₂ breakthrough curve was similar to that with a fixed bed flow pattern, but with a much shorter invariable reaction time than in the fixed bed flow pattern. This can be explained by the higher gas velocity in the bubbling fluidization flow pattern. For the turbulent fluidization flow pattern, the CO₂ breakthrough curve decreased sharply from the beginning stage because the reaction time for the gas flowing through the bed was insufficient for the

transportation of reactant gas into the solid sorbent surface. When the solid sorbents were operated in a fast fluidization flow pattern, they were elutriated out of the system by the fluidizing gas. Then, they were recovered and returned to the bottom of the riser column. It took 8 min for all 300 g of fresh solid sorbent to pass through the riser column. During the first 8 min, the solid sorbent adsorbed about 70% of the CO₂ in the feed gas due to the extremely high operating velocity. After 8 min, the adsorption rate gradually decreased as a result of the returning of used solid sorbents. In real operation, the used solid sorbents can be regenerated using heat or vacuum pressure in the downer column before send back to the riser column. The used solid sorbent can regenerate and operate in semi-continuous or continuous system design. Conventionally, the residence time in the riser column is also short. When comparing the breakthrough and exhaustion points, the fixed bed flow pattern had higher breakthrough and exhaust points than the bubbling and the turbulent fluidization flow regimes, respectively. This is because the difference of amount of inlet CO₂ gas between flow patterns or regimes. For the fast fluidization flow regime, the clearly trend was not observed with the other flow patterns or regimes. This is because the continuous feeding the fresh and used solid sorbents. These two points are important parameter to operate the reactor system and to perform regeneration.

The regression results by the deactivation model are also displayed in Fig. 3, where this model could accurately predict the overall breakthrough behaviors. For the fast fluidization flow pattern, the results were slightly different due to the assumption of the employed model. The kinetic parameter data for all inlet gas velocities or flow patterns/regimes are summarized in Fig. 3. The kinetic parameters were highly dependent on the operating flow regime/pattern inside the reactor. In general, the kinetic parameters are those that describe the reaction rate and they then should be the same irrespective of the reactor type. However, as stated in the introduction section, the kinetic models in this study were the overall or simplified kinetic models including mass transfer and chemical reaction resistances. Because the obtained kinetic parameters were different in each type of flow regime, it can be concluded that mass transfer resistance occurred and governed these systems. When considering the simulated CO₂ breakthrough curve in Fig. 3, the fixed bed flow pattern gave the best sorption result due to the high reaction time. Although the fixed bed flow pattern had the best performance result, the value of initial sorption rate constant or k_0 was very low. The solid sorbent packing on each other (high mass transfer resistance) caused the loss of the active sites and resulted in a low reaction speed. In the case of the bubbling fluidization flow pattern, the k_0 value showed that the higher gas-solid particle contacting surface area gave better k_0 . For turbulent and fast fluidization flow patterns, the solid sorbent could not remove all CO₂ in the feed gas except at the early beginning stage. Considering the values of k_0 , the fast fluidization flow pattern showed a similar range with the bubbling fluidization flow pattern due to system back-mixing. The turbulent fluidization flow pattern provided the most promising of k_0 values because of the suitable reaction time and system backmixing. For the deactivation rate constant, k_d , all the results had the same trend similar to the initial sorption rate constant, k_0 . For the fixed-bed and the bubbling fluidization flow patterns, the k_d values were lower than k_0 values, while the opposite results were observed for the other two flow patterns due to the low system reaction time, which implied a low solid sorbent deactivation in the last two flow patterns. In order to obtain the optimum operating condition for CO₂ capture, a suitable inlet velocity should give the largest value of k_0 and smallest value of k_d . Also, the operating condition with largest positive difference between k_0 and k_d was preferable. In this study, the turbulent fluidization



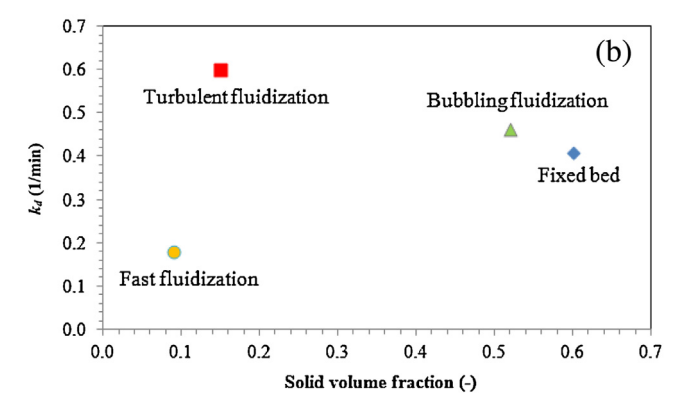


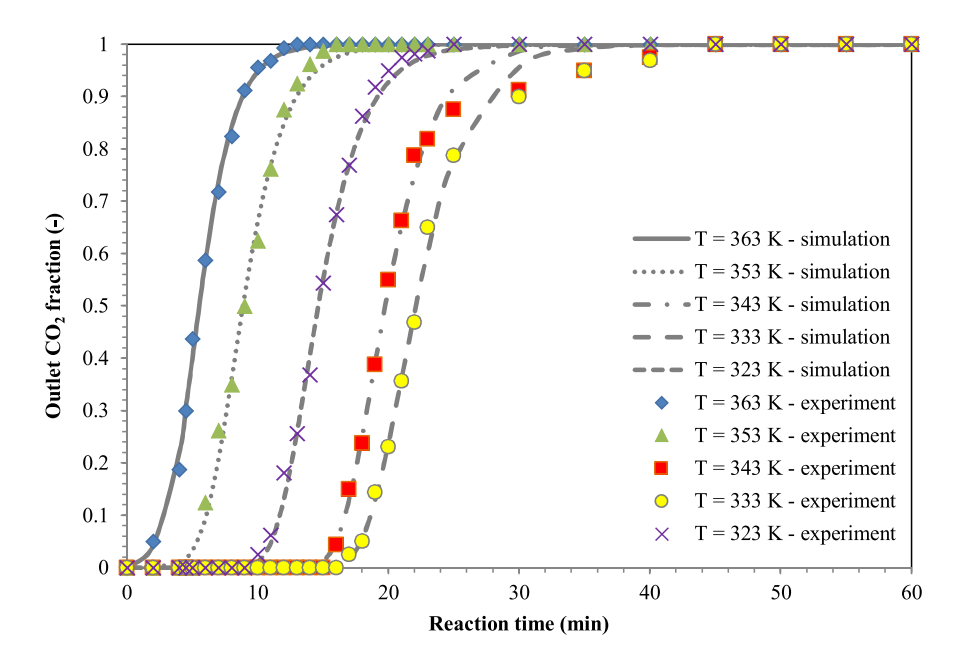
Fig. 4. Effect of solid volume fractions on (a) initial sorption rate constant (k_0) and (b) deactivation rate constant (k_d) .

was the suitable flow pattern since it inferred a low mass transfer resistance.

Next, the effect of a solid volume fraction on the kinetic parameters, initial sorption rate constant and deactivation rate constant were explored as illustrated in Fig. 4(a) and (b), respectively. From the figures, the highest kinetic parameter was obtained at the moderate value of the solid volume fraction. This could be explained by the appropriate solid volume fraction inside the system. At a low solid volume fraction, the solid particles were diluted and distributed across the column. At a high solid volume fraction, the solid particles were too dense inside the system and blocked the active surface area. Both of the solid volume fractions then had a negative effect on the sorption reaction rate.

4.3. Effect of sorption temperature

As shown in Fig. 5, the effect of sorption temperature on CO₂ breakthrough curves for K₂CO₃/Al₂O₃ solid sorbent was investigated using the reference operating condition with the inlet gas velocity of 0.01 m/s. Five different sorption temperatures were explored including 323, 333, 343, 353 and 363 K. Two trends of experimental outlet CO₂ fraction were observed. For the temperature range of 323–333 K, CO₂ sorption increased whereas for the temperature range of 333–363 K, CO₂ sorption decreased. Correspondingly, the breakthrough and exhaust points were highest at 333 K. The system with high breakthrough and exhaustion point are favorable. The decrease of the outlet CO₂ fraction at low and high temperatures was attributed to the rate of carbonation or sorption chemical reaction and the highly exothermic chemical reaction. At low sorption temperature, the observed trend was consistent with the experiment [15]. The slow chemical reaction



Sorption temperature	k_o	k_d
(K)	(m³/kg·min)	(1/min)
323	0.223	0.418
333	0.285	0.348
343	0.293	0.402
353	0.150	0.471
363	0.117	0.589

Fig. 5. Effect of different sorption temperatures on breakthrough curve of outlet CO₂ fraction and their corresponding kinetic parameters with m = 1, n = 1 and 18.4% vol. H₂O).

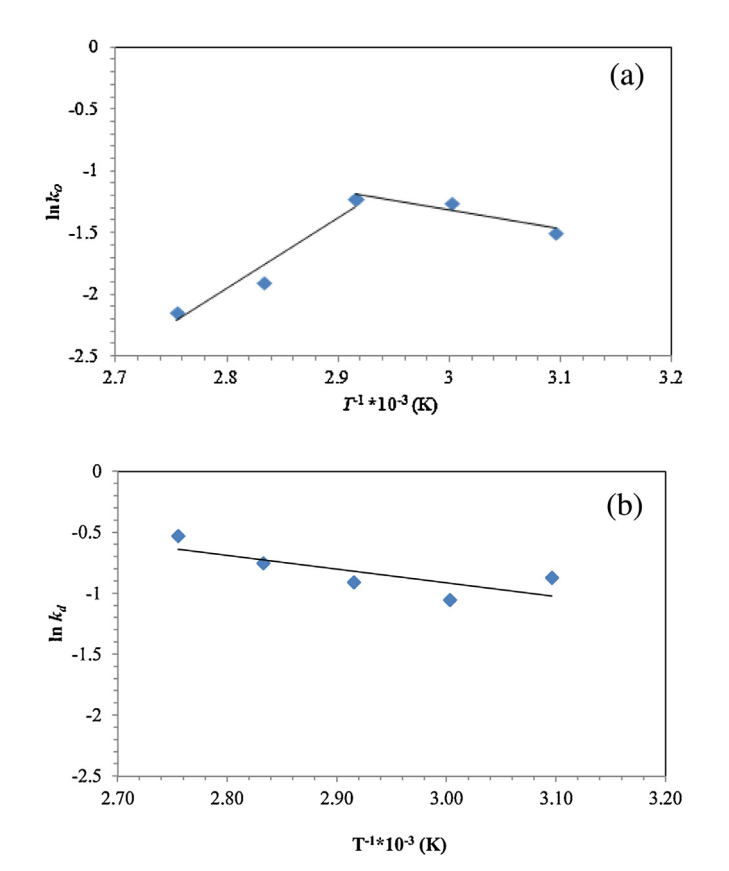
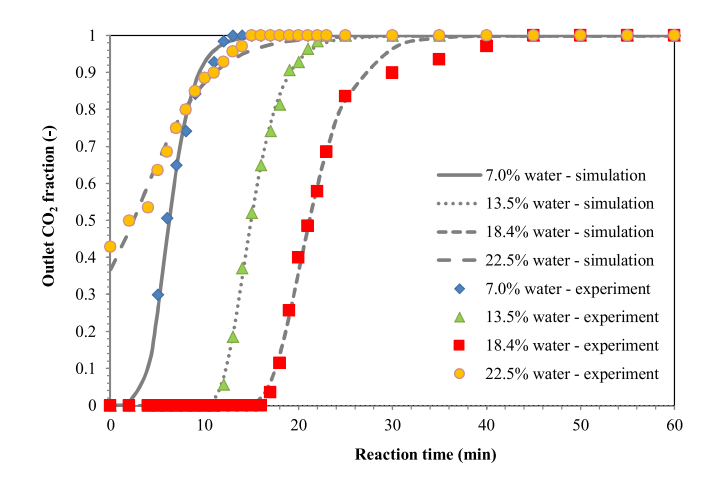


Fig. 6. Effect of sorption temperatures on (a) initial sorption rate constant (k_0) and (b) deactivation rate constant (k_d) .



Water vapor content (% vol. H ₂ O)	k _o (m³/kg·min)	k _d (1/min)
7.0	0.135	0.602
13.5	0.250	0.455
18.4	0.261	0.355
22.5	0.038	0.249

Fig. 7. Effect of different water vapor contents on breakthrough curve of outlet CO_2 fraction and their corresponding kinetic parameters (with m = 1, n = 1 and 333 K sorption temperature).

rate will occur with low sorption temperature. At high sorption temperature, the observed trend was firstly proposed and confirmed by several high sorption temperatures. The chemical reaction will decrease with the increasing of sorption temperature in exothermic chemical reaction. An exothermic chemical reaction releases heat and provides net energy to its surroundings. The energy needed to initiate the reaction is less than the energy that is subsequently released.

The simulated and experimental breakthrough curves were consistent with each other. As shown in Fig. 5, the k_0 increased with the increase of sorption temperature from 323 to 343 K. When increasing the sorption temperature above 343 K, the rate of sorption reaction became unfavorable. Thus, the optimum sorption temperature was 343 K for k_0 . The overall trend of k_d increased with the increase of sorption temperature except with the condition at 323 K. The slightly deviation is due to the diffusion resistance of unreacted reactant layer over the solid sorbent. The lowest observed value was at 333 K. Similar to the previous reason, the backward reaction and the activation energy explained the observed results. The low deactivation of solid sorbents then found. When considering the optimum sorption temperature with the same concept in the Section 4.2, effect of inlet gas velocity, the suitable sorption temperature was 333 K.

Similar to the general chemical reaction, the relationship between kinetic parameters and the sorption temperature (*T*) can be explained using the Arrhenius's form [5,13]:

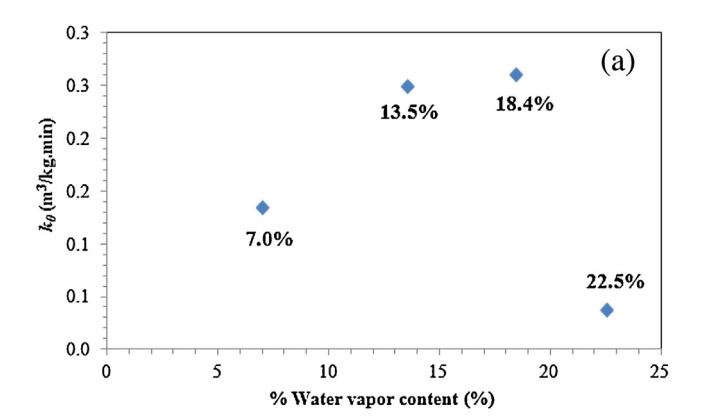
$$\ln k_0 or \ln k_d = \ln A - \frac{E_a}{RT} \tag{9}$$

where A is the frequency factor or pre-exponential factor, E_a is the activation energy and R is universal gas constant. The plot of $\ln k_0$ vs T^{-1} and $\ln k_0$ vs T^{-1} are shown in Fig. 6(a) and 6(b), respectively. The activation energy and frequency factor could then be calculated using the slope and intercept of the graph, respectively. k_0 showed a different trend between the sorption temperature range of 323–343 K and 343–363 K. At low sorption temperature, the regression produced the positive activation energy of 12.66 kJ/mol and frequency factor of 25.81 m³/kg min (calculated using the first

three points). The positive activation energy was generally found in many chemical reactions and this chemical reaction was called a barrier reaction. To occur the chemical reaction, the reactant molecules must have translational and vibrational energies equal to or greater than the activation energy. At high sorption temperature, the regression produced the negative activation energy of $-48.07 \, \text{kJ/mol}$ and frequency factor of $6.69 \times 10^7 \, \text{m}^3 / \text{m}$ kg·min (calculated using the second three points). Negative activation energy does not obstruct the reaction. The reaction proceeding relies on the capture of the molecules. The increase of the sorption temperature increased the Brownian motion and led to the higher probability of the colliding molecules. However, the more glancing collisions were not leading to reaction as the higher momentum carried the colliding particles apart from each other. The rate of reaction thus was decreased [5]. The k_d , the experimental results showed the same overall trend for all temperature ranges with the activation energy of 17.40 kJ/mol and frequency factor of 182.91 m³/kmol min. However, at 323 K sorption temperature, the k_d value was surprisingly increased by the unconverted solid sorbent.

4.4. Effect of water vapor content

The effect of water vapor content in feed gas on CO_2 breakthrough curves for K_2CO_3/Al_2O_3 solid sorbent was also investigated using the reference operating condition with the inlet gas velocity of 0.01 m/s. In actual normal operation, the combustion reaction gave comparable amount of contents of water vapor and carbon dioxide. Nevertheless, unusual operations, shortage and surplus of water vapor from non-ideal reactor mixing or chemical reaction, were also considered to explore their effect on



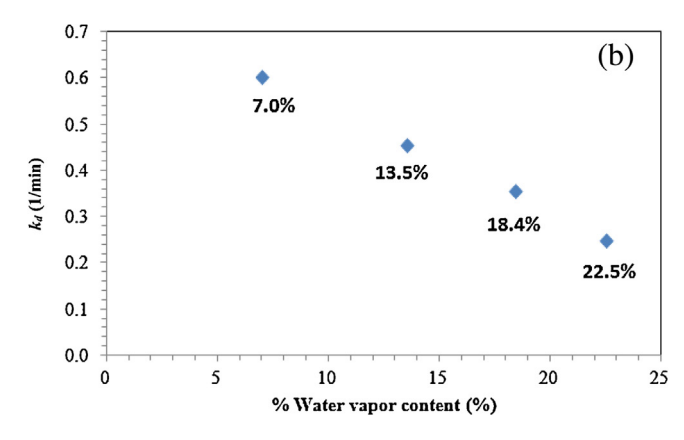


Fig. 8. Effect of water vapor contents on (a) initial sorption rate constant (k_0) and (b) deactivation rate constant (k_d) .

carbon dioxide sorption in this study. Therefore, this study results can reflect the whole range of reactor phenomena. Four different water vapor contents were carried out as 7.0, 13.5, 18.4 and 22.5% vol. H₂O. The measured values of the CO₂ breakthrough curves were plotted against the reaction time as shown in Fig. 7. Two trends of the outlet CO₂ fraction were observed. For 7.0-18.4% vol. H₂O, the reaction times increased with increasing water vapor content. This result implies that the sorption reaction increased as the water vapor content increased. For 18.4–22.5% vol. H₂O, the chemical reaction decreased with the increasing water vapor content. The exceptional excess water vapor content exhibited the CO₂ sorption reaction similar to the previous literature [24]. This is because this sorption chemical reaction needs equal stoichiometry of CO₂ and water vapor reactants. However, little higher water vapor enhanced the chemical reaction as its can help the pretreatment of solid sorbents [21]. Similar to the explanation in the previous section, the breakthrough and exhaust points were then highest at 18.4% vol. H₂O which was the suitable sorption operating condition.

The evaluated values of k_0 and k_d and simulated breakthrough curve are plotted in Fig. 7. [28] reported that the same K₂CO₃ solid sorbent conversion were obtained with the changing of water vapor content under the condition that the concentration of H₂O was comparable or higher than that the concentration of CO₂. Therefore, the deactivation model should be zeroth-order with respect to the concentration of H₂O reactant. With this system operating condition, the employed deactivation model was thus appropriate. For the case of 7% vol. water vapor content, the slight deviation was occurred. However, all the simulated and experimental breakthrough curves were reliable with each other. For the effect of water vapor content on the kinetic parameters, the initial sorption rate constant and deactivation rate constant were explored as illustrated in Fig. 8. The values of k_0 increased with the increase of water vapor content from 7.0 to 18.4% vol. H₂O. One mole of K₂CO₃ can adsorb one mole of CO₂ and one mole of H₂O and produce two moles of KHCO₃. The effect of water vapor content then could be explained by the above stoichiometric. However, some excess water vapor content may assist the occurrence of the CO_2 sorption reaction as stated by [21]. As the concentration was increased to 22.5% vol. H_2O , the value of k_0 decreased. This can be explained by the surplus water content in the feed gas which decelerates sorption reaction rate. All the values of k_d decreased with the increase of the water content. Some previous literature reported that the excess water could deactivate or decrease the active surface area of solid sorbent [24].

5. Conclusions

The deactivation kinetic model was effectively used to compute the kinetic parameters for CO₂ sorption using K₂CO₃/Al₂O₃ solid sorbent in a fixed/fluidized bed reactor. The deactivation model of the first-order with respect to both the solid active site and the concentration of CO₂ reactant was consistent with the experimental data. With this model, the simulated data and experimental breakthrough curves coincided with each other. Then, the effect of various system operating conditions on model kinetic parameters were also investigated. The obtained reaction rate constants were the highest at the moderate solid volume fraction value due to the system hydrodynamics and reaction time. The turbulent fluidization showed a suitable flow pattern for the occurrence of the CO₂ sorption. This infers a low mass transfer resistance in this flow pattern. The optimum sorption temperature for the CO₂ sorption was 333 K. The backward reaction and the activation energy are the explanation for the observed results. The reaction rate constant could be fit into the Arrhenius's form. The initial sorption and deactivation rate constants were increased and decreased with the increase of water content, respectively. However, this condition was exceptional for the excess water vapor content condition. The obtained results provide useful information to design a better chemical reactor for use in all system dimension mathematical modeling and computational fluid dynamics simulation codes. The obtained deactivation kinetic model can be used as an input parameter for the modeling and simulation. With this model, the full-scale reactor system in fossil fuel power plant can be simulated and designed, accurately. In addition, the effect of several operating parameters was revealed and used as simulation guideline for reactor operation.

Acknowledgements

This study was financially supported by the 90th Anniversary of CU Fund, the Thailand Research Fund for fiscal year 2014–2016 (TRG5780205), the Faculty of Science of Chulalongkorn University and the Ratchadaphiseksomphot Endowment Fund 2015 of Chulalongkorn University (CU-58-059-CC).

References

- [1] P. Chaiwang, B. Chalermsinsuwan, P. Piumsomboon, D. Gidaspow, CFD design of a sorber for CO₂ capture with 75 and 375 micron particles, Chem. Eng. Sci. 105 (2014) 32–45.
- [2] B. Chalermsinsuwan, P. Piumsomboon, D. Gidaspow, A computational fluid dynamics design of a carbon dioxide sorption circulating fluidized bed, AIChE J. 56 (11) (2010) 2805–2824.
- [3] T. Dogu, Extension of moment analysis to nonlinear systems, AIChE J. 32 (1986) 849–852.
- [4] B. Ficicilar, T. Dogu, Breakthrough analysis for CO₂ removal by activated hydrotalcite and soda ash, Catal. Today 115 (2006) 274–278.
- [5] H.S. Fogler, Elements of Chemical Reaction Engineering, 3rd edition, Prentice-Hall, New Jersey, 1999.
- [6] M. Foroughi-dahr, M. Esmaieli, H. Abolghasemi, A. Shojamoradi, E.S. Pouya, Continuous adsorption study of congo red using tea waste in a fixed-bed column Desalin, Water Treat. 57 (18) (2016) 8437–8446.
- [7] J. Hansen, M. Sato, P. Kharecha, D. Beerling, R. Berner, V. Masson-Delmotte, B. Pagani, M. Raymo, D.L. Royer, J.C. Zachos, Target atmospheric CO₂: where should humanity aim? Open Atmos. Sci. J. 2 (2008) 217–231.
- [8] E.M. Homem, M.G. Vieira, M.L. Gimenes, M.G. Silva, Nickel, lead and zinc removal by adsorption process in fluidised bed, Environ. Technol. 27 (10) (2006) 1101–1114.
- [9] O.A. Jaiboon, B. Chalermsinsuwan, L. Mekasut, P. Piumsomboon, Effect of flow patterns/regimes on CO₂ capture using K₂CO₃ solid sorbent in fluidized bed/ circulating fluidized bed, Chem. Eng. J. 219 (2013) 262–272.
- [10] N. Lamia, L. Wolff, P. Leflaive, D. Leinekugel-Le-Cocq, P.S. Gomes, C.A. Grande, A.E. Rodrigues, Equilibrium and fixed bed adsorption of 1-butene, propylene and propane over 13X zeolite pellets, Separ. Sci Technol. 643 (5) (2008) 1124– 1156
- [11] S.C. Lee, H.J. Chae, S.J. Lee, Y.H. Park, C.K. Ryu, C.K. Yi, Novel regenerable potassium-based dry sorbents for CO₂ capture at low temperatures, J. Mol. Catal B Enzym. 6 (2–3) (2009) 179–184.
- [12] D.K. Lee, D.Y. Min, H. Seo, N.Y. Kang, W.C. Choi, Y.K. Park, Kinetic expression for the carbonation reaction of K₂CO₃/ZrO₂ sorbent for CO₂ capture, Ind. Eng. Chem. Res. 52 (2013) 9323–9239.
- [13] O. Levenspiel, Chemical Reaction Engineering, 3rd edition, Wiley, New York, 1999.
- [14] S.W. Park, D.H. Sung, B.-S. Choi, J.W. Lee, H. Kumazawa, Carbonation kinetics of potassium carbonate by carbon dioxide, J. Ind. Eng. Chem. 12 (4) (2006) 522– 330.
- [15] S.W. Park, D.H. Sung, B.S. Choi, J.W. Lee, H. Kumazawa, Sorption of carbon dioxide onto sodium carbonate, Separ. Sci. Technol. 41 (2007) 2221–2223.
- [16] S.W. Park, D.H. Sung, B.S. Choi, J.W. Lee, H. Kumazawa, Carbonation kinetics of potassium carbonate by carbon dioxide, Korean J. Chem. Eng. 26 (5) (2009) 1383–1388.
- [17] H.W. Pennline, D.R. Luebke, K.L. Jones, C.R. Myers, B.I. Morsi, Y.J. Heintz, J.B. Ilconich, Progress in carbon dioxide capture and separation research for gasification-based power generation point sources, Fuel Process. Technol. 89 (2008) 897–907.
- [18] C.G. Phillipsen, A.C.F. Vilela, L.D. Zen, Fluidized bed modeling applied to the analysis of processes: review and state of the art, J. Mater. Res. Technol. 4 (20) (2015) 208–216.
- [19] E. Rezaei, O. Mowla, D. Mowla, Aqueous phase adsorption of organic compounds on activated carbon in fluidized bed, Desalin. Water Treat. 28 (1–3) (2011) 35–41.
- [20] B.S. Sampath, P.A. Ramachandran, R. Hughes, Modelling of non-catalytic gassolid reactions-II transient simulation of a packed bed reactor, Chem. Eng. Sci. 30 (1) (1975) 135–143.

- [21] Y. Seo, S.H. Ryu, H.D. Bae, C.K. Yi, Effect of water pretreatment on CO₂ capture using a potassium-based solid sorbent in a bubbling fluidized bed reactor, Chem. Eng. J. 24 (2007) 457–460.
- [22] J.L. Sotelo, G. Ovejero, A. Rodríguez, S. Álvarez, J. García, Adsorption of carbamazepine in fixed bed columns: experimental and modeling studies, Separ. Sci. Technol. 48 (17) (2013) 2626–2637.
- [23] X.C. Wang, K. Li, Z.H. Li, Characteristics of physicochemical adsorption of soluble matter by particles formed in a fluidized pellet bed reactor, Environ. Technol. 32 (7–8) (2011) 713–719.
- [24] C.K. Yi, S.H. Jo, Y. Seo, J.B. Lee, C.K. Ryu, Continuous operation of the potassium-based dry sorbent CO₂ capture process with two fluidized-bed reaction, Int. J. Greenh. Gas Control 1 (2007) 31–36.
- [25] C.W. Zhao, X.P. Chen, C.S. Zhao, Y.K. Liu, Carbonation and hydration characteristics of dry potassium-based sorbents for CO₂ capture, Energy Fuel 23 (2009) 1766–1769.
- [26] C. Zhao, X. Chen, C. Zhao, Study on CO₂ capture using dry potassium-based solvents through orthogonal test method, Int. J. Greenh. Gas Control 4 (2010) 655–658.
- [27] C. Zhao, X. Chen, C. Zhao, Multiple-Cycles behavior of K₂CO₃/Al₂O₃ for CO₂ capture in a fluidized-bed reactor, Energy Fuel 24 (2010) 1009–1012.
- [28] C. Zhao, X. Chen, C. Zhao, Carbonation behavior and the reaction kinetic of a new dry potassium-based sorbent for CO₂ capture, Ind. Eng. Chem. Res. 51 (2012) 14361–14366.
- [29] C. Zhao, X. Chen, E.J. Anthony, X. Jiang, L. Duan, Y. Wu, W. Dong, C. Zhao, Capturing CO₂ in flue gas from fossil fuel-fired power plants using dry regenerable alkali metal-based sorbent, Prog. Energy Combust. 39 (6) (2013) 515–534.

Dear Nathphatsorn Jongartklang, Ratchanon Piemjaiswang, Pornpote Piumsomboon and Benjapon Chalermsinsuwan:

This is APCETA'15 official letter for notification of acceptance.

Congratulation!!

Based on the recommendations of the reviewers and the Program Committee, I am very pleased to inform you that your paper:

1570220600 - CO2 sorption using Na2CO3/Al2O3 sorbent with various flow patterns of fixed/fluidized bed reactors

-+*%\$%*+-+*%\$%*+-+*%\$-+*%\$%*+

STATUS # ACCEPTED with MINOR REVISIONS
-+*%\$%*+-+*%\$%*+-+*%\$-+*%\$9**+

You are cordially invited to present the paper at 2015 Advancement in Petroleum and Chemical Engineering Technology and Applications International Conference (APCETA'15).

It is a prestigious international academic conference organized by Malaysia Technical Scientist Association (MALTESAS). This conference is also supported by Universiti Malaysia Perlis (UNIMAP). The APCETA'15 will provide a platform where researchers, professionals, academicians and industries to share and generate a forum of recent development, new ideas and new discoveries. The APCETA'15 will be held in Krabi, Thailand from on 1-3 December 2015.

Hotel Venue for Conference: Deevana Plaza Krabi – Aonang 186 Moo 3, Ao Nang Soi 8, Ao Nang Beach, Muang, Krabi 81180 Thailand

All ACCEPTED and REGISTERED papers will be published in the Special Issues in Jurnal Teknologi (Indexed by Elsevier: SCOPUS)

Regards,

Secretariat of APCETA Program Chair

CFD MODELING OF SO₂ Capture Using Limestone In Industrial Scale Circulating Fluidized Bed Boiler

Article history
Received
TBA
Received in revised form
TBA
Accepted
TBA

Rattapong Tritippayanon^{1,2}, Veeraya Jiradilok³, Pornpote Piumsomboon¹, Benjapon Chalermsinsuwan^{1,2,*}

*Corresponding author benjapon.c@chula.ac.th

- ¹ Department of Chemical Technology, Faculty of Science, Chulalongkorn University, 254 Phayathai Road, Patumwan, Bangkok 10330, Thailand
- ² Center of Excellence on Petrochemical and Materials Technology, Chulalongkorn University, 254, Phayathai Road, Patumwan, Bangkok 10330, Thailand
- ³ D.A. Research Center Co., Ltd., 122 Moo 2, Thatoom, Srimahaphote, Prachinburi 25140, Thailand

Graphical abstract

2.17 e-01 2.18 e-01 1.18 e-01 2.75 e-02 2.05 e

OXYGEN MOLE FRACTION CONTOUR

Abstract

The unsteady state computational fluid dynamics model for gas-solid particle flow in industrial scale circulating fluidized bed boiler combining with combustion and desulfurization (using limestone solid sorbent) chemical reactions, both homogeneous and heterogeneous, was developed in this study. The effects of solid sorbent feeding position and solid sorbent particle size on sulfur dioxide concentration were investigated. The results showed that both the solid sorbent feeding position and solid sorbent particle size had an effect on the sulfur dioxide capture. Entering solid sorbent at the upper secondary air position gave lower sulfur dioxide concentration than the one at the lower secondary air position and fuel feed position, respectively. This can be explained by the influence of suitable temperature at the upper secondary air position for desulfurization chemical reaction. About the solid sorbent particle size, the sulfur dioxide capture was the lowest when using the largest solid sorbent particle size due to the system hydrodynamics.

Keywards: CFD modeling; circulating fluidized bed boiler; combustion; desulfurization; sulfur dioxide capture.

© 2015 Penerbit UTM Press. All rights reserved

1.0 INTRODUCTION

The increasing of world population leads to a higher energy demand. Currently, the coal-biomass power plants are still the important source of energy. However, the fuel power plant operation will lead to the significant amount of pollution emissions including sulfur dioxide gas (SO₂). This SO₂ gas can cause the acid rain, climate change and human health problems [1]. The limestone (CaCO₃) is a well-known solid sorbent to react with the flue gas from power plants. This is because it can be easily combined with the conventional combustion power plant process and it has low price [2, 3].

For the controlling of SO_2 emission, some alternative solutions to capture SO_2 gas are explored in the literature such as altering the solid sorbent circulation rates and the solid sorbent inventory [4]. However, the effect of other process conditions is still unknown.

Circulating fluidized bed (CFB) has been extensively used in chemical, petrochemical and energy industries, especially power generation, because it gives high combustion efficiency. In CFB boiler, the solid particle and gas phases react with each other in the riser section. In addition, the CFB boiler has the cyclone and downer sections to separate large or unreacted solid particles and to return them into the process [5-6].

Computational fluid dynamics (CFD) are recently used mathematical tool for predicting the engineering problem. This method can accurately predict the flow behavior, heat and mass transfers and chemical reactions by using numerical approaches. The advantages of using this method are being easy to use even in the non-safe process operating condition and reducing the cost and time on the real experiment [7-8].

In this study, the modeling SO_2 capture using $CaCO_3$ in industrial scale CFB boiler therefore was developed using CFD simulation. At first, the developed model was compared its correctness with the actual collecting data from a power plant, including the outlet SO_2 concentration, the outlet oxygen (O_2) concentration and the outlet system gas velocity. Then, the effects of solid sorbent feeding position and solid sorbent particle size on SO_2 concentration were investigated to propose the appropriate guidelines for SO_2 capture.

2.0 MODEL DESCRIPTION

The configuration and detailed dimension of the simplified riser section of a CFB boiler are shown in Figure 1. The employed model was two-dimensional model. The maximum dimensions of the height and diameter of CFB boiler were 20.00 m and 7.96 m, respectively. Fuel entered the system at fuel feed position at 1.23 m from the primary air position. The auxiliary air was fed to the system at two positions to improve the combustion efficiency. The lower and upper secondary airs entered the system at 2.37 and 3.80 m from the primary air position, respectively. In addition, all the three input positions were fed with 30° of depression.

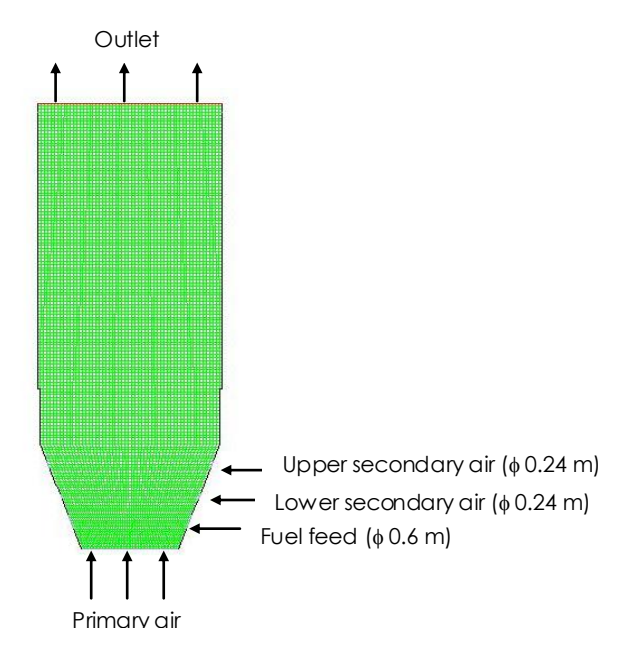


Figure 1 Dimension of the riser section of industrial scale CFB boiler.

The model was unsteady state Eulerian-Eulerian CFD model. The governing, including momentum, energy and mass conservation equations, and constitutive equations were solved separately for each phase as the continuous (gas) and dispersed (solid particles) phases [9-10]. About the constitutive equations, the set of equations was selected from the kinetic theory of granular flow theory. This theory was effectively employed in many literatures on CFB boiler modelling.

2.1 Chemical reaction conditions

The chemical reactions of solid particle phase consisting of fuel solid particle (lower calorific value (LCV) coal, higher calorific value (HCV) coal and biomass (wood chip)) and $CaCO_3$ (sorbent) solid particle are shown below:

Fuel
$$\rightarrow$$
 Volatile + Char + Ash (R₁)

$$CH_4 + \frac{3}{2}O_2 \rightarrow CO + 2H_2O$$
 (R₂)

$$C_2H_6 + \frac{5}{2}O_2 \rightarrow 2CO + 3H_2O$$
 (R₃)

$$CO + \frac{1}{2}O_2 \rightarrow CO_2 \tag{R_4}$$

$$H_2 + \frac{1}{2} O_2 \rightarrow H_2 O$$
 (R₅)

$$C_{(s)} + \frac{1}{\kappa} O_2(g) \rightarrow \left(2 - \frac{2}{\kappa}\right) CO_{(g)} + \left(\frac{2}{\kappa} - 1\right) CO_{2(g)}$$
 (R₆)

$$C_{(s)} + CO_{2(g)} \rightarrow 2CO_{(g)}$$
 (R₇)

$$CaCO_3 \rightarrow CaO + CO_2$$
 (R₈)

$$CaO + SO_2 + \frac{1}{2}O_2 \rightarrow CaSO_4$$
 (R₉)

First, the fuel solid particles were dried and devolatilized (R₁). The volatile matter includes methane (CH₄), ethane (C₂H₆), carbon monoxide (CO), CO₂, water vapour (H₂O) and hydrogen (H₂). Then, the combustion of volatile (R₂-R₅), the combustion of char (R₆), the gasification of char (R₇) and the capturing of impurity gas (R₈-R₉) reactions were occurred.

For the drying and devolatilization reaction (R_1), this step was assumed to be fast reaction step. The fraction of char, ash and volatile gas composition were then determined based on real experimental information using the proximate and ultimate analysis of each fuel solid particle [11-12] as shown in Tables 1, 2 and 3. Then, the overall gas compositions were obtained according to the feeding weight percent of each fuel component. The obtained specie mass fractions of volatile gas composition are 0.046 for CH₄, 0.057 for C_2H_6 , 0.226 for CO, 0.031 for CO₂, 0.580 for H₂O, 0.030 for H₂, 0.013 for SO₂ and 0.015 for NO₂ respectively.

Table 1 Analysis of coal (HCV)'s properties.

Proximate (wt%)		Ultimate (wt%)	
Fixed carbon	38.29	С	51.17
Volatile matter	29.00	Н	3.91
Ash	8.54	Ν	1.27
Moisture	24.17	0	10.19
		S	0.76

Table 2 Analysis of coal (LCV)'s properties.

Proximate (wt%)			Ultimate (wt%)
Fixed carbon	31.68	С	45.96
Volatile matter	33.29	Н	3.75
Ash	4.79	Ν	0.62
Moisture	30.24	0	14.16
		S	0.48

Table 3 Analysis of biomass (wood chip)'s properties.

Proximate (wt%)			Ultimate (wt%)	
Fixed carbon	21.59	С	27.43	
Volatile matter	33.05	Н	2.55	
Ash	0.36	Ν	0.07	
Moisture	45.00	0	24.59	
		S	0.01	

The combustion of volatile component occurred according to various homogeneous chemical reactions. The homogeneous chemical reactions included the CH₄ oxidation (R₂), C₂H₆ oxidation (R₃), CO combustion (R₄) and H₂ oxidation (R₅). Their reaction rate and chemical reaction kinetics are summarized in Table 4 [13-15].

The solid fuel heterogeneous chemical reactions consisted of the char combustion (R_6) [16] and the boudouard reaction (R_7). Their reaction rate and chemical kinetic constants are also summarized in Table 4 [14-17].

Generally, the desulfurization process using solid sorbents consisted of indirect and direct desulfurization mechanisms. In this study, CaCO₃ was calcined to be CaO and CO_2 (R_7). Then, the CaO was used as the sorbent for SO₂ capture [5, 18-20]. Therefore, the CaCO₃ solid particles consisted of pseudo-species, including CaCO₃, CaO and CaSO₄. The calcinations reaction (R₈) took place at system temperature between 873-1,273 K. However, some literature study claimed that the proper operating temperature was between 1,073-1,173 K [5, 21, 22]. This is because the temperature in this range was appropriate for driven the chemical reaction of SO₂ capture. Their reaction rate and chemical kinetic constants are summarized in Table 4. In this study, the employed reaction rates were obtained from the similar fluidized bed literatures [5, 22].

Table 4 Reaction rates used in the simulations [5,22].

	Reaction rate	Reaction rate constant
R ₁	R_1	Experimental data
R ₂	$R_2 = k_2 \left(\frac{\gamma_{\mathcal{O}_2} \sigma_{\mathcal{S}}}{M_{\mathcal{O}_2}} \right)^{0.8} \left(\frac{\gamma_{\mathcal{C}H_4} \sigma_{\mathcal{S}}}{M_{\mathcal{C}H_6}} \right)^{0.7}$	$k_2 = 1.58 \times 10^{10} \exp\left(\frac{-24242}{\tau_g}\right)$
R ₃	$R_3 = k_3 \left(\frac{r_{C_2 H_6} \sigma_g}{M_{C_2 H_6}} \right) \left(\frac{r_{O_2} \sigma_g}{M_{O_2}} \right)$	$k_3 = 1.585 \times 10^{10} \exp\left(\frac{-24157}{\tau_g}\right)$
R ₄	$R_4 = k_4 Y_{CO} Y_{H2O} 0.5 \frac{17.5 Y_{O_2}}{1 + 24 Y_{O_2}} \left(\frac{p}{R T_p}\right)^{1.5}$	$k_4 = 3 \times 10^{10} \exp\left(\frac{-8.699 \times 10^7}{\pi T_g}\right)$
R ₅	$R_5 = k_5 \left(\frac{\gamma_{\mathcal{O}_2} \sigma_{\mathcal{B}}}{m_{\mathcal{O}_2}} \right) \left(\frac{\gamma_{\mathcal{H}_2} \sigma_{\mathcal{B}}}{m_{\mathcal{H}_2}} \right)^{1.5}$	$k_5 = 1.63 \times 10^9 T_g^{1.5} \exp\left(\frac{-z_4 z_0}{\tau_g}\right)$
R ₆	$R_6 = \frac{s_{\sigma_{21}\sigma_{21}Y_c}}{d_{**}\sigma_*} k_6 Y_{\sigma_2}$	$k_6 = \frac{\kappa \tau_{s1}/M_c}{(1/k_{cr}) + (1/k_{cd})}, k_{cr} = 8910 \exp\left(\frac{-1.4947 \times 10^4}{8\tau_{rt}}\right), k_{cd} = \frac{\sin_0\left(\sigma_g + \frac{M_g}{\sigma_g S c_t}\right) M_c}{d_{s1} R_g T_g}$
R_7	$R_7 = \frac{{}^{\kappa_7 r_{eO_2} r_e}}{{}^{1+k_{7,CO_2} r_{eO_2} + k_{7,CO} r_{eO}}}$	$k_7 = 3.1785 \times 10^{10} \exp\left(\frac{-2.55 \times 10^{2}}{8T_{ex}}\right), k_{7,CO_2} = 66 \exp\left(\frac{-2.55 \times 10^{7}}{8T_{ex}}\right), k_{7,CO} = 120 \exp\left(\frac{-2.55 \times 10^{7}}{8T_{ex}}\right)$
R ₈	$R_8 = k_8 \alpha_{sz} \rho_{sz} Y_{caco_2} S_{caco_2} \frac{\pi_e - \pi_{co_2}}{\pi_e}$	$k_8 = 6.078 \times 10^4 \exp\left(\frac{-1.05 \times 10^6}{8T_{co}}\right),$ $p_e = 4.192 \times 10^{12} \exp\left(\frac{-1.702 \times 10^6}{8T_g}\right), S_{coco_3} = 1.26 \text{ m}^2\text{g}^{-1}$
R ₉	$R_9 = k_9 \alpha_{sz} \rho_{sz} Y_{cad} S_s Y_{co_2} a$	$k_9 = 490 \exp\left(\frac{-1.75 \times 10^7}{8T_{22}}\right),$ $\alpha = \exp\left[\frac{-5717 \cos \sigma_4}{(7\cos \sigma_2 + 7\cos \sigma_4)^{36}\cos \sigma_2}\right], S_g = \begin{cases} -38.4T_{s2} + 5.6 \times 10^4 & \tau_{s2} \approx 1253 \text{ M} \\ 35.9T_{s2} - 3.67 \times 10^4 & \tau_{s2} \approx 1253 \text{ M} \end{cases}$

where d: solid particle diameter (m) k: reaction rate constant of reaction i, M: molecular weight of species i, p: gas pressure, p: pressure of species i, p: diffusion coefficient, p: gravity acceleration, p: net production rate of reaction i, p: universal gas constant, p: Sherwood number, p: Schmidt number, p: density, p: mass fraction of species i, p: volume fraction, p: temperature and p: viscosity.

2.2 Simulation, initial and boundary conditions

About the modeling setting, the employed viscous model was laminar. The density of gas species was calculated using an incompressible ideal gas law while the density of solid particle species was calculated using a volume-weighted-mixing-law. The specific heat capacities, thermal conductivities and viscosities for each phase were calculated using a mixing-law function of temperature, mass-weighted-mixing-law, and weighted-mixing-law, respectively. The maximum packing of solid particle was set as 0.60. The calculated time step was set as 0.001 s.

The other simulation, initial and boundary conditions for simulation are showed in Table 5 comparing with the experimental ones. For the initial condition, the industrial scale CFB boiler was filled with sand solid particles for using as the heating medium inside the system with static bed height of 0.61 m and volume fraction of 0.30. The temperature of each phase was set equal to 673 K. For the boundary condition, the velocities of gas phase in different inlet positions were already listed in Table 5. At the currently feeding location (fuel feed position), the velocities of fuel solid particle and CaCO₃ solid sorbent were set equally as 0.35 m/s with solid volume fraction of 8.81x10⁻⁴ and 2.30x10⁻⁴, respectively. The inlet temperature at fuel feeding position was set as to 1,073 K due to the returning of unreacted fuel solid particle assumption. The inlet temperatures at primary, lower secondary air and upper secondary air positions were set as 673 K. There was no sand solid particle entered the system. At the outlet, the operating pressure was fixed as 101,325 Pa. The other important assumptions in this study were mono-sized solid particle and two-dimension model.

Table 5 Parameters used in the simulations.

	Unit	Experiment	Simulation
Inlet gas velocity at primary air	m/s	1.40	1.40
Inlet gas velocity at lower secondary air	m/s	37.80	37.80
Inlet gas velocity at upper secondary air	m/s	48.41	48.41
Diameter of fuel solid particle	micron	700	700
Diameter of CaCO ₃ solid particle	micron	350	350
Diameter of sand solid particle	micron	180	180
Density of fuel solid particle	kg/m³	2,000	2,000
Density of CaCO ₃ solid particle	kg/m³	2,800	2,800
Density of sand solid	kg/m³	2,659	2,659
Restitution coefficient	-	-	0.90
Specularity coefficient	-	-	0.01

3.0 RESULTS AND DISCUSSION

Before comparing the CFD results, the validation of the model and the time independency test (steady state time) were investigated. This study results showed that, after simulation time of 100 s, the absolute pressure began to stable indicating that the system starting to reach steady state time. After 100 s of simulation time, the chemical reactions were then analyzed and compared with the actual collecting experimental data from the power plant. Several modeling adjustments were performed to match the obtained simulation results with the real experimental information.

Table 6 illustrates the comparison of optimum simulation and obtained experimental results. It could be seen that, after the modeling adjustment, the simulation results were consistent with experimental results. The outlet SO₂ concentration, O₂ concentration and system gas velocity were compared. The ranges of simulation results were similar to the ones of the experiment. This confirmed the correctness of the developed model. Then, this model was used in the following simulations. Figure 2 shows the corresponding contours of (a) O_2 and (b) SO₂ mole fractions for the optimum simulation. Both the gas concentrations were highest at the solid feeding location and then decreased throughout the industrial scale CFB Boiler due to the occurrence of chemical reaction.

 Table 6
 Comparison of optimum simulation and obtained experimental results.

Case	O ₂ (%)	SO ₂ (ppm)	Velocity outlet (m/s)
Experiment	7	211 – 566	4.14 - 5.23
Simulation	7.22 – 10.85	319.70 – 432.17	3.46 – 4.18

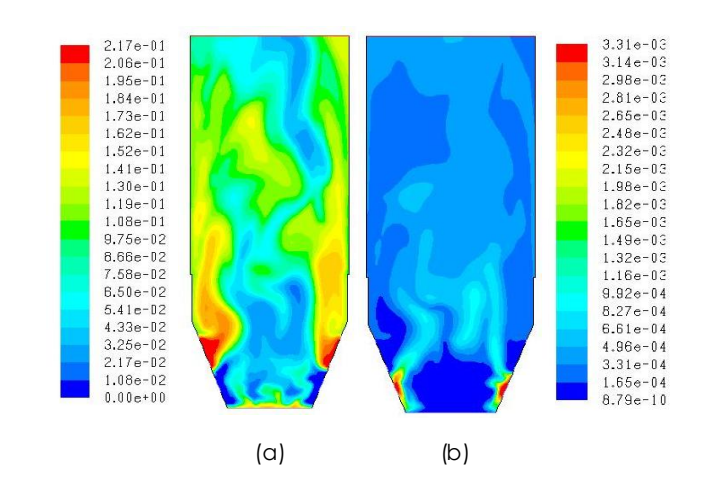


Figure 2 Contours of (a) O_2 and (b) SO_2 mole fractions for the optimum simulation (using 350 micron solid sorbent particle size and feeding solid sorbent at fuel feed position).

3.1 Effect of solid sorbent feeding position

In this study, the effect of solid sorbent feeding position on the SO_2 capture was investigated. The assumption is that the $CaCO_3$ solid sorbent should be fed at the position which has suitable temperature for desulfurization to occur. Here, three solid sorbent feeding position were compared which were the conventional solid sorbent feeding position at the fuel feed position and the other two new solid sorbent feeding position at the lower secondary air and upper secondary air positions. For comparison of the results, these three simulations were carried out with the same input amount of $CaCO_3$ solid sorbent.

Figure 3 shows the change in outlet CO₂ concentration, outlet O2 concentration and outlet SO₂ concentration with three different solid sorbent feeding positions. From the results, the outlet O₂ concentrations were quite similar with three different solid sorbent feeding positions. The solid sorbent chemical reaction did not change the overall main combustion chemical reaction. However, slightly lower outlet O2 concentrations were found from fuel feed, lower secondary air and upper secondary air positions, respectively. Therefore, the outlet CO₂ product concentrations were increased according to the following order: fuel feed, lower secondary air and upper secondary air positions. The outlet SO₂ concentrations for upper secondary air were lower than the outlet SO₂ concentration for lower secondary air and fuel feed positions, respectively. This is because the suitable higher system temperature with the upper secondary air position which accelerates the reaction rate of desulfurization chemical reaction.

In this study, the outlet SO_2 concentration for upper secondary air, lower secondary air and fuel feed positions were 384.39, 387.12 and 389.50 ppm, respectively. The difference of SO_2 gas with the changing of the location of solid sorbent injection was within 10 ppm, the location of solid sorbent injection therefore had a minor impact on improvement SO_2 capture efficiency. As stated above, this is because the slightly deviation in temperature between the feeding positions.

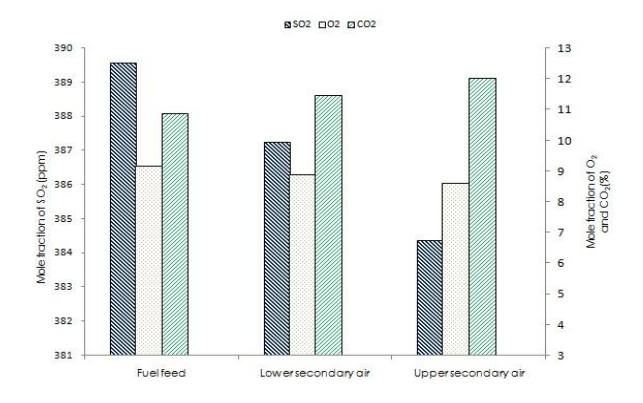


Figure 3 The outlet gas composition with three different solid sorbent feeding positions.

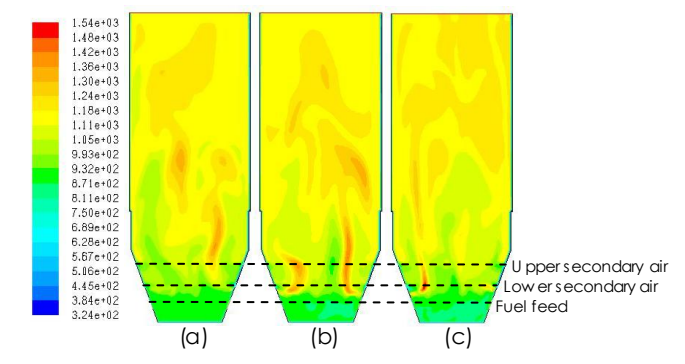


Figure 4 Contours of gas temperature (K) inside the riser section of industrial scale CFB boiler for (a) fuel, (b) lower secondary air and (c) upper secondary air feeding positions.

Figure 4 shows the contour of gas temperature in industrial scale CFB boiler. All the solid sorbent feeding position exhibited quite similar gas temperature profiles. The results validated the above explanations that the suitable temperature inside the system was the reason for higher SO_2 capture [5]. This phenomenon occurred due to the buoyancy of high temperature gas product.

3.2 Effect of solid sorbent particle size

The effect of solid sorbent particle size on the SO_2 capture was also investigated. The assumption is that the $CaCO_3$ solid sorbent which has higher resident time will be appropriate to use inside this industrial scale CFB boiler. Here, three solid sorbent particle size were compared which were 200, 350 (conventional) and 500 micron. The other operating condition was similarly set for each case.

Figure 5 shows the change in outlet CO_2 concentration, outlet O_2 concentration and outlet SO_2 concentration with three different solid sorbent particles size. From the results, the increasing solid sorbent particles size decreased O_2 and SO_2 concentrations and increased CO_2 concentration. The solid sorbent particle with largest particle size will have higher system residence time which then appropriates to occur sorption reaction inside this industrial scale CFB boiler. Also, the large solid sorbent helps the mixing behavior inside the system which then assists the chemical reaction to occur.

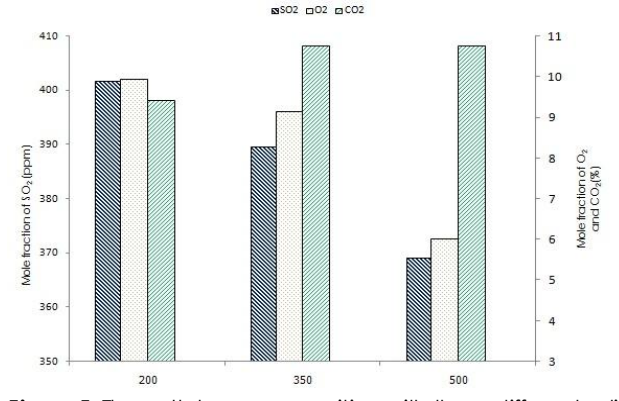


Figure 5 The outlet gas composition with three different solid sorbent particle sizes.

In this study, the outlet SO_2 concentration for 200, 350 and 500 micron solid sorbent particle size were 401.76, 392.641 and 369.19 ppm, respectively. Figures 2 and 6 confirmed that the SO_2 mole fraction was lowest for 500 micron solid sorbent particle size.

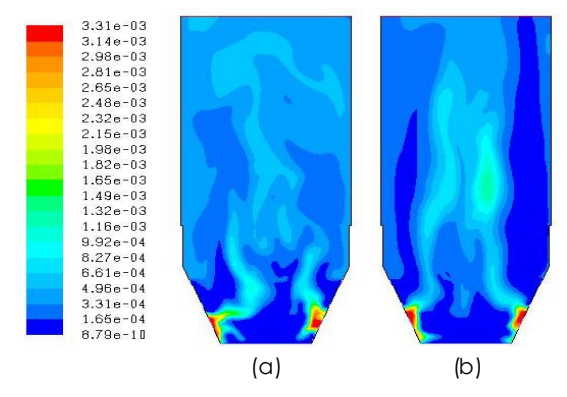


Figure 6 Contours of SO₂ mole fractions for solid sorbent particle size of (a) 200 and (b) 500 micron.

4.0 CONCLUSION

In this study, the SO_2 capture modeling using $CaCO_3$ in industrial scale CFB boiler was developed using CFD simulation. The obtained CFD results were consistent with the real operation data.

For the effect of solid sorbent feeding position on SO_2 capture, entering solid sorbent at the upper secondary air position gave lower sulfur dioxide concentration than the one at the lower secondary air position and fuel feed position, respectively. This can be explained by the influence of suitable temperature at the upper secondary air position for desulfurization chemical reaction.

For the effect of solid sorbent particle size on SO_2 capture, the SO_2 capture was lowest when using the largest solid sorbent particle size due to the system hydrodynamics. The $CaCO_3$ solid sorbent which has higher residence time will be appropriate to use inside this industrial scale CFB boiler.

Acknowledgement

The PETROMAT, the Ratchadaphiseksomphot Endowment Fund 2015 of Chulalongkorn University (CU-58-059-CC), the Thailand Research Fund (TRG5780205), and the D.A. Research Center Co. Ltd are gratefully acknowledged.

References

- Staudt, J.E. 2011. Control technologies to reduce conventional and hazardous air pollutants from coal-fired power plants. M.J. Bradley & Associates LLC. United states of America
- [2] Ryu, H., Grace, J. and Lim, C. 2006. Simultaneous CO₂/SO₂ Capture Characteristics of Three Limestones in a Fluidized-Bed Reactor. Energy Fuels: 1621–1628.
- [3] Ma, L., Cao, L. and He, R. 2015. Numerical study of pore structure effect on SO₂–CaO reactions. Chinese Journal of Chemical Engineering 23: 652–658.

- [4] Arias, B., Cordero, J.M., Alonso, M., Diego, M.E. and Abanades, J.C. 2013. Investigation of SO₂ capture in a circulating fluidized bed carbonator of a Ca looping cyde. Industrial & Engineering Chemistry Research 52(7): 2700– 2706.
- [5] Shuai, W., Juhui, C., Guodong, L., Huilin, L., Feixiang, Z. and Yanan, Z. 2014. Predictions of coal combustion and desulfurization in a CFB riser reactor by kinetic theory of granular mixture with unequal granular temperature. Fuel Processing Technology 126: 163–172.
- [6] Chinsuwan, A., Dutta, A. and Janlasad, N. 2014. Prediction of the heat flux profile on the furnace wall of circulating fluidized bed boilers. Journal of the Energy Institute 87:314– 320
- [7] Qiu, G., Ye, J. and Wang, H. 2015. Investigation of gassolids flow characteristics in a circulating fluidized bed with annular combustion chamber by pressure measurement sand CPFD simulation. Chemical Engineering Science 134: 433–447.
- [8] Patankar, S.V. 1980. Numerical heat transfer and fluid flow. Hemisphere Publishing Corporation. New York
- [9] Verstreeg, H. K. and Malalasekera, W. 2007. An Introduction to Computational Fluid Dynamics: The Finite Volume Method. 2nd ed. Longman Group Limited. England.
- [10] Balakin, B. V., Hoffmann, A. C., Kosinski, P., and Rhyne, L. D. 2010. Eulerian - Eulerian CFD model for the sedimentation of spherical particles in suspension with high particle concentrations. Engineering Applications of Computational Fluid Mechanics. Vol. 4. No. 1: 116–126.
- [11] Halwachs, M., Hofbauer, H. and Kampichler, G. 2009. Low temperature pyrolysis of agricultural residues-first results of a pilot plant. International Conference on Polygeneration Strategies.
- [12] Shuai, W., Juhui, C., Guodong, L., Huilin, L., Feixiang, Z. and Yanan, Z. 2014. Predictions of coal combustion and desulfurization in a CFB riser reactor by kinetic theory of granular mixture with unequal granular temperature. Fuel Processing Technology 126: 163-172.
- [13] Busciglio, A., Vella, G., Micale, G. and Rizzuti, L. 2009. Analysis of the bubbling behaviour of 2D gas solid fluidized beds Part II. Comparison between experiments and numerical simulations via Digital Image Analysis Technique. Chemical Engineering Journal 148: 145–163.
- [14] Gungor, A. and Eskin ,N. 2008. Two-dimensional coal combustion modeling of CFB, International Journal of Thermal Sciences 47: 157–174.
- [15] Gungor, A. 2008. Two-dimensional biomass combustion modeling of CFB, Fuel 87: 1453–1468.
- [16] Zhou, W., Zhao, C., Duan, L., Liu, D. and Chen, X. 2011. CFD modeling of oxy-coal combustion in circulating fluidized bed. International Journal of Greenhouse Gas Control 5(6): 1489–1497.
- [17] Ross, I.B. and Davidson, J.F. 1982. The combustion of carbon particles in a fluidized bed. Transactions of the institution of Chemical Engineers 60: 109-114.
- [18] Rajan, R.R. and Wen, C.Y. 1980. A comprehensive model for fluidized bed coal combustors. AIChE Journal 26: 642–655.
- [19] Mattisson, T. and Lyngfelt, A. 1998. A sulphur capture model for circulating fluidized-bed boilers. Chemical Engineering Science 53: 1163–1173.
- [20] Borgwardt, R.H. 1970. Kinetics of reaction of SO_2 with calcined limestone. Environmental Science & Technology 4: 59–63.
- [21] Mattisson, T. and Lyngfelt, A. 1998. A sulfur capture model for circulating fluidized-bed boilers. Chemical Engineering Science 53: 1163–1173.
- [22] Field, M.A., Gill, D.M., Morgan, B.B. and Hawskley, P.G.W. 1987. Combustion of Pulverized Coal. BCURA. Leatherhead. England.

Acceptance Notification and Invitation Letter

2014 International Conference on Chemical and Material Engineering (ICCME 2014)

Xiamen, China, December 13-14, 2014

www.iccme.org







Pilaiwan Chaiwang, Benjapon Chalermsinsuwan, Pornpote Piumsomboon

Department of Chemical Technology, Faculty of Science, Chulalongkorn University, Thailand Email: benjapon.c@chula.ac.th

Dear Pilaiwan Chaiwang, Benjapon Chalermsinsuwan, Pornpote Piumsomboon,

We are pleased to inform you that, after our double-blind peer review (please refer to the attached files), your manuscript identified below has been accepted for publication and oral presentation by 2014 International Conference on Chemical and Material Engineering (ICCME 2014) to be held in Xiamen, China, during December 13-14, 2014.

Paper ID: <u>ME2014-202E</u>

Paper Title: Thermogravimetric Analysis and Chemical Kinetic for Regeneration of

Sodium Carbonate Solid Sorbent

All papers, both invited and contributed, will be reviewed by two or three experts from the committees. After a careful reviewing process, all accepted paper will be published in international journal "Advanced Materials Research Journal" (ISSN: 1022-6680). AMR journal is indexed by Elsevier. Scopus and Ei Compendex (CPX), Cambridge Scientific Abstracts (CSA), Chemical Abstracts (CA), Google and Google Scholar, ISI (ISTP), Institution of Electrical Engineers(IEE), etc.(For index information, please refer to AMM official website: http://www.scientific.net/AMR/details).The full text is online available via platform www.scientific.net. Trans Tech Publications will provide online camera-ready paper submission system.



Registration Instruction

There are 6 steps to complete your registration:

- 1. Revise your paper according to the Review Comments carefully.
- Format your paper according to the Template carefully.
 AuthorInstructions.doc (4-10 pages DOC Format)
- Download and complete the Registration Form.ICCMEreg (author).doc
- 4. Finish the payment of Registration fee. (The information can be found in the Registration form) ICCME2014reg (author).doc
- 5. Finish the Copyright Form.

Copyright Form

- 6. Send your final papers (both doc and pdf format), filled registration form (doc format), copyright form (jpg format less than 100KB) and the scanned payment proof* to iccme@saise.org (Before November 10, 2014)
- *If you pay by on-line Credit Card Payment, please fill your confirmation number in the registration form after paying.
- *If you pay by bank transfer, please scan the payment slip as the payment proof for checking.

Maybe some authors couldn't attend the conference to present their papers due to some unavoidable matters, so if you and your co-author(s) could not attend ICCME 2014 to present your paper for some reasons, and please inform us, we will send you, the official receipt and proceeding after conference free of charge.

Please strictly adhere to the format specified in the conference template while preparing your final paper. If you have any problem in preparing the final paper, please feel free to contact us via iccme@saise.org; for the most updated information on the conference, please check the conference website at www.iccme.org. The Conference Program will be available at the website in December 2014.

Effect of Operating Parameters on System Mixing Inside Air Reactor of Chemical Looping Combustion Using CFD Simulation

Abstract

In this study, the effect of operating parameters on system mixing inside air reactor of chemical looping combustion was analyzed using factorial experimental design analysis. The flow behavior was simulated using computational fluid dynamic model with the Eulerian approach. The EMMS drag model was used since it showed comparable quantitative result to the experimental one. The results summarized that gas velocity was the significant parameter that affected average and standard deviation of radial and axial solid volume fractions. Besides, the interaction between diameter of solid particle and gas velocity also had an effect on standard deviation of radial solid volume fraction.

1. Introduction

Reducing carbon dioxide (CO₂) emissions from industrial section is receiving more attention from researchers and engineers. This is because the CO₂ capture from power generation systems is expensive and consumes a lot of energy¹. One solution is to use circulating fluidized bed (CFB) technology for CO₂ capture using the chemical looping combustion (CLC) concept. In a CLC system, the process shown in Fig. 1 is separated into two interconnected fluidized bed reactors called air reactor and fuel reactor^{2,3}. A solid oxygen carrier circulates between two reactors and transports oxygen from air reactor to fuel reactor. With this concept, CO₂ is separated from the other flue gas components. Therefore, a subsequent CO₂ separation process is not necessary because the air is not directly mixed with the fuel. The gas separation equipment is then not needed that reducing the cost in this process. Lu et al. found that the riser simulation result for Geldart A particle using EMMS-based drag coefficient model were in good agreement with the experimental data⁴. Zhou et al. used the same drag coefficient model to investigate the effect of wall boundary condition in CFB

system. The specularity coefficient had a significant effect on gas-solid flow behavior⁵. From the above previous research study, the effect of modeling parameters was mainly explored while the effect of operating parameter was limited, especially for the air reactor in CLC process.

In this study, the hydrodynamics of solid particles and gas were investigated using computational fluid dynamics (CFD) simulation inside air reactor of CLC. An Eulerian-Eulerian two-phase model that treats interprenetrating continua for each phase was used^{3,6}. The CFD simulation results then were compared with the experimental data. In addition, the effect of different operating parameters were explored using 2⁴ factorial experimental design. The selected response

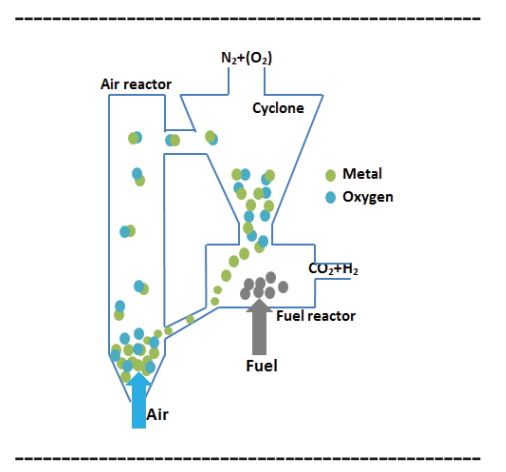


Fig. 1. The CLC process.

variables were the average of solid volume fraction (ASVF) and the standard deviation of the solid volume fraction in radial (SDSVF-RD) and axial directions (SDSVF-AD).

2. Experimental

2.1 System and computational domains

In this study, the CFD simulation was performed using commercial software, ANSYS FLUENT 14.0. The obtained results were compared the accuracy and correctness with the experimental data by Shuai et al.⁶ The air reactor had 0.0762 m diameter and 6.10 m height. The gas phase was fed at the bottom of the air reactor and solid particle phase was fed from two side inlets. Then, the gas-solid particle mixture flew out the system from the top of the air reactor. The gas was air while the solid particle was metal particle. The solid particles were laid in Geldart A classification. The suitable two-dimensional computational domain had 9,500 cells after testing the grid independency.

The time independent summarize that the system reached steady state after 20 s. simulation time. The other simulation condition settings are listed in Table 1.

As stated above, factorial experimental design analysis was selected for study the effect of operating parameters. The four varying operating parameters were solid particle diameter (A) at 0.00015 m and 0.00020 m, solid circulating flux (B) at 300 and 400 kg/m².s, temperature (C) at 1073 and 1273 K and superficial gas velocity (D) at 1 and 3 m/s. The selected values of operating parameters were chosen from the available

Table 1. Parameters used in CFD simulation.

Description	Value
Time step (s)	0.0001
Maximum solid volume fraction (-)	0.60
Operating pressure (atm)	1
Gas viscosity (kg/m s)	1.85×10^{-5}
Gas density (kg/m ³)	1.20
Solid particle density (kg/m ³)	1,600
Solid particle diameter (µm)	70
Solid particle-solid particle	
coefficient of restitution (-)	0.97
Wall-solid particle coefficient of	
restitution (-)	0.90
Specularity coefficient (-)	0.5
Drag coefficient model	EMMS
Wall boundary condition (-)	Johnson-
	Jackson ⁷

Table 2. The condition for the 2⁴ factorial experiment design analysis with the CFD simulation results.

Case	Particle diameter (m) (A)	Solid circulating flux (kg/m s) (B)	Temperature (K) (C)	Inlet gas velocity (m/s) (D)	Average of solid volume fraction (-)	SD of radial solid volume fraction (-)	SD of axial solid volume fraction (-)
1	0.00015	300	1073	1	0.1651	0.0035	0.0061
2	0.00020	300	1073	1	0.1625	0.0029	0.0058
3	0.00015	400	1073	1	0.1757	0.0076	0.0110
4	0.00020	400	1073	1	0.1671	0.0033	0.0063
5	0.00015	300	1273	1	0.1626	0.0038	0.0052
6	0.00020	300	1273	1	0.1603	0.0022	0.0057
7	0.00015	400	1273	1	0.1738	0.0048	0.0059
8	0.00020	400	1273	1	0.1648	0.0036	0.0060
9	0.00015	300	1073	3	0.1069	0.0016	0.0028
10	0.00020	300	1073	3	0.1096	0.0026	0.0048
11	0.00015	400	1073	3	0.1171	0.0014	0.0027
12	0.00020	400	1073	3	0.1175	0.0028	0.0039
13	0.00015	300	1273	3	0.1036	0.0026	0.0028
14	0.00020	300	1273	3	0.1070	0.0026	0.0044
15	0.00015	400	1273	3	0.1126	0.0024	0.0026
16	0.00020	400	1273	3	0.1154	0.0024	0.0038

theoretically and empirically information in the literature. The 2^4 two-level factorial experimental design analysis is summarized in Table 2.

2.2 Mathematical model

The Euler-Euler (Eulerian) multiphase model was selected for gas-solid particle two-phase flow. The energy conservation equations for gas and solid phase were ignored for the hydrodynamics study⁷. The employed conservation equations mass and momentum, as well as solid particle phase fluctuating energy with their constitutive equations are summarized below⁸:

2.2.1 Conservation equations

The mass conservation equations for gas (g) and solid particle (s) phases are shown in Eqs. (1) and (2)

$$\frac{\partial}{\partial t} \left(\varepsilon_g \rho_g \right) + \nabla \left(\varepsilon_g \rho_g V_g \right) = 0 \tag{1}$$

$$\frac{\partial}{\partial t} (\varepsilon_s \rho_s) + \nabla (\varepsilon_s \rho_s V_s) = 0 \tag{2}$$

where ε is the volume fraction, ρ is the density and V is the velocity and t is the time. The mass exchange between two phases was not considered in this study.

The momentum equation for the gas and solid particle phases are represented by the Navier-Strokes equation.

$$\frac{\partial}{\partial t} \left(\varepsilon_g \rho_g V_g \right) + \nabla \left(\varepsilon_g \rho_g V_g V_g \right) = -\varepsilon_g \nabla P + \nabla \tau_g + \varepsilon_g \rho_g g - \beta_{gs} \left(V_g - V_s \right)$$
(3)

$$\frac{\partial}{\partial t} (\varepsilon_s \rho_s V_s) + \nabla (\varepsilon_s \rho_s V_s V_s) = -\varepsilon_s \nabla P + \nabla \tau_s + \varepsilon_s \rho_s g + \beta_{gs} (V_g - V_s)$$
(4)

where g is the acceleration due to gravity, P is the hydrodynamic pressure, τ is the stress tensor and β_{gs} is the momentum transfer between gas and solid particle phases.

The fluctuating kinetic energy or granular temperature (θ) equation is summarized as shown below.

$$\frac{3}{2} \left[\frac{\partial}{\partial t} (\varepsilon_s \rho_s \theta) + \nabla (\varepsilon_s \rho_s \theta) V_s \right] = (-\nabla P_s I + \tau_s) : \nabla V_s + \nabla (K_s \nabla \theta) - \gamma_s$$
 (5)

where K_s is the conductivity of solid fluctuating kinetic energy, γ_s is the collisional dissipation of solid fluctuating kinetic energy and I is unit vector.

2.2.2 Constitutive equations

The constitutive equations used in this study were based on the conventional kinetic theory of granular flow (KTGF) such as solid pressure, solid viscosity and radial distribution function³. In addition, the employed interphase momentum exchange coefficient or drag force model (β_{gs}) is based on the energy minimization multi-scale (EMMS) concept proposed by

Yang et al.⁹ The EMMS model was developed based on the particle cluster occurrence concept. The previous study by Chalermsinsuwan et al.¹⁰ had successfully used this model to simulate the Geldart A particles operated in fast fluidization regime¹¹.

$$\beta_{gs} = 150 \frac{\left(1 - \varepsilon_g\right)^2 \mu_g}{\varepsilon_g d_p^2} + 1.75 \frac{\left(1 - \varepsilon_g\right) \rho_g |V_g - V_s|}{d_p} \tag{6}$$

$$\beta_{gs} = \frac{3}{7} \frac{(1 - \varepsilon_g) \varepsilon_g}{d_p} \rho_g |V_g - V_s| C_{D0} \omega (\varepsilon_g)$$
 (7)

with
$$0.74 < \varepsilon_g \le 0.82$$
, $\omega(\varepsilon_g) = -0.5769 + \frac{0.0214}{4(\varepsilon_g - 0.7463)^2 + 0.0044}$

with
$$0.82 < \varepsilon_g \le 0.97$$
, $\omega(\varepsilon_g) = -0.0101 + \frac{0.0038}{4(\varepsilon_g - 0.7789)^2 + 0.0040}$

with
$$\varepsilon_g > 0.97$$
,
 $\omega(\varepsilon_g) = -31.8295 + 32.8295\varepsilon_g$
and Re \Box 1000,
 $C_{D0} = \frac{24}{\text{Re}} (1 + 0.15 \,\text{Re}^{0.687})$
Re \geq 1000, $C_{D0} = 0.44$
where μ is the viscosity.

3. Results and Discussion

As stated in the experimental section, the appropriate simulation time obtained by time independency test had to be considered. The calculated results

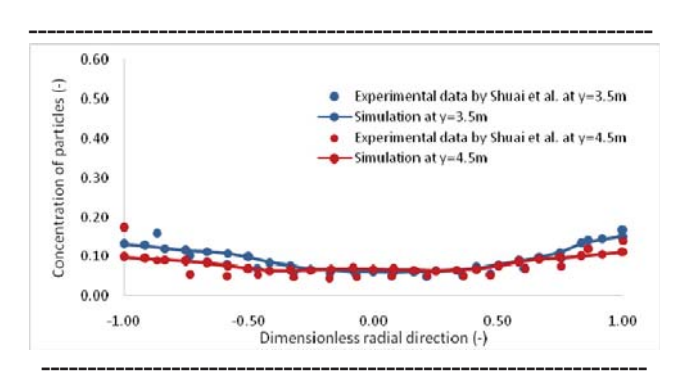


Fig. 2. Distribution of solid particle concentration comparing with the experimental data at 3.5 m and 4.5 m heights of air reactor in CLC.

showed that the solid particles in air reactor of CLC took around 20 s to fill up the system and came into quasi-steady state condition after 20 s. Therefore, the total simulation time for each simulation case was selected as 50 s to ensure the stability of the result.

3.1 Comparison with Shuai et al. experiment. [6]

The results in Fig. 2 displays distribution of the solid volume fraction at two different heights of air reactor in CLC. The simulation results showed the that simulation model got closely qualitative and quantitative results with the experimental data by Shuai et al. [6]. This confirms the accuracy and correctness of the numerical model. The results gave high and low concentrations of solid particles at the

Table 3. The analysis of variance when the response variable was ASVF.

110 , 1 .					
Source of	Sum of	Degree of	Mean	F value	p-value
variation	squares	freedom	square		
D	0.012213	1	0.012213	422.4054	< 0.0001
Error	0.000405	14	2.89E-05		
Total	0.012618	15			

Table 4. The analysis of variance when the response variable was SDSVF-RD.

Source of	Sum of	Degree of	Mean	F Value	p-value
variation	squares	freedom	square		
A	1.64E-06	1	1.64E-06	1.5628	0.2351
D	1.11E-05	1	1.11E-05	10.5178	0.0070
AD	6.27E-06	1	6.27E-06	5.9712	0.0310
Error	1.26E-05	12	1.05E-06		
Total	3.16E-05	15			

Table 5. The analysis of variance when the response variable was SDSVF-AD.

Source of	Sum of	Degree of	Mean square	F value	p-value
variation	squares	freedom			
D	3.67E-05	1	3.67E-05	17.5967	0.0009
Error	2.92E-05	14	2.08E-06		
Total	6.58E-05	15			

wall and center of air reactor in CLC, respectively. This profile is called core-annulus flow structure.

3.2 2⁴ factorial experimental design analysis

As stated above, the response variables in this study were the ASVF, the SDSVF-RD and the SDSVF-AD along the height of air reactor in CLC. For the suitable system condition, the highest value of ASVF is required which means that the quantity of solid particles in air reactor of CLC were high. In contrast, the low value of SDSVF-RD and SDSVF-AD shows the good mixing or homogeneity inside the system. The 2^k factorial experimental design analysis results are summarizes in Table 2. From the results, case 3 and case 13 showed the highest and lowest ASVF at 0.176 and 0.104, respectively. With respect to the SDSVF-RD,

case 3 had the highest value similar to ASVF while the lowest one was found in case 11. Besides, case 3 and case 15 represented the highest and lowest SDSVF-AD at 0.011 and 0.003, respectively.

Table 3 summarizes the analysis of variance (ANOVA) of the ASVF. The superficial gas velocity (D) affected the quality of solid volume fraction in air reactor. This is indicated by the lower value of p-value than 0.05. The ANOVA of the SDSVF-RD is shown in Table 4, the superficial gas velocity (D) and the interaction between the solid particle diameter and the superficial gas velocity (AD) were the affected parameters. In addition, from the experimental design theory, if the interaction (AD) is a significant effect, their first order effects (A and D) should be considered even as

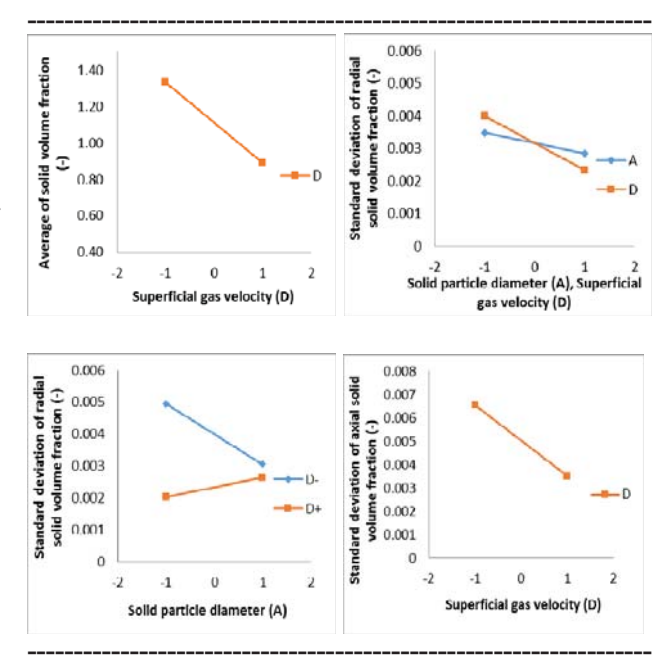


Fig. 3. The main effect and interaction effects for (a) ASVF (b-c) SDSVF-RD and (d) SDSVF-AD.

p-values are higher than 0.05. The operating parameter that had an effect on the SDSVF-AD is summarized in Table 5 which was the superficial gas velocity (D). Fig. 3 illustrates the plots of the main effects and interaction effects for each response variable. From the result of Fig. 3(a), a negative effect of superficial gas velocity (D) on ASVF was observed. When the superficial gas velocity (D) is decreased, the ASVF increases due to the increasing of supporting force. A high value of ASVF showed high solid particle concentration along the height of air reactor. In Fig. 3(b), the main effects of solid particle diameter (A) and superficial gas velocity (D) on SDSVF-RD were explored. The increasing of both solid particle diameter (A) and superficial gas velocity (D) had a negative effect on SDSVF-RD. This means that solid particles had uniform mixing in radial direction in air reactor of CLC. For the explanation, the high solid particle diameter is more difficult to form a cluster comparing to the low one while the high superficial gas velocity made the flow to be more homogeneous in radial direction. Moreover, Fig. 3(c) indicated that there was an interaction between the solid particle diameter and superficial gas velocity (AD). When the superficial gas velocity was high and low, the increasing of solid particle diameter then gave low and high values of SDSVF-RD, respectively. This also can be explained by the uniform velocity distribution and particle clustering inside the system. Fig. 3(d) represented the main effect plot of SDSVF-AD. When the superficial gas velocity (D) is increased, the SDSVF-AD decreases because a high superficial gas velocity effects collision between solid particles and particle cluster flow along the height of air reactor. This low value of the SDSVF-AD shows the homogeneous system mixing in axial direction in air reactor.

The contour plots of the solid volume fraction at 30 s for Cases 3, 11, 13 and 15 are shown in Fig. 4. The red and navy blue colors represent high and low values of the solid volume fraction, respectively. The solid volume fraction in Case 3 had high solid volume fraction than the other three cases while case 13 had low solid volume fraction which almost showed green and navy colors in air reactor of CLC, respectively. For case 11 and 15, the solid volume fraction had uniformly mixing along the axial and radial directions of air reactor of CLC, respectively. So both case had a low value of SDSVF-RD and SDSVD-AD. The obtained results confirmed the results from statistically ANOVA analysis.

4. Conclusion

This study used ANSYS FLUENT 14.0 to simulate hydrodynamics and mixing in the air reactor of CLC with different operating parameters. The EMMS drag model gave the similar results to the experimental data. The simulation showed the formation of core-annulus flow structure. From the factorial experimental design analysis, the superficial velocity (D) had an affected on the ASVF and the SDSVF-AD. The parameters that affected on the SDSVF-RD were solid particle diameter (A), superficial gas velocity (D) and interaction between solid particle diameter and the superficial gas velocity (AD). From all the results, it can be concluded that the most significant parameter for the gas-solid particle mixing inside air reactor of CLC was the superficial gas velocity (D). The results in

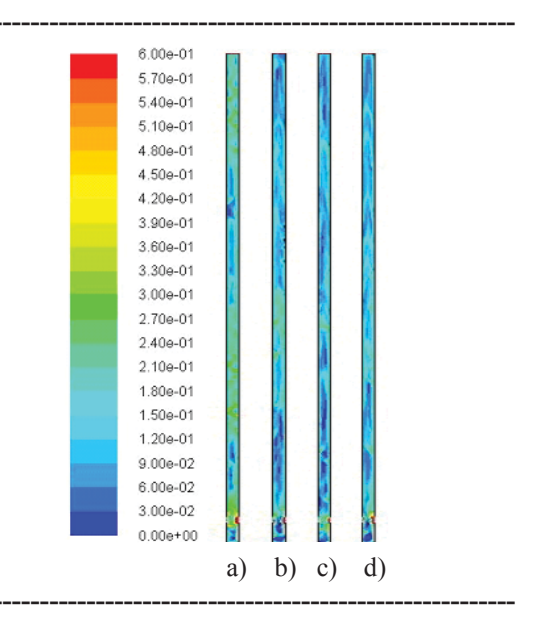


Fig. 4. The contours of solid volume fraction at 30 s in air reactor with a) Case 3, b) Case 11, c) Case 13 and Case 15.

this study can be used to improve the mixing in conventional air reactor of CLC and to design and scale-up of the optimum novel CLC system.

Acknowledgements

This study was financially supported by National Research University Project, Office of Higher Education Commission (WCU-044-CC-57), the CU Graduate School Thesis Grant and the Grant from PETRO-MAT, also, partially supported by TRF (TRG5780205) and the Ratchadaphisek Somphot Endowment Fund by CU Fund.

References

- 1. Wolf et al. Comparison of nickel- and iron-based oxygen carriers in chemical looping combustion for CO capture in power generation. *Fuel*, 84:993-1006 (2005).
- 2. Gayán et al. Assessment of technological solutions for improving chemical looping combustion of solid fuels with CO₂ capture. *Chemical Engineering Journal*, 233:56-69 (2013).
- 3. Wang et al. Simulation of flow behavior of particles by cluster structure-dependent drag coefficient model for chemical looping combustion process: Air reactor modeling. *Fuel Processing Technology*, 104:219-233 (2012).
- 4. Lu et al. Eulerian simulation of gas-solid flows with particles of Geldart groups A, B and D using EMMS-based meso-scale model. *Chemical Engineering Science*, 66:4624-4635 (2011).
- 5. Zhou et al. Effect of wall boundary condition on CFD simulation of CFB risers. *Particuology*, 11:556-565 (2013).
- 6. Shuai et al. Fluid dynamic simulation in a chemical looping combustion with two interconnected fluidized beds. *Fuel Processing Technology*, 92:385-393 (2011).
- Chalermsinsuwan et al. Computational fluid dynamics of circulating fluidized bed downer: Study of modeling parameters and system hydrodynamic characteristics. *Chemical Engineering Journal*, 189-190:314-335 (2012).
- 8. Ye et al. Two-fluid modeling of Geldart A particles in gas-fluidized beds. *Particulogy*, 6:540-548 (2008).
- 9. Yang et al. Simulation of heterogeneous structure in a circulating fluidized-bed riser by combining the two-fluid model with the EMMS approach. *Industrial and Engineering Chemistry* research, 43:5548-5561 (2004).
- 10. Chalermsinsuwan et al. A computational fluid dynamics design of a carbon dioxide sorption circulating fluidized bed. *AIChE Journal*, 56(11):2805-2824 (2010).
- 11. Zhou et al. Three-dimensional simulation of dense suspension upflow regime in high-density CFB risers with EMMS-based two-fluid model. *Chemical Engineering Science*, 107:206-217 (2014).







Effect of operating parameters in fuel reactor of chemical looping combustion using computational fluid dynamic simulation

R. Sornumpol¹, B. Chalermsinsuwan^{1,2}, P. Piumsomboon^{1,2}*

¹ Department of Chemical Technology, Faculty of Science, Chulalongkorn University,

254 Phayathai Road, Patumwan, Bangkok 10330, Thailand

² Center of Excellence on Petrochemical and Materials Technology, Chulalongkorn University,

254, Phayathai Road, Patumwan, Bangkok 10330, Thailand

*E-mail: pornpote.p@chula.ac.th

Abstract - Mixing of particles is an important factor in fluidized-bed reactors. The horizontal mixing of fuel particles affects the performance of the beds since it has a great influence on the distribution of heat release from the fuel. In bubbling fluidized bed, the particle movement is caused by rising bubbles. The bubbles transport particles upwards in their wakes and particles then flow downwards. In the literature, there are many variables affecting on mixing. In this study, the effect of operating parameters on hydrodynamics in the fuel reactor was conducted by using commercial computational fluid dynamics (CFD) simulator, ANSYS FLUENT. The CFD simulation of the bed hydrodynamics was based on the concept of Euler-Euler two-fluid model in combination with kinetic theory of granular flow (KTGF). Hydrodynamic behavior was investigated in a bubbling fluidized bed reactor. The Gidaspow drag model was selected to use for computing the momentum exchange coefficients. The mixing behavior of gassolid bubbling fluidized bed had been studied in terms of initial static bed height, properties of particle and fluidization velocity. The mixing index or standard deviation of solid volume fraction in axial and radial directions was selected as response parameter to determine mixing efficiency. The twodimensional Cartesian mathematical model was validated by comparing with literature experiment. The simulated axial solid velocity, the granular temperature and the solid volume fraction profiles were consistently matched with the experimental results. From the analysis of variance, particle diameter and initial bed height had a significant effect on mixing in axial direction.

Keywords: Chemical looping, Computational fluid dynamics, Fuel reactor, Mixing, ANOVA.

I. Introduction

Since the beginning of industrialization, carbon dioxide is the primary greenhouse gas emitted from industries. The main sources of CO₂ emissions were the combustion of fossil fuels (coal, natural gas, and oil) from, transportation and industrial processes. The released CO₂to the atmosphere has caused the earth's surface temperature to rise, since its lifetime in the atmosphere is long. Consequently, the globally averaged CO₂ concentration in the atmosphere has enhanced from the pre-industrial levels of 285 ppm, to a current 401.33 ppm [1]. Chemical looping combustion is a carbon capture technology where air and fuel are not directly mixed. Therefore CO2 is not diluted by N₂ and no energy is required for gas separation. For the literature review of computational fluid dynamics of chemical looping combustion (CLC), Harichandan et al. [2] studied CFD analysis of bubble hydrodynamics in a fuel reactor for a hydrogen-fueled chemical looping combustion system. The numerical result showed similar trend in mole fraction of products with the experimental results. Wang et al. [3] investigated hydrodynamic simulation of fuel reactor in CLC by using NiO oxygen carrier and CH₄ fuel. The EMMS drag model was applied. It gave more accurate result comparing with the experimental gas product composition results. Zhang et al. [4] studied the cold flow experiment and modeling of chemical looping combustion using Fe₂O₃/Al₂O₃ oxygen carrier and CH₄ fuel. The results revealed that, under the design situation, the conversion rate of CH₄ reaches 88.2% and unburned methane escapes from the reactor with large bubbles. Until now, only few investigation of operating variable effect on hydrodynamic behavior in bubbling fluidized bed has been studied. In addition, there are no literature studies on operating variable effect on mixing by simulation of cold flow in bubbling fluidized reactor.

The objective of this study is to investigate the effect of initial bed height, particle size, particle density

and fluidization gas velocity on mixing of gas-solid particle in axial and radial directions using experimental design method and to develop numerical model to describe a steady state performance of fuel reactor in bubbling fluidized bed chemical looping combustion. Numerical results were validated with experimental result by Jung et al. (2005).

II. Material and Methods

2.1. Numerical model

The Euler-Euler model was employed for the simulation of gas-solid hydrodynamic in bubbling fluidized bed. The Eulerian-Eulerian model assumes that both the gas and solid phases are continuous phase. The hydrodynamic model consists of the conservation of mass and momentum for each phase, the constitutive equations and the interaction between two phases. The Gidaspow interphase exchange coefficient model was selected to calculate in this study.

Mass conservation equations:

$$\frac{\partial (\varepsilon_g \rho_g)}{\partial t} + \forall (\varepsilon_g \rho_g u_g) = \dot{m}_g$$
 (1)

$$\frac{\partial(\varepsilon_s \rho_s)}{\partial t} + \forall(\varepsilon_s \rho_s u_s) = \dot{m}_s \qquad (2)$$

where ε is the concentration of each phase, u is the velocity, $\underline{\rho}$ is the density, t is the time, (s) is for the solid particle phase and (g) is for the gas phase.

Momentum conservation equations:

$$\frac{\frac{\partial(\varepsilon_{g}\rho_{g}u_{g})}{\partial t} + \forall(\varepsilon_{g}\rho_{g}u_{g}) = -\varepsilon_{g}\nabla p + \varepsilon_{g}\forall\tau_{g} + \varepsilon_{g}\rho_{g}g - \beta(u_{g} - u_{s}) + m_{g}u_{g}}{\beta(u_{g} - u_{s}) + m_{g}u_{g}}$$
(3)

$$\frac{\frac{\partial(\varepsilon_{s}\rho_{s}u_{s})}{\partial t} + \forall(\varepsilon_{s}\rho_{s}u_{s}) = -\varepsilon_{s}\nabla p + \varepsilon_{s}\forall\tau_{s} + \varepsilon_{s}\rho_{s}g - \beta(u_{g} - u_{s}) + \dot{m}_{s}u_{s}}{\beta(u_{g} - u_{s}) + \dot{m}_{s}u_{s}}$$
(4)

where g is gravity acceleration, P is the pressure, β is the momentum interphase exchange.

Granular temperature conservation equation:

$$\frac{3}{2} \left[\frac{\partial (\varepsilon_s \rho_s \theta)}{\partial t} + \forall (\varepsilon_s \rho_s \theta) u_s \right] = (\forall p_s I + \tau_s) : \forall u_s + \forall (k_s \forall \theta) - \gamma_s$$
 (5)

where $\underline{\theta}$ is the solid fluctuating kinetic energy, \underline{K}_{2} is the conductivity of solid fluctuating kinetic energy, I is







the unit vector and \mathbf{y}_3 is the collisional dissipation of solid fluctuating kinetic energy.

A finite volume method based on phased-coupled SIMPLE algorithm was used. In this study, the simulations were run for 20 s with time step of $1x10^{-4}$ sec.

2.2. System description

Commercial simulator, ANSYS FLUENT, was used to compute 2D Cartesian fuel reactor as shown in Fig. 1(a). The reactor had 0.155 m diameter and 0.40 m height. The solid particles were filled with a height of 0.20 m and solid volume fraction of 0.40. The bottom of reactor was set according to the inlet velocity and the top of reactor is set according to the outflow condition. The used system descriptions and variables are defined in Table 1. These system was referred to the experimental procedure by Ahuja and Patwardhan [5].

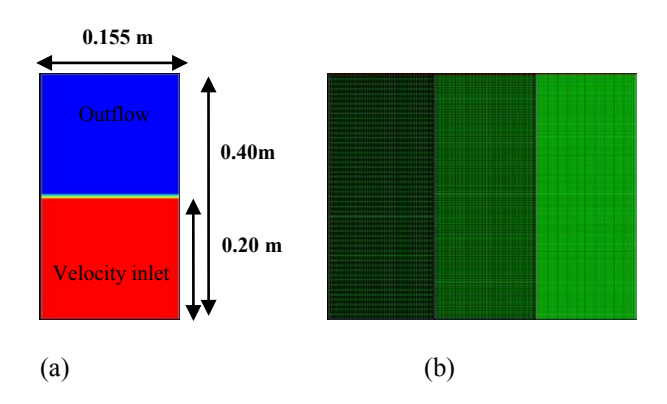


Fig. 1. (a) Schematic of the fuel reactor and (b) two-dimensional computational domain with (i) 38x50 (ii) 75x100 (iii) 150x200.

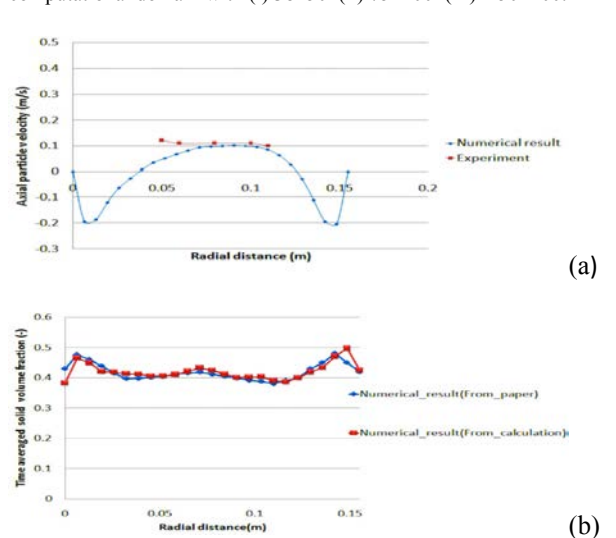


Fig. 2. (a) time-averaged axial particle velocity in radial direction at the height of 0.14mand (b)time-averaged solid volume fraction in radial direction at the height of 0.14m.

Table 1. System description and variables.

Description	Value
Operating pressure(Pa)	101325
Gas density(kg/m³)	1.22
Gas viscosity(kg/m·s)	1.82x10 ⁻⁵
Solid particle density(kg/m³)	2500
Solid particle diameter (µm)	530
Restitution coefficient between particles(-)	0.99
Restitution coefficient between particles and wall(-)	1
Specularity coefficient (-)	0.60
Solid inlet volume fraction at maximum packing limit(-)	0.63
Gas inlet velocity (m/s)	0.59

2.3. Experimental design

This study examined the impact of operating conditions on the mixing in axial and radial directions by analyzing the complete set of CFD analysis data composed of 16cases. Experimental design method was used to determine the set of cases that the CFD code will run. A complete factorial design, 4 factors with 2 levels, requires 16 experimental runs.

In this study, properties of nickel oxide/nickel aluminate metal oxide particle were referred from Brandvoll [6]. Particle size was selected from geldart group B with 200 and 600 micron. Particle density was used with 1300 and 2350kg/m^3 . Initial static bed height and fluidization velocity were selected based on Escudero[7]. Initial static bed height was varied from 0.50D to 0.75D and gas velocity was varied from 1.50 to 1.75 U_{mf} (minimum fluidization velocity). Because the bubbling fluidized bed is batch operation, if we run initial static bed height and gas velocity over this range, the particle will lost out from the system. As stated above, the required total numbers of experiments for four variables at two levels were $2^4 = 16$ as shown in Table 2.

III. Results Discussion

3.1. Model validation

Before analyzing the data, the simulation based on the condition in Table 1 was investigated. The axial particle velocity and solid volume fraction in radial direction at the height 0.14 m were collected between 5 to 20 s as shown in Figs. 2(a) and (b), respectively. All the numerical results were consistent with the experiments of Jung et al. [8]. Both the result of solid volume fraction and axial particle velocity showed core annular flow structure. The solid particles were carried up by the gas at central region and fallen down at annular region.







3.2. Grid independence study

With the high grid resolution, the computational fluid dynamic then took a long time for calculating step. Therefore, a minimum resolution but sufficient grid numbers should be explored for the accurate and correct data. This simulation compared three different mesh sizes $(38 \times 50, 75 \times 100 \text{ and } 150 \times 200)$ to investigate grid independency test as shown in Fig. 3.

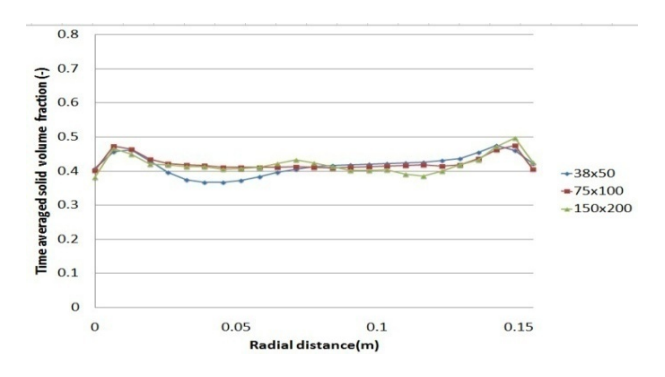


Fig. 3. Grid independency test for solid volume fraction at z=0.14m.

Fig. 3 displays the result of solid volume fraction in radial direction at $z=0.14\,$ m with three different meshes. All the mesh sizes showed the same trend. However, the medium mesh(75 x 100) and fine mesh (150 x 200) showed more consistent data than the coarse mesh (38 x 50). Therefore, the grid with medium size(75x100) was selected to compute 2D - Cartesian bubbling fluidized bed of fuel reactor in CLC in this study.

3.3. Time independency test

In this study, the total simulation time was $25~\rm s$. The steady state operating condition was achieved when the absolute pressure reached an approximately constant value which was after $5~\rm s$ simulation time. The time averaged results presented here were then calculated between $5~\rm and~20~\rm s$. Fig. 4 shows time independency test by overall pressure drop across bed in bubbling fluidized bed reactor.

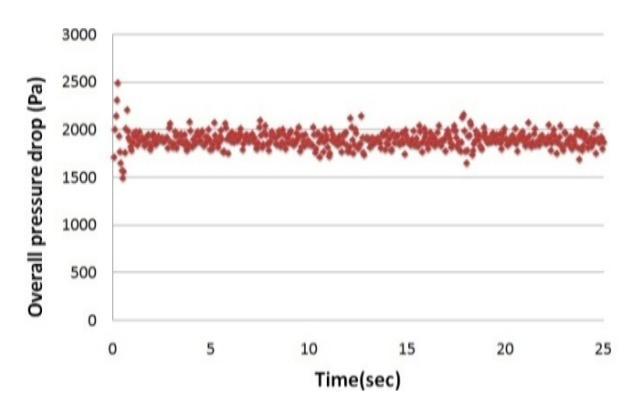


Fig. 4. Time independency test for overall pressure drop.







Table 2. Summary result of standard deviation of solid volume fraction in radial and axial directions.

Treatment	A(micron)	B(m)	$C(kg/m^3)$	D(m/s)	SD axial direction	SD radial direction
1	200	0.50D	1300	1.5Umf	0.1844	4.29E-05
a	600	0.50D	1300	1.5Umf	0.1774	4.51E-04
b	200	0.75D	1300	1.5Umf	0.2449	1.17E-03
ab	600	0.75D	1300	1.5Umf	0.2334	1.01E-03
с	200	0.50D	2350	1.5Umf	0.1846	4.66E-03
ac	600	0.50D	2350	1.5Umf	0.1701	5.72E-04
bc	200	0.75D	2350	1.5Umf	0.2464	3.94E-03
abc	600	0.75D	2350	1.5Umf	0.2235	3.40E-03
d	200	0.50D	1300	1.75Umf	0.1800	8.35E-04
ad	600	0.50D	1300	1.75Umf	0.1687	3.04E-04
bd	200	0.75D	1300	1.75Umf	0.2377	2.17E-03
abd	600	0.75D	1300	1.75Umf	0.2223	2.29E-03
cd	200	0.50D	2350	1.75Umf	0.1817	1.96E-03
acd	600	0.50D	2350	1.75Umf	0.1594	1.67E-03
bed	200	0.75D	2350	1.75Umf	0.2400	6.42E-03
abcd	600	0.75D	2350	1.75Umf	0.2072	3.69E-03

3.4. Experimental design

The independent variables affecting mixing in radial and axial directions which were (i) initial static bed height (ii) diameter of particle (iii) fluidization velocity and (iv) density of particle and their response are shown in Table 2. In heterogeneous reaction, the degree of reaction rate depends on rate of mass transfer and mixing index. Therefore solid distribution in bubbling fluidized bed is key parameter for high conversion. In this study, standard deviations (S.D.) of solid volume fraction in axial and radial directions were selected as the response parameters.

3.4.1.Effect of operating conditions on S.D. of solid volume fraction in axial direction

In this study, the results were analyzed with ANOVA for two level factorial design. The analysis of variance for standard deviation of solid volume fraction in axial direction was shown in Table 3. The highly significant variable on s tandard deviation of solid volume fraction in axial direction were particle diameter, initial static bed height and fluidization velocity. In addition, the analysis showed mild interaction between particle diameter and particle density. Figs. 5(a) and (b) show the main effect and interaction plots of each significant factor. From the results, increasing initial static bed height (B) from 0.50D to 0.75D will enhance standard deviation in axial direction. The standard deviation in axial direction decreases with the increasing of particle

diameter (A) and fluidization velocity (D). Norouziet al. [10]concluded similar effect of aspect ratio of the bed (H/D) and fluidization velocity. The increasing of gas velocity caused gross internal circulation while the increasing of aspect ratio changed the solid flow pattern in the bed. For static bed height, if the same amount of solid particle and fluidization velocity were set ,the solid particle distribution will not be uniform along the bed. From Fig. 5(b), the significant interaction effect can be seen from the lines in graph not being parallel. The result revealed the presence of interaction between experimental variables. The particle density and diameter had negative interaction effect. Large particle size and high particle density increases the mixing in axial direction more than small particle size and low particle density. According to minimum fluidization equation, minimum fluidization velocity depends on particle properties. With different operating conditions, different circulation will occur which promotes mixing in bubbling fluidized bed.

Table 3:The analysis of variance for standard deviation of solid volume fraction in axial direction.

Source	Sum of squares	DF	Mean square	F- Value	Prob> F
A	1.18E-03	1	1.18E-03	65.32	< 0.0001
В	0.013	1	0.013	694.97	< 0.0001
D	2.89E-04	1	2.89E-04	15.93	0.0021
AC	1.40E-04	1	1.40E-04	7.73	0.0179
Residual	1.99E-04	11	1.81E-05		
Total	0.014	15			

The 4th TIChE International Conference 2014 "Changes: Cleaner Energy, Leaner Processes, Better Living" Chiang Mai, Thailand, December 18-19, 2014

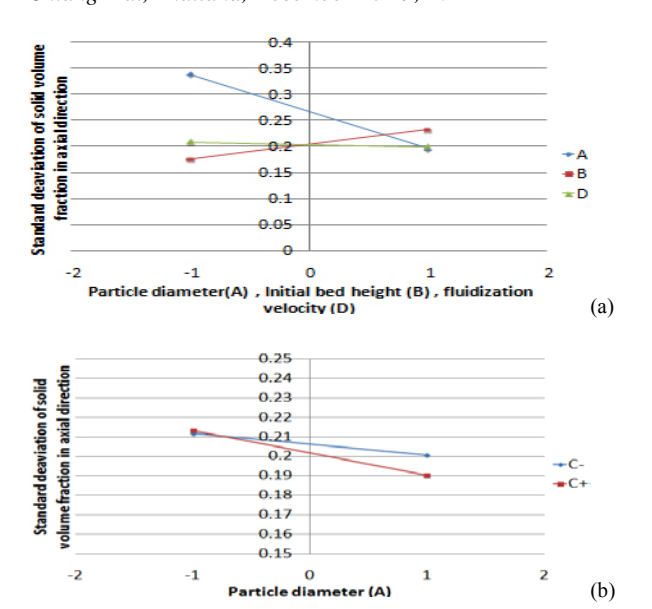


Fig. 5. The effect of different factors (a) and their interaction (b) on standard deviation in axial direction.

3.4.2.Effect of operating conditions on S.D. of solid volume fraction in radial direction

Table 4: The analysis of variance for standard deviation of solid volume fraction in radial direction.

	Sum of		Mean		
Source	squares	DF	square	F-value	Prob> F
Α	3.39E-06	1	3.39E-06	55.7442837	0.0175
В	1.08E-05	1	1.08E-05	177.299219	0.0056
С	1.93E-05	1	1.93E-05	317.520296	0.0031
D	1.29E-06	1	1.29E-06	21.1394989	0.0442
AB	1.70E-07	1	1.70E-07	2.78668632	0.2370
AC	3.09E-06	1	3.09E-06	50.7408562	0.0191
ВС	6.15E-07	1	6.15E-07	10.1083398	0.0863
BD	2.61E-06	1	2.61E-06	42.9032912	0.0225
ABC	1.35E-07	1	1.35E-07	2.21574994	0.2750
ABD	1.71E-06	1	1.71E-06	28.0415009	0.0339
ACD	2.05E-07	1	2.05E-07	3.36772321	0.2079
BCD	6.32E-07	1	6.32E-07	10.3912584	0.0843
ABCD	3.66E-06	1	3.66E-06	60.1186358	0.0162
Residual	1.22E-07	2	6.09E-08		
Total	4.77E-05	15			

The analysis of variance for standard deviation of solid volume fraction in radial direction was shown in Table 4. From the table, all the main effects had a significant effect on the response. The two variable interaction between diameter of particle and density of particle and that between initial bed height and fluidization velocity also had considerable effect. Fig. 6(a) reveals the significant main effect on







the mixing in radial direction. For the large main effect, the high particle density will decrease gas-solid mixing efficiency. Gan et al. [11]found three main solids mixing mechanisms for the solids in fluidized beds under bubbling conditions: 1) the solid particles are pulled upwards by the wake behind rising bubbles, 2) particles flow downwards with the emulsion phase around bubbles and 3) particles are scattered over the dense bed surface when a bubble erupts. The solid mixing in dense fluidized bed is then caused by bubbles which mainly depend on particle density. In addition, lateral dispersion coefficient increases with the decreasing of particle size and increasing of superficial gas velocity. When increasing gas velocity, it will enlarge bubble size. The bubble moves faster and more vigorous. The lateral mixing increases with increasing static bed height. With this condition, the bubble becomes larger and faster caused by the coalescence as they rise up through the bed.

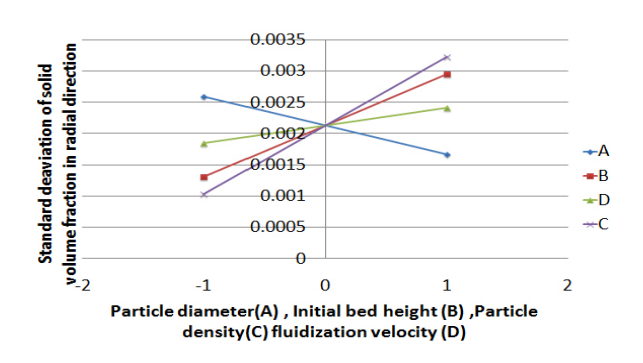


Fig. 6. The main effect of different factors on standard deviation in radial direction

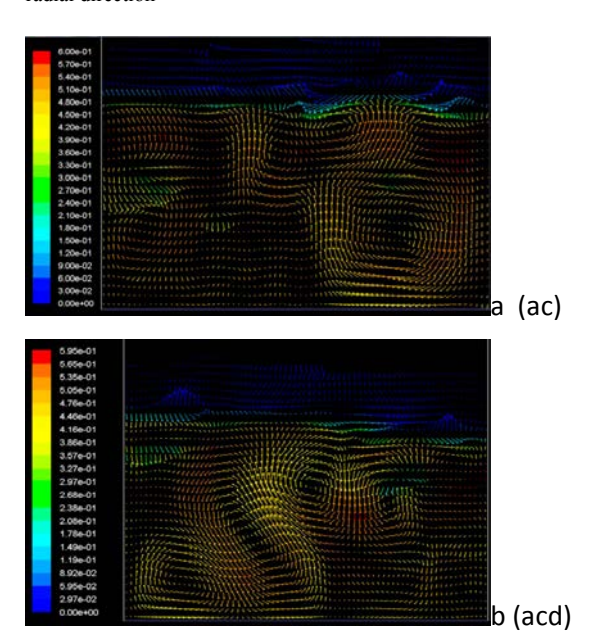


Fig.7.Solid volume fraction contours and solid flux vector for (a) ac and (b) acd at 15 s.

3.4.3. Effect of operating condition on flow pattern

When increasing fluidization velocity or properties of solid, the bubble grows and induces particle in a circulation loop. This is a mechanism for mixing in bubbling fluidized bed. From Fig. 7, contour plot of solid volume fraction shows some internal circulation in "acd" case more than "ac" case when enhancing fluidization velocity.

IV. Conclusion

In this study, the combination of computational fluid dynamic and design of experiment was used to study the effect of operating parameters based on sixteen simulation cases.

From the ANOVA result, it can be concluded that three main parameters had the significant effect on mixing in axial direction and all main parameters had the significant effect on mixing in radial direction. In addition, some mild interaction effects were obtained. For mixing in axial direction, negative interaction between particle size and particle density was found. From the contour of solid volume fraction at 15 s, adjusting operating parameters to high level such as particle size, particle density and fluidization velocity, the bubble were then generated and coalesced to form larger bubble. It is commonly recognized that solids mixing in a fluidized bed is mainly caused by the movement of bubbles. Bubbles induce the solids mixing by stirring the bed material as they are rising through the dense phase. The lateral solids mixing has a major influence on the performance of fuel reactor.

Acknowledgment

This study was financially supported by the Grants from the National Research University Project, Office of Higher Education Commission (WCU-044-CC-57), from the Thailand Research Fund for fiscal vear 2014-2016 (TRG5780205), from Chulalongkorn University (Ratchadaphiseksomphot Endowment Fund), from the Faculty of Science of Chulalongkorn University and from the Center of Excellence on Petrochemical and Materials Technology, Chulalongkorn University.

References

[1] IEA, 2008, "World Energy Outlook 2008", International Energy Agency (IEA), Paris, France, available online at www.iea.org.







- [2] Harichandan, A., Shamim, T., CFD Analysis of Bubble Hydrodynamics in a Fuel Reactor for a Hydrogen-Fueled Chemical Looping Combustion system, Energy Conversion and Management, Volume 86, October 2014, Pages 1010-1022.
- [3] Wang, S., Lu, H., Li, D., Tang, Y. Simulation of the Chemical Looping Reforming Process in the Fuel Reactor with a Bubble-based Energy Minimization Multiscale Model, Energy & Fuels, 2013, 27 (8), Pages 5008–5015.
- [4] Zhang, S., Ma, J., Hu, X., Zhao, H., Wang, B., Zheng, C. Reactor Design, Cold-Model Experiment and CFD Modeling for Chemical Looping Combustion, Cleaner Combustion and Sustainable World. Springer,2013, Pages 1209-1217.
- [5] Loha, C., Chattopadhyay, H., Chatterjee, K.P. Assessment of drag models in simulating bubbling fluidized bed hydrodynamics, Chemical Engineering S cience, 2012, 75, Pages 400-407.
- [6] Brandvoll, O. Chemical Looping Combustion

 Reduction of nickel oxide/nickel aluminate
 with hydrogen. Doctoral thesis in Norwegian
 University of Science and Technology,
 Faculty of Engineering Science and
 Technology, Department of Energy and
 Process Engineering, 2005.
- [7] Escudero, D.R. Be d height and material density effects on f luidized bed hydrodynamics. Master thesis Iowa State University Ames, Iowa, 2010.
- [8] Jung, J., Gidaspow, D., Gamwo, K.I. Bubble computation, Granular temperatures, and Reynolds stresses, Chemical Engineering Communications, 2006, 193, Pages 946–975.
- [9] Montgomery, D.C. Design and Analysis of Experiments, Wiley, USA.
- [10] Norouzi, H.R., Mostoufi, N., Mansourpour, Z.,Sotudeh-Gharebagh, R., Chaouki, J. Characterization of solids mixing patterns in bubbling fluidized beds, Chemical Engineering Research and Design,2011, 89, Pages 817-826.
- [11] Gan, L., Lu, X., Wang, Q., Hu, Q., Chen, Y., Xu, J., Experimental study on lateral mixing of particles in a quasi-slot-rectangular spouted bed, Powder Technology 2013, 243, Pages 1-8.